

# Atomic Force Microscopy of Biological Systems: Quantitative Imaging and Nanomotion Detection

THÈSE N° 8334 (2018)

PRÉSENTÉE LE 13 AVRIL 2018

À LA FACULTÉ DES SCIENCES DE BASE  
LABORATOIRE DE PHYSIQUE DE LA MATIÈRE VIVANTE  
PROGRAMME DOCTORAL EN PHYSIQUE

ÉCOLE POLYTECHNIQUE FÉDÉRALE DE LAUSANNE

POUR L'OBTENTION DU GRADE DE DOCTEUR ÈS SCIENCES

PAR

**Petar STUPAR**

acceptée sur proposition du jury:

Prof. F. Mila, président du jury  
Prof. G. Dietler, Dr S. Kasas, directeurs de thèse  
Prof. G. Greub, rapporteur  
Prof. R. Willaert, rapporteur  
Prof. Ph. Renaud, rapporteur



ÉCOLE POLYTECHNIQUE  
FÉDÉRALE DE LAUSANNE

Suisse  
2018



## Résumé

Cette thèse concerne l'application des différentes modalités de la microscopie à force atomique (AFM) pour l'étude de systèmes vivants. Le premier chapitre contient une introduction à l'AFM et au mode d'imagerie appelée Quantitative Imaging. Les nombreuses applications de cette technique à des bactériennes des levures ainsi qu'à des cellules végétales et de mammifères sont présentés dans ce chapitre. On y trouve également un compte rendu d'une étude visant à déterminer les modifications du cytosquelette d'ostéoblastes lors de leur exposition à des conditions simulant l'absence de gravité. La deuxième section du chapitre concerne l'exploration des propriétés adhésives de bactéries au moyen de pointes AFM fonctionnalisées par des anticorps. Cette propriété bactérienne, encore mal comprise, joue un rôle important lors de la première phase de l'infection. L'étude des propriétés mécaniques de cellules végétales est également abordée dans ce chapitre.

Une grande partie de la thèse est dédié au développement et aux applications d'une nouvelle technique de détection basée sur le mouvement nanométrique des organismes vivants. Cette technique accélère de manière spectaculaire la détermination de sensibilité aux antibiotiques des bactéries et son application à large échelle permettrait de freiner considérablement la prolifération de ces microorganismes. La prolifération de germes résistants aux antibiotiques étant un problème majeur de santé publique au niveau mondial.

Le chapitre 3 commence par une description de cette nouvelle technique de détection et de ses applications potentielles. La première application présentée concerne la détermination rapide de sensibilité aux antibiotiques (DRSA) de germes présents dans le sang. Les sections suivantes concernent la DRSA de bactéries à croissance lente comme la *Bordetella pertussis*, l'exploration de l'activité métabolique des mitochondries et la détermination de sensibilité des cellules cancéreuses aux antimétabolites.

La dernière section du chapitre 3 traite de l'origine des mouvements nanométriques des organismes vivants. La thèse se termine par un résumé et une discussion des possibles applications de cette technologie.

**Mots-clés:** Microscopie à Force Atomique, AFM, imagerie quantitative, cartographie des forces, rigidité, adhérence, nanomotion, biomécanique, propriétés nanomécaniques, biocapteur, résistance aux antimicrobiens, dépistage des drogues, tests DRSA



## Abstract

The core of this thesis is the application of different modalities of atomic force microscopy to study living systems. After a brief introduction, quantitative imaging state of the art is presented and the applications for mammalian, plant, bacterial, and yeast cells are reviewed. The same chapter contains research effort about exploring nanomechanical properties of bone cells exposed to conditions that simulate the ones in outer space, in order to investigate the changes in architectural rearrangements of cells during space flight. The next section takes the focus on probing bacterial adhesion sites with an antibody-modified tip, a research important for the understanding of how bacterial cells adhere to the host and establish an infection. Plant cells and their nanomechanical profiles are also covered in the chapter.

A large portion of the thesis consists in development of a new nanomechanical sensing technique, and the exploration of its potential applications. The technique is based on the AFM detection method and focuses on transducing small fluctuations that define living systems into a measurable mechanical change in the cantilever. The fact that there is a disproportionate rise in antimicrobial-resistant bacteria and that our lives depend on the new drugs and diagnostic tools to fight them has fueled the first and largest application of the technique – rapid antimicrobial susceptibility testing. Chapter 3 starts with the introduction of the technique, basic principles and guidelines for its use, and continues on potential applications. Proof of principle of the technique is presented, showing experimental results using blind clinical samples of bloodstream infectious agents. A separate section is devoted to investigations concerning slow-growing bacteria and the application of the technique to rapidly determine which antibiotic would best work against them. It then expands on the applications towards detecting metabolic activity of mitochondria and their response to substrates and inhibition. Furthermore, the method has been described as a rapid anti-cancer profiling tool that might pave the way towards a diagnostic platform for personalized medical treatment.

The final section of the third chapter contains the current knowledge of the origins of oscillatory movement that governs the nanomotion technique. It presents different hypothesis and results towards exploring them. The thesis ends with a summary of the main ideas and conclusions about the presented work and future perspectives.

**Keywords:** Atomic Force Microscopy, AFM, quantitative imaging, force mapping, stiffness, adhesion, nanomotion, biomechanics, nanomechanical properties, biosensor, antimicrobial resistance, drug screening, AST testing



*To Helena and Petar,  
my family and friends*





## Acknowledgements

Staying within one research field was not my thing and I was extremely happy to have an opportunity for a PhD in a rather multidisciplinary environment. Even within a single day, during my PhD, I have touched various fields, spanning from biology of sample preparation and handling, chemistry of its attachment, physics of method's principles, programming for the signal analysis, etc. Apart from being grateful for all that, I very much appreciate the kindness of all my colleagues and people I met during this journey.

First and foremost, I would like to express my deepest gratitude to Sandor, a valuable and supporting mentor, kind friend and colleague! Ever since the first day, his guidance and understanding kept me going and his cheerful character, stories and jokes told are something I will always gladly remember. His innovative approach, ideas, creativity and thirst for knowledge were highly motivating, and I can only say words of appreciation.

I would also like to thank Giovanni for allowing me to embark on this journey and to become an independent researcher. His expertise and wide knowledge helped me learn a lot, and his full support and trust gave me confidence in academic world.

Much of support and guidance came from Gianni as well, to whom I owe a great deal of thanks. He was always keen on sharing his knowledge and experience, and gave me valuable advice whenever I stumbled upon a problem.

Wonderful atmosphere in our group was always present, owing to great colleagues I had! I thank Wojtek, not just for a nice time we had sharing the office, but also for the help with instrumentation and technical difficulties. I also acknowledge the help from Carine, her attention and commitment in our work together. Thanks to Michel and Christine I never had technical or administrative issues. Special thanks to Katya, who was always happy to discuss the subjects of personal and professional growth, a kind and supportive friend. I thank to all members of our group: Anton S., Jiangtao, Serguei, Kamila, Philippe, Zeno, Raphael, Anton M., Caroline, Ines, for being great colleagues and good friends.

I would also like to extend my appreciation to all the lovely collaborators I worked with. In particular, I am grateful to Onya for his valuable advice, suggestions, friendly and compassionate attitude towards our work.

Lastly, I express my deepest gratitude to my family for their endless support and love, and all my friends for being a huge part of my life.

Thank you all,

Petar

A handwritten signature in blue ink, appearing to read 'Петар Љуѓуап' (Petar Lyujap).



# Table of Contents

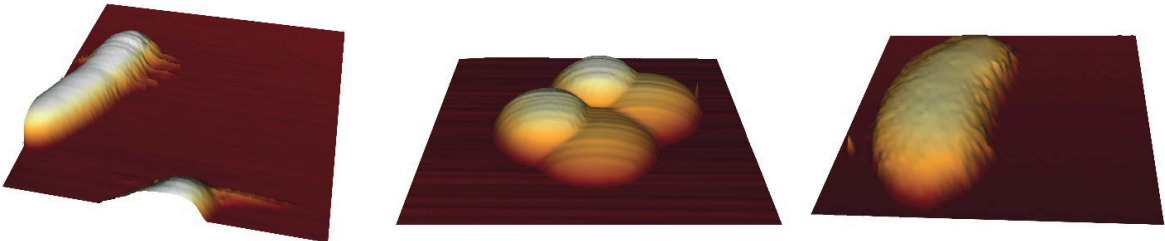
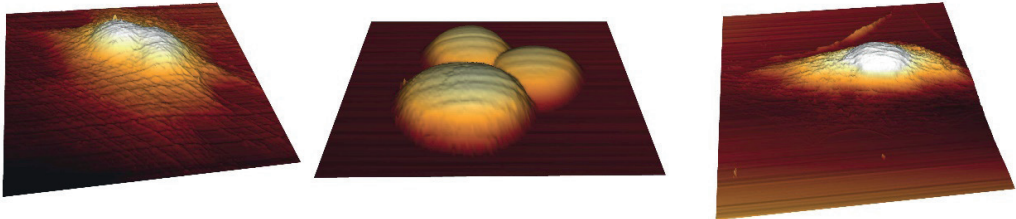
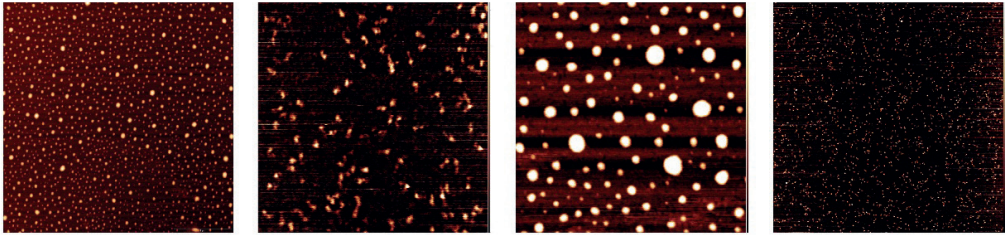
<b>RÉSUMÉ</b> .....	<b>2</b>
<b>ABSTRACT</b> .....	<b>4</b>
<b>ACKNOWLEDGEMENTS</b> .....	<b>8</b>
<b>TABLE OF CONTENTS</b> .....	<b>10</b>
<b>CHAPTER 1: INTRODUCTION</b> .....	<b>1</b>
1.1 ATOMIC FORCE MICROSCOPY FUNDAMENTALS.....	3
1.1.1 <i>Cantilever calibration</i> .....	5
1.1.2 <i>Cantilevers in liquid environment</i> .....	7
1.1.3 <i>Detection method</i> .....	8
1.2 AFM MODES.....	9
1.2.1 <i>Contact Mode</i> .....	10
1.2.2 <i>Tapping Mode</i> .....	10
1.2.3 <i>Non-contact Mode</i> .....	11
1.2.4 <i>Force Spectroscopy</i> .....	11
1.3 BIOSENSORS.....	14
1.3.1 <i>Biosensor classification</i> .....	14
1.3.2 <i>Cantilever-based nanomechanical biosensors</i> .....	16
1.3.3 <i>Sample attachment</i> .....	19
<b>CHAPTER 2: QUANTITATIVE IMAGING AND MAPPING</b> .....	<b>21</b>
2.1 QUANTITATIVE IMAGING TECHNIQUE.....	22
2.1.1 <i>QI™ mode by JPK Instruments</i> .....	24
2.2 STATE OF THE ART.....	26
2.2.1 <i>AFM of bacteria</i> .....	26
2.2.2 <i>AFM of yeast cells</i> .....	28
2.2.3 <i>AFM of plant cells</i> .....	30
2.2.4 <i>AFM of mammalian cells</i> .....	32
2.2.5 <i>Conclusion</i> .....	36
2.3 REORGANIZATION OF CYTOSKELETON ARCHITECTURE UPON MECHANOBIOLOGICAL EXPOSURE.....	37
2.3.1 <i>Introduction</i> .....	37
2.3.2 <i>Materials and methods</i> .....	37
2.3.3 <i>Results</i> .....	39
2.3.4 <i>Conclusion</i> .....	46
2.4 LOCALIZATION OF ADHESINS ON THE SURFACE OF A PATHOGENIC BACTERIAL ENVELOPE.....	47
2.4.1 <i>Introduction</i> .....	47
2.4.2 <i>Materials and methods</i> .....	48
2.4.3 <i>Results</i> .....	50
Force–distance curve analysis.....	50
Specific adhesion events on the surface of <i>B. pertussis</i> cells through molecular recognition experiments.....	52
Dynamics of recognition events on individual bacterium. Force and elasticity maps.....	53

2.4.4 Conclusion.....	56
2.5 CHANGES IN TOPOGRAPHY OF THE COTYLEDON SURFACE CAN LEAD TO BOTRYTIS CINEREA RESISTANCE.....	57
2.5.1 Introduction.....	57
2.5.2 Materials and Methods.....	57
2.5.3 Results.....	57
2.5.4 Conclusion.....	59
<b>CHAPTER 3: NANOMOTION DETECTION.....</b>	<b>61</b>
3.1 TECHNIQUE PRINCIPLES AND METHODOLOGY.....	62
3.1.1 Introduction.....	62
3.1.2 Results.....	63
Instrument and cantilever selection.....	63
Cantilever functionalization.....	64
Sample attachment.....	64
Laser alignment.....	66
Medium optical purity assessment.....	66
Oscillations recording.....	67
Fluid exchange system.....	68
Data processing.....	69
3.1.3 Conclusion.....	72
3.2 BACTERIAL SUSCEPTIBILITY TO ANTIBIOTICS THROUGH NANOMOTION.....	73
3.2.1 Introduction.....	73
Antimicrobial resistance.....	73
Susceptibility testing tools.....	73
3.2.2 Materials and Methods.....	74
3.2.3 Results.....	74
Cantilever functionalization and sample attachment.....	75
Nanomotion as a susceptibility testing tool.....	78
MIC and MBC determination.....	82
3.2.4 Conclusion.....	84
3.3 ANTIBIOTIC SUSCEPTIBILITY TESTING AGAINST AGENTS OF BLOODSTREAM INFECTIONS.....	86
3.3.1 Introduction.....	86
3.3.2 Materials and Methods.....	87
3.3.3 Results.....	89
3.3.4 Conclusion.....	92
3.4 ANTIBIOTIC SUSCEPTIBILITY TESTING AGAINST SLOW-GROWING BACTERIA.....	94
3.4.1 Introduction.....	94
3.4.2 Materials and Methods.....	95
3.4.3 Results.....	95
3.4.4 Conclusion.....	100
3.5 MITOCHONDRIAL ACTIVITY DETECTION THROUGH NANOMOTION.....	101
3.5.1 Introduction.....	101
3.5.2 Materials and Methods.....	102
3.5.3 Results.....	104
3.5.4 Conclusion.....	107
3.6 CANCER CELL VIABILITY TESTING THROUGH NANOMOTION.....	108
3.6.1 Introduction.....	108

3.6.2 <i>Materials Methods</i> .....	109
3.6.3 <i>Results</i> .....	111
3.6.4 <i>Conclusion</i> .....	115
3.7 THE ORIGINS OF NANOMOTION.....	117
3.7.1 <i>Introduction</i> .....	117
3.7.2 <i>Materials and Methods</i> .....	117
3.7.3 <i>Results</i> .....	117
Mechanical effect.....	117
Thermal effect.....	121
Optical effect.....	123
Local pH effect.....	126
3.7.4 <i>Conclusion</i> .....	127
<b>CHAPTER 4: CONCLUSION</b> .....	<b>129</b>
AFM – A VERSATILE TOOL FOR QUANTITATIVE IMAGING.....	130
NANOMOTION – A PROMISING TOOL FOR VIABILITY ASSAYS.....	130
<b>APPENDICES</b> .....	<b>133</b>
MATLAB SCRIPT FOR SIGNAL ANALYSIS .....	134
NANOSIGNAL: SIGNAL ANALYSIS TOOLBOX .....	140
BACTERIAL ATTACHMENT PROTOCOL.....	147
<b>BIBLIOGRAPHY</b> .....	<b>153</b>
<b>CV</b> .....	<b>177</b>



Chapter 1: Introduction







## 1.1 Atomic Force Microscopy Fundamentals

Having roots from a scanning tunneling microscope (STM), the atomic force microscope (AFM) is a member of scanning probe microscopy group and is based on a strong distance-dependent interaction between the tip and a sample. It has been invented in 1986 (1) by Binnig, Quate and Gerber, who knew that significant forces are acting between single atoms during the STM scan and could have anticipated achieving atomic resolution with a new approach. As electrical conductivity of the sample is not required in AFM, many samples can be imaged with minimum preparation and in ambient conditions.

AFM is a “blind microscopy”, as it uses touch to reconstruct an image of the surface, unlike light or electron microscopies. The key component of the AFM system is a nanometer-sharp tip grown on the free end of a cantilever that serves as a transducer of the interaction between the tip and the sample. Image is reconstructed by scanning the tip under a stationary sample or moving the sample under the tip. Scanning the surface, and subsequent topography mapping is allowed by moving sub-nanometer precision piezoelectric components. Due to interactions with the sample, the cantilever changes its initial position and is deflected (displaced). There are multiple possibilities to detect deflection of the flexible cantilever, but the most prominent method is amplification by a reflection of a laser beam focused on the cantilever’s apex and re-direction towards the quadrant photodiode. Therefore, there are five essential elements every force microscope needs: a sharp tip grown on a cantilever spring, a way of sensing its deflection, a feed-back system to monitor and control the deflection, piezoelectric scanning system and a display system that converts signal into an image.

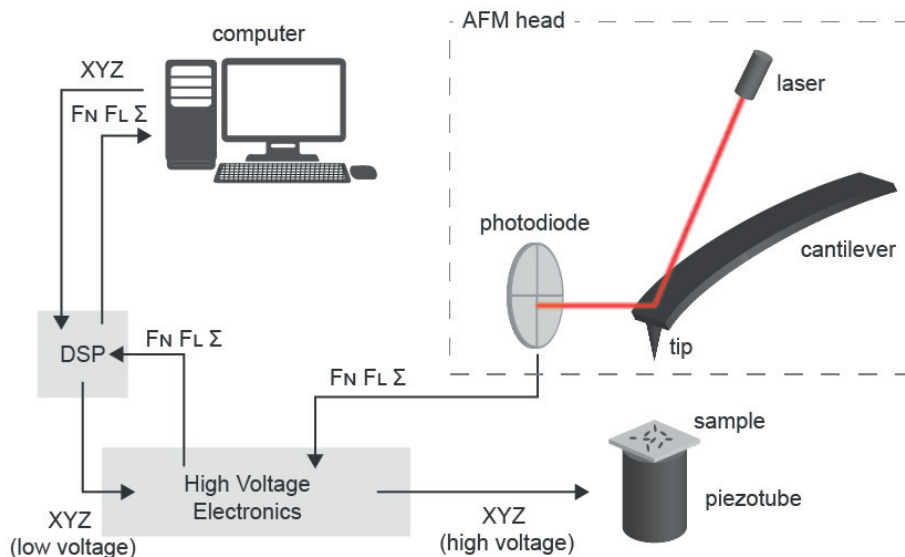


**Figure 1.1** Schematics of a typical model of the atomic force microscope. The cantilever deflects as it interacts with the sample, and this deflection is monitored by a laser beam displacement on the photodiode detector. Vertical (normal) and lateral force signals (FN and FL), but also the total intensity ( $\Sigma$ ) are recorded and sent to the digital signal processor (DSP). This component collects the signals from the detector and amplifies voltages from the DSP to move piezo tube element (XYZ voltages). Finally, computer controls the AFM system and collects all the data.

**Figure 1.1** represents a scheme of a typical AFM setup where the sample is scanned over the tip. The AFM stage contains, apart from the positioning mechanisms, the cantilever, the laser used for the tracking the cantilever deflection, and the photodiode detector. It is placed over a piezoelectric element that holds and moves the sample. During the scan, vertical (FN) and lateral (FL) deflections are being recorded and, together with the total intensity ( $\Sigma$ ) are sent to high voltage electronics. Here, the low voltage XYZ signal from the digital signal processor (DSP) is amplified and forwarded to piezoelectric scanner (XYZ high voltage). Furthermore, the analog signal from the photodiode detector is transferred to DSP, which performs all the signal processing in real-time as the scan proceeds. Finally, computer software allows the control and management of the scan, but also collects the data.

Sub-nanometer precision positioning of the cantilever tip and sample related to each other is allowed by applying potential difference on the opposite sides of a non-conductive piezoelectric crystals. Large number of AFMs use thin-walled tubes made of piezoelectric ceramics, to which a bias voltage is applied to one of the segments of the wall, and the same voltage of opposite sign to the opposite side for scanning movement. The apparent drawback from this type of piezo elements is non-linearity and hysteresis in forward and backward traces. Furthermore, they have limiting scanning speed, due to kilohertz-ranged resonant frequencies. When it comes to imaging in liquids, a setup where the tip is moving relative to the sample is used, with proper piezo shielding and isolation.

AFM techniques require a feedback loop to keep a constant interaction between the imaged sample and the probe (cantilever tip) during the scan. Depending on a particular mode of AFM imaging, the constant parameter could be deflection, amplitude, phase shift, frequency change, etc. The user specifies a desired value of the parameter, while the feedback system maintains its value throughout the scan. The difference between the given value (set-point) and the actual value is measured as the error ( $\epsilon$ ), which is scaled by the gain and the signal is further sent to control the Z drive of the scanner. The scaling is obtained using three terms: proportional (**P**), integral (**I**) and differential (**D**) gains. They are used as factors in the sum that corresponds to the Z-scanner position at a given time (**t**):

$$Z_t = P\epsilon_t + I dt \sum_{i=0}^t \epsilon_i + D \frac{\epsilon_t - \epsilon_{t-1}}{dt}$$

Cantilevers are typically of silicon or silicon nitride material, made in rectangular or triangular (“V” shape) geometry. They are usually coated with reflective coating on the back-side (Au, Al), to promote reflectivity of a laser beam. Considering that a cantilever scans a surface with its tip in contact with the sample, a spring constant of that cantilever should be smaller than the bonding force within the sample. To reach atomic resolution, cantilever’s spring constant needs to be much smaller than 10 N/m, which is the order of forces in a crystalline solid (2). Knowing the formula for a spring’s constant:

$$k = \frac{Et^3w}{4l^3}$$

it is evident that a silicon nitride lever (Young’s modulus  $E = 1.5 \times 10^{11}$  N/m<sup>2</sup>), needs to have micrometer dimensions (thickness – **t**, width – **w**, and length – **l**), to obtain a spring constant smaller than the interatomic spring constant of crystal lattice, for a non-destructive imaging. However, the

lower bound limitation of the spring constant is dictated by the thermal equilibrium at temperature T. Therefore,

$$\frac{1}{2}kA^2 = \frac{1}{2}k_bT; A = \sqrt{\frac{k_bT}{k}}$$

where **A** is the cantilever oscillation amplitude, and  $k_b$  is the Boltzmann's constant. This brings the value of 2 Å, for a spring constant of 0.1 N/m at 25°C, which corresponds to corrugation height of graphite surface, for example (3).

The resonant frequency of a harmonic oscillator is given by:

$$f = \frac{1}{2\pi} \sqrt{\frac{k}{m}} = \frac{1}{4\pi} \frac{t}{l^2} \sqrt{\frac{E}{\rho}}$$

If we consider a cantilever of thickness 0.3 μm, width of 10 μm, length of 100 μm, and mass of 1 ng (due to density of 3.44 g/cm<sup>3</sup>), we obtain a resonant frequency approximately of 16 kHz. Insensitivity of the AFM to external vibrations is dictated by the frequency of oscillation relative to the lowest resonant frequency of the cantilever and the rest of the machine. If the lowest resonant frequency is greater than 20 kHz, then 20 Hz building vibrations of 1 micron amplitude are affecting the cantilever motion by only 0.01 Å. Furthermore, the resonant frequency is a very important factor in the overall speed of the AFM imaging. Scanning a 5 x 5 μm surface of structures that are 2 nm, taking 1 s per line, it would need to scan up and down with a frequency of 2.5 kHz. Therefore, for a good response and imaging, the resonant frequency of the cantilever should be higher than the frequency associated with the surface roughness. It means that for contact with soft materials, a good choice of the cantilever would be the one with high resonant frequency and low spring constant. However, the appropriate choice of a cantilever always depends on the specific application. In dynamic modes, stiffer cantilever overcome capillary forces. Soft cantilevers in contact mode suffer from "jump to contact" phenomenon cause by attractive forces, making it impossible to deal with chemically reactive surfaces at atomic scale. There are ways to go around the problem, such as: operating AFM in liquids or ultra-high vacuum eliminates the capillary forces. The choice of the appropriate media could diminish the attractive van der Waals forces, or the application of an active force compensation as negative loading force before approach (4).

### 1.1.1 Cantilever calibration

For any kind of quantitative application, analysis or imaging, precisely determined parameters of the cantilever are needed. The cantilever spring constant is usually provided as an approximative value, and should be regarded as such. As the AFM cantilever is not a single point mass, taking an effective mass into consideration gives:

$$k = 2w(\pi lf)^3 \sqrt{\frac{\rho^3}{E}}$$

knowing  $\omega^2 = \frac{k}{m^* + m_0}$  and  $f = \frac{\omega}{2\pi}$ . The effective mass ( $m^*$ ) is obtained by measuring the unloaded resonant frequency of the cantilever.

One of the most prominently used methods for the cantilever calibration is the “thermal calibration” method (5). The method approximates the cantilever as a simple harmonic oscillator in equilibrium, fluctuating in response to thermal noise (**Figure 1.2a**). The normal stiffness of the cantilever can be brought into connection with its thermal energy during vibration by:

$$\frac{1}{2}k\langle z^2 \rangle = \frac{1}{2}k_bT$$

where  $\langle z^2 \rangle$  is the mean square cantilever deflection. The value can be obtained experimentally by calculating the area under the power spectrum ( $p$ ) (**Figure 1.2b**), and expressing spring constant as  $k = \frac{k_bT}{p}$ .

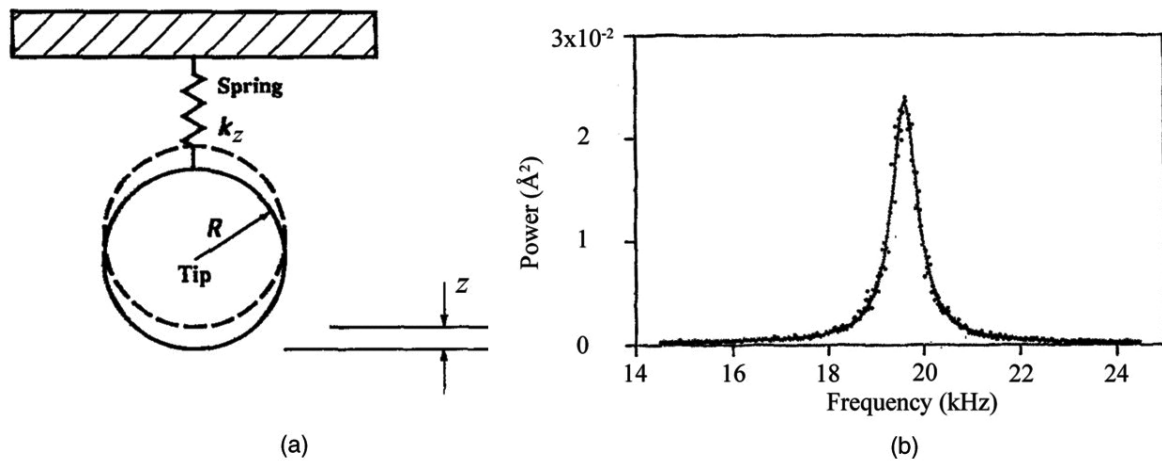


**Figure 1.2** Illustration of the thermal noise calibration principle. **(a)** An AFM cantilever has been approximated to a simple harmonic oscillator with one degree of freedom. **(b)** Power spectral density plot of the cantilever fluctuations.

The advantage of this method is that it eliminated the need for cantilever dimensions and mechanical properties. However, it has been shown that the accuracy depends on the laser spot size and position (6), cantilever geometry (7), and other factors. Furthermore, different AFM instruments have slightly different approaches for calculation and calibration of the spring constant. In addition to that, variability in the material and dimensional properties of cantilevers cause differences in calibration accuracy and force measurements between different laboratories and users. Sader et al, started an initiative to standardize AFM force measurements and calibration of cantilevers of any geometry, by means of a web application (8). They have developed an online tool for AFM users to compare force measurements, by uploading their thermal method measurement parameters and obtaining the average of the spring constant in order to reduce uncertainty.

### 1.1.2 Cantilevers in liquid environment

Operating an AFM while the tip is immersed in liquids has advantages over the forces that govern the interaction with the sample. Apart from the elimination of capillary forces, there is a reduction of the attractive van der Waal's forces. Most important advantage, however, is the possibility to scan biologically oriented samples in their physiological condition.

When an object is submerged in a liquid, ions from the liquid chemically react with the surface of the object forming a surface charge. On top of that, ions of the opposite sign are attracted via the Coulomb force, electrically screening the first layer. The resulting arrangement of charges around a submerged object, called the electric double layer, has a large impact on interactions between charges in liquid environment. The same phenomenon happens with an immersed cantilever tip, making electrostatic forces most relevant ones in imaging in liquids. Therefore, high resolution imaging in solutions would require tip-sample contact, and imaging soft biological samples further demands soft cantilevers. Due to the effect of lateral forces and shear stress on the cantilever during the contact scan, various other modes of scanning have been introduced, such as force volume. Proper adjustment of electrolyte concentration is necessary to cancel out the influence on the tip-sample interaction and to allow high resolution imaging.

Even though the spring constant of the cantilever depends only on its geometry, dimensions and properties, in liquid environment, viscosity affects the mechanical response of the cantilever. As a result of higher density of liquids, compared to the density of air, the effective mass of the cantilever increases by a factor of 10 – 40 (9). Therefore, by dragging the surrounding liquid, cantilever vibration resonates at a lower frequency, 15 – 30 % of the resonant frequency in air.

$$\omega_0^{DDO} = \sqrt{\omega_0^2 - \frac{1}{2} \left(\frac{b}{m^*}\right)^2}$$

In the equation, **b** is the damping coefficient,  $\omega_0$  the resonant frequency of the undamped oscillator ( $\omega_0 = \sqrt{k/m^*}$ ) and the effective point mass **m\***. Another effect of the hydrodynamic interaction between the cantilever and the liquid is lowering of the quality factor Q about two orders of magnitude. Oscillation of the cantilever is asymmetric and anharmonic (non-sinusoidal) when the quality factor is low. This dimensionless parameter is a measure of the damping of the oscillating system and is calculated as the ration of the stored energy to the amount of energy lost per cycle. Therefore, it represents the sharpness of the resonant peak:

$$Q = \frac{m^* \omega_0^{DDO}}{b}$$

It has been found that the importance of the viscous effect is dependent on the cantilever dimensions, and decrease in size of the cantilever enhances the viscous effect, resulting in increased broadening and shifting of the resonant peak from its value in vacuum (10). Few theoretical models have been developed to describe the vibration of the cantilever in liquid environment. One group of models describes the resonant frequency change due to oscillations close to the surface of the sample, which gives rise to an additional damping effect, whereas the other group models the behavior of the

cantilever in liquids far from the surface (11). The latter group of models includes Sader's inviscid model, Vancura's viscous model and effective mass replacement model.

### 1.1.3 Detection method

Translation of the force acting upon the cantilever tip needs to be a precise method governed by the Hooke's law of direct proportionality of the interaction force and cantilever deflection. Among various methods for cantilever deflection detection, there are tunneling of electrons (1), capacitive displacement (12), piezoelectric effects and tuning forks (13), optical interferometry (14) and laser beam method (15). The latter is being used in most of the modern commercial instruments today. The deflection of the cantilever is detected by tracking the position of the laser beam reflected off the cantilever's reflex coating and directed towards a photodiode detector (**Figure 1.3**). The detector is usually a quadrant photodiode, a four-segment semiconductor device capable of turning the integrated laser spot intensity into an electrical voltage signal. Vertical movements of the cantilever are detected by measuring the voltage difference between the upper and lower segments of the photodiode, while lateral (torsional) movements by calculating the voltage difference between left and right segments. The resolution of the laser beam deflection method reaches Å, and is limited by thermal excitation of the cantilever. Using an optical lever method, Alexander et al. successfully measured cantilever displacements of less than 1 Å, imaging native oxide of silicon, Al, iron and steel (16).

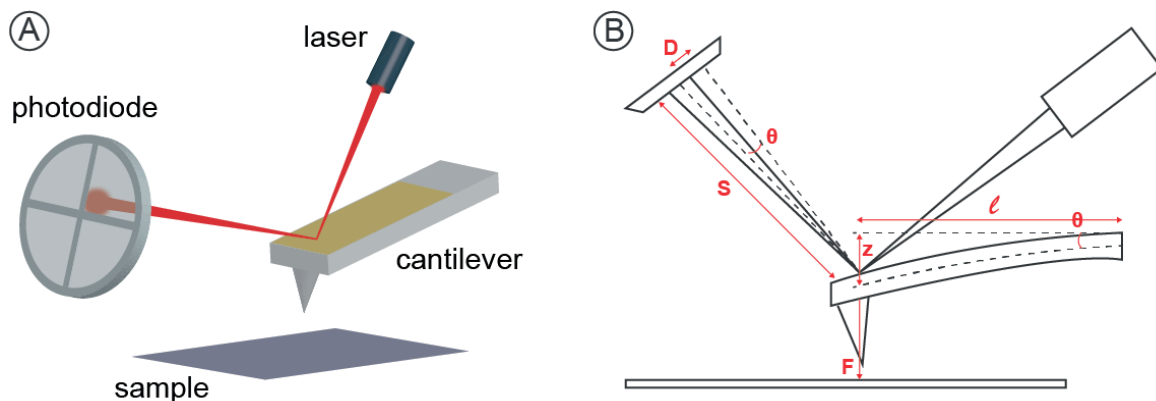


**Figure 1.3** Laser beam deflection method for detecting cantilever deflection. A laser beam is focused on the back side of the cantilever, coated with reflexive material and reflected towards the photodiode detector, where the laser intensity is translated into voltage, tracking the cantilever deflection.

An external force produces a torque on the cantilever that induces bending along the length of the cantilever. Deflection of a beam with a concentrated load **F** at free end is given by:

$$z = \frac{Fl^2}{6EI} (3L - l)$$

where **L** is the cantilever length and **l** is the distance of bending measured from the fixed end of the cantilever (17). Derivation of the equation for deflection gives the angle of bending:  $\theta = \frac{Fl}{2EI}$  where **E**

is the Young's Modulus and  $I$  the area moment of inertia. If the cantilever is rectangular, of spring constant  $k$  and length  $l$ ,

$$EI = \frac{kl^3}{3}$$

therefore  $\theta = \frac{3z}{2l}$ , and knowing that  $\tan \theta = \theta$ ,  $D = \frac{3Sz}{2l}$ . The amplification of the 200  $\mu\text{m}$  long cantilever oscillations at a distance of 5 cm is by a factor of 375. On top of its sensitivity, it is very simple to implement and it is a preferred choice of detection in liquid environments. The only need for such a system is a well-defined fluid cell with a transparent window for the laser beam path. Any instabilities of the liquid-solid interface would scatter the laser beam, introducing noise. Therefore, it is important to design a fluid cell and a cantilever holder so that no surface waves of the liquid interfere with the laser pathway.

## 1.2 AFM Modes

AFM is a versatile tool, with many different possible applications, spanning many research domains. Initially, it was employed as an imaging tool. However, later development brought it towards non-imaging modes, such as chemical and biological sensing. Apart from the applicational distinction, imaging and non-imaging, AFM modes could be classified as static and dynamic. The latter classification is based on the oscillation of the cantilever: in static mode, cantilever oscillations are not driven, while in dynamic mode, cantilever is forced to oscillate at or near its resonant frequency. Typical imaging modes include contact, intermittent contact and non-contact modes (**Figure 1.4**).

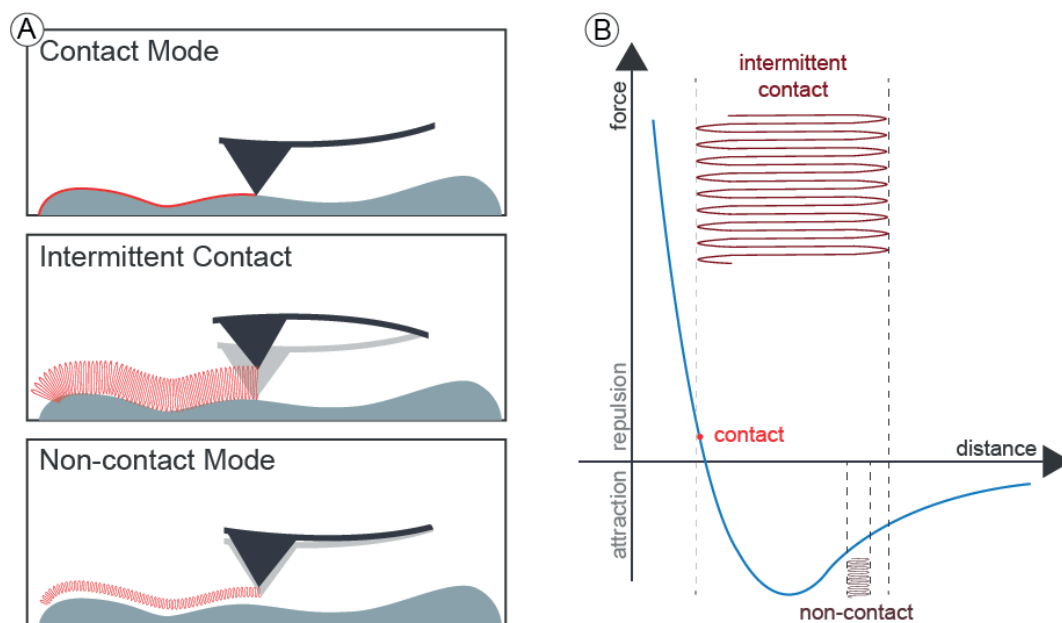


**Figure 1.4** Typical AFM imaging modes. **A)** Schematic representation of contact, intermittent contact and non-contact modes. **B)** Force-distance curve with operational ranges of different AFM modes. Contact mode stays in the repulsive part of the curve, while intermittent contact moves between the attractive and repulsive areas of the curve. Non-contact mode is performed within the attractive regime.

### 1.2.1 Contact Mode

This static imaging mode is the oldest mode described along with the fundamentals of the atomic force microscope (1). Binnig et al. applied the so-called “fourth mode” to image topography of different areas of a ceramic ( $\text{Al}_2\text{O}_3$ ) surface. The stylus (cantilever tip) is brought in contact with the scanned sample, where repulsive forces are deflecting the cantilever. A feedback loop is used to keep the force acting on the cantilever tip at a constant level. In case of an optical lever detection method, the signal given by the photodiode is used in a feedback loop to control the cantilever and corresponds to vertical cantilever deflection. The operator of the instrument chooses the value (set-point) at which the image is taken. During the scan, the Z-scanner is responsible for maintaining the signal from the photodiode equal to the given set-point. If the measured deflection is different from the set-point value, the feedback applies a voltage to the piezo in order to regain the chosen value of deflection. The voltage that the feedback mechanism applies to the piezo element is a measure of the height of the imaged sample. It is measured as a function of the lateral position of the scanner.

Contact mode applied in biology, under liquid environment has limitations. The given set-point value may not represent a fixed force applied to the biological sample, as the photodiode signal may drift in time. Therefore, images taken at a constant deflection may not be at constant force. Another problem in the same application domain is that the normal force in combination with lateral movement as scan proceeds may induce lateral forces that could drag and distort soft biological samples. In this mode, low spring constant cantilevers are usually used to achieve deflection signal large enough while keeping the interaction force low.

Another form of contact mode is a lateral force mode (frictional force mode). In this case, the cantilever motion of the scan is performed perpendicular to the axis of the cantilever (18). The mode is especially useful for doing friction measurements on surfaces, by calibrating the cantilever torsional spring constant and converting lateral force measurements into frictional force.

### 1.2.2 Tapping Mode

The motivation for this mode is to overcome difficulties in all the previously developed AFM modes. It has been realized with the aim to reduce lateral forces, minimize the contact between the tip and the sample, to increase the oscillation amplitudes and the possibility to overcome sample adhesion forces (19). In tapping mode (also known as intermittent contact, or AC mode), the cantilever is driven to oscillate at or near its resonant frequency and to strike the sample surface at each oscillation. Different methods exist for driving the oscillatory movement of the cantilever, such as through a small piezo element in the holder, AC magnetic field, piezoelectric cantilevers or periodic heating. The amplitude of the driven oscillations is up to 200 nm, and it is kept constant, as well as the frequency of those oscillations. Once the cantilever interacts with the surface of the sample, the interaction forces of the intermittent contact cause perturbations of the amplitude of the driven oscillations. The change is larger if the tip is closer to the surface. This change in amplitude is used as a parameter that goes into the feedback mechanism and controls the height of the cantilever above the sample. Feedback takes care that the set-point amplitude is kept constant and will shift the cantilever height accordingly. Scanning the surface from point to point generates a topographic image of the sample. Even though the tip forces applied to the sample can be greater than ones in



contact mode, the intermittent mode does less damage to the scanned sample, as the duration of the applied force is rather short and the lateral forces are minimized. Another possibility of the mode is to record the phase of the cantilever oscillations. This gives valuable information about the energy dissipation of the cantilever in each oscillation cycle. A different stiffness of the material would provide contrast in the phase image, while the topography would stay the same. However, those mechanical properties can be quantitatively studied with other AFM modes. In general, stiff cantilevers are used for creating images with this mode ( $k \sim 20$  to  $50$  N/m), with a high quality factor. One of the drawbacks that follows how this mode of operation is the low imaging speed, due to the time needed to complete each cycle.

### 1.2.3 Non-contact Mode

In non-contact mode, the probe is forced to oscillate in a close proximity to the sample (order of  $\text{\AA}$ ), at very small amplitudes. The cantilever is then moved to probe all the points of interest on the sample and the image is constructed by detecting force gradient variations. The force of interaction perturbs the driven oscillations of the cantilever, by changing their amplitude at a constant frequency, slightly off resonance. This type of measurement is called the amplitude modulation. One form of amplitude modulation is imaging by measuring phase shifts, which gives hints about the mechanical properties of the imaged sample. Moreover, another way of measuring the perturbations of the driven oscillations is possible, by detecting the change in resonant frequency of a constant amplitude oscillator - frequency modulation (20). In this modality, interaction with the sample changes the oscillator frequency and the system applies positive feedback to retain the cantilever oscillations at the set-up frequency. Constant amplitude is usually kept through a separate feedback loop, and by observing this parameter, a complementary image of dissipative forces is obtained.

### 1.2.4 Force Spectroscopy

Apart from high-resolution imaging, it can also provide information about the interaction forces between the cantilever tip and the sample surface. The new application possibilities using force spectroscopy started with a study on distance dependence of the force between the cantilever and a single crystalline lithium fluoride sample, plotting the force against the sample position (21). With pioneering works and first studies, it has been clear that capillary forces dominate all interactions between the lever and the sample, while performing in air. To avoid such problems, interaction forces have been studied in liquid environment, which brings a new application field into play – biology. In life sciences, tools to detect and measure specific molecular interactions are of extreme importance. A study that introduced biotin-avidin interaction as a model system for such experiments was one of the first to functionalize the cantilever tip with one molecule, a ligand, and use it to probe the other molecule on a surface – a receptor (22). Plots that allow studying such interactions are called “force-distance curves”, and represent a plot of tip-sample interaction force versus their distance (in other words: deflection of a cantilever versus the extension of the piezoelectric scanner). **Figure 1.5** shows an example of a force-distance signature.

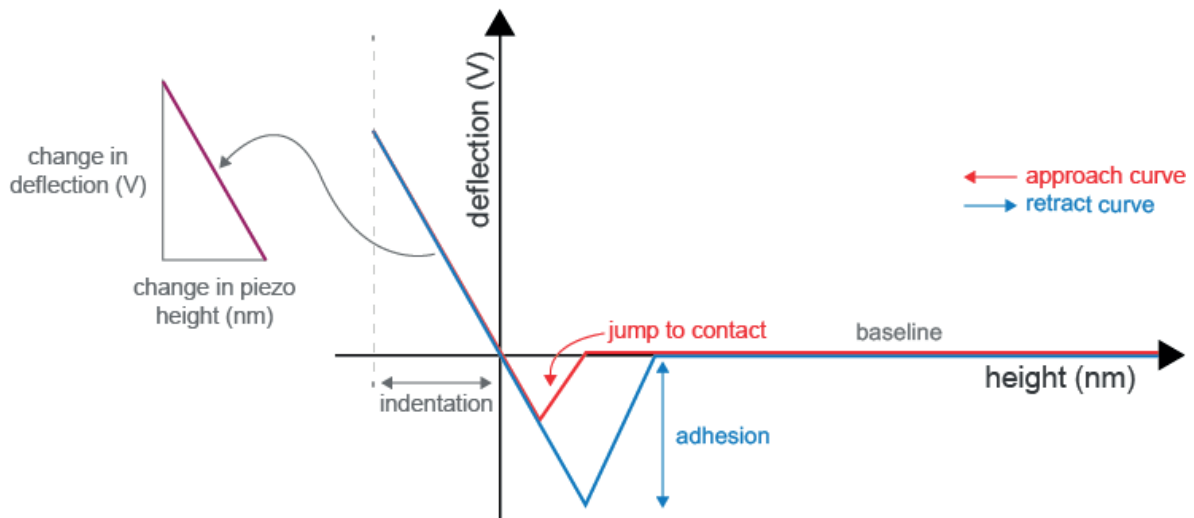


**Figure 1.5** Schematic notation of force-distance curves. The approach curve (red) corresponds to the piezo element approaching the sample surface. In this region, the force is zero and it represents the baseline that needs to be used for signal correction. After the contact point, further deflection of the cantilever shows tip indentation of the sample. If elastic, the retract curve (blue) will take the same values back, up to the point where there is adhesive attraction of the sample.

When the cantilever is far from the sample surface, no interaction occurs and a photodiode detector shows a constant value that corresponds to a condition with no force. Usually, this value is used as a reference for the rest of the deflection values. Once the cantilever is sent towards the surface, deflection occurs. The tip-sample force is given by the Hooke's law:  $F = -kz$ . However, the tip-sample distance (**D**) needs to be corrected, as it is actually the distance between the sample surface and the cantilever in resting position (**Z**), without taking cantilever deflection (**z**) and sample deformation (**z<sub>s</sub>**) into account:  $D = Z - (z + z_s)$ .

An important parameter to know before realizing force-distance experiments is the sensitivity of the system – how much the cantilever deflects per 1V of the difference in laser beam intensities on the photodiode detector top and bottom segments ( $\Delta z/\Delta V$ ). One of the methods to obtain the sensitivity value is to do a force-curve on a hard and flat substrate before the experiment, and to measure the increase in cantilever deflection voltage and connect it with the distance travelled by the Z scanner (**Figure 1.5**).

The contact section of the force-distance curves is a valuable source of information regarding elastic and adhesive properties of the probed sample. The curve that represents the approach of the cantilever tip towards the sample is called an approach curve, while the process of retraction corresponds to a retract curve. Theoretically, if the sample was ideally elastic (**Figure 1.6A**), approach and retract curves overlap. From a point **O** to point **A**, the approach, sample gets deformed due to the force applied by the tip. As it is ideally elastic, all the energy is transferred back to the tip, which receives the same force. Therefore, the retract curve (from **O** to **A**) takes the same values. If the sample is ideally plastic (**Figure 1.6B**), after the deformation by the tip, it does not return to the initial conformation or shape. As the tip retracts, the penetration depth stays the same. However, in

the real-life samples, the situation is somewhere in between the two presented cases. **Figure 1.6C** shows a simplified example with a noticeable difference between the approach and retract curves, named “hysteresis”.

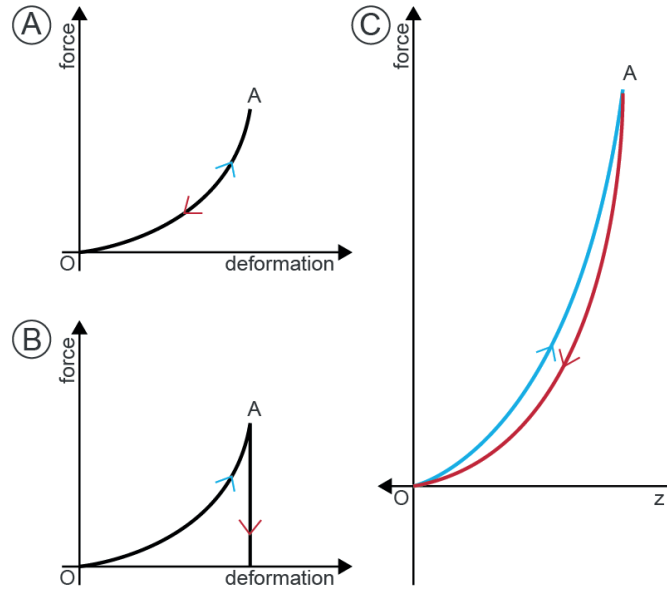


**Figure 1.6** Cantilever tip load against the penetration depth for an ideally elastic (A) and ideally plastic (B) sample. (C) Force-distance curve for a semi-elastic sample (simplified real-life example). Modified from (23).

The calculation of the sample’s Young’s modulus is conducted as follows: in a first step the force distance curve obtained on the soft sample is subtracted from another one that was recorded on a rigid substrate. The resulting curve is referred to as the indentation curve, that basically indicates the force that is required to push the tip to a certain depth into the sample. The shape of this curve depends not only on the sample’s elastic properties but also on the geometry of the AFM tip as well (24). To obtain the sample’s Young’s modulus numerical value one has to fit the newly obtained indentation curve with a function that takes into account also the geometry of the AFM tip. The two most widely used functions are those from Hertz (25) and Sneddon (26). The Hertz model describes the elastic deformation of two spheres, whereas the Sneddon’s model accounts for other geometries such as conical or paraboloidal tips against a flat sample. As an illustration, the equation that determines the force  $F$  required to indent the tip to a given depth ( $\delta$ ) for conical tips is

$$F(\delta) = \frac{2 \tan(\alpha)}{\pi} E' \delta^2$$

and for paraboloidal ones

$$F(\delta) = \frac{4\sqrt{R}}{3} E' \delta^{1.5}$$

$\alpha$  is the opening angle of the tip and  $R$  its radius of curvature.  $E'$  corresponds to the reduced Young’s modulus that is related to the sample’s Young’s modulus  $E$  through

$\frac{1}{E'} = \frac{1-\mu^2}{E}$  if it can be assumed that the numerical value of  $E$  of the sample is much lower than the  $E$  of the AFM tip.  $\mu$  is the Poisson ratio of the sample that is ranging from 0 to 0.5. This last value is usually used for living cells.

Alternative models such as JKR or Tatara (27) models are also sometimes used. The JKR model considers also adhesive forces, whereas the Tatara model simulates the case of a spherical sample compressed between two parallel plates. Recently, somewhat more specific analysis techniques were developed, such as the Multi-Regime (28) or the Multiscale Decomposition Analysis (29) methods. The first considers cells as a multi spring system, whereas the second permits one to highlight and quantify the nonlinearity of the mechanical response of the cantilever upon cell wall indentation. Both analysis techniques were developed with the aim to process indentation data recorded on plant cells.

## 1.3 Biosensors

### 1.3.1 Biosensor classification

A device with a physical element (sensor, transducer) that is able to transform certain biological signal into a measurable output, is called a biosensor. In recent times, their development and demand increased largely in biomedical research, biotechnology, healthcare, drug discovery and clinical diagnosis. Biosensors are mainly classified based on their transformation element (**Figure 1.7**), but a distinction by a biological signal is also possible. An optical biosensor, for example, is a device with a biorecognition sensing element in connection with an optical transducer system. Fluorescence-based detection, as a subtype of optical biosensing, is biorecognition of fluorescently labeled molecules, where the intensity indicates molecular concentration, in example. In label-free optical detection, where molecules are not altered or tagged, the detection method may differ from refractive index changes, optical absorption, to various spectroscopic methods (30). An important and well-studied approach in optical sensing is the exploitation of surface plasmon-polaritons for probing interactions between an analyte in solution and a biomolecular recognition element. Yet another approach is the utilization of optical fibers for the determination of biological species (31).

Converting biological recognition event into a useful electrical signal classifies the device as an electrical biosensor. This kind of biosensors were one the first ones implemented, including the famous Clark's electrochemical oxygen biosensor (32). One of the most commonly used electrochemical biosensors are amperometric, where a bioelectrochemical reaction creates a detectable current, and potentiometric, where a measurable potential or charge accumulation is detected (33). Conductometric approaches that detect measurable change in medium conductivity, and voltammetry (measuring current while applying controlled variation of the potential) are other ways of detecting the signal in electrical biosensors. It is important to mention also the cylindrical graphite of nanometer scale diameter – carbon nanotubes, used for sensing by detecting changes in their physical properties, such as: electrical or thermal conductivity, photoluminescence, scattering, and other (34).

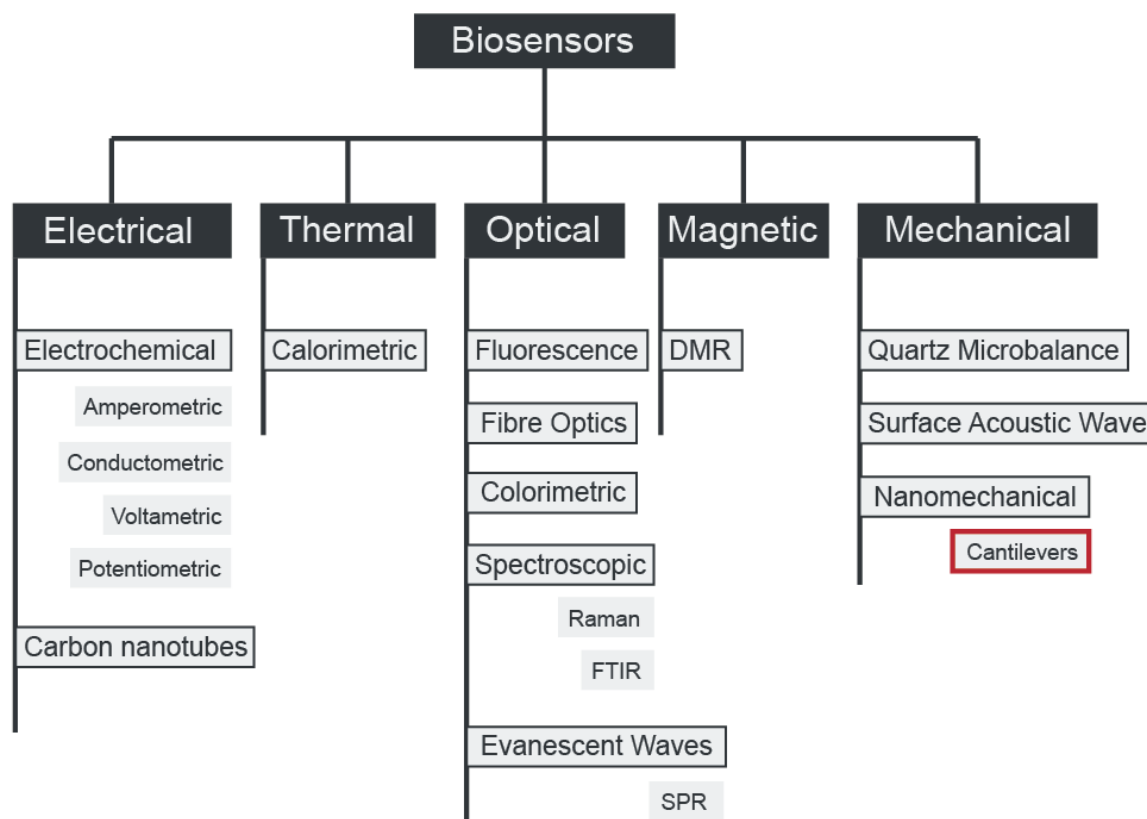


**Figure 1.7** Selected biosensor subclasses: a schematic representation. Depending on the measured physical change in the transducer element, biosensors can be classified as electrical, thermal, optical, magnetic and mechanical. Each of the subclasses branch further, and listing all the possible biosensing methods would not be an easy task.

Other biosensing methods, like thermometric measurements for various applications are also possible. Such biosensors take advantage of the important property of biological reactions – absorption or evolution of heat (enthalpy change), which is reflected as a change in the temperature within the reaction medium. The principle is to flow target molecules through a chamber where biocatalysts are immobilized on a heat-sensing element (35). The total heat absorption or change is proportional to the molar enthalpy and to the total number of product molecules created in the reaction.

Exploiting magnetism in a biosensing application has also gained some interest. Research has been done in magnetic biosensing in magnetic actuation, hyperthermia treatment, targeted drug delivery and the use of magnetic nanoparticles as MRI contrast agents (36).

Among the mechanical sensing methods, the quartz crystal microbalance has enjoyed the most interest (37). It is a high-resolution mass sensing technique, capable of detecting a surface mass binding, from small-molecule monolayer coverage, to big-molecule complexes and whole-cells. The working principle of the technique is that an alternating electric field applied across the crystal imposes its mechanical oscillations at the mechanical resonance. An increase in mass bound to the

surface of the quartz crystal changes the resonance frequency, and this shift is used to calculate the added mass. Liquid conditions are not optimal for this type of mass sensing, but measurements can still provide valuable information about interactions between the liquid and the solid. For example, studies include biomimetic systems, biochemical processes investigation, biosensing by attachment of biological species to the crystal, and investigation of drug-target complexes (37). A reversed piezoelectric effect to the one described is exploited in the technique based on surface acoustic waves. Such devices generate and detect acoustic waves using interdigital transducers on the surface of a piezoelectric crystal, by measuring the alternating voltage caused by mechanical oscillations (38).

### 1.3.2 Cantilever-based nanomechanical biosensors

Microelectromechanical systems (MEMS) include micro- and millimeter scale devices, produced using microfabrication technology, such as: actuators, sensors, miniaturized structures and microelectronics. Cantilevers as beams anchored at one end are one of the examples of the MEMS biosensor technology. Considering that if the main component of a mechanical biosensor has the nanoscale size of at least one of its dimensions, it is referred to as a nanomechanical (NEMS) biosensor. Therefore, a cantilever can be used as a nanomechanical biosensing tool by following its mechanical oscillatory properties. Detection of oscillatory movements of the cantilever can be performed using the same methods as in AFM imaging. However, even in this domain of cantilever utilization, optical lever method is the preferred choice. The attention for cantilevers as diagnostic tools has been realized less than two decades ago by a study showing the potential in single-nucleotide polymorphism detection and receptor-ligand binding, using a pair of cantilevers coated with oligonucleotides (39). Since then, different approaches and applications have been realized. Nanomechanical biosensors can be split into two categories: static and dynamic, depending on the measured parameters (**Figure 1.8**). In both cases, nanomechanical system undergoes changes once biomolecules adsorb onto the cantilever surface.

In case of static bending, only one side of the cantilever is rendered sensitive to a specific target molecule, while the other one is passivated. High affinity binding between biological molecules and their recognition occurs only in the liquid phase. Specificity and affinity of the binding layer is critical and limiting factors of this type of sensing mode. Typically, a detection limit and the biological noise level are governed by the amount of non-specific binding events that still impose an effect, despite the fact that they might be short-lived. The fluid dynamics and the kinetics of analyte binding are also important in this regard. Therefore, blocking chemistries are usually employed in order to reduce non-specific binding events. Apart from the added mass from the adsorbed layer, cantilever surface stress changes, its effective Young's modulus and viscoelasticity are also subjected to change.

Surface stress is defined as reversible work per unit area needed to elastically stretch a surface. Once the target molecules interact with the sensitized surface of the cantilever, the modification of the surface stress between the two cantilever sides results in a measurable mechanical deflection. It has been shown that the adsorption-induced changes in the electronic charge density at the cantilever surface contribute the most to the surface stress (40). Interactions described by the Lennard-Jones potential or Coulombic repulsion between adsorbed molecules have the relatively small effect on the

overall surface stress changes. The surface energy variation of the sensitized side is minimized by elastic expansion or contraction compared to the passivated side bends the cantilever. This phenomenon is the working principle of most static nanomechanical biosensing systems that investigate ligand-receptor interactions. The curvature change due to the changes in surface stress can be calculated using Stoney's formula:

$$\Delta k = \frac{Eh^2}{6(1-\nu)\Delta s}$$

where  $\Delta s$  and  $\Delta k$  are changes in surface stress and curvature,  $E$  is Young's modulus,  $\nu$  is Poisson's ratio and  $h$  is cantilever thickness. However, this formula is valid only for plates that are free on their ends, which is not the case with cantilevers that are fixed to the chip substrate at one end.

One modality of this sensing type is to evaluate stress changes of the cantilever material bulk, caused by temperature differences. Cantilevers with a reflexive coating of different thermal expansion coefficient than the one of the bulk material may be used as extremely sensitive thermometers. The bending of the cantilever with temperature changes is due to the bimorph effect, and may be used to resolve enthalpy changes as low as 10 nJ (41).

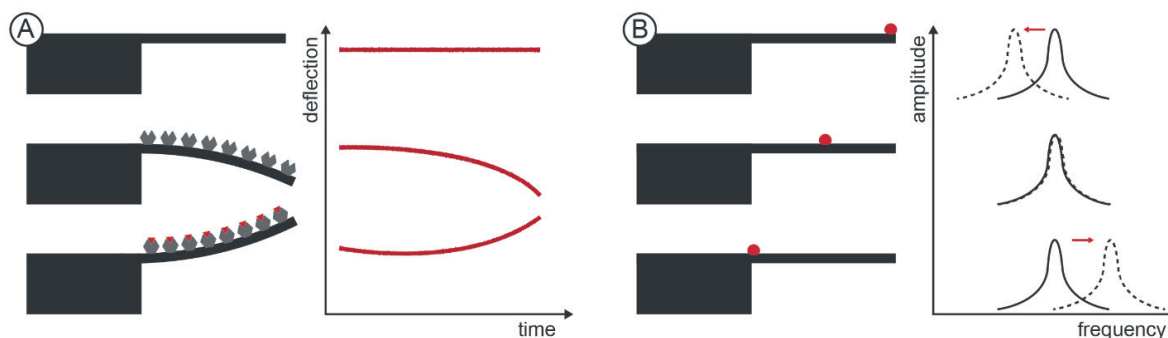


**Figure 1.8** Two operation modes of cantilever biosensing: static mode (A) and dynamic mode (B). One-sided coating on the cantilever allows detection of ligand-receptor interaction by observing the static cantilever bending. In dynamic mode, the added mass changes the resonant frequency of the cantilever oscillations.

Like quartz crystal microbalance, cantilevers can also be set to oscillate at their natural resonant frequency in order to act as a high-precision mass detectors. The usual way of quantifying the added mass on the cantilever is by:

$$\frac{\Delta\omega}{\omega_0} = -\frac{1}{2} \frac{\Delta m}{m}$$

where  $\omega_0$  is the angular resonant frequency,  $\Delta\omega$  is the angular resonant frequency shift,  $m$  is the cantilever mass and  $\Delta m$  is the adsorbed mass. This approach is suitable for a uniform and rigidly-attached coverage of the mass over the cantilever surface (42). However, it has been shown that discrete masses shift the resonant frequency differently, depending on their position (43). By ink-jet printing, a small mass deposited on the cantilever apex shifted the oscillation resonant peak towards lower frequencies. Depositing a mass on the middle of the cantilever, however, did not affect the

change in resonant frequency. Furthermore, the deposition of a discrete mass near the clamped end of the cantilever increased its resonant frequency. This suggests that the effect of the added mass is not the main origin of the response, as the resonant frequency shift is not always negative. The suggested model is that the mass effect dominates when the mass is deposited close to the cantilever apex, while higher flexural rigidity of the cantilever due to the stiffness of the deposited sample is taking an effect as the deposition is done more to the clamped end of the lever (44).

To overcome low quality factor problems caused by liquid media damping, the excitation of higher vibrational modes has been used under physiological conditions (45). For high sensitivity mass measurements, it is very important to avoid anomalous additional acoustic frequencies. A study in this regard reported an increase in quality factor from 1 to 30 by switching to 16<sup>th</sup> vibrational mode (46). Higher harmonics introduce nodes in the resonance and therefore decrease the effective mass of the cantilever, improving sensitivity.

Cantilevers used in biosensing applications are typically very thin (less than a micron). In such cases, the thickness of a biological layer is comparable to the sensor itself and modeling the vibration systems would demand removing the thin film approximations (47). Therefore, elastic properties of the attached biological material do influence the mechanical properties and bending responsivity to surface stress changes. More precisely, direction and amplitude of bending is dictated by the mixture of factors like chemical, elastic and entropic properties of the active layer deposited on the cantilever.

The sensitivity of the cantilever in resonant mode is defined as the change in frequency ( $\Delta\omega_0$ ) due to a change in mass (added mass:  $\Delta m$ ), and can be represented as follows:

$$S = \frac{\partial\omega_0}{\partial m_{eff}} = -\frac{\omega_0}{2m_{eff}} \approx \frac{\Delta\omega_0}{\Delta m}$$

To improve sensitivity, resonator must have a high resonant frequency, which is possible by having a large Young's modulus, low density, higher mode oscillations or small dimensions. Nanoelectromechanical sensors can be manufactured and tuned to measure as low as attogram masses under vacuum conditions (48), and some carbon nanotube systems reach even yoctogram (1 yg = 10<sup>-24</sup> g) resolution (49). Cantilevers with a larger surface area have relatively large mass resolution per area or distributed mass resolution. Therefore, depending on the desired application, reduction in dimensions is sometimes not desirable. The resolution, or smallest detectable mass of the cantilever ( $\Delta m_{min}$ ) is defined by the inverse sensitivity times the minimum detectable frequency change ( $\Delta\omega_{min}$ ):

$$\Delta m_{min} = S^{-1}\Delta\omega_{min}$$

An oscillating cantilever experiences damping and dissipation of its kinetic energy. This dissipation is defined as the ratio of energy lost per cycle to the stored energy (the inverse of the quality factor). When it comes to a detection limit, it has been shown that thermomechanical noise is the most prominent factor contributing to the anticipated resonator noise level (50,51). Other contributions to the noise level are non-specific adsorption, differences in mechanical properties and geometry between the measurement and reference cantilevers, fluctuations in pH and ionic strength etc.



Knowing the equipartition theorem expressed by the average displacement fluctuation  $\langle w_n^2 \rangle = \frac{k_b T}{k_n}$ , where  $k_n$  is the effective spring constant  $k_n = 4\pi^2 m_b f_n^2$ , the static noise brings:

$$\langle w_n^2 \rangle \approx \frac{1}{2\pi^3} \frac{B k_b T}{m_b f_0^3 Q}$$

with  $B$  being the frequency bandwidth of the measurement. It is proposed that the minimal detectable mass in liquid environment using a cantilever with uniform distribution of the adsorbed layer is about 0.25 ag (52).

Microfluidic lab-on-a-chip research and development are motivating the miniaturization of many analytical tools, including MEMS and NEMS. Either incorporation of these resonators into a microfluidic system or the generation of microfluidic channel within them, both ways hold great promise, especially in combination with a good separation technique for blood or urine sample testing.

The application areas of these resonators experienced a tremendous rise, spanning from gas and chemical detection, to detection of biological compounds, where most of the focus is. Applications cover genomic and proteomic fields, environmental and industrial control, clinical diagnostics, drug screening, and pathogen detection (53). One of the pioneering studies in the application of resonators for cell detection showed that a single *E. coli* cell can be detected in ambient conditions, by observing the resonant frequency shift (54). Studies on detecting other biological systems expanded ever since. Those studies included detection of virus particles (55), proteins (56), DNA (57), enzyme activity (58), etc.

### 1.3.3 Sample attachment

Certain biosensors, especially nanomechanical ones, require a biological material to be attached to some of its elements. Depending on the sensor type and application, different procedures are used. In case of static nanomechanical cantilever sensors, biological recognition element is typically adsorbed onto one of the cantilever sides. For mass sensing, both sides of the cantilever may be used for adsorption, but the cantilever apex is the area which gives largest sensitivity. Before attachment, the cantilever needs to be chemically functionalized with active groups that promote the attachment of recognition molecules. Usually, after the attachment of molecules of interest, other chemically active sites are blocked to minimize non-specific binding events. Regardless of the type, all biosensors require of the attached molecule to have unchanged binding activity, bioavailability, and uniformity.

The choice of the best immobilization agent depends on the cantilever material and coating. Most of the cantilever sensors used in static bending detection mode are coated with gold as the reflective layer for the laser reflection. In case of the biomolecular attachment on that side of the cantilever, high affinity of sulfur for gold is exploited by harnessing compounds with a thiol group (-SH). On the other hand, if the other side of the cantilever is of interest, silanization procedures are used to take advantage of silanol groups (Si-OH) created on silicon and silicon nitride cantilevers, as silicon oxide

easily accepts water molecules. From such a procedure, the connection silicon-oxygen-silicon is easily formable using organosilicon molecules. **Figure 1.9** depicts that.

One of the crucial conditions in sample attachment is that the reaction with the surface does not change the biological activity of the attached system. In the case of proteins, the three-dimensional structure of the protein must remain intact, cells need to survive the attachment procedure, etc. Typically, amino acids from proteins themselves or on cellular surface are responsible for the interaction with the active moieties on the cantilever surface. Most of the modification reactions are nucleophilic, consisting in a direct displacement of a leaving group by the attacking nucleophile (amino acid side chain in reaction with the surface molecules). The pH of the medium has an influence on the nucleophilic reactions. Protonation decreases the nucleophilicity of a species. Furthermore, temperature, ionic strength of the solvent and the microenvironment of the ionizable groups also have an effect. Carbonyl compounds such as aldehydes readily and reversibly react with amino groups of proteins to form Schiff bases (59). Therefore, glutaraldehyde is often used after the silanization procedure to promote attachment of amine amino-acid groups to aldehyde moieties from the cantilever surface.

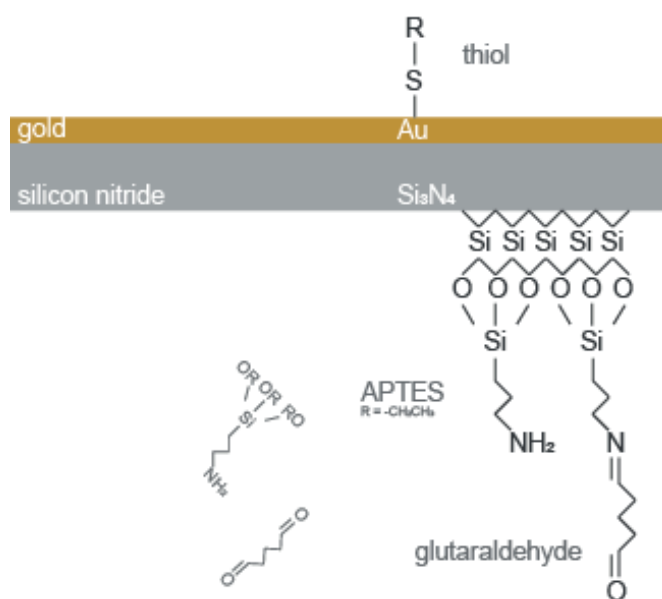
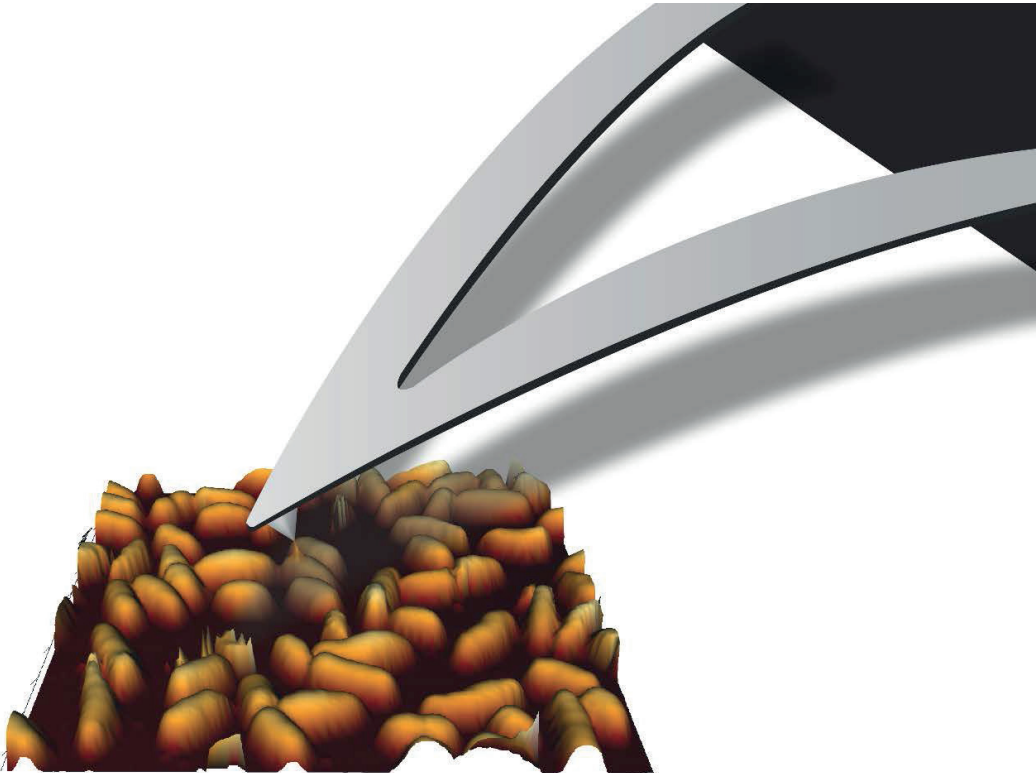


**Figure 1.9** Functionalization procedures often used to promote attachment of biological systems (proteins, cells, etc.). For gold coated cantilevers, thiol-based compounds are used for gold functionalization, while on the silicon nitride side, APTES silanization and glutaraldehyde are combined to obtain amine or aldehyde active groups.

Chapter 2: Quantitative Imaging and Mapping



## 2.1 Quantitative imaging technique

*This section contains published work:*

Kasas, S., Stupar, P. and Dietler, G., 2017, August. **AFM contribution to unveil pro-and eukaryotic cell mechanical properties**. In *Seminars in Cell & Developmental Biology*. Academic Press.

Acquiring a single force distance curve is usually of limited interest, and very soon imaging modes allowing the mapping of the entire surface of the sample appeared. The first was referred to as force volume imaging. It consists of recording successively force distance curves all over the sample. Such an image is composed typically of 1024 (322) or 4096 (642) force distance curves and the information content of such a file is tremendous: the sample's stiffness, adhesion or topography at zero force can be relatively easily extracted. The main drawback of the technique is the time required to complete the acquisition, depending on the resolution it can require hours. In an attempt to accelerate the acquisition process, certain AFM manufacturers developed variants of the force volume imaging mode such as the Quantitative Imaging (QI™) mode of JPK Instruments™, the Peak Force™ tapping mode of Bruker™ or "Jumping Mode" of Nanotec™. In these modes, the tip is oscillated in the vertical direction at high frequency using a sinusoid waveform rather than the triangular wave used in the classical force volume mode. This modification tremendously accelerates the data acquisition process and permits high-resolution imaging of the surface with a reasonable acquisition time. For a detailed comparison between the results obtained with the QI™, Peak Force™ and standard force volume imaging on bacteria, the interested reader can refer to the recent work of Smolyakov et al. (60).

Increasing the scanning speed brings new drawbacks. It should be highlighted that indentation measurements contain two components, an elastic and a viscous one. The viscous component influence increases with the indentation speed explaining why samples appear stiffer when indented at high speed. As an illustration, entering in water by walking from a beach or falling off a jet-ski painfully demonstrates the increase of the viscous component at higher speeds. To get rid of this effect peculiar imaging modes were developed, such as the rate-jump method (61,62). It consists of indenting the sample at a certain speed up to a given indentation depth. The indentation process is then stopped for several seconds before the retraction of the tip starts. The Young's modulus of the sample is calculated according to the cantilever deformation during the retraction cycle. The main drawback of this method is the tremendous time it requires to acquire a single frame, as an illustration recording a 256 × 256 pixel image can last up to 20 h (with 40 ms extension and retraction delay and a one second stop in between).

Another technique referred to as multi-harmonic AFM consists of monitoring the higher harmonics of the cantilever oscillations while the tip is interacting with the sample (63,64). Information such as stiffness, adhesion or viscoelastic dissipation can be extracted from images that have been acquired much faster than with the previously mentioned method.

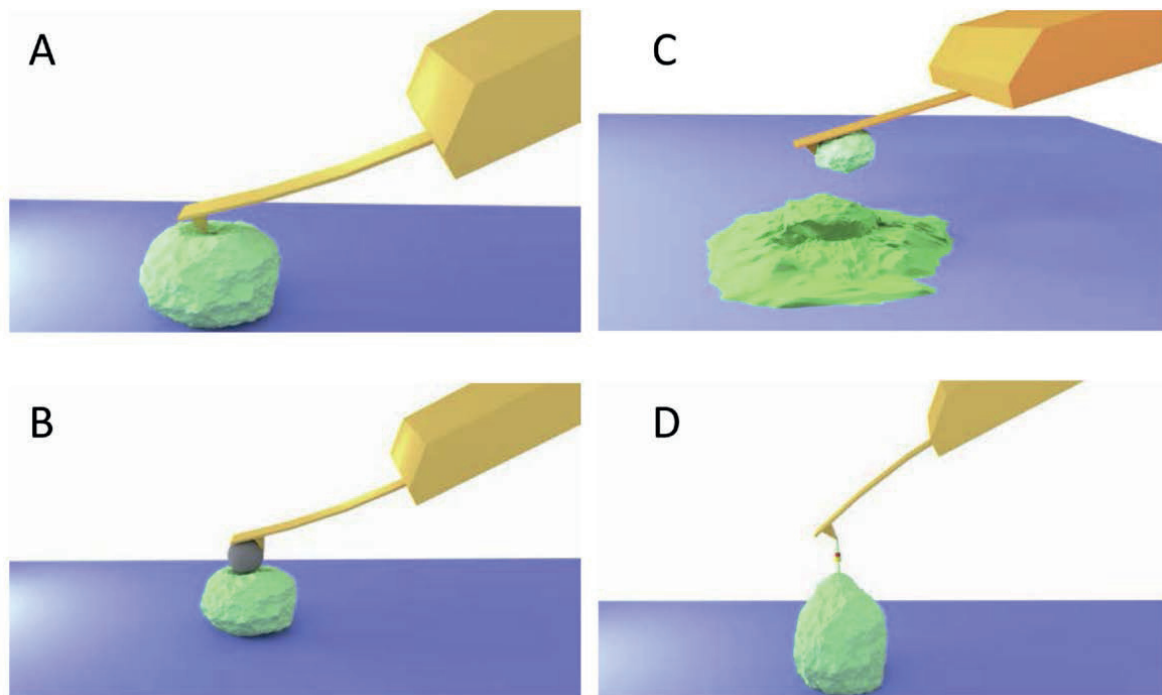


**Figure 2.1** Some possible types of AFM experiments on cells. **A)** Imaging and nano-indentation experiments: in nano-indentation experiments the tip is pushed into the cell and the cantilever deformation is used to calculate the cell mechanical properties. **B)** Similar nano-indentation experiment, but in this case the AFM tip is replaced by a spherical bead to probe a wider area. **C)** Cell-cell interaction force measurement: Instead of the spherical bead a cell is attached to the cantilever end and its interaction (essentially adhesive forces) is measured by approaching it to another cell present onto the substrate. **D)** Single-molecule recognition: the AFM tip is coated with molecules that interact with other molecules present on a cell attached to the substrate.

The techniques mentioned previously only provide one stiffness (or viscosity) value per pixel (or force distance curve). However, information about the stiffness distribution underneath the surface can be also addressed by AFM when using some particular approaches. The simplest one is the so called stiffness tomography (65,66). The technique is based on the classical force volume imaging mode and differs from it only in its data processing step. During indentation, the AFM tip penetrates into the sample and encounters different “layers” and each of them might have different elastic properties. In the “classical” approach, the contribution of all these layers is integrated provide one single numerical value (i.e. the Young’s modulus). In stiffness tomography the indentation curve is sliced in small segments and each of them is fitted with the theoretical model (Hertz or Sneddon) to give the distribution of stiffness as a function of the indentation depth. This simple approach permits the detection of structures located underneath the surface of the sample according to their mechanical properties (67). Another, somewhat more complex technique is the so-called scanning near field ultrasonic holography. In this technique, the sample is submitted to ultrasonic waves that travel through the cell and drive an AFM cantilever that is kept in contact with the sample. In case the cantilever is independently oscillated, nonlinear tip-surface coupling can occur that is used to probe the interior of the sample (68). As illustrated on **Figure 2.1**, AFM can be used in different configurations and an extensive review on the principles and applications of advanced force-

distance-based AFM techniques for the quantitative analysis of cellular and biomolecular systems can be found in Dufrene and Pelling (69).

### 2.1.1 QI™ mode by JPK Instruments

The main advantage of this mode is that there are no lateral forces applied to the imaged sample, and that the user can control vertical force at each pixel. High lateral forces in other imaging modes usually damage or stretch soft biological samples under investigation, especially if they are loosely attached to the substrate. Minimum interaction force of the tip towards the sample is less than 50 pN in this mode. There is also a possibility of setting a separation distance between the sample and the tip. Furthermore, no XY movement is performed, making sure all force curves are measured under constant velocity. In every pixel, up to 512 x 512 pixels resolution, it is possible to collect height topography and mechanical properties at the same speed as normal imaging. All the information, including height, are extracted out of each force-distance curve. The slope, making a linear fit to the extend part of the force-distance curve at every pixel, is used as an indication of the sample's stiffness. Furthermore, the maximum unbinding force is calculated online during measurements and is displayed in the adhesion image. However, for more precise values in elasticity and adhesion maps, the image and its force curves must be post-processed using the Hertz fit. Batch processing feature allows quick processing of thousands of force-curves, and can be done using the JPK's Data Processing Software.

Soft indenters, such as cantilevers, allow local probing of biological samples. To calculate the characteristic parameter of interest (elasticity or adhesion), various models are used, but the most prominent one is the extended Hertz model. There are several approximations used in the model. It approximates the sample as isotropic and linear elastic solid, occupying infinitely extending half-space. Also, it assumes that the cantilever tip is not deformable and that there are no additional interactions (adhesion) between it and the sample.

The choice of cantilever tip geometry dictates which equation should be used further in the model, as different indenter shapes lead to different radii of the contact point. For a four-sided pyramid, as in the case of DNP-10 (Bruker) cantilevers, the force can be obtained from:

$$F = \frac{E}{1 - \nu^2} \frac{\tan \alpha}{\sqrt{2}} \delta^2$$
$$\alpha = \frac{\tan \alpha}{\sqrt{2}} \delta$$

In the equation,  $\alpha$  is the face angle, indicated on the panel B of **Figure 2.2**. The Poisson's ration  $\nu$  is typically used as 0.5 for incompressible materials like rubber.  $E$ , the elasticity, can be derived from the equation differently, but the most often used method is to fit the force indentation curve (F- $\delta$  curve) using  $E$  as a fit parameter.

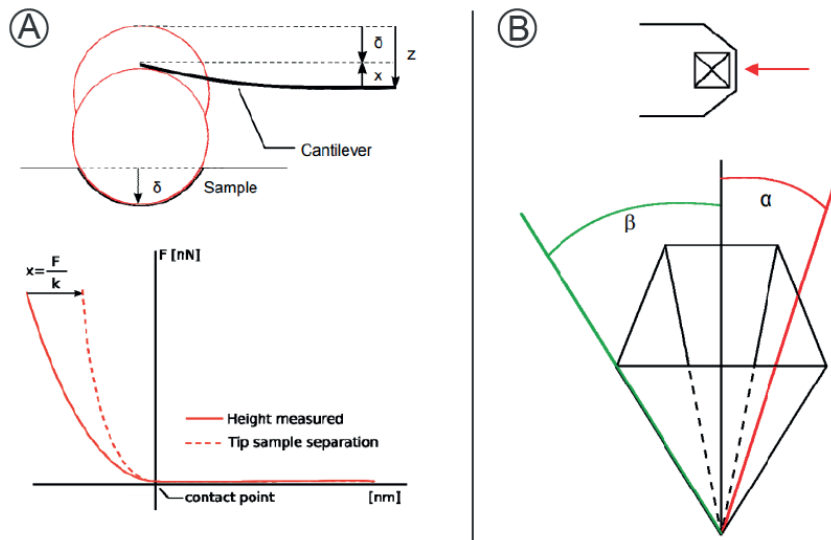


**Figure 2.2 Panel A)** Schematics of an indentation experiment. The cantilever is approached onto the sample by distance  $z$ , and bent in the opposite direction for  $x$ , while the sample is indented for  $\delta$ . The indentation is calculated by subtracting the cantilever deflection from the distance  $z$ . Correction of the height is represented in the bottom figure. **Panel B)** Schematic representation of a tip geometry as a four-sided pyramid.

The Hertz model, although easy to implement, has its limitations. Only small indentations of approximately 5-10% of the sample's height should be performed in order to keep the validity of the model. The assumption that the sample is elastic and homogeneous does not hold for biological material such as cells, which exhibit inhomogeneities on different areas (nucleus and other organelles). Dissipation of the energy delivered by the tip due to the samples plasticity is appearing as a hysteresis between the approach and retract parts of the curve.

In addition to the calibration method described in a previous chapter, JPK software takes into an account several correction factors for the sensitivity calculations. The thermal noise method is based on the simple harmonic oscillation equation of the amplitude-frequency dependence.

$$A^2(f) = \eta^2 + A_{DC}^2 \frac{f_0^4}{(f^2 - f_0^2)^2 + \frac{f_0^2 f^2}{Q^2}}$$

$A_{DC}$  is the amplitude,  $\eta$  is the white noise background,  $f_0$  is the resonant frequency and  $Q$  is the quality factor. The values are fitted from the thermal noise curve in the software, using the area under the fit curve. The user may change parameters such as the temperature, for calculations of thermal energy, the angle of the cantilever mount, or add the customized correction factor that depends on the cantilever type. Any additional correction factor used will be multiplied with the result of the basic calculation to provide an actual value used by software. For the fitting curve, normally, the first resonance is used, due to the largest amplitude and signal to noise ratio. Furthermore, the shape of the cantilever affects thermal noise measurements. Deviation from the simple harmonic approximation is corrected by using a factor of 0.92 for triangular cantilevers oscillating on the first mode.

## 2.2 State of the art

*This section contains published work:*

Kasas, S., Stupar, P. and Dietler, G., 2017, August. **AFM contribution to unveil pro-and eukaryotic cell mechanical properties**. In *Seminars in Cell & Developmental Biology*. Academic Press.

### 2.2.1 AFM of bacteria

Bacteria are simultaneously the smallest and the most numerous cells living on Earth. Depending on the species, their size varies between 0.3 and 5  $\mu\text{m}$  with very diverse shapes such as spheres (cocci), rods (bacilli) or spirals (spirilla and spirochetes). According to their staining affinity, they are usually classified in Gram-positive or Gram-negative groups. From the structural point of view, they are relatively simple, possess no cell nucleus and are therefore referred to as prokaryotes.

Among the very first AFM measurements that were targeting the mechanical properties of bacteria and bacteria-like organisms, we should mention Xu et al. (70) who conducted AFM indentation experiments on the archaeobacterium *Methanospirillum hungatei*. Archaeobacteria or archaea, were initially classified as bacteria, but for many this classification is nowadays outdated. Despite the fact that archaeobacteria and bacteria have similar shapes, archaea possess numerous genes and metabolic pathways that are present in eukaryotes. *M. hungatei* AFM indentation measurements gave Young's moduli ranging between 20 and 40 GPa, implying that the bacterium can sustain internal pressures up to 400 atm.

Later, Amoldi et al. (71) explored the stiffness of a spiral shaped bacteria, *Magnetospirillum gryphiswaldense* in a liquid medium. These types of bacteria possess magnetic particles in their cytoplasm that orient the organism according to earth magnetic field. It should be highlighted that the indentation depth an AFM tip reaches under a given force not only depends on the cell wall stiffness but also on the internal osmotic pressure of the organism. In order to separate the individual contribution of these two components the authors performed their measurements in liquid medium and varied the osmotic pressure outside the organism. This setup separated the contribution of the bacterial internal osmotic pressure from the cell wall stiffness.

*Haemophilus influenzae* is a commensal germ living in the human upper airways but can in some cases be responsible for pathologies such as pneumonia or meningitis. *H. influenzae*, like several other bacteria, can be equipped with different surface appendages such as pili, fimbriae, exopolysaccharides or flagella. These structures are the morphological support for numerous important physiological or pathological functions such as motility, adhesion or cell-cell communication. Arce et al. (72) studied the mechanical properties of different *H. influenzae* variants (PittEE and PittGG) and highlighted that those that possess pili have different mechanical properties than those without. The team extended its studies to biofilm formation and biofilm mechanical properties as well. Under certain conditions, bacteria attached to a surface modify their phenotype and secrete a polymeric matrix that embeds the microorganisms and modifies numerous features of their properties. As an illustration, bacteria embedded in such biofilms can develop antibiotic resistance up to 1000-fold greater than their freely swimming (planktonic) counterparts. Lau et al. (73) also explored *Pseudomonas aeruginosa* biofilm visco-elastic and adhesive properties.



Some bacteria such as *Klebsiella pneumonia* synthesize an extracellular polysaccharide capsule that protects them from desiccation, disinfectants and antibiotics. It also increases their capacity to adhere on surfaces and to form biofilms on catheters and other medical devices. Wang et al. (74) measured wild type and capsule deficient *K. pneumonia* mechanical properties under extreme osmotic conditions. Their results suggest that the polysaccharide capsule lessens the effects of the environment by protecting bacteria from osmotic stress.

Some bacteria, when exposed to nutrient-deprived conditions, undergo differentiation processes referred to as sporulation in which they secrete 100–200 nm thick polymer and protein barriers and become metabolically dormant. These spores are one of the most resistant form of life. Once nutrients become available, the spores germinate into their vegetative form and become pathogenic. The difference in the mechanical properties of *Bacillus anthracis* spores were assessed by Pinzon-Arango (75) to be 15 times stiffer than those of the vegetative forms. In a recent work Li et al. (76) pushed further the study of the mechanical properties of bacterial spores by exploring the properties of their inner constituents. The authors used a stiff cantilever equipped with a diamond AFM tip to section individual spores and a soft cantilever to image and characterize the spore's interior constituents. The authors observed that numerous parameters such as the elastic modulus, the adhesion force as well their thermal responses at elevated temperatures, varied significantly in different regions of the spore section.

Up to now we only mentioned the global stiffness of whole bacteria, however it should be mentioned that several authors highlighted inhomogeneous spatial distribution of Young's moduli on the surface of different bacteria such as *Bordetella pertussis* (77) with the presence of rigid nanodomains. Similarly, stiffness inhomogeneities were also highlighted underneath the surface in *E. coli* by using stiffness tomography by Longo et al. (67). The same team later monitored bacteria superficial and deep stiffness modifications upon exposure to antibiotics (78).

Bailey et al. (79) recently explored the mechanical properties of the dividing Gram-positive *Staphylococcus aureus*. Gram-positive bacteria, contrary to their negative counterparts possess a thick cell wall that encapsulates their single cell membrane. Its main function is to maintain cellular integrity by resisting the high internal osmotic pressure of the cytoplasm. The authors recorded time-lapse stiffness maps of dividing bacteria and noticed that cell wall mechanical properties change throughout the division cycle. A local softening of the cell wall along the division circumference was observed, whereas the cell wall on either side of the division circumference became stiffer. The newly formed septum between the two bacteria daughters was also measured to be stiffer than the surrounding older cell wall.

Penicillin binding proteins (PBP) play an important role in the synthesis of the peptidoglycans that composes the Gram-positive bacterial cell wall. These proteins are the target of a whole class of antibiotics referred to as  $\beta$ -lactams. However, *Staphylococcus aureus* developed a remarkable ability to resist their action by destroying the antibiotic with  $\beta$ -lactamases or by modifying its penicillin binding proteins. The peptidoglycans that compose the cell wall are heavily cross-linked and Loskill et al. (80) used PeakForce™ AFM imaging and different *S. aureus*™ mutants to investigate the

importance of this proteoglycan cross-linking on the mechanical properties of the cell wall. The authors observed that mutants lacking PBP4, a transpeptidase that is strongly involved in the cross-linking of the cell wall proteoglycans, possess much softer cell walls than their wild type counterparts.

Tokarska-Lodak et al. (81) recently investigated the effects the human natural defense system on the elastic and adhesive properties of *Borrelia burgdorferi* spirochetes. These bacteria spread among humans through the bite of ticks and are the agents of Lyme disease. The authors explored the nanomechanical modifications induced by exposure of *B. burgdorferi* to different defense molecules of our immune system. The authors measured a significant decrease in bacterial Young's modulus and adhesive properties in samples exposed to the complement system and different specific antibodies. These modifications in the nanomechanical properties highlight the damaging effects of natural defense system on the bacterial wall.

Among the different methods used to fight bacteria, nanoparticle based approaches seems nowadays a promising alternative. Ramanilgam et al. (82) studied the effects of silver based nanoparticles (AgNP) on *Escherichia coli* and *Pseudomonas aeruginosa*. In the frame of their study the authors employed AFM to evaluated alterations in the mechanical properties of the bacterial wall upon exposure to AgNPs. The study was very thorough and involved AFM for imaging, roughness and mechanical properties measurements, but also other techniques such as Fourier transform infrared (FTIR) spectroscopy to conduct chemical analysis of the cell membrane or dynamic light scattering to monitor the effect of AgNPs on the membrane surface potential. Here again, the AFM nanomechanical measurements demonstrated a reduction of the cell wall stiffness following exposure to AgNPs.

All these experiments clearly show that AFM is a powerful tool to measure bacterial stiffness. It also permits to monitor stiffness changes as a function of time or the chemical composition of the medium. Before finishing this section dedicated to the measurements of the mechanical properties of bacteria by AFM we would like to mention some recent review articles that focus on similar topics and which the interested reader could refer. Longo and Kasas (83) focus on the use of AFM to explore activity of antibacterial drugs. An excellent article comparing the different high speed stiffness mapping modes applied on bacterial cells can be found in Smolyakov et al. (60). More general reviews covering AFM nanomechanical measurements involving not only bacteria but also other cell types can be found in Refs. (84,85). These authors also review studies involving adhesion measurements.

### 2.2.2 AFM of yeast cells

Yeast cells are classified as members of the fungus kingdom. Yeast cells play an important role not only in several industrial processes involving fermentation (beer, baking, biofuel) but also in numerous human and animal infectious diseases. Yeast is also an important model organism in fundamental cell biology research. Yeast cells are unicellular, eukaryotic organisms that are believed to have evolved from multicellular ancestors. Most yeasts reproduce by mitosis and by budding. Budding is a specific process in which the new organism develops as an outgrowth (bud) of its mother cell. Yeast cells are surrounded by a thick cell wall that maintains the cellular shape and permits them

to resist turgor pressure. The cell wall essentially consists of a glucan microfibrillar matrix that embeds numerous components such as polysaccharides, proteins, lipids, inorganic phosphate and chitin. Touhami et al. (86) were among the first to study yeast cell wall mechanical properties by AFM. The authors were particularly interested in the mechanical properties of the cell wall domains involved in budding. Force volume AFM measurements revealed that these regions were up to 10 times stiffer (6 MPa) than the surrounding cell wall. The stiffness increase was attributed to the accumulation of chitin which also plays an important structural role in the exoskeleton of arthropods and insects.

*Saccharomyces cerevisiae* cell wall can relatively easily be chemically modified and AFM used to directly assess the consequences of the modifications in terms of stiffness and topographic changes. Suchodololskis et al. (87) treated *S. cerevisiae* cell wall with lithium acetate and dithiothreitol and noticed a significant increase in the cell wall stiffness.

El-Kirat Chatel et al. (88) and Formosa et al. (89) studied the effects of caspofungin on the cell wall of *Candida albicans*. *C. albicans* is usually a commensal organism living in the gastrointestinal tract of healthy adults. However, it can become pathogenic in immunocompromised patients. Caspofungin is a novel drug known to alter yeast cell wall biogenesis by inhibiting  $\beta$ -1,3-d-glucan synthesis. In their very complete study, the authors explored morphological, adhesive and mechanical modifications of the organism upon drug exposure. The AFM measurements highlighted a decrease in the cell wall stiffness and a massive exposure on the cell wall of the adhesion protein Als1. By using hydrophobic AFM tips the authors also demonstrated an increase in the cell wall hydrophobicity. The technique used in the study implies functionalization of the AFM tip with specific functional groups (CH<sub>3</sub>) to map and probe the hydrophobic character of living cell surfaces (90).

Recently Mercade-Prietro (91) pointed out severe discrepancies between stiffness values obtained by AFM and those measured by micromanipulators on *Saccharomyces cerevisiae*. AFM measurements report values between 0.2 and 1.6 MPa whereas micromanipulator studies around 100 and 200 MPa. According to the authors, the 3 orders of magnitude difference is due to the use of inappropriate mathematical models to fit measurement data. AFM measurements are accomplished by indenting a sharp tip into the outermost part of the cell wall, whereas micromanipulation studies consist of compressing the whole yeast cell between two parallel plates. The Hertz-Sneddon model used to interpret AFM data considers that the whole cell is composed of a single continuum material. Such an assumption is of course inappropriate for complex structures such as yeast cells. The authors therefore developed and tested by finite element method a new mathematical model that considers that the cell wall consists of two different layers: one external that is relatively soft (essentially composed of mannoproteins) and a stiff inner layer (made of  $\beta$ -1,3-glucan fibers and chitin). This new model suggests that AFM experiments measure the elastic modulus of the external layer only, whereas micromanipulation data provides information of the total cell wall stiffness.

Yeast, like algae and plant cells, can in certain conditions adopt a growth pattern referred to as tip growth. In yeast it occurs during pseudo-hyphal growth in response to nutrient depletion, as well as during mating. During mating tip growth, the initially spherical cell grows a projection in direction of

a mating partner to overcome the distance between the two cells and achieve cell fusion and zygote formation. To achieve such an asymmetric growth, cells need to generate inhomogeneous cell walls by either local synthesis and/or local lysis of the cell wall material. Recently Goldenbogen et al. (92) used AFM to explore cell wall elasticity distribution on *Saccharomyces cerevisiae* during tip growth. Stiffness maps of the of *S. cerevisiae* demonstrated that the emerging mating projection is significantly softer than the rest of the cell, whereas the tip of the projection is harder. The authors used these measurements to construct and simulate a virtual model of a *S. cerevisiae*. The model was built by using the finite element method. It consisted of a pressurized sphere built with triangular elastic and elastoplastic elements. The mechanical properties and thickness of certain elements were modified to permit an asymmetric deformation under the internal pressure. It permitted the simulation of the dynamics of tip growth and calculation of numerous mechanical parameters such as the different stresses and strains that appear in the cell wall during growth.

These experiments show that yeast cell wall mechanical properties depend on numerous factors such as cell division or exposure to different chemicals.

The readers interested in review articles focused on yeast exploration by AFM are invited to refer to Refs. (85,93).

### 2.2.3 AFM of plant cells

Up to now plant cells were relatively poorly explored by AFM as compared to mammalian cells or bacteria. The large size and rough surfaces of plant cells usually complicates AFM imaging. Plant cells also mechanically behave differently from mammalian cells. Their cell shape and mechanical properties are essentially determined by the cell wall, whereas in mammalian cells these functions are fulfilled by the cytoskeleton. The mechanically rigid plant cell wall also permits cells to attain high turgor pressure (internal hydrostatic pressure) which explains why the wall experiences a high tensile stress. Some authors compared plant cells to “hydraulic machines” due to the similar concept of balanced counterforce between the primary wall stresses and the turgor pressure (94). Typical turgor pressures in plants are in the range of 0.3–1.0 MPa, that translates to between 10 and 100 MPa of tensile stress in the cell wall (95).

The very first mechanical AFM measurements involving plants were accomplished by Yamada et al. (92) on chloroplasts, the organelles that perform photosynthesis. The group estimated their Young's modulus to 26 kPa. Later, Lesniewska et al. (96) studied the cell wall stiffness of grapevine. To resist microorganism attacks, plant cells can strengthen their cell wall and change its mechanical properties. Lesniewska et al. induced a very similar structural modification by UV light and witnessed an increase in stiffness of the cell wall from 72 to 100 MPa. Plant cuticle is a thin lipophilic layer that covers plant organs exposed to air and that protects them from excessive water loss. In addition, it defends aerial organs from hostile microorganisms and external physical and chemical aggressions. The cuticle is essentially composed of two components: cutin, a polymer of mainly C16 and C18 hydroxy fatty acids or diacids, and waxes. Isaacson et al. (97) explored by AFM the mechanical properties of the tomato fruit (*Solanum lycopersicum*) cuticle in cutin deficient mutants. Among

other results, the measurements revealed that cutin deficiency is correlated with an increase in the cuticle stiffness but not with its permeability to water.

The plant cell wall consists of a fiber-reinforced composite in which rigid cellulose microfibrils are embedded, and cross-linked by a hemicellulose and pectin matrix. In order to permit the plant and its organs to grow, a fine-tuned interplay between turgor-driven cell expansion and the resistance provided by the cell wall is required. This explains why numerous structural and biochemical modifications have to occur. These modifications essentially affect a specific region, referred to as meristem. It is an un- or poorly differentiated structure that gives rise to roots, leaves and flowers. Peaucelle et al. (98) used AFM to study living *Arabidopsis thaliana* meristem and correlated its elastic properties during organ growth modifications with demethylesterification of the cell wall pectins. Elasticity measurements were accomplished by fixing spherical beads at the end of the AFM cantilever. This approach allows the enhancement of the sampling area and to provide a better fit to theoretical models since the shape of the indenter is better-defined (sphere) than with conventional AFM tips. Usually, large spherical indenters are better suited to capture the internal pressure of the cell, whereas conical or pyramidal tips are more appropriate for measuring the local mechanics of the cell wall. A similar study involving *A. thaliana* living roots was conducted by Fernandes et al. (99). For this study, the authors developed a particular sample preparation technique that permitted the examination by AFM of different regions along *A. thaliana* roots. The measurements were recorded in liquids, providing for the variation of the internal turgor pressure in live cells. In these experiments, the authors did not observe clear differences in the mechanical properties along the length of the root.

Radotic et al. (100) employed stiffness tomography to follow *Arabidopsis thaliana* cell wall modifications as a function of time, i.e. growth phase. For these experiments, the authors used individual *A. thaliana* cells grown in suspension. The technique highlighted the incorporation of novel material in the wall and to follow its displacement towards the surface. The cell wall chemical composition was simultaneously monitored by using FTIR spectroscopy. Similar to the previous work, suspended cells extracted from tomato pericarp were used to explore the mechanical properties of single plant cells by AFM (101). In this study the authors used a wide range of indenters with a radius of curvature varying between 20 nm and 5  $\mu\text{m}$ , allowing the evaluation of the effect of the tip geometry on the measurements. The experiments showed a great cell variability regarding the elastic modulus. The role of the pectin component of the cell wall was also addressed by Xi et al. (102), who studied onion cell walls in liquid medium. Working in liquids affords the ability to easily modify the imaging medium composition and to expose the studied structure to various chemicals. By adding  $\text{Ca}^{++}$  ions to the solution the authors induced an increase in the pectin network crosslinking and noticed a dramatic increase in the cell wall Young's modulus. On the other hand, reducing free  $\text{Ca}^{++}$  in the imaging solution with the chelating agent EDTA decreased the pectin network crosslinking resulting in a significant decrease in the cell wall stiffness.

Despite AFM stiffness measurements of plant cells are not as numerous as those of bacteria or mammalian cells, interesting and scientifically relevant data about the nano-mechanical properties of the cell wall and its internal structure can be obtained by this technique.

Before closing this paragraph, we invite the interested readers to refer to the recent and excellent review of Vogler et al. (103) that covers most of the available methods to determine the mechanical properties of cell walls and discuss their advantages and disadvantages.

#### 2.2.4 AFM of mammalian cells

In this section, we will essentially focus on AFM conducted nano-mechanical studies involving mammalian cells. The number of publications focusing on this topic dramatically increased during the recent years, essentially thanks to the availability of rapid force mapping imaging modes such as the PeakForce™ or QI™ mode and the recent discovery that the mechanical properties of single cells are closely related to a major public health issue, i.e. cancer. Unfortunately, most of the cancers are still resistant to efficient treatments, but if detected early, the disease is curable and tremendous means are dedicated nowadays to early detection and prevention. Numerous AFM based studies explore the possibility of AFM early detection of cancer exploiting the nano-mechanical modifications induced by cancer. Due to space limitations in this section we will essentially focus on the most recent contributions. The first part of the section covers the study of different components of mammalian cells that play a role in the establishment of the mechanical properties of the cells, whereas the rest is dedicated to the changes in the mechanical properties occurring in the frame of various pathologies.

The majority of eukaryotic cells are surrounded by a layer of polysaccharides and glycoproteins attached to the membrane, called the pericellular layer. This layer can also include other molecules frequently referred to as the glycocalyx. The mechanical properties of this pericellular layer were recently explored with AFM (104). The team studied the mechanical changes of this layer upon exposure to hyaluronidase. Hyaluronidases are enzymes that disrupt some components of the pericellular layer and increase tissue permeability. They are frequently used to enhance the speed of drug delivery. The team also analyzed force-distance curves using a dedicated mathematical (brush) model that permitted one to distinguish the contributions of the cell body and the brush, on the shape of the indentation curve. The pericellular layer was also targeted by Simon et al. (105) who also extended the study to the mechanical properties of this layer in cortical neurons. Liang et al. (106) employed the mechanical properties of the extracellular matrix to distinguish differentiated cells from stem cells. This application could potentially have an impact in stem cell therapy protocols.

The eukaryotic cell membrane is a 10nm thick phospholipid layer whose role has largely been neglected in AFM nanomechanical studies. However, nowadays it is widely accepted that this membrane contains specific domains referred to as lipid rafts. These domains participate in numerous important physiological processes such as signal transduction. The chemical composition (amongst others, the cholesterol content) of lipid raft domains is different from the rest of the membrane. Roduit et al. (107) explored by AFM the nanomechanical properties of lipid rafts in living neuronal cells. The measurements indicated that lipid raft domains are about 30% stiffer than the surrounding membrane.

Underneath the cellular membrane, cytoskeletal components determine the mechanical properties of eukaryotic cells. The cytoskeleton is a dynamic network composed of actin, microtubules and

intermediate filaments, that plays an important role in numerous basic physiological processes, such as: determination of the cell mechanical properties, maintenance of the cellular shape, motion, cell division, or intracellular organelle transportation. In addition, the cytoskeleton is the preferential target of numerous anti-cancer drugs, explaining why from the very beginning of the AFM technology, numerous studies focused on the exploration of its mechanical properties and modifications upon drug exposure. Rotsch and Radmacher (108) applied AFM to study the effects of various drugs to disrupt or stabilize components of the cytoskeleton. Disrupting the actin cytoskeleton decreased the stiffness of fibroblasts; however, stabilizing microtubules did not lead to any observed effect on the cell stiffness. Later, Kasas et al. (109) conducted a somewhat similar study, designed to distinguish the role actin and tubulin networks play in the mechanical properties of living cells. In most mammalian cells the actin cytoskeleton is located immediately under the cellular membrane, whereas microtubules reside mostly in the interior parts of the cell. In this study, the authors selectively depolymerized the actin and tubulin cytoskeleton and observed the changes occurring on the indentation curves. These studies demonstrated that the very first part of the indentation curve reflects the mechanical properties of the actin cytoskeleton, whereas regions of the curve recorded at higher indentation depths were mostly reflecting the state of the microtubular network. Recently Fallqvist et al. (110) investigated the influence of the actin cytoskeleton on the mechanical properties of fibroblasts under the effects of Latrunculin B, a drug that disrupts the cellular actin network. The study showed that the treatment not only reduced cellular stiffness, but also increased largely the relaxation rate of the cytoplasm, suggesting that the actin network is not only influencing the stiffness of the cell, but also its viscous properties. Recently, similar experiments were extended to primary chondrocytes, fibroblasts, endothelial cells, hepatocellular carcinoma cells, and fibrosarcoma cells (111). In this study the cells were exposed to cytochalasin D and nocodazole in order to disrupt respectively their actin and/or microtubule cytoskeleton. Here again, in the majority of the tested cell types actin filaments were found to contribute more to the stiffness of the cells than the microtubules. Readers interested in the mechanical properties of different types of mammalian cells are invited to refer to the excellent review of Kuznetsova et al. (112).

Biological systems are characterized by a close relationship between structure and function. Since structure is essentially determined by the mechanical properties of its building blocks and the way they are assembled, one can expect to observe mechanical modifications upon function alteration. It is the main reason why numerous studies were designed to relate the modifications of the mechanical properties with pathological states. These studies involved numerous diseases and biological structures. Most of the studies focus on cellular components, however some, such as that of Argyropoulos (113) concern alterations of extracellular components of the human body in pathological states. In this study, the authors tested the mechanical properties of collagen fibrils in diabetic skin sections. The authors observed an increase in the fragmentation of collagen fibrils. Mechanical alterations involved an overall increase in the traction force of fibers and tensile strength as compared to intact collagen fibrils in non-diabetic skin.

Among cells, erythrocytes were found to express modifications in their mechanical characteristics in numerous pathologies such as anemia (114), Parkinson's (115) or Alzheimer's diseases (116). Readers interested in AFM explorations of erythrocytes and their modifications occurring in the

frame of various pathologies are invited to refer to the excellent and exhaustive review of Mukherjee et al. (117).

Another cell type that was exhaustively studied for its alterations in the mechanical properties in the frame of different diseases are endothelial cells. These cells cover the interior face of blood vessels and play an important role in numerous physiological and pathological processes such as blood pressure regulation, hypertension or atherosclerosis. Hayashi et al. (118) conducted AFM measurements on endothelial cells from cholesterol-fed rabbits. AFM indentation data demonstrated that the stiffness of endothelial cells covering atherosclerotic plaques increased with atherosclerosis progression. A similar study was conducted by Yan et al. (119) in which the authors studied the cholesterol repletion effect on the nano-mechanical properties of human umbilical cord vein endothelial cells. AFM measurements demonstrated that both stiffness and viscosity were increased over 30% under the effect of cholesterol. The readers interested in AFM exploration of endothelial cells are invited to refer to the very clear and exhaustive review article of Szymonski (120).

Wu et al. (121) used AFM to study membrane plasticity and mechanical dynamics of individual neurons in mice suffering chronic epilepsy. The study highlighted that neuronal cell elasticity was significantly increased in this disease. Readers interested in AFM exploration of neuronal cell biomechanics are invited to refer to the very complete review of Spedden and Staii (122). Readers interested in the correlation between cell mechanics and disease can refer to Morton et al. (123–125) or to the more recent article of Rianna and Radmacher (126).

The remainder of this section is dedicated to studies targeting cancer and its treatment. AFM studies related to this topic essentially focus on the differences in migration ability, morphology and stiffness (127,128) of cancerous cells compared to their healthy counterparts. Breast cancer is the most frequently diagnosed cancer among women. In a pioneering study, Plodinec et al. (129), demonstrated that the AFM indentation technique can be used for probing human breast biopsies at the tissue level. High-resolution stiffness mapping allowed the team to distinguish between the cells from the extracellular matrix in tissue samples and to reveal that cancer progression is associated with a significant softening of tumor epithelial cells in comparison to normal mammary tissue. As the tumor progresses, broadening of the stiffness distribution results from the cancer cells infiltrating the surrounding tissue, stromal disorganization and tumor vascularization. This discovery could be a useful marker to diagnose cancer and grade the level of invasiveness. The study supports the hypothesis that metastatic cells need a certain degree of flexibility and elasticity to leave their original place of growth and the data suggests a direct link between cancer cell softening in the primary tumor and its metastatic potential. Coceano et al. (130) compared three different human breast cell lines by measuring their elastic modulus and mapping their stiffness distribution. The authors found that the region on top of the nucleus provided the most reliable results. Aggressive basal breast cancer cells were also found to be significantly softer than their normal counterparts. Ansardamavandi et al. (131) used Fuzzy-logic algorithms to classify and categorize breast tissue according to the Young's modulus. Stiffness coefficients gathered on cellular, non-cellular and fibrous regions of cancerous breast tissue were classified in three groups (Young's modulus of up to 3 kPa, 3–7 kPa and above 7 kPa). Here again the study demonstrated a 50% decrease in the average Young's modulus of cellular



region of cancerous tissues compared to their healthy counterparts. Smolyakov et al. (132) used AFM to analyze elasticity, cell–cell interaction forces and membrane tether extrusion of four breast cancer cell lines with different invasiveness. The data suggests that invasive breast cancer cells are softer, more adhesive and possess a higher ability to extrude tethers.

Calzadomartin et al. (133) studied cytoskeleton arrangement by means of Peak-Force™ modulation AFM for high-frequency topography and stiffness mapping. The study revealed that the actin stress fibers are present in apical cell regions and are the dominant contributor to cellular stiffness in healthy cells. In the case of malignant cells, the stress fibers appear to be confined to the basal regions only, and therefore, do not contribute to the overall stiffness of the cell.

Numerous other cancer types affecting bladder (134), cervix (135), oral mucosa (136), bone (137,138), prostate (139), lung (140) or brain (141) were imaged and their mechanical properties mapped by AFM. All these studies concluded that cancer cells can be distinguished from their healthy counterparts according to their mechanical characteristics.

Before closing this section, it should be mentioned that the effects of diverse anticancer drugs on the mechanical properties of cancer cells are also intensively studied by AFM. Here again due to space limitations we will only mention some of the most recent publications. Kung et al. (142) investigated nanoscale biological modifications in melanoma cells undergoing cisplatin treatment. Melanoma is a highly aggressive skin cancer that resist chemotherapy. The authors noticed that the drug alters cellular morphology, making them rougher, flat and enlarged. The Young's modulus of cells undergoing cisplatin treatment was significantly reduced as compared to the untreated counterparts. Lian et al. (143) explored the effects of a traditional Chinese medicine drug, artesunate, on glioma cells. The drug is traditionally employed against malaria but has shown beneficial effects on some cancers as well. Glioma is the most frequent malignant brain tumor and the study aimed to identify the anticancer effects of the drug by assessing, among other parameters, cell proliferation, migration and the biomechanical properties of treated glioma cells. According to the study, the Young's modulus of artesunate treated cells decreased from 23 to 3 KPa. The effects of other drugs such as methotrexate (144) or cytochalasin D (145) were also recently investigated in terms of cancer cell Young's modulus modifications upon treatment. Readers interested in cancer cell diagnostics by AFM can refer to the recent and very complete reviews by M. Lekka (128), A. Stylianou and T. Stylianopoulos (146).

It should be highlighted that AFM measurements on cancerous cells and tissue are far from being straightforward: the experimental setup is complex, obtaining statistical significance is time consuming and a large number of parameters can interfere with the measurements. In addition, some reports such as Maherally et al. (147) indicate a decrease in some cancer cell (glioma) stiffness in less invasive cell lines. It suggests that low stiffness is not necessarily correlated to cancer aggressiveness and that this parameter varies for different cancer cell types and depends on micro-environmental conditions. However, despite all these difficulties, AFM remains a strong candidate for cancer research and diagnosis. In the near future, it will certainly help to improve the understanding of the pathophysiology and to explore more effective therapeutic approaches (146).

### 2.2.5 Conclusion

The emergence of new techniques in recent decades has spurred the investigation of biological matter on length scales down to the Angstrom, and on time scales down to the femtosecond. Often it is possible to push the investigation to the level of single molecule/single cell. Not only small length and time scales were accessible by these new techniques, but also properties thought to be inaccessible became available. We refer here to mechanical properties of cells and tissues that are nowadays investigated with tools that can deliver in almost physiological conditions (most of the studies presented in this review were carried out in liquid medium) elastic and viscoelastic parameters on a spatial scale down to the nanometer. The well-known fact that the differentiation of stem cells is strongly influenced by the elastic properties of the substrate is an important indication of how mechanical properties of living matter are an essential parameter to be studied. Together with other techniques, the Atomic Force Microscope has become one of the main tools to investigate the mechanical properties on length scales relevant for the biological specimen. The research presented here is just the tip of the iceberg of what is today feasible and investigated and should stimulate life science scientists to seriously consider the use of these novel techniques. For example, certain applications of the mechanical investigations by the Atomic Force Microscope might lead to diagnostic tools for early cancer detection.

## 2.3 Reorganization of cytoskeleton architecture upon mechanobiological exposure

*This section contains a manuscript in preparation.*

### 2.3.1 Introduction

The bone is constantly being re-modelled in a dynamic process in which bone-synthesizing cells osteoblasts are responsible for the formation of the bone. The equilibrium between bone matrix resorption and bone building is very important, and its disruption may lead to bone demineralization and fracture or malformation and structural instability.

Mechanical signals largely influence cellular behavior and cells readily respond to external stimuli such as fluid shear stress by changing conformation of membrane proteins, deforming the membrane itself, and re-structuring and re-organizing dynamic cytoskeletal network. Fluctuations in gene expressions that follow up those changes make up a complex signaling pathway.

It has been shown that many cellular and metabolic disruptions of humans and animals occur during the exposure to conditions of microgravity (148,149). Apart from the critical loss in muscle mass, there is a considerable loss of fluid and electrolytes, space motion sickness, anemia, reduction in immune response, and loss of calcium. Findings show that the observed changes in osteoblast growth are induced by alterations in the molecular mechanisms affected by microgravity (150).

The main goal of this project is to assess cellular cytoskeleton rearrangements after the simulated exposure to different environmental conditions, such as: flow-induced shear stress, pressure and microgravity. These conditions are intended to mimic the ones on a space flight. Part of the work consists in fluorescence staining and microscopic investigation of the actin fibers. The position and orientation of actin filaments are observed and compared between the cells grown in different growth conditions and the normal environment. The other part of the work consists in AFM quantitative imaging assessment, where stiffness and adhesion maps are obtained for a number of cells grown in those conditions. Comparison of each condition with the static (normal) growth environment gives information about the effect of that particular condition on the bone cell.

### 2.3.2 Materials and methods

**Cell culture and sample preparation.** Murine MC3T3-E1 cells, established as an osteoblastic cell line, were provided from Sigma (99072810). Osteoblasts were grown in alpha-modified minimal essential medium ( $\alpha$ -MEM; Life Technologies) supplemented with 10% fetal bovine serum (Life Technologies), 1% L-glutamin (Life Technologies) and 1% penicillin/streptomycin (Life Technologies) in an incubator at 5% CO<sub>2</sub> heated at 37°C. The medium was changed twice weekly, and the cells were subcultured into 75 cm<sup>2</sup> culture flasks by detaching them gently after a brief PBS rinsing step followed by Trypsin treatment once the cells were reaching subconfluency. For mechanical (un)loading and the static control, MC3T3-E1 cells were plated into Ibidi  $\mu$ -slide device ( $\mu$ -Slide I 0.4 Luer, ibiTreat, Ibidi, Martinsried, Germany) at a concentration of  $1.5 \times 10^4$  cells/mL. After overnight culture, the medium was replaced by  $\alpha$ -MEM (powder exempt of Bicarbonate, Life Technologies), 10% FBS, 1% L-glutamin, 1% penicillin/streptomycin, 25 mM HEPES (Life Technologies) adjusted to pH 7.4 for 4 hours in the incubator without CO<sub>2</sub> at 37°C.

**Immunofluorescence staining and imaging.** After 4 hours of mechanical loading or unloading, the cells were rinsed in PBS and chemically fixed with 4% (PFA) for 15 minutes. Before immunostaining the cells were rinsed twice in phosphate saline buffer (PBS). Eventually, the fixed cells were incubated with PBS 0.2% Triton X100 for 20 minutes, and exposed to Alexa Fluor 568 phalloidin (Molecular Probes) for 1 hour at room temperature. Finally, the cells were rinsed again with PBS before a quick water rinse and coverage with cover glass (by using polyvinylalcohol (Sigma)). A static osteoblast culture, in the same Ibidi device, was performed and actin stained as control.

**Simulated mechanobiological exposure.** A high hydrostatic pressure device was used to apply loads to the cells, using a servomotor-driven linear actuator assembly with a piston. Its exposure force is within a range from 0 to 15 atmospheres. Osteoblasts seeded on the ibidi devices were introduced into the apparatus, and the reservoir was fully filled with a pre-warmed water at 37°C. An interface controller allowed adjusting the pressure, while a feedback controller maintained the pressure constant during the experiments.

The shear stress system consisted of the two containers and a pump. A gravity driven constant flow of culture medium was allowed in the chamber with osteoblasts. The flow rate was adjusted by setting the container at the appropriate height above the osteoblasts. Applied shear stress were in the range between 9 and 12 dyn/cm<sup>2</sup>. The direction of the shear stress flow is estimated around 80°.

A Random Positioning Machine (RPM) is a laboratory instrument used to provide continuous random change in orientation relative to the gravity vector. The RPM was used to generate effects comparable to the ones of true microgravity when the changes in direction are faster than the object's response time to gravity.

**AFM force volume spectroscopy.** After adhesion and spreading, MC3T3-E1 osteoblasts were fixed in 3.7% paraformaldehyde (PFA) (Sigma) for 20 min and rinsed in PBS. Standard triangular cantilevers of silicon nitride (DNP-10, Bruker), having a nominal spring constant of 0.06 N/m, were used. AFM measurements were performed with a JPK Nanowizard III AFM (JPK) coupled with an Axiovert X optical microscope (Zeiss Microscopy) (**Figure 2.3**). The imaging was performed in the QI mode with the following parameters: 90 x 90 µm areas with 64 x 64 pixels were taken, using the Z length of 1500 nm, speed of 37.5 µm/s and the applied setpoint of 1 nN. The data were post-processed using the JPK software. Hertz-Sneddon fit was applied incorporating a pyramidal shape of the tip with a half-angle of 15° and radius of 20 nm.

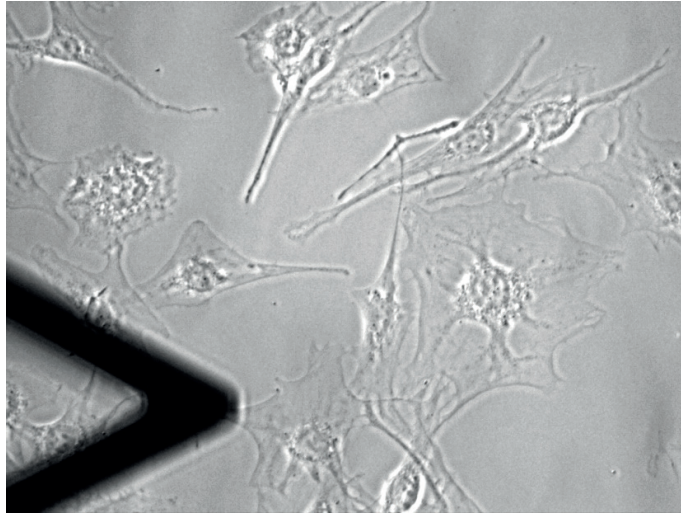


*Figure 2.3* Optical image of the cantilever ready to be approached onto the fixed osteoblasts for quantitative imaging. Using the inverted microscope and the XY stage positioner, cells are selected for imaging.

### 2.3.3 Results

Osteocytes, grown on micropatterns, were first imaged to observe the topography, stiffness and adhesion profiles over the whole cell surface. A crucial part of the experiment is to find the right application force that the AFM tip will exert onto the sample. Using the same force across all four images presented on **Figure 2.4**, differences in nanomechanical profiles are observed. The height images of micropatterned, fixed cells show that the nuclear area is the highest part, spanning up to 4  $\mu\text{m}$ . Stiffness maps show that the nuclear area is the stiffer part of the cell (up to 150 kPa), while the adhesion profile shows a rather weak force of interaction with the AFM tip. Those findings are not surprising, considering that the nucleus is a large part of the cell that brings stiffness inhomogeneities and stretches the membrane so that less adhesion occurs when the tip scans over it. When the tip interacts with the thin membrane parts of the cell body, if the force of interaction is strong enough, the stiffness profile picked up will be of the substrate itself. Pressure that the tip exerts onto the soft and thin membrane causes it to bend accordingly, and to “feel” the substrate below (as shown on **Figure 2.4** in the middle stiffness image).

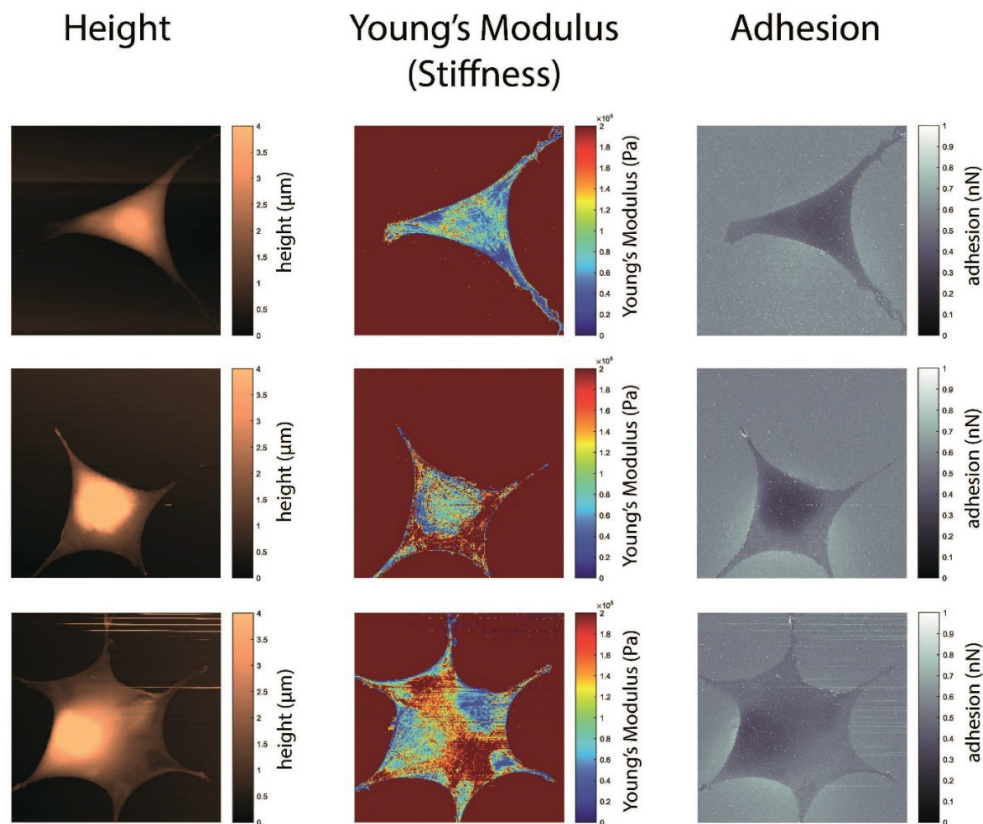


*Figure 2.4 Topography, stiffness and adhesion maps of micropatterned osteocytes, imaged by the AFM.*

Next, images of 10 – 15 osteoblast cells for each condition (static, microgravity, pressure and shear stress) have been obtained in all three respects (height, elasticity and adhesion), using the setpoint force of only 1nN. **Figure 2.5** shows Young's modulus, adhesion and height profiles of a group of cells grown in static conditions. Each color of the histogram represents a different cell and its distribution of values for the respective parameter. As it can be seen, cells have varying height distributions, somewhat similar stiffness profiles and rather similar adhesion response among each other, within one condition. For the purposes of comparison between the conditions, parametric values are taken together across all the cells within one condition and histograms of these quantities are presented on the **Figure 2.6**. The possible general conclusions are that mechanobiological loading and unloading somewhat reduces the cell height, increases the stiffness, while the adhesion profile remains similar. The stiffness distribution changes upon the mechanical exposure, and in case of microgravity, adhesion distribution mean shifts towards higher values. An attempt to visualize stiffness changes of 10 osteoblasts under all conditions is shown on Young's modulus maps on the **Figure 2.7**.

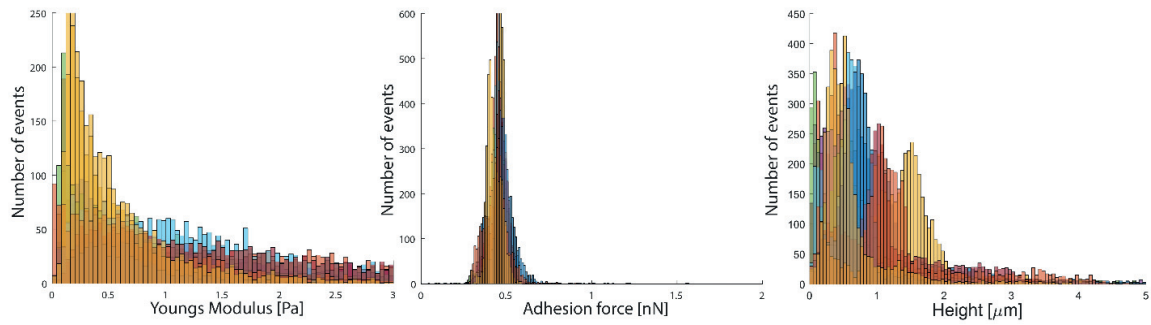


**Figure 2.5** Histogram plot of Young's modulus, adhesion force and height values for different cells grown under normal conditions. Imaged cells have varying height, somewhat different elasticity and rather similar adhesion profiles.

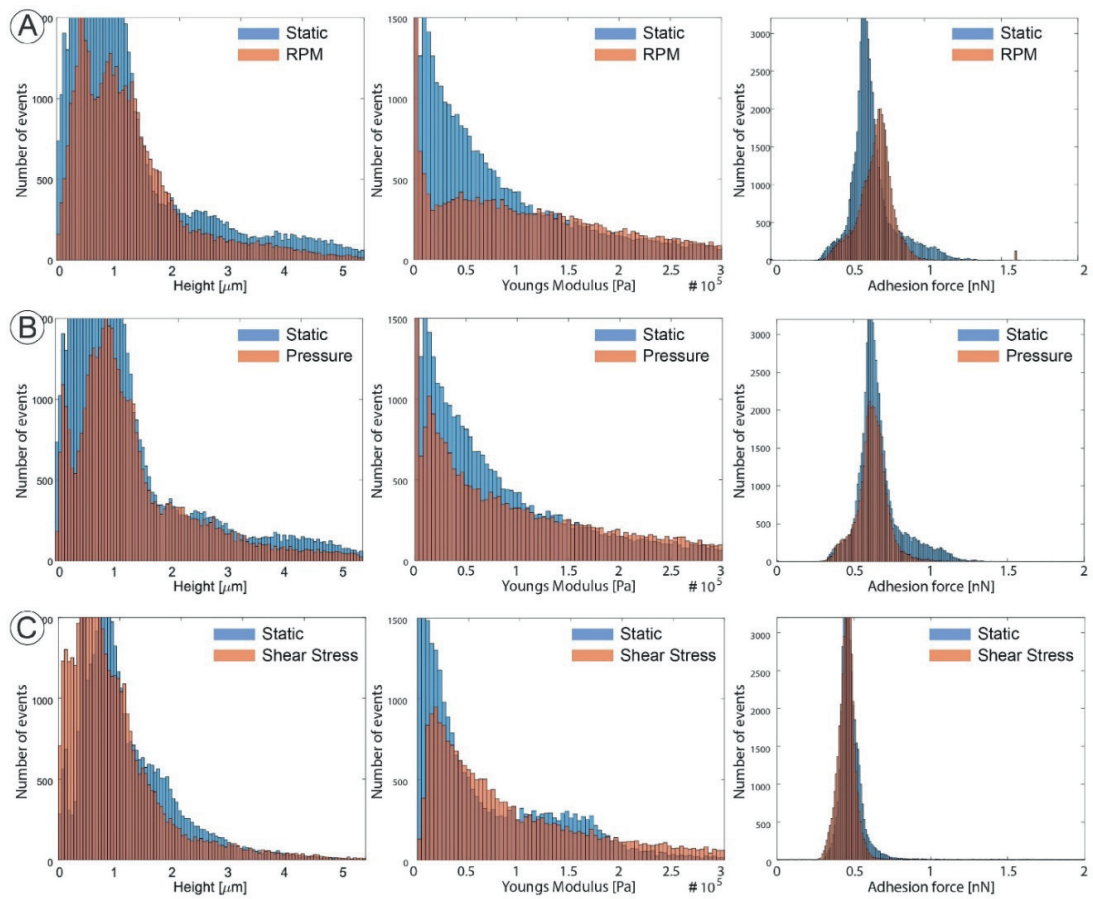


**Figure 2.6** Height, Young's modulus and adhesion force distribution comparison between static and other conditions: microgravity (A), pressure (B), and shear stress (C).

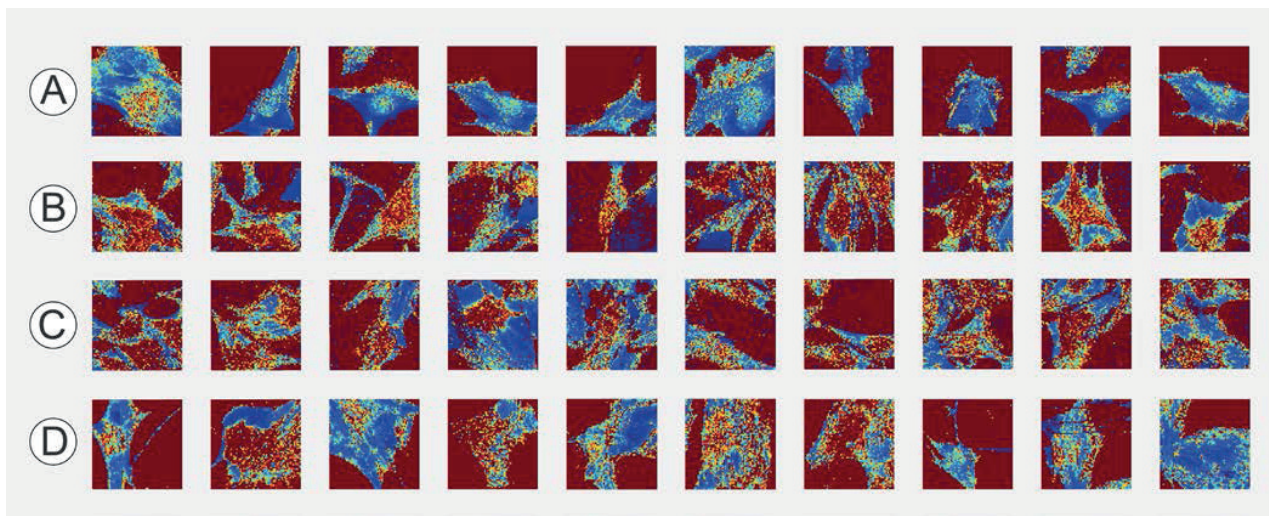


**Figure 2.7** Young's modulus maps of 10 osteoblasts exposed to different conditions: static (A), microgravity (B), pressure (C), and shear stress (D). Red color represents high stiffness values, while blue color – low.

Overall, cells under the three conditions do have an increase in red pixels across their bodies, mostly over the nuclear area. To better quantify the changes, a contribution separation from the nucleus and the rest of the cell body was performed. Manual selection of the nuclear area for all cells and conditions allowed separating height, stiffness and adhesion distributions. An example of the selection criteria is presented on the **Figure 2.8**, where the highest part of the nucleus is confined. Height images were used for nucleus position determination and the cut area was applied to stiffness and adhesion image accordingly. Distribution of height, stiffness and adhesion values for all conditions, separating the nucleus area (blue histograms) and the rest of the cell (orange) is presented on the **Figure 2.9**. As expected, values at the high-end of the distribution for height, mostly come from the nucleus area in all conditions. Distribution of adhesion forces in all cases is easily distinguishable: nucleus area comes from the distribution with lower mean than the rest of the cell, meaning the nucleus area has lower values of adhesion forces. However, the stiffness contribution from the nucleus changes from static to other conditions, as the distribution gets broadened and consists of higher values. This is an important indication and is investigated further.

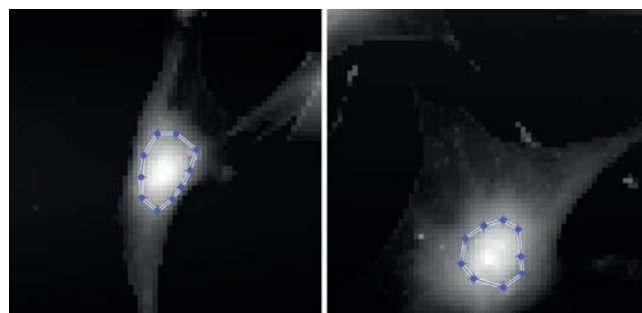


**Figure 2.8** Nucleus contribution separation. Values for height, stiffness and adhesion were extracted from the corresponding maps by cutting out the section of the image containing cell nucleus. They are compared to the values from the rest of the cell.



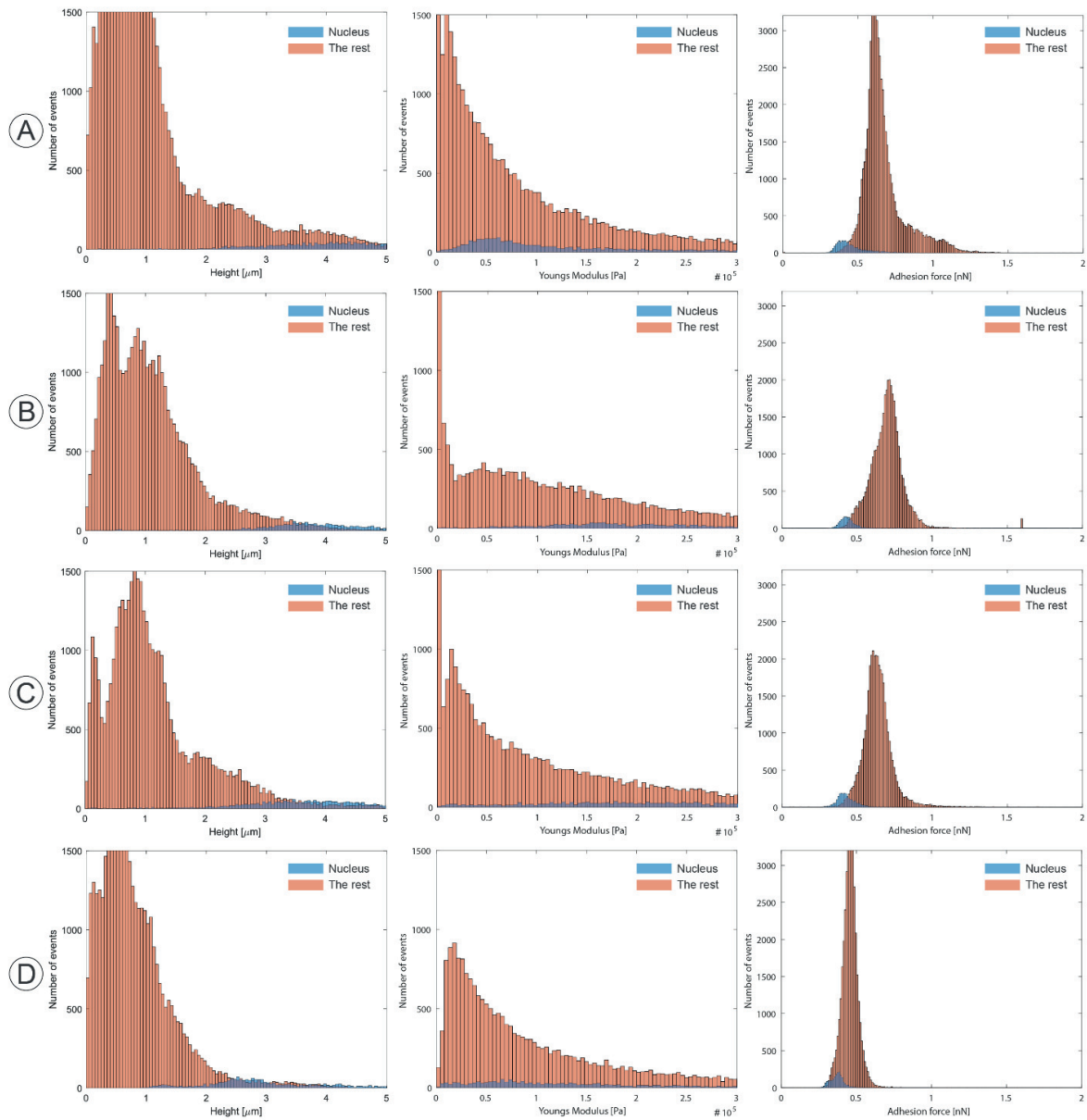


**Figure 2.9** Height, Young's modulus and adhesion distributions for different conditions: static (A), microgravity (B), pressure (C), and shear stress (D). Nucleus area has been separated from the rest of the cell and its distribution is in blue. Distribution of values across the remaining cell area is in orange.

Looking at the contributions from the nucleus area only, comparison has been made between the static condition and microgravity and pressure, and separately, between static condition and shear stress (due to different times of the two sets of experiments).

**Figure 2.10** shows the difference in distributions of height values, and highlights that microgravity and pressure conditions tend to lower the nucleus height, while shear stress increases it. Medians in all cases have similar values, while the distribution mean is shifted towards lower values in cases of

microgravity and pressure, and higher values in the case of shear stress. **Figure 2.11** points out the differences in Young's modulus distributions on top of the nucleus in all conditions of mechanical exposure. As it can be seen from the distribution shape, in static condition, Young's modulus values come from a unimodal right-skewed distribution. Upon mechanical exposure, stiffness tends to increase in the nucleus area, and the distribution shapes change to more symmetrical, but still unimodal. Higher values, of 100 – 500 kPa are more dominant after the mechanical exposure. Boxplots highlight this increase with a large increase in median, and the broadening towards higher stiffness values. Adhesion distribution does not change in a drastic manner, as it can be seen on the **Figure 2.12**. However, boxplot representation suggests a slight decrease in adhesion force after the mechanical exposure in all cases, when compared to relevant static condition.

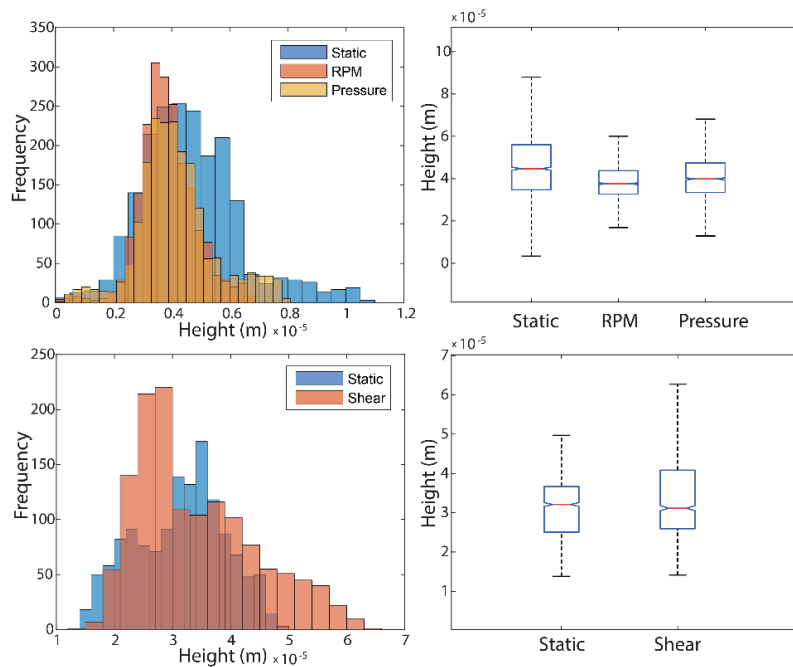


**Figure 2.10** Comparison of height distributions for nucleus area of cells exposed to different conditions. Static condition is compared to microgravity and pressure (**top**), and to shear stress (**bottom**). Corresponding boxplots are presented on the right.

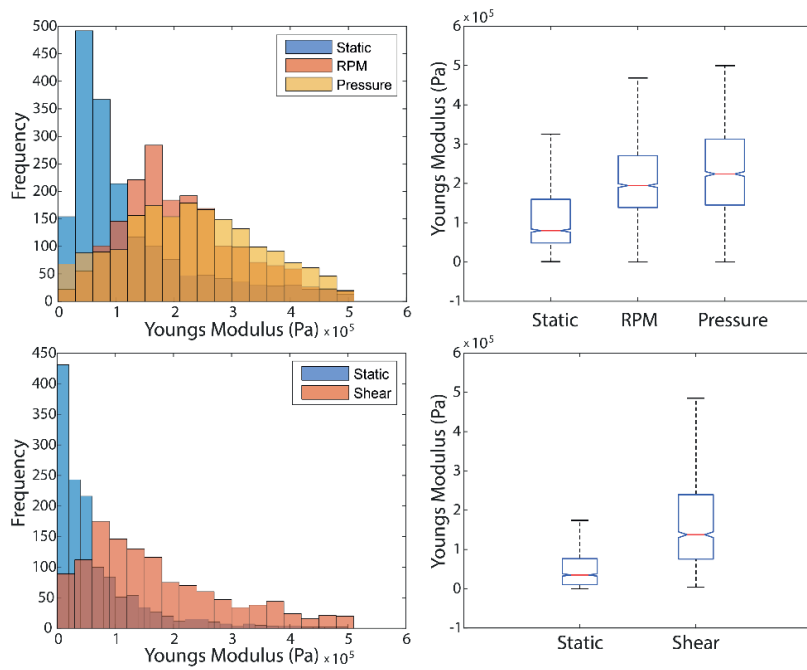


**Figure 2.11** Comparison of Young's modulus distributions for nucleus area of cells exposed to different conditions. Static condition is compared to microgravity and pressure (**top**), and to shear stress (**bottom**). Corresponding boxplots are presented on the right.

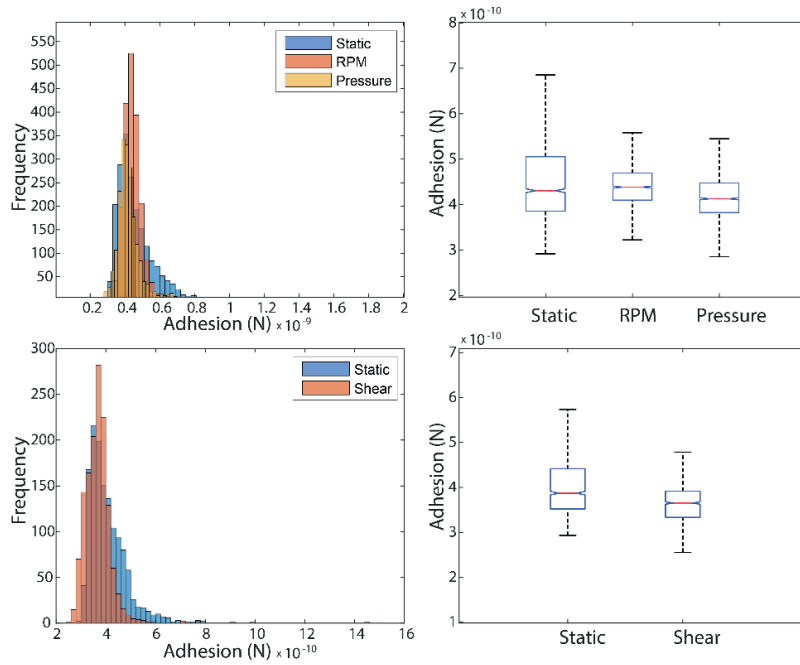


**Figure 2.12** Comparison of adhesion distributions for nucleus area of cells exposed to different conditions. Static condition is compared to microgravity and pressure (**top**), and to shear stress (**bottom**). Corresponding boxplots are presented on the right.

Lastly, combining fluorescence microscopy with AFM imaging, we have noticed a peculiar phenomenon in the arrangement on actin filaments surrounding the cell nucleus. **Figure 2.13** shows the height, elasticity and fluorescence image of an osteoblast, highlighting actin fibers. As it can be seen, fluorescence image shows caging structures, where actin filaments intercross perpendicularly. However, we were not able to see the same structure by the AFM height nor elasticity imaging. Therefore, the structure of a cage is most probably enclosing the cell nucleus from the bottom part of the cell, where AFM indentation cannot reach.



**Figure 2.13** An osteoblast cell investigated with an AFM (height - **left**, stiffness - **middle**) and fluorescence microscopy (**right**), after simulated exposure to microgravity.

#### 2.3.4 Conclusion

Studies from space flights suggest a change in physiology of astronauts during the flight. This has important consequences, as weight-bearing bone mass can decrease substantially. It is well known that bone cells have the ability to adapt to mechanical perturbations, and the relationship between changes in cell cytoskeleton architecture and different mechanical conditions is a subject of this project. To simulate space flight, cells were exposed to microgravity, pressure and flow-induced shear stress, and nanomechanical profiles after such exposure were compared to the static condition. Height, Young's modulus (elasticity), and adhesion forces were collected and quantified for a number of osteoblast cells in all conditions of mechanical perturbation. Using, AFM's capabilities of quantitative imaging, 64 x 64 pixel maps were collected for each nanomechanical property and values were compared by extracting the contribution of the cell nucleus from the rest of the cell body.

Data suggest that there is an overall tendency of cell heights to reduce after the mechanical exposure, but cell's stiffness increases. Mechanical stimulation can cause significant variations in the cells geometry, triggering actin filaments polymerization/depolymerization to balance the applied extra-cellular forces. The actin polymerization response produces filaments, which in bundles form the actin stress fibers. A more detailed analysis has been performed by discerning contributions from the nucleus area and the rest of the cell body. However, the most prominent changes occur regarding the Young's modulus of cell nucleus area. A large increase in stiffness values are suggesting the effects of mechanical disturbance, when compared to static condition. As seen from the presented data and images, cell architecture does seem to change in response to treated conditions.

## 2.4 Localization of adhesins on the surface of a pathogenic bacterial envelope

*This section contains published work:*

Arnal, L., Longo, G., Stupar, P., Castez, M.F., Cattelan, N., Salvarezza, R.C., Yantorno, O.M., Kasas, S. and Vela, M.E., 2015. **Localization of adhesins on the surface of a pathogenic bacterial envelope through atomic force microscopy.** *Nanoscale*, 7(41), pp.17563-17572.

### 2.4.1 Introduction

Pertussis, or so-called whooping cough is contagious human respiratory tract infection caused by the Gram-negative bacteria *Bordetella pertussis*. Despite the sustained high vaccination coverage worldwide since the 1950s, the disease remains endemic with infection peaks every 3–5 years (151,152). Interestingly, over the last two decades the reported cases of pertussis have been increased in several countries and changes in the age of the affected patients, from young children of less than 6 months to adolescents and adults, have been reported. A decrease in acellular vaccine effectiveness and pathogen adaptation to the immunity conferred by vaccines has been suggested as possible causes for pertussis reemergence. This new scenario implies bacterial persistence in the vaccinated population and represents a risk of contagion for non-vaccinated children. A possible explanation for the continued persistence of pertussis in the community could be associated with the ability shown by *Bordetella* spp. to form a biofilm in the upper respiratory tract of infected animals (153–155). The successful establishment of a biofilm community relies strongly on the adhesion step to the surface, which is mediated by different adhesins exposed in the cell surface that irreversibly interact with the substrate (156). Bacterial adhesion is the first and a significant step in establishing infection. In the course of colonization, adhered bacteria have to resist shear forces that act as natural defense to remove them. Therefore, bacterial adhesins must prove strong interactions with their target cells in order to maintain the adhered bacteria under these hydromechanical stressing conditions. Protein and non-protein factors have been shown to function as adhesins and promote biofilm formation in *Bordetella pertussis* (157). In the case of proteins, they interact with different components of the respiratory epithelium to allow the attachment of the cells. Among them, the most studied proteins are Pertactin, a 69 kDa autotransporter adhesion (158); Fimbriae, which is a filamentous protein; (158) and a 220 kDa adhesin named filamentous haemagglutinin (FHA). The latter is a lineal filamentous protein belonging to the b-solenoid family, found on the outer membrane, but also secreted. FHA contains recognition domains to adhere to ciliated respiratory epithelial cells and macrophages, and two domains composed of tandem repeat motifs (159–161). FHA has been demonstrated to participate not only in the first adhesion step during biofilm development but has also been proved to participate in cell–cell interactions to generate the definitive structure of a mature biofilm in vitro. Thus, the study of the spatial organization under specific recognition forces should contribute to understand the role of FHA in the adhesion step of biofilm formation (155,162).

The studies of the presence and distribution of adhesins on the cell-surface are essential to understand the adhesion capacity of a particular bacterium in the first step of pathogenesis. In this aspect, atomic force microscopy (AFM) constitutes a powerful technique not only by its capability to explore the surface heterogeneity of the cell envelope with nanometer resolution, but also because it

allows mapping of the distribution of particular molecules on the cell surface. Such maps are obtained using the specificity of ligand–receptor interactions in experiments performed under physiological conditions, using functionalized AFM tips (163–167). In particular, the role of the spatial organization of surface adhesins has been explored by single-molecule AFM experiments (168–170).

In this work, using atomic force microscopy we obtained information on the cell-surface localization and distribution of *B. pertussis* adhesin-FHA. The quantitative evaluation of the adhesion forces between FHA placed on the cell surface of *B. pertussis* was performed and a specific antibody-functionalized AFM tip was employed to this aim. We made use of this information to build a map of the spatial distribution of the adhesin which revealed a non-homogeneous pattern. Moreover, our experiments showed a force induced reorganization of the adhesin on the surface of the cells, which could explain a reinforced adhesive response under external forces. This single-molecule information contributes to the understanding of basic molecular mechanisms used by bacterial pathogens to cause infectious disease and to gain insights into the structural features by which adhesins can act as force sensors under mechanical shear conditions.

#### 2.4.2 Materials and methods

**Bacterial strains and growth conditions.** *B. pertussis* Tohama I, a wild-type strain (8132 collection of Pasteur Institute, Paris, France) and *B. pertussis* GR4, a Tohama I derivative mutant lacking the expression of FHA (FHA–) (171), were used throughout this study. Stock cultures were grown on Bordet-Gengou agar (BGA; Difco Laboratories, Detroit, USA) plates supplemented with 1% w/v Bactopeptone (Difco) and 15% v/v defibrinated sheep blood (Instituto Biológico, La Plata, Argentina) at 37 °C for 72 h, and then subcultured for 48 h under the same conditions. In the case of the FHA– strain, 50 µg ml<sup>-1</sup> streptomycin (Sigma, St Louis, MO, USA) were added to the culture media to maintain the restrictive conditions. Liquid cultures were performed by inoculating bacteria into 100 ml Erlenmeyer flasks containing 30 ml of Stainer–Scholte (SS) broth, adjusting the optical density at 650 nm (OD<sub>650</sub>) to 0.20 and incubating the flasks at 37 °C under shaking conditions (160 rpm). The cells of the two strains were harvested at the middle-exponential phase (centrifugation at 8000g for 5 min) and washed twice with Phosphate Buffered Saline (PBS) buffer.

**Sample preparation.** Bacteria were electrostatically-immobilized onto polyethylenimine (PEI) pre-coated glass slides (Sigma) according to previous protocols (172,173). Briefly, the glass slides were washed twice with 96% (v/v) ethanol and Milli-Q water and then incubated overnight at 4 °C with 0.1% (w/v) aqueous PEI solution. After incubation, PEI-coated slides were rinsed twice with Milli-Q water. Bacteria were immobilized by depositing 50 µl of bacterial suspension at an OD<sub>650</sub> of 1.0 over the PEI-coated slides and they were allowed to attach to the substrate for 2.5 h. Afterwards, the slides were washed three times with distilled water to remove non-adhered cells before AFM imaging.

**Cantilever's tip functionalization.** To functionalize the AFM tip, we used the glutaraldehyde linking method already published (107,174,175). After cleaning the cantilevers with Milli-Q water, 30 µl of glutaraldehyde solution (0,5%) were added to the extreme end of the cantilever, they were incubated for 15 min and then washed three times with Milli-Q water. Afterwards, the tip was functionalized

for 15 min with 30  $\mu\text{l}$  of anti-FHA IgG antibody solution (1 ng  $\mu\text{l}^{-1}$ , NIBSC, London, England) in PBS. Finally, the cantilevers were washed and were ready to be mounted on the AFM's liquid chamber.

**AFM measurements and force spectroscopy assays.** The interactions between the antibody-functionalized tip and bacterial cells were performed through force–volume (FV) images using a MultiMode Scanning Probe Microscope (Bruker, Santa Barbara, CA, USA) equipped with a Nanoscope V controller and a Nano Wizard III Bioscope (JPK, Berlin, Germany). Each sample was attached to a steel sample puck (Bruker, Santa Barbara, CA) using a small piece of double sided adhesive tape and immediately transferred into the AFM liquid chamber. Two hundred  $\mu\text{l}$  of PBS buffer were added into the AFM fluid chamber in order to keep the samples hydrated during the course of the experiment. All measurements were done using contact sharpened silicon nitride probes (NP-10, Bruker) with a nominal tip radius of curvature of 20–60 nm. Clean flat muscovite mica surfaces (SPI V-1 grade) were used as rigid substrates for photodetector sensitivity calibration. The spring constants of the cantilevers ( $K_s$ ) were measured using the thermal tune method and their characteristic values ranged between 0.05 and 0.08 N  $\text{m}^{-1}$ . The surfaces were scanned using the Force–Volume (FV) imaging mode at a scan rate of 1 Hz maintaining a maximal applied force of 1 nN and 500 ms of surface delay.

Unbinding forces between receptors and ligands depend on the loading rate, i.e. the rate at which the force is applied to the bond (66,166,176–178). To study this issue for our FHA–anti-FHA pair we recorded 1000 force vs. distance (FD) curves at different retraction velocities (72, 100, 500  $\text{nm s}^{-1}$ ) using a 500 nm Z range. The recorded data were analyzed to build the force vs. ln loading rate curve. After selecting a suitable pulling velocity, we performed the FV images on living *B. pertussis* Tohama I cells. For these experiments, we used a 1000 nm Z range in order to allow the correct detachment of the tip from the sample before starting the next FD curve of the FV array. Two consecutive images were obtained on single cells, the first image corresponded to  $t = 0$  and the second to  $t = 40$  min since that was the time period separating the acquirement of both images. Ten cells were analyzed from five independent cultures.

The specificity of the interaction events was controlled through blocking experiments. Both, purified FHA on mica and *B. pertussis* Tohama I cells were incubated with a solution of anti-FHA antibody (10 ng  $\mu\text{l}^{-1}$ ) for 1 h before performing the force spectroscopy experiments. Another assay was made by performing force spectroscopy measurements on bacterial samples of FHA–strain, which do not express the adhesin on their surface.

Force vs. distance curve analysis to detect specific adhesion events between the antibody on the tip and the surface envelope of living *B. pertussis* Tohama I cells was performed off-line using the OpenFovea software developed by C. Roduit et al (66). Each FD curve was analyzed to quantify the magnitude of the force of each specific rupture event and the distance from the point of contact where it occurred. The collected data are represented in the corresponding histograms. Non-specific events (adhesion peaks without any length separation from the point of contact) were automatically excluded by using the software and very low adhesion events (below 50 pN) were also excluded as they were considered to be outside the range of antigen–antibody interaction forces (179).

**Force–distance curve analysis.** In the case of bacterial cells, nanoindentation analysis was performed seeking to discriminate the presence of specific recognition events and rigid domains on the surface. The analysis was done using an in-house developed software, following the procedure described in previous studies (180–182). The zero-force height ( $z_0; y_0$ ) value of each force curve was manually defined by detecting the point at which the curve begins to lift off from the non-contact baseline when the tip approaches the sample (183). After defining the point of contact, the force vs. distance curves were transformed into force vs. indentation depth curves (77), and the resulting data were fitted using a Hertz model for elastic (182,184) samples and conical indenters (181,185,186).

$$F = \frac{2E \tan \alpha}{\pi(1 - \nu^2)} \delta^2$$

where  $F$  is the loading force,  $E$  is the Young's modulus,  $\alpha$  is the half opening angle of the conical indenter ( $53^\circ$ ; based on geometrical characteristics of the tip and SEM observations),  $\nu$  is the Poisson ratio (0.5 for cells (75,187)) and  $\delta$  is the indentation.

**Force and elasticity maps.** FD curves that presented a recognition event on the surface of a single bacterium were correlated to their ( $x, y$ ) positions on the FV image and plotted as a force map. The values ranged from 50 to 900 pN and they were represented using a black-white scale. The Young's modulus values calculated for *B. pertussis* Tohama I cells were also plotted on surface elasticity maps. The values between 0.15 and 1.1 MPa are depicted on a cyan-blue scale, whereas the values between 1.1 and 2 MPa are on a pink-red scale.

### 2.4.3 Results

#### *Force–distance curve analysis*

An AFM cantilever's tip functionalized with a specific antibody as indicated in the Materials and methods section was used to recognize the presence of FHA adhesin on the surface of live *B. pertussis* cells through force spectroscopy assays. The force vs. Z-piezo retraction curves shown in **Figure 2.14** are representative of more than 6000 curves acquired in the above-mentioned experiments. During the analysis, the non-specific interactions were automatically excluded by using the software by discarding the events that did not show any length separation with the contact point (188). Most of the recorded FD curves showed no adhesion events (**Figure 2.14a**), and are associated with the surface areas with no expression of FHA. Other typical FD curves showed one adhesion peak, like the one depicted in **Figure 2.14b**, that exhibits an adhesion event with a magnitude of 130 pN, characteristic for an antigen–antibody interaction (107,189). A fewer number of FD curves presented two events occurring at different tip-sample separations (**Figure 2.14c**). In this case the absolute value of the adhesion force ( $F_{adh}$ ) was double the value (300 pN) detected for the most probable single antigen–antibody interaction. This behavior is likely to evidence the interaction of two antigen–antibody pairs at the same time. It is important to remark that during the functionalization of the tip it is not possible to guarantee that only one antibody was attached to the tip of the cantilever. In this context when more than one antibody interacts at the same time with proteins on the surface, the magnitude of the interaction peak in the FD curve is typically a multiple of the single interaction force (107,177). Other types of FD curves found in our experiments exhibited multiple



FHA–antibody interaction events, like the curve represented in **Figure 2.14d** that shows three adhesion events that could be understood as three antibodies interacting with three epitopes of the same FHA protein or interacting within neighboring FHA molecules on the underlying surface. Taking a closer look into the last FD curve, it is possible to observe a “plateau” that is associated with a different type of interaction, a “tether”-like rupture event (190). Such adhesion events were frequently observed in our experiments (10–15%) and can be related to the stretching of a portion of the extracellular membrane as was previously described (179). When the tip is being pulled off from the surface, in some cases, it makes the external membrane to detach from the structures that maintain its sticking to the cell wall, generating a nanotube of the external membrane. When the nanotube is disengaged from the tip a tether rupture event occurs. In the case of Gram-negative bacteria, like *B. pertussis*, the membrane is attached to a thin layer of peptidoglycan present in the intermembrane space through an anchorage lipoprotein (191).

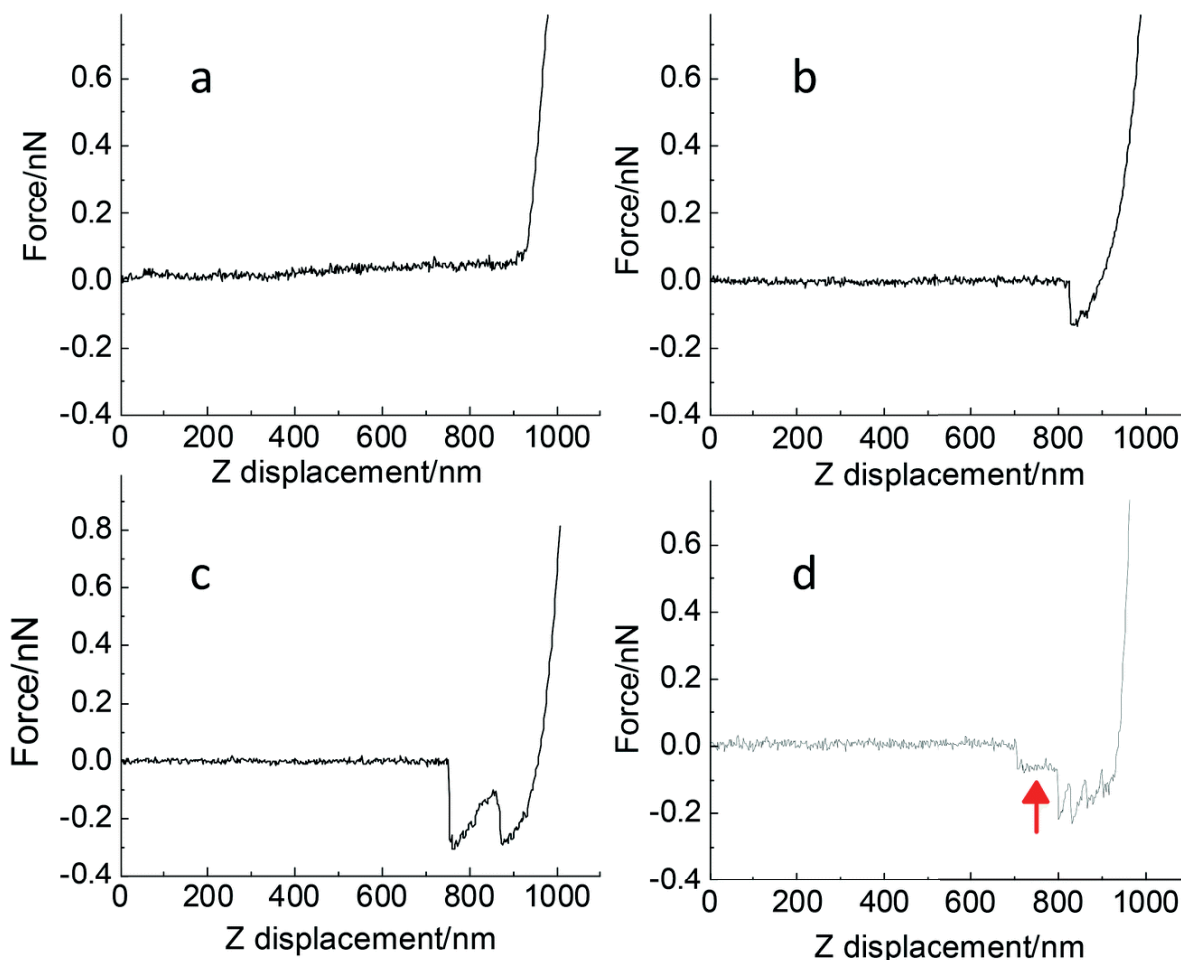


**Figure 2.14** Representative force vs. Z-piezo displacement measured with an anti-FHA functionalized tip on *B. pertussis* Tohama I cells supported on glass. (a) Nonspecific tip–sample interactions, (b) one adhesion event, (c) two adhesion events in the same FD curve that doubles the typical  $F_{adh}$ , and (d) a FD curve with three specific antibody–antigen interactions at different distances followed by a latter “tether” event (shown by the red arrow) characteristic of the dissociation of a membrane nanotube generated during the retraction of the cantilever.

#### *Specific adhesion events on the surface of *B. pertussis* cells through molecular recognition experiments*

As mentioned, two consecutive FV images were recorded on the surface of single *B. pertussis* Tohama I cells with a 40 min time lapse between each of them. These studies allowed us to determine the amount as well as the magnitude of the recognition events between the antibodies adhered to the tip and the protein FHA on *B. pertussis*' surface. The histograms shown in **Figure 2.15a and b** represent the adhesion forces detected on 12 individual cells for time = 0 (first scan) and time = 40 min (second scan on the same cells). In both cases, a large number of retraction curves did not show any adhesion event, representing areas on the bacterial surface with no expression of the adhesin FHA. For the specific recognition events, the distributions of the histograms are very similar. They include a range of adhesion values from 50 pN to 900 pN, although the majority of the events correspond to low values of the interaction forces. In both cases the most probable values correspond to 150 pN, which is a typical interaction value for antigen–antibody pairs as has been previously reported (152,192,193). Nevertheless, it was possible to differentiate in both histograms the local maxima around values such as 225 and 300 pN. These subpopulations could be associated with the rupture events between two antibodies and one or more proteins on the surface at the same time, which would throw an adhesion value corresponding to double the individual rupture event or to the interaction of one antibody and a Fab fragment of another antibody, as reported by Hinterdorfer et al (189). Another parameter calculated from the FD curves was the distance at which the rupture events occurred. These data are represented in **Figure 2.15c and d** for the two studied times. Once again, the distribution of the two populations is the same, meaning that there was no tip contamination during experiments, which could have led to different lengths in the rupture events. Both histograms for time 0 and time 40 min could be fitted using a LogNormal function. The distance distributions for anti-FHA-Bp Tohama I interactions showed a most probable distance value between 120–160 nm. These values are a bit higher than those expected, considering that the length of the non-elongated FHA protein is 50 nm (194) and the length of an antibody is 20 nm (195). Nevertheless, it has to be considered that when the rupture of the interaction occurs, depending on the position of the recognition site, the molecule could be partially or totally extended. It has been reported that the FHA60 fraction (60 kDa N terminal of native FHA) exhibits a 256 nm extension under force induced elongation (196). Thus, in our experiments, the typical rupture length (120–160 nm) data indicate that the protein is moderately extended. Moreover, the histogram values rise up to 800–1000 nm, which represent not only the stretching of the protein but also the stretching of the cell membrane during cantilever's retraction.

An important feature to be noticed is that after 40 min (in the second scan), the total amount of recognition events increased from 1013 to 1274, indicating an increase in the number of affinity sites detected during the second trial. In order to test the specificity of the recognition events, the force–distance curves were recorded after exposing *B. pertussis* cells to the same solution of specific antibodies. As a result, the force spectroscopy measurements presented a drastic reduction in the recognition event number. This phenomenon can be interpreted as a demonstration of the existence of specific ligand–receptor interactions. Moreover, we made a force spectroscopy assay on mutant cells not expressing FHA observing only a few adhesion events whose distribution lacks a well-

defined maximum. The observed interactions could represent unspecific events between the antibody and chemical structures on the surface of a cell, probably being of electrostatic nature.

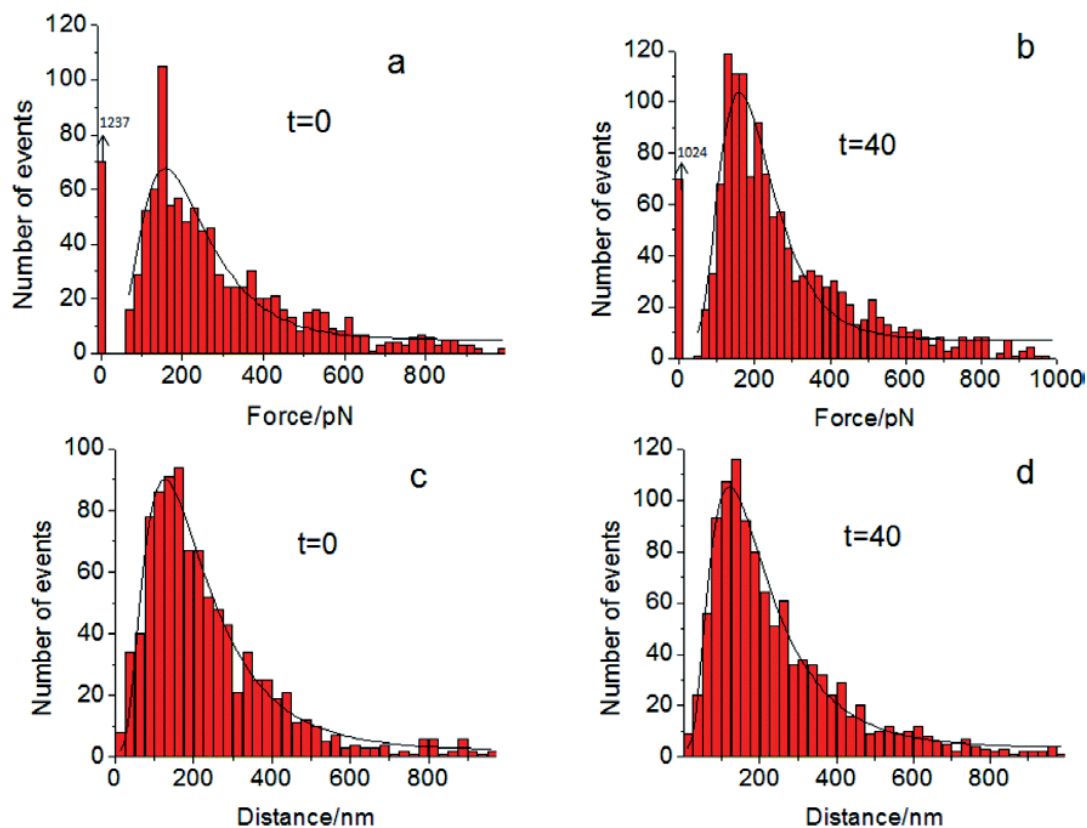


**Figure 2.15** Adhesion force histograms of the interaction of an anti-FHA functionalized tip and FHA present on the surface of 12 cells of *B. pertussis* Tohama I at time = 0 and time = 40 min (**a, b**). All curves were obtained using a retraction speed of 500 nm s<sup>-1</sup> and a surface delay time of 500 ms. (**c, d**) The distance histogram at which the rupture events plotted in the force histograms occurred for the two times studied.

#### *Dynamics of recognition events on individual bacterium. Force and elasticity maps*

To evaluate if the increase in the number of found recognition events was representative of each individual studied cell, we constructed independent force histograms for each bacterium for 12 cells from 6 independent cultures. **Figure 2.16a** shows a representative FV image of three cells of *B. pertussis* Tohama I strain with their associated force histograms (**Figure 2.16b**). The data on the force histograms can be divided into two subpopulations, in the case of cell **ii** it is possible to detect a first distribution around 200 pN and a second distribution around 400 pN, whereas cells **i** and **iii** present a first population around 150 pN and a second population around 300 pN. The most probable values for each distribution are multiple values between them, and are in agreement with the behavior depicted by using the overall data described previously. In every individual cell, the amount of specific recognition events rose between the first and the second scans, in cell **i** the percentage increased from 49% to 73%, in cell **ii** from 40 to 48% and in cell **iii** from 50 to 71%, suggesting that the general behavior observed for the whole population of studied cells is representative of the

individual performance of the cells. Moreover, the other 9 analyzed cells also showed an increase in the recognition events from 8 to 28% after 40 minutes.

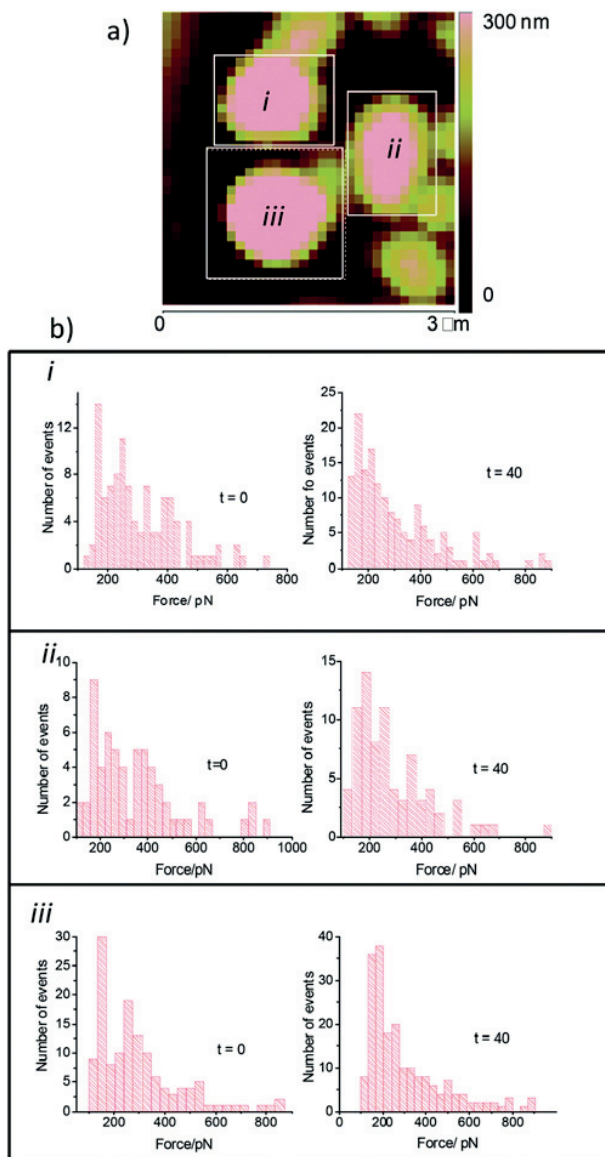


**Figure 2.16** (a) Force-volume image of three individual *B. pertussis* Tohama I cells acquired with a functionalized tip. (b) The specific recognition events between FHA-anti-FHA on the surface of cells shown in (a) are represented in the corresponding histograms for

To elucidate if the new recognition events on the surface of the cells are distributed randomly or if they are organized in any special arrangement we decided to build the associated force maps by correlating the FD curves with their (x, y) coordinates on the corresponding FV image (**Figure 2.17**). It is possible to observe that in every case the amount of non-null force pixels is higher in the second scan (40 min) compared to the first scan ( $t = 0$ ) although it is not possible to define if they are being organized in any specific way. Nevertheless, one particular area (inside the red circle in **Figure**

**2.17a)** on bacterium **iii** drew our attention. It corresponds to a cell to cell contact area and it has, clearly, more recognition events clustering in the zone after the second scan with the functionalized tip (**Figure 2.17b and c**). Surprisingly, the neighboring cell (**ii**) also showed clustering or adhesion events in the contact area after 40 min. This result is very interesting since FHA is the major adhesin of *B. pertussis*, responsible not only for the initial attachment to human cells, but also as an important element of bacterium–bacterium interactions involved in the autoagglutination capacity and microcolony formation (155). An enhancement in the number of FHA binding sites in the contact area between two cells would be indicating a stimulus for cell to cell interactions. Taking into account the previously published results from our group suggesting that nanodomains of FHA on the surface of *B. pertussis* correlate with more rigid areas in the envelope (77), we decided to evaluate the Young's modulus for this particular bacterium and plotted it as an elasticity map of the surface. From **Figure 2.17d and e** it is possible to observe the corresponding maps where the soft values are represented in a blue-cyan scale and the stiffer values are represented in a pink-red scale. The circled area (red line) represents the contact area between the two cells, and it is clearly observable that the elasticity of the envelope rises from soft to rigid values in the second scan, accompanying the increase of recognition events in the same area.

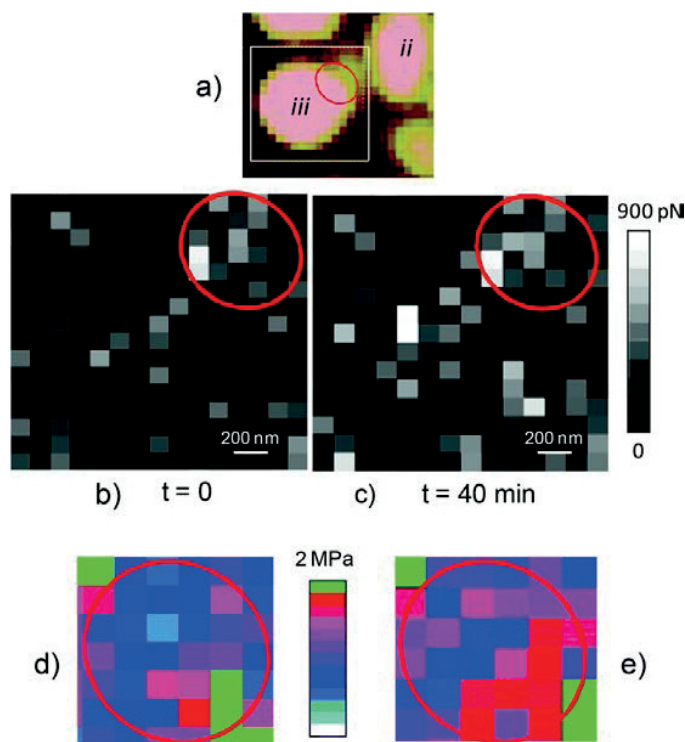


**Figure 2.17** (a) The circled area (red line) represents the contact zone between two bacteria (iii and ii in Fig. 3a), where it is possible to observe an increase in the recognition events after 40 min (b and c). The same contact area in the elasticity maps (d and e)

The absolute values of Young's modulus calculated from the approach curves in the present analysis are much higher (up to 2 MPa) than the values obtained from our previous report, where the maximum value was 1 MPa (77). This issue can be explained taking into account the difference in the

Z range of the FD curves in each experiment. In the current assays, the Z range was 1  $\mu\text{m}$  in order to allow a correct detachment of the interacting molecules from the tip and the surface. This Z range, even though needed for these experiments, represents a compromise situation for selecting correctly the nonlinear zone of the approach curve to be fitted with the Hertz model. In this sense, a part of the linear behavior of the curves is being incorporated to the nonlinear fit, resulting in enhanced Young's modulus values. Nevertheless, as this effect existed in every studied curve, the calculated E values can be compared in a relative manner.

#### 2.4.4 Conclusion

The reported results provide information on the cell-surface localization and distribution of the *B. pertussis* adhesin FHA using an antibody-functionalized AFM tip. Through the analysis of specific molecular recognition events we built a map of the spatial distribution of the adhesin which revealed a non-homogeneous pattern. Moreover, our experiments showed a force induced reorganization of the adhesin on the surface of the cells, which could explain a reinforced adhesive response under external forces. This single-molecule information contributes to the understanding of basic molecular mechanisms used by bacterial pathogens to cause infectious disease and to gain insights into the structural features by which adhesins can act as force sensors under mechanical shear conditions.

## 2.5 Changes in topography of the cotyledon surface can lead to *Botrytis cinerea* resistance

*This section contains manuscript in preparation.*

### 2.5.1 Introduction

The first step in establishing a parasitic interaction with the plant host is the passive or active attachment of fungal spores to the host surface (197). Subsequent adherence, maintenance of spore position and prevention from being removed from the surface are of crucial importance for the spore to succeed. Therefore, adhesion is considered as a virulence factor for pathogenicity and contribution towards developing a disease. Spore germination, formation of appressoria and further penetration into the host are the next steps of infection (198). Further outgrowth produced by spores and spore-releasing fungi during germination depends on multiple factors, such as: surface hardness, hydrophobicity and topography. Perturbation in one of these factors, results in that the germ growth is arrested or reduced. Therefore, investigation of cotyledon topography in wild-type (WT) *Arabidopsis thaliana* plants and fatty acid desaturase mutants are the aim of the project.

To examine the difference in cell morphology in mutants and WT *Arabidopsis thaliana* cotyledons, as it is an important factor influencing pathogen development, we used AFM quantitative imaging to visualize and characterize cotyledon epidermal pavement cells at the stage of 7-day-old seedlings. Height, elasticity and adhesion are probed at the same time.

### 2.5.2 Materials and Methods

7-day-old cotyledons of *Arabidopsis thaliana* (WT and *fad2-3*) were dissected in a moist environment. Each cotyledon was fixed with double-sided tape in a small Petri-dish and quickly covered with ultra-pure water. Measurements were done on a NanoWizard III (JPK Instruments, Berlin, Germany) mounted on an Axiovert inverted optical microscope (Zeiss, Jena, Germany). Quantitative Imaging (QI) mode and DNP-10 (Bruker Probes, Camarillo, USA) cantilevers with spring constants of 0.06 N/m were used. Properly calibrated (glass indentation, thermal tuning) cantilevers indented the samples with 2.5 nN force at 40  $\mu\text{m/s}$  with Z length of 2  $\mu\text{m}$ . Resolution of 0.7  $\mu\text{m}$  per pixel was kept constant throughout imaging. All measurements were conducted within 1h of cotyledon attachment. JPK SPM Data Processing software (JPK Instruments, Berlin, Germany) was used for force-curve fitting, while Matlab was used for data presentation. The Hertz model was used for force-curve fitting, assuming the Poisson ratio of 0.5, and pyramidal geometry of the tip (front angle of 15°). For histogram representations of pavement cells only a masking parameter was applied on the height, stiffness and adhesion maps.

### 2.5.3 Results

The atomic force microscopy-based nanoindentation method (quantitative imaging) has been used for examining the non-uniform spatial distribution of mechanical properties such as height, elasticity and adhesion of *Arabidopsis thaliana* pavement cells at the epidermal component.

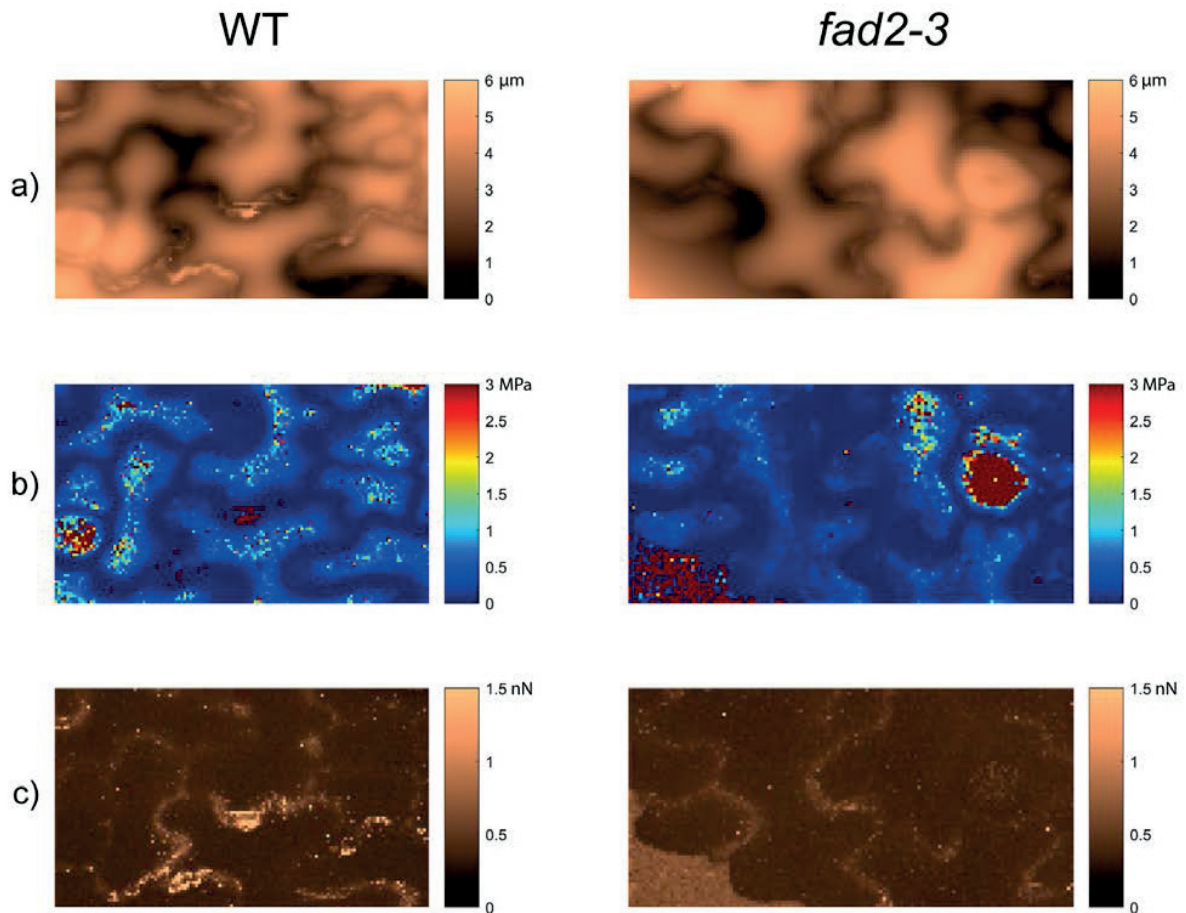


**Figure 2.18** Atomic force microscopy images of 7-day-old *Arabidopsis thaliana* cotyledons. (a) Height, (b) Young's modulus (stiffness) and (c) adhesion maps were obtained. Five cotyledons were analyzed in this work, representative images were chosen for each map.

**Figure 2.18** shows height (a), stiffness (b) and adhesion (c) maps of *A. thaliana* wild-type and *fad2-3* mutant epidermal pavement cells, respectively. Elastic modulus (Young's modulus), a measure of stiffness, is slightly different from wild-type and the mutant. However, differences in height and adhesion are not evident from the presented maps. Considerable presence of non-uniformity could be connected with the heterogeneous composition of the cell wall, as macromolecular components of the wall have a crucial role in mechanical properties of cells (199). Due to the observed differences in stiffness maps and for more detailed results we performed quantitative analysis of these features.

The stiffness of the cell wall has been proposed to play a crucial role in control of the cell growth rate, with low values being proposed as a precondition for cell growth and cell-wall expansion (100). **Figure 2.19** shows averaged Young's modulus, adhesion force and height values of 20 wild-type and 15 mutant cells of early-growth *A. thaliana* cotyledons. Significant difference occurs in Young's modulus values and might be in correlation with their differences in chemical composition. Mean Young's modulus for wild-type *A. thaliana* pavement cells of early-grown cotyledons is 0.7 MPa, which is very similar to previously reported results (100,199,200). However, the *fad2-3* mutant



shows 0.4 MPa mean value. Mean values for adhesion are 0.3 and 0.4 nN for wild-type and the mutant, respectively, while the mean height remained 4 μm in both cases.

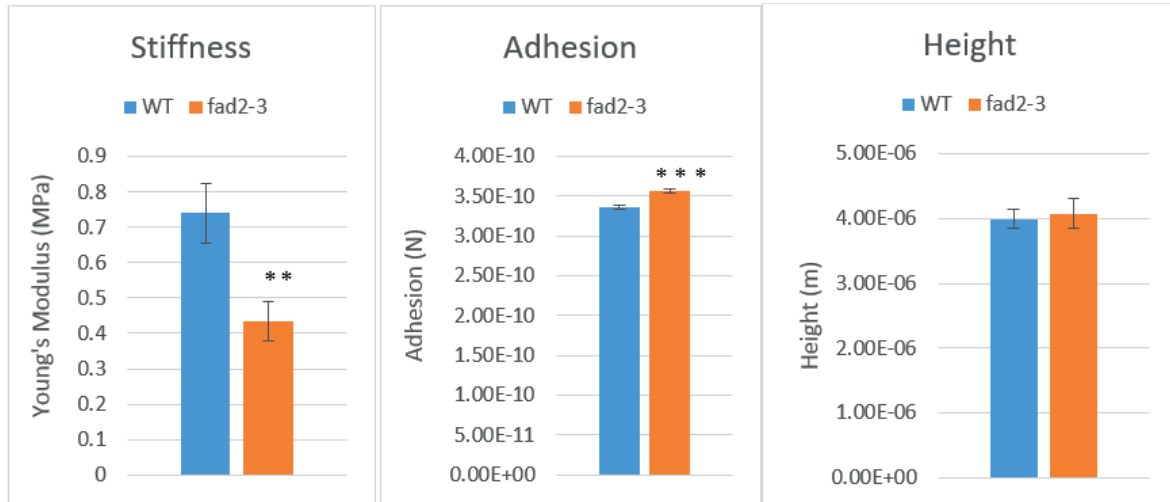


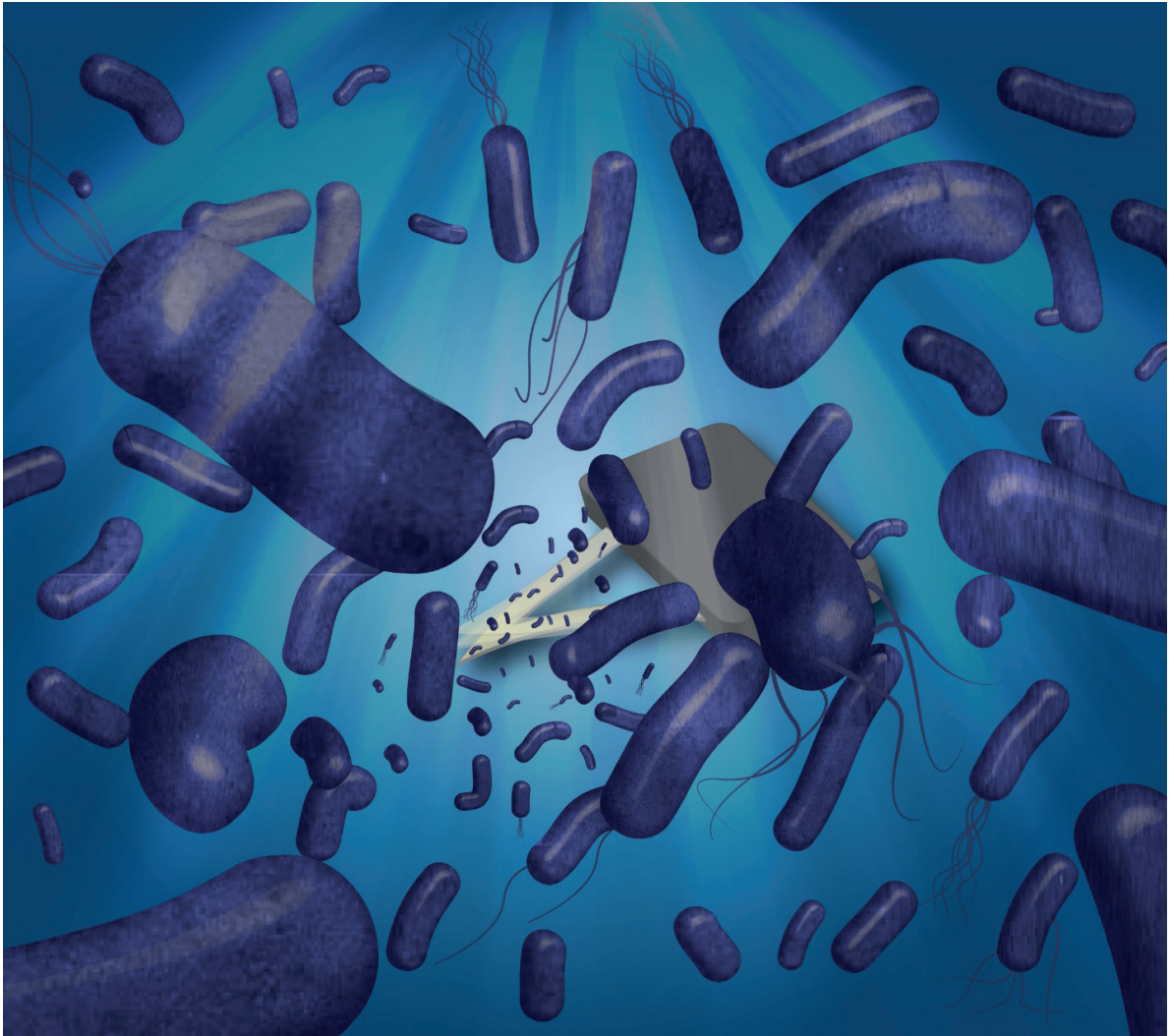
**Figure 2.19** Quantitative analysis of atomic force microscopy results. **(left)** Young's modulus, **(middle)** adhesion and **(right)** height were measured. Error bars represent the means of 15 to 20 pavement cells parameters obtained from five cotyledons ( $\pm$ SD). Statistical significance in pair-wise comparison control vs treatment was evaluated by Student's test, where \*\*  $p \leq 0.01$ ; \*\*\*  $p \leq 0.001$ .

#### 2.5.4 Conclusion

These results revealed multiple non-uniformities that could be explained by heterogeneous composition of the cell surface in the WT and the fad2-3 mutant. Unfortunately, such a slight change in morphology of the pavement cells cannot explain resistance to *B. cinerea* in fad2-3 mutant, but might explain slight changes in adhesion of *B. cinerea* spores on cotyledons of fad2-3 mutants relative to the WT.



## Chapter 3: Nanomotion Detection



### 3.1 Technique principles and methodology

*This section contains manuscript in preparation:*

Petar Stupar, Wojciech Chomicki, Maria Ines Villalba, Aleksandar Kalauzi, Ksenija Radotic, Massimiliano Bertacchi, Simone Dinarelli, Marco Girasole, Milica Pesic, Jasna Bankovic, Maria Elena Vela, Osvaldo Yantorno, Ronnie Willaert, Giovanni Dietler<sup>1</sup>, \*Giovanni Longo, \*Sandor Kasas. **A practical guide to reliable AFM-based nanomotion detection**. In preparation.

#### 3.1.1 Introduction

The atomic force microscope (AFM) is a versatile tool consisting in a micro-fabricated tip, fixed at the end of a small cantilever. The tip is placed in contact or near vicinity of a sample, and a laser beam is focused onto the cantilever's apex to track its deflection as the tip scans the sample. Initially, the AFM was employed to produce high-resolution topographic images of its surface, with resolutions in the order of 0.1 Å (16). Over the last 20 years, the range of information obtainable with the AFM has evolved to include the characterization of the nanomechanical properties of the sample (67,78,83,201–204) or the localization of the effect of drugs on biological specimens (205).

Very soon after its development, it has been shown that cantilevers can serve as very sensitive sensors (206). For instance, they can be used as micro-balances, to measure extremely small masses directly deposited on their surface. In other applications, it was shown that if one side of a cantilever is coated with a molecular layer, it will undergo a static bending that depends on the abundance, interaction and type of molecules. These measurements can monitor with high sensitivity the binding of targeted molecules to biomolecular receptors (207–210).

Recently, we demonstrated that cantilevers can characterize the nanometer scale fluctuations produced by movements of living organisms (211). The principles of this detection method are presented in **Figure 3.1, panel A**. Living specimens attached to such a sensor induce fluctuations and such measurable movements are correlated to their metabolic activity. We employed such nanomotion sensor to study various biological systems, such as bacteria, yeasts, mitochondria, plant and mammalian cells (212–215). In all cases, as long as the attached sample was metabolically active, the cantilever oscillated, but as soon as the viability was lost, the oscillations stopped. In fact, we demonstrated a direct correlation between energy consumption and cantilever fluctuations (216).

We used nanomotion detection to provide a rapid and reliable determination of the response of bacteria to antibiotics (217). The very same setup can be implemented to explore cancer cell sensitivity to chemotherapeutics (218). Indeed, the potential application domains of this versatile technique are vast and the simplicity of its working principle allows foreseeing its proliferation in medical centers and research laboratories (219).

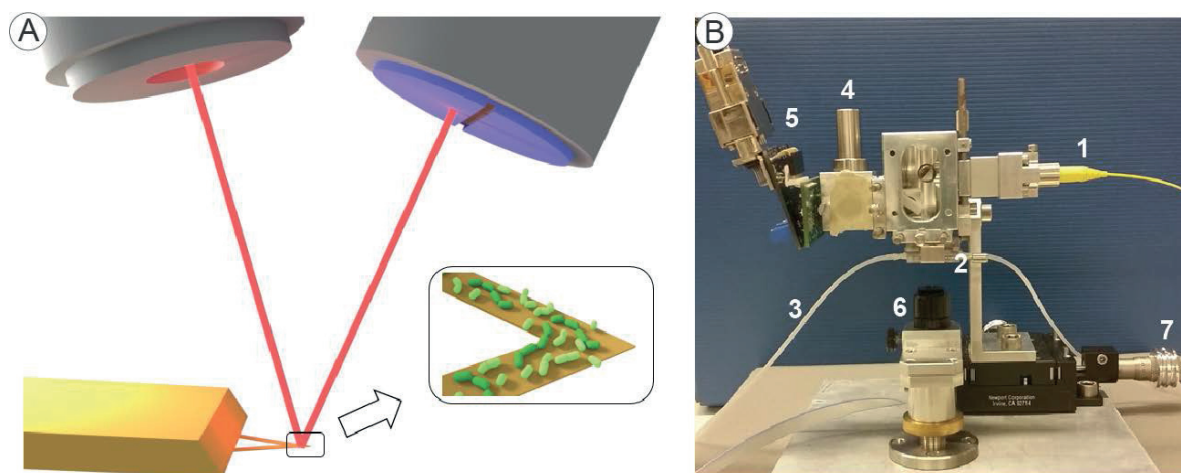


**Figure 3.1 Panel A:** schematics of the technique's working principles: a laser beam is focused on the cantilever sensor and reflected back to the photo-diode detector, tracking the motion of the cantilever, induced by the presence of living specimens attached. **Panel B:** Custom-made device developed for simplicity and portability. A laser beam (1) is focused onto the cantilever, which sits in a closed fluid cell (2), where a gravity-driven fluid exchange (3) is possible. The laser beam is reflected back to a beam splitter (4) and finally to the photodiode detector (5). A small camera (6) allows easy laser alignment, using translation stage (7).

However, despite the technical simplicity of the nanomotion sensor, the use of extremely sensitive cantilevers requires a certain number of precautions in order to obtain reliable results. Here, we present a step-by-step description of typical nanomotion experiments. The following protocols are the result of years of intensive use of the technique. In this short communication, we show the optimal experimental conditions and the overall working envelope of the technique.

### 3.1.2 Results

#### *Instrument and cantilever selection*

Any commercially available AFMs, equipped with custom liquid cells can be used to conduct nanomotion experiments (220). Biologically oriented AFMs are the most convenient, since they are mounted atop of an inverted optical microscope. The optical image of the cantilever permits determination of the position and the number of specimens present onto the cantilever. In addition, a non-commercial and dedicated apparatus performs similarly well (221–223). As an example, a device developed in our lab has been used intensively (**Figure 3.1, panel B**).

The choice of the cantilever is of utmost importance. Stiffer cantilevers give lower amplitude oscillations, whereas softer ones can break more easily during manipulation and are exposed to larger thermal drift. In most of our experiments, we used triangular silicon or silicon nitride ( $\text{Si}_3\text{N}_4$ ) cantilevers (0.06 – 0.12 N/m by Bruker), but, when working with peculiar experimental setups (e.g. the SCALA hardware) we also used rectangular sensor arrays. In all our experiments, we employed commercial cantilevers directly from the packaging box, but we are working on the development of optimized sensors for nanomotion experiments.

### *Cantilever functionalization*

Strong attachment of the specimens on the cantilever is of paramount importance in the setup of a nanomotion experiment. A specific chemical functionalization protocol must be chosen for each biological system (214,215), such as (3-aminopropyl)triethoxysilane (APTES) and/or glutaraldehyde for bacteria, poly-lysine or fibronectin for cells, concanavalin A for yeast, etc. Attention should be paid to the fact that some chemicals compromise the viability of the attached specimens. In case of bacterial samples, to assess their viability, a convenient option is the use of DEAD/LIVE BacLight stain. Naturally, the purity and quality of the chemicals must be taken into consideration: APTES and glutaraldehyde exposed to humidity lose their adhesive properties, whereas complex attaching media can be subjected to unwanted bacterial or yeast contaminations. Therefore, it is advisable to prepare a fresh solution for each experiment.

In most cases, the cantilever exposure time to the functionalizing agent determines the amount of chemical on its surface. A non-complete coating of the sensor can reduce the number of specimens and the strength of the attachment, while an excessive functionalization can lead to release of functionalizing agent in the solution, causing adverse effects on the living specimens throughout the measurements.

As an example, in the experiments involving bacterial samples, we coated the sensors by exposing them to 20  $\mu\text{l}$  of 0.5% glutaraldehyde for 10 min, rinsing with ultrapure water, drying, and then incubating with 10  $\mu\text{l}$  of a high-density bacterial suspension ( $\text{OD}_{600}$ : 0.6 with 10  $\mu\text{l}$  of suspension diluted in 1ml of phosphate buffer saline). When performing experiments with yeast, we obtained a good attachment using a 10-minute exposure to 1 mg/ml concanavalin A (ConA), or in other cases we chose 1-minute exposure to 0.1% APTES. For the attachment of mammalian cells, the choice was fine-tuned for each particular cell line: osteoblasts and cancer cells (i.e. the NCI-H460 cells) were attached exposing the cantilever for 30 minutes to the medium containing 50  $\mu\text{g}/\text{ml}$  fibronectin, while neurons required a 15-minute exposure to 1 mg/ml poly-l-lysine. In all cases, after the functionalization, the sensors were thoroughly and gently rinsed in ultra-pure water and used to approach on individual cells to promote the attachment (1 nN force).

Recently, more controlled functionalization procedures have been proposed. For instance, localized and highly controlled functionalization of surfaces can be obtained using ink-jet printing of the chemicals. This protocol can be extended to a direct printing and immobilization of the biological specimens on the sensor. These novel and controlled procedures could allow fast sensor preparation and will lead to more controlled parallelization of the nanomotion setup, and should be taken in high consideration in the case of industrial extension of some of these applications.

### *Sample attachment*

The main goal of the preparation protocols involves the attachment of viable specimens on the cantilever surface. There are several possible protocols to ensure a reliable immobilization of the samples on the sensor, often depending on the sample's nature and abundance.

In the case of bacterial or yeast cells, a droplet (typically 10 - 20  $\mu\text{l}$ ) of medium bearing a high concentration of specimens is placed on the cantilever, left to incubate around 35 minutes and

immersed into growth medium. After such preparation, the cantilever is mounted on the holder and inserted into the AFM. The procedure is depicted on the **Figure 3.2**. Overall, such external method is relatively simple and requires only a small amount of functionalizing agent. The main drawback lays in the need for the transfer of the sensor from the preparation to the analysis chamber, and this manipulation can produce sensor damage or contamination of the sample. Furthermore, each subsequent immersion step can induce detachment of specimens from the sensor, due to capillary forces. Generally, such random attachment procedures are quite fast and easy to perform, but have a down-side in the loss of control in the number and positioning of the specimens on the sensor.

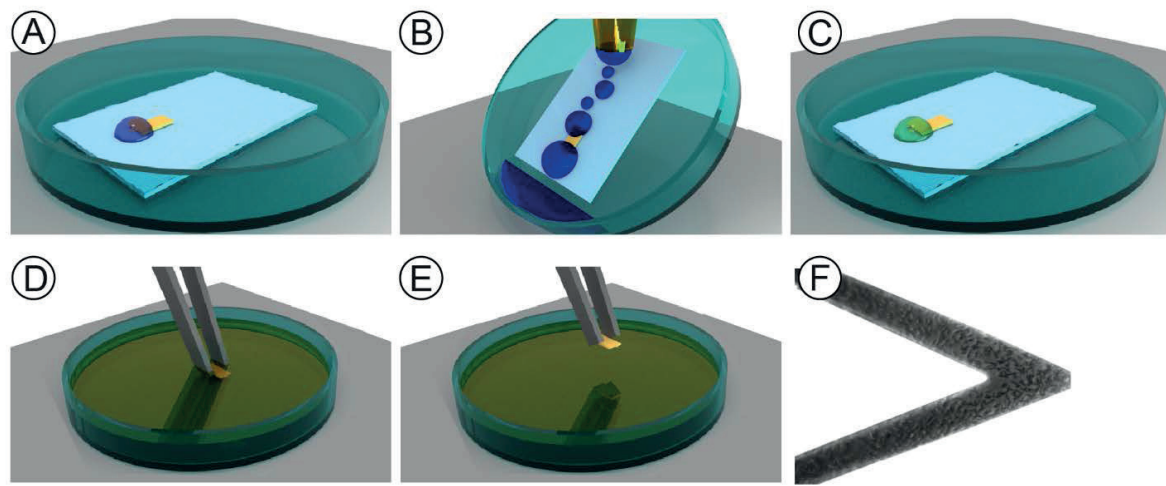


**Figure 3.2** Graphical representation of the functionalization and the attachment protocol. **A)** ~20  $\mu\text{l}$  of functionalizing chemical is deposited on the cantilever side of the chip, for 10 minutes. **B)** One milliliter of ultra-pure water is used to wash out the residual chemical. The cantilever is let to dry (5 min). **C)** ~20  $\mu\text{l}$  of suspension of the sample is deposited on the cantilever side of the chip for 35 minutes. **D, E)** Chip is immersed in and out of the culture medium for few times and observed under optical microscope for validation of the sample attachment. This step has to be done carefully and is specific to each sample. **F)** A good attachment yield with sufficient number of bacteria and no loosely attached groups (clumps).

An alternative method for the sample attachment is to insert the functionalized sensor directly in the analysis chamber, which is then flushed with a sample-rich medium. The system is left to incubate 1-15 minutes to ensure the immobilization of the viable specimens followed by gentle flushing with clean medium to remove the floating or loosely attached microorganisms. In some cases, even the very functionalization of the sensor can be performed in the analysis chamber, which must be then thoroughly washed to reduce the presence of dissolved chemicals. The main disadvantages of this procedure are the possible contamination of the analysis chamber or the possibility of the presence of debris or unattached organisms floating in the chamber.

Mammalian and plant cells requires some user intervention. In this direct attachment protocol, the cells are seeded on the analysis chamber and micrometer, high-precision motors are employed to place the sensor in the near proximity of a particular cell (the piezo-motors of an AFM are ideal for this kind of high-precision movement). The motors are then used to press the functionalized sensor on the cell, applying a controlled small pressure. Depending on the sample, a force in the range of 1-

15 nN is employed for about 3-5 min, to promote cell adhesion to the sensor. In particular cases, this procedure can be repeated to immobilize more than one cell in selected locations. Once the sensor is retracted, and the cells appear to be firmly attached, the nanomotion experiments can begin.

To retain the chemical activity of the functionalizing layer, some precautions should be taken into consideration. For instance, complex molecules from some growth media, such as lysogeny broth (LB, also known as Luria broth) typically used to grow bacteria, can compete with bacterial proteins for active moieties on the surface functionalized with glutaraldehyde or APTES. In these cases, the bacterial suspension needs to be centrifuged and the LB replaced by the phosphate buffer saline (PBS). This washing step should be repeated at least three times, until the concentrated PBS-bacteria suspension can be used for the attachment.

Another important precaution is to obtain sample attachment only on the cantilever surface, without partially attached and floating species, as they may introduce additional noise to the signal. **Figure 31F** illustrates an example of a good bacterial coverage.

#### *Laser alignment*

In most AFMs, the detection of the sensor fluctuations is obtained through a laser-based system. A laser is focused on the apical area of the cantilever and its reflection is collected using a low-noise photodetector. This allows a deflection sensitivity in the range of few angstroms. Due to such a high sensitivity, the alignment of the laser transduction system is fundamental to ensure the high-resolution detection of the movements of the cantilever. This is valid for conventional AFM measurements as well as for the nanomotion analyses. The laser beam must be focused on the apical region of the cantilever and its reflection should be centered on the photodiode to ensure a dynamic range of detection.

In the case of nanomotion analyses, we noticed that a special care should be taken in keeping a correct alignment of the laser and the photodiode throughout the experiment. Indeed, thermal drift over longer period of measurements can induce a decrease in sensitivity and the resulting variation in amplitude of the fluctuation signal can be mistakenly interpreted as a biological response. As a test of the constant sensitivity of the setup, we often rely on the Fourier analysis of the resulting nanomotion signal by recording the amplitude and shape of the cantilever's resonance frequency before and after the measurement, we can determine if a misalignment has occurred.

#### *Medium optical purity assessment*

Closely correlated to the previous step is the need for an accurate control over the laser pathway inside the analysis chamber. Any small floating particles inside the analysis chamber, such as detached specimens, undiluted chemicals or small debris, can modify the laser pathway strongly affecting the results. Thus, a "purity" check of the medium should always be taken into consideration. Such a test can simply be accomplished by recording the oscillations of a cantilever with no living biological samples attached. Any fluctuation measured in this condition can be considered the baseline for the subsequent experiment and can influence greatly the outcome of a measurement.



### *Oscillations recording*

The final outcome of a nanomotion experiment is a time-dependent graph of the fluctuations of the cantilever. The properties of this graph will indicate the metabolic activity of the biological specimens over time and their response to the exposed chemical agents. The oscillations are usually recorded by an external software and require a high acquisition rate, due to the innate variability of the measured signal. The collection of the nanomotion signal can be carried out in several ways. For instance, many commercial AFMs have dedicated software that can collect in real-time the deflection of the cantilever through built-in routines. In the experiments performed using the JPK Nanowizard III AFM, we exploited the Real-Time measurement option to visualize and store the nanomotion signal over time. In the cases in which such options are not available, we have employed I/O cards and developed custom LabVIEW routines to perform the measurements.

To measure the response of bacteria and cells, we have usually worked with acquisition rates of 20 kHz at 16 bits. Such a high sampling rate is chosen to record the resonance frequency of the cantilever. According to our experience, the most important information regarding the metabolic activity of the biological specimens is located at frequencies lower than the resonance frequency of the sensor (mainly up to 1000 Hz).

Any noise of external origin can have a large impact for nanomotion experiments. Most noise sources can be reduced by confining the instrument in acoustic boxes and using vibration isolation tables. In addition to such vibrations, any electrical circuit bears an electrical noise that has a typical frequency fingerprint decreasing with the increase of the frequency (1/f noise). Luckily, high-level instrumentation and specific electronic filters can be used to reduce these unwanted signals, and to allow the extraction of the metabolically-relevant information.

Before starting the oscillations recording, we strongly recommend monitoring the cantilever with optical microscope at high magnification. Especially in the case of larger plant or mammalian cells, high magnification optical imaging of the sensor throughout the measurements allows correlating large scale cellular displacements with cantilever oscillations. We have demonstrated the importance of this combined characterization in our previous works (215,219), and in **Figure 3.3** we illustrate the usefulness of such a correlation in the case of NCI-H460 cancer cells. In the latter case, one of the attached cells was undergoing cell division during a nanomotion experiment. By simultaneously collecting nanomotion signal and optical images, it was possible to correlate the increased oscillations with the cell replication. During division of eukaryotic cells, the actin cytoskeleton undergoes drastic changes and rearrangements. Entering mitosis, the extensive actin network is dismantled and rearranged, giving mitotic cells a characteristic round shape. Furthermore, microtubules play a crucial role by precisely organizing the establishment of the bipolar spindle and accurate segregation of chromosomes. In the experiment, cells were allowed to spread on a substrate coated with fibronectin, where integrin-mediated adhesion-dependent signaling supports cell cycle progression and survival. After some time, it entered mitotic phase and the signal increased substantially (variance plot on **Figure 3.3**). Looking at the timescale of the signal and corresponding images, the increase in variance can be attributed to the internal cellular rearrangements prior to division.

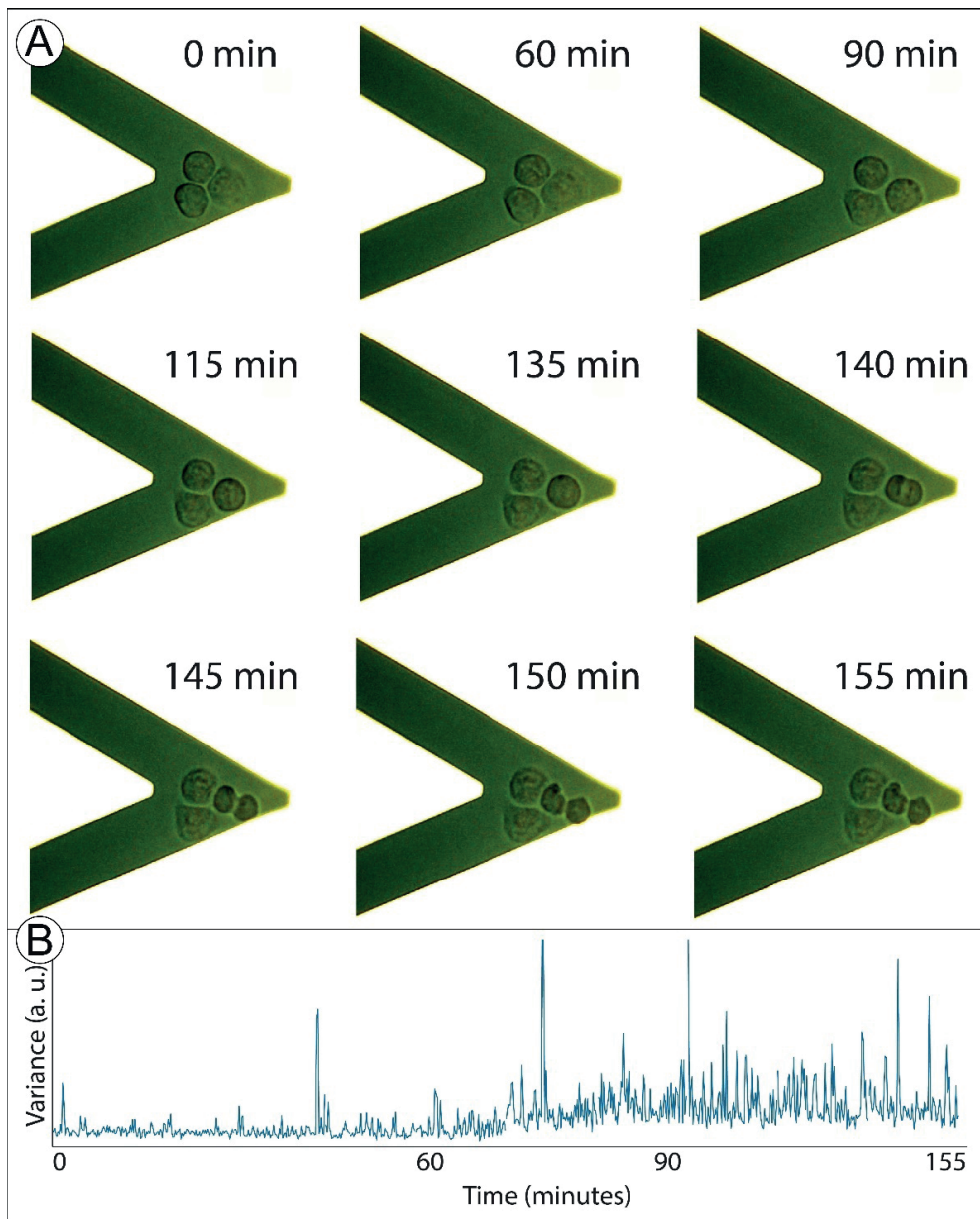


**Figure 3.3** Correlation between the optical images **(A)** and the variance **(B)** of the nanomotion signal. The increase in variance happens following the rearrangements of the cellular actin networks, before and during the division.

#### *Fluid exchange system*

In most nanomotion experiments, liquid exchange is a fundamental step to expose the specimens to a different chemical or physical condition, such as the introduction of a drug in the case of bacteria or cells. Unfortunately, the liquid flow can be an additional noise source and it may generate shear stress that can detach from the sensor some of the organisms under investigation. While a nanomotion experiment can be performed even in the presence of very slow liquid flow (216), we

advise discarding the data collected during the liquid exchange and allowing 5-10 minutes for the medium to stabilize in the analysis chamber.

Numerous methods can be used to exchange liquids in the small analysis chamber. For most experiments, the use of slow, low-noise systems or dedicated devices (220) is advisable to ensure that the gentle liquid flow does not disrupt the experimental setup and results. In order to determine the exact moment of the arrival of the new medium into the analysis chamber and the completion of the liquid exchange, we suggest using a timer if the flow rate has been previously determined (224). An alternative consists in controlled injection with precisely graduated syringes (225). In many cases, we have employed a gravity-driven flow, which generates even smaller disturbance to the sensor. In the case of experiments involving an open Petri dish, the direct manual injection of the drug or medium can replace the liquid exchange.

#### *Data processing*

To analyze the data collected in our experiments, we developed a MATLAB (Mathworks - Natick, Massachusetts, USA) software that accesses the raw data and performs the necessary analysis. This software was used to produce all the graphs and diagrams presented in this work. Once the nanomotion data has been collected as a raw deflection against time (**Figure 3.4, panel A**), the goal of the signal analysis is to extract the biologically-related information. Often, during the acquisition process, a thermal drift of the cantilever occurs. Most frequently, this happens at the beginning of the experiment or immediately after the liquid exchange procedure, when temperature differences are present in the analysis chamber. This phenomenon induces a slow bending of the cantilever, which behaves as a bimetal due to the metal coating present on one of its sides. If such long-term change in the mean level is present, it is advisable to remove it. In our experiments, we have often employed a windowed linear fit: we choose a window of 20 to 200 seconds (depending on the speed of the drift) and apply a linear fit to each window throughout the dataset and subtract it from the raw signal, as illustrated in **Figure 3.4, panel B**. After flattening, a moving average or a low pass filter (1000 Hz) can be applied, since most of the metabolically-related information is concentrated at lower frequencies.

After these preparation steps, the signal can be finally analyzed. While the more fundamental information (such as the specimens' viability) can be extracted, more complex analyses should be employed to achieve a more in-depth characterization of the biological system. The important information that can be extracted from the data requires the calculation of a windowed variance of the oscillations: the data is divided in small 10-30 second chunks and the variance for each of these blocks is calculated. The resulting plot, obtained using the software published in the appendix, depicts the evolution of the signal variance throughout the experiment (**Figure 3.4, panel C**). This can yield information on the strength of the oscillations and viability of the specimens over time and in different conditions. Also, it is a very useful representation, as it evidently points out any outliers, trends and, most importantly, expected signal changes. Furthermore, the user can perform an additional averaging of the variance values in the different experimental conditions (e.g. before vs. after the exposure to antibiotics). An example of averaging is presented on **Figure 3.4, panel D**,

where each bar represents the averaged variance of the deflection as a final quantitative measure that determines the outcome.

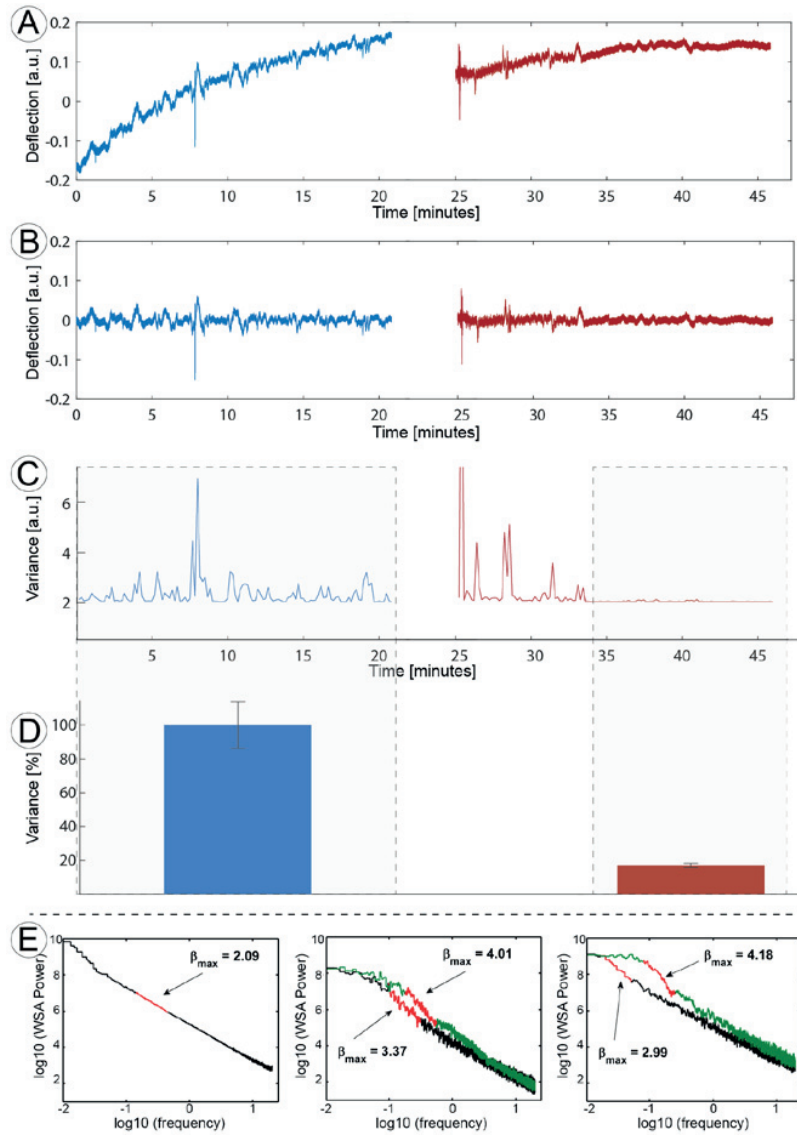


**Figure 3.4** Panel A: Nanomotion deflection signal recorded while the attached *Bordetella pertussis* were in growth media (blue) and in the presence of the antibiotic (red). Panel B: the same signal, flattened and centered around zero. Linear fit over 200s window has been applied. Panel C: Variance of the flattened deflection signal. For every 10s of the signal, variance has been calculated and plotted as it evolves in time for both conditions. Panel D: Normalized variance averages for the selected areas on variance plot. Blue bar shows 100% value, while the red bar represents the variance average calculated 10min after the drug exposure, and shows the reduction of fluctuations to less than 20%. Panel E: Another way of analyzing the signal. Log-log plots of deflection signals power spectra, obtained by applying Interval Weighted Spectral Averaging (IWSA) method for three cases: cantilever without living specimens (left); *Bordetella pertussis* (middle); *Escherichia coli* (right). Green curves refer to untreated, black to treated bacteria or bare cantilever. In all cases a sliding regression window was applied. Window positions with maximal values of exponent  $\beta$  were drawn in red, while the corresponding  $\beta_{max}$  values are indicated in each panel.

In addition to the variance, more complex signal analysis procedures can be taken into consideration. We have investigated different approaches to the characterization of the signal, producing other Matlab and Labview routines to perform more advanced characterizations, such as FFT analyses and signal filtering, but in this regard much work still must be done. Indeed, the nanomotion signal is mainly a colored noise, which contains a white noise component, peaked at the resonance frequency, electronic noise at low frequencies and the biological component in between. In this framework, a simple FFT analysis, a method generally used to detect putative frequency components of the oscillatory signal, might not be optimal. In our studies, we have seen that the multitude of specimens and oscillating sources yield no particular isolated frequency. The presence of living specimens on the sensor produces only an increased intensity of the lower frequencies in the power spectrum of the data (<1000 Hz). The result of the metabolic activity of the samples is spread over wider frequency regions.  $1/f$  dependence noise is superimposed on frequency-independent white noise, and analysis of these factors will likely be important for the understanding of the cell-generated noise. There is evidence that a log-log power spectrum analysis is more suitable to allow the emerging and characterization of relevant peaks. Therefore, one could apply Interval Weighted Spectra Averaging (IWSA) method (**Figure 3.4, panel E**) instead of simple power FFT (**Figure 3.5**) (226). In addition to this, other more refined spectral and non-linear analyses including multi-fractal (227), time-frequency using the Stockwell-transform (228,229), or multiscale entropy analyses (230) could be well suited.

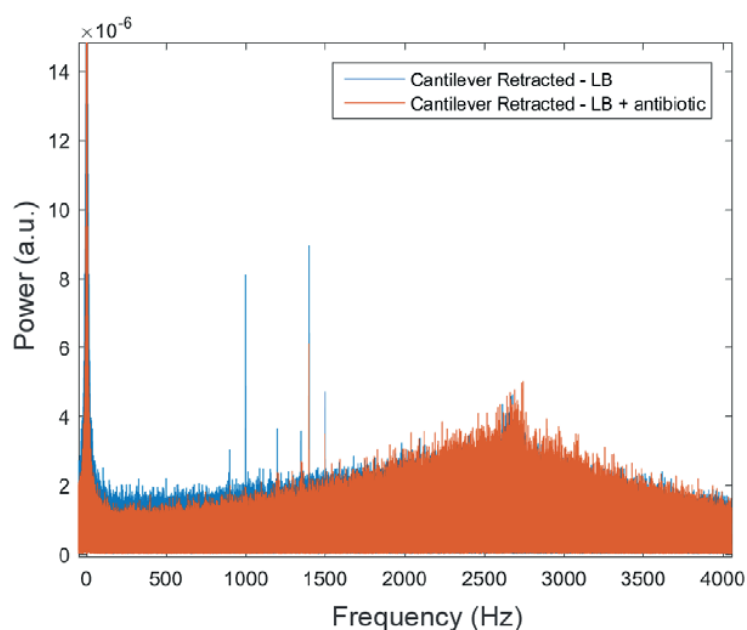


*Figure 3.5* FFT analysis of oscillatory movement in growth media (*blue*) and in the presence of the antibiotic (*orange*).

It must be noted that the response of living biological systems can be extremely variable. The phenotypic response of the specimens to a particular drug or condition can require long stabilization times. For example, when studying bacteria exposure to antibiotics, we identified several cases in

which the initial nanomotion response did not reflect the effective susceptibility to the particular drug. In some cases, resistant species reduced their fluctuations, only to return to a normal oscillation after tens of minutes. Also, care should be taken when averaging, to avoid the initial part of the signal, as the drug might still not take its effect.

### 3.1.3 Conclusion

Nanomotion analysis of microscopic samples is a simple and rapid method to assess the viability and metabolic response of a wide range of simple organisms in different conditions. Here, we have detailed the best practice to achieve successful measurements with this innovative technique. We described all the steps required to determine the best protocols for the experiments, while also highlighting some of the problems that can occur during measurement and, for most of them, the way to avoid them.

Due to the young age of this technique, its limitations and development possibilities are still unexplored. For instance, the laser-photo-detection system is extremely simple and efficient but also a major source of noise. Electronic noise, susceptibility to impurities in the analysis chamber or from laser misalignment can affect a good nanomotion experiment. Such problems would be in part reduced by employing other kinds of high-sensitivity fluctuation detection, such as piezo resistive sensors or capacitive transduction systems.

Overall, the nanomotion sensor is a very versatile and powerful instrument which can be the base for new investigation tools. Indeed, we have already combined nanomotion and fluorescence microscopy analyses and the increasing control over the grafting of micro fluidics or micro contacts directly on the cantilever can open the way to even more complex characterization platforms, merging, on the same sensor, nanomotion and conventional tools. This would be a step towards integrated diagnostic tools, Lab-on-a-Lever sensors, which can deliver an unprecedented view of the overall activity of biological specimens and of their response to external stimuli.

## 3.2 Bacterial susceptibility to antibiotics through nanomotion

### 3.2.1 Introduction

#### *Antimicrobial resistance*

Microbes, diverse living organisms of microscopic dimensions, have the innate ability to develop a mechanism to resist the drug treatment. Most of the microbes are harmless or even beneficial to our lives, but there are also the ones who cause disease, the pathogens (germs, bugs). They can all develop a resistance to drugs designed to destroy them. Antimicrobials are drugs used to treat disease-causing microbes, and the most commonly known are the antibiotics, which target bacteria. Simply using them creates resistance, as the mechanism itself occurs as part of a natural process in which bacteria evolve. There are several major bacterial resistance strategies: 1) by disabling the antimicrobial entry and reducing its cell-penetration ability, 2) by using the efflux pumps to expel the antibiotic out of the cell, 3) by inactivating the antibiotic molecules via modification or degradation, and 4) by changing the target to which antibiotic was supposed to bind. All those abilities are genetically encoded and if the resistance is naturally coded and expressed by a particular strain of bacteria, it is called intrinsic. The other form of resistance is called acquired, when changes in bacterial genome occur through mutation or horizontal gene transfer. These abilities allow bacterial strains that are capable of surviving exposure to a particular drug to grow and spread, due to a lack of competition from other strains. This has led to the emergence of the multi-drug resistant strains, such as Methicillin-resistant *Staphylococcus aureus* (MRSA) and extremely drug-resistant tuberculosis, bacteria which are difficult or impossible to treat with the existing medicines.

Listed as one of the greatest threats to human health, multi-drug resistant bacterial infections are predicted to kill 25,000 people in Europe each year, costing up to 1.5 billion euros annually (231). It is possible to slow the antibiotic resistance down. However, it does not seem possible to put it to a complete stop. Human kind might always need new antibiotics to keep up with the resistant pathogens, as antibiotics lose effectiveness over time. Furthermore, there is an immense need for new diagnostic tools to test bacterial susceptibility and track the resistance development.

#### *Susceptibility testing tools*

Antibiotic susceptibility testing methods are *in vitro* procedures that are used to detect antibiotic resistance in individual bacterial isolates. They are typically employed to test the bacterial isolate against several antibiotics under different concentrations, to determine clinical breakpoint values. These values are normally determined as threshold values for each pathogen-antibiotic combination, and indicate the level of resistance as sensitive, intermediate or resistant.

Although today's tests are relevant in every clinical microbiology laboratory, they are fundamentally slow. Most of the antibiotic susceptibility tests are based on growth, meaning that the time to obtain a result whether a bacterium is sensitive or not, is dictated by the organism's doubling rate. This time can range from a day, to several weeks, depending on the pathogen, which is not ideal particularly in critical clinical cases demanding urgency.

Dilution methods (broth, agar) are based on bacterial growth in series of dilutions of the antibiotic in broth or agar environments. The lowest concentration at which the isolate is inhibited (no visible

growth) is recorded as the minimal inhibitory concentration (MIC), as opposed to the minimum bactericidal concentration (MBC) - the lowest concentration that will kill organism after subculture. Another approach is a disk diffusion method, where pre-prepared disks containing a standard concentration of the antibiotic are dispensed and pressed onto the agar surface. The antibiotic diffuses outward from the disk, creating a gradient of antibiotic concentration. A newer method that also utilized antibiotic gradient is E-test (AB Biodisk, Sweden), a plastic strip with gradually decreasing antibiotic concentrations and a numeric scale for each of them. There are also mechanism-specific tests, that detect particular resistance mechanism, like chromogenic cephalosporinase test for detection of beta lactamase. Furthermore, specific genes that confer resistance may be tested using genotypic methods, like PCR or DNA hybridization. Nowadays, however, more tools are being developed using different approaches and degrees of automatization, such as: Vitek2 (bioMerieux, France), Sensititre (Thermo Scientific, USA), MicroScan WalkAway (Beckman Coulter, UK), Micronaut (Merlin, Germany), Phoenix (Becton Dickinson, USA), etc. One major limitation follows most of above-mentioned tools: the cost entailed in initial purchase, operation and maintenance of the machinery.

### 3.2.2 Materials and Methods

**Bacterial culture.** Frozen stocks of all the bacterial strains were stored at  $-80\text{ }^{\circ}\text{C}$  in glycerol-supplemented growth medium (LB, SS, THB, etc.). In preparation for the experiments, these bacteria were streaked on agar media. A bacterial colony was then isolated and incubated overnight at  $37\text{ }^{\circ}\text{C}$  in 4 mL of growth media. After incubation, the bacteria were washed three times in PBS. Between each rinse, they were sedimented by centrifugation at  $2,300 \times g$  for 5 min and were finally resuspended in 0.2 mL of PBS. This concentrated solution was used in the nanomotion experiments. Cantilever functionalization and attachment procedures are described in the previous chapter.

### 3.2.3 Results

The first and most important step in these experiments is the attachment of bacterial cells on the cantilever surface. This step is crucial in multiple ways: if the number of bacteria is lower than the minimum detectable ( $\approx 10^2$  (214)), the noise will dominate the signal. On the other hand, if the attachment procedure produces large clumps of bacterial cells, biofilm or any sort of layered and interconnected structures that span across the cantilever and the chip, the signal will mostly be falsely positive. Therefore, an optimal attachment is the key to all nanomotion experiments and one should always make sure that the attached sample will stay on the cantilever under the experimental flow (if flow exchange is used). We have tested multiple cantilever functionalizing agents in order to find the right chemical for the non-specific attachment that could be used for most of bacterial strains. Furthermore, we investigated their viability, as the other crucial parameter is the retained cell viability after the attachment procedure.

Staining bacteria with the LIVE/DEAD BacLight Bacterial Viability Kit (Thermo Fisher Scientific) is a way to test their viability. This staining procedure uses a mixture of the SYTO 9 green-fluorescent nucleic acid stain and propidium iodide, the red-fluorescent nucleic acid stain. These stains differ in their spectral characteristics and their ability to penetrate healthy bacterial cells. With an appropriate mixture of the both stains, the bacteria with intact cell membranes stain fluorescent green, whereas the bacteria with damaged membranes stain fluorescent red.



### Cantilever functionalization and sample attachment

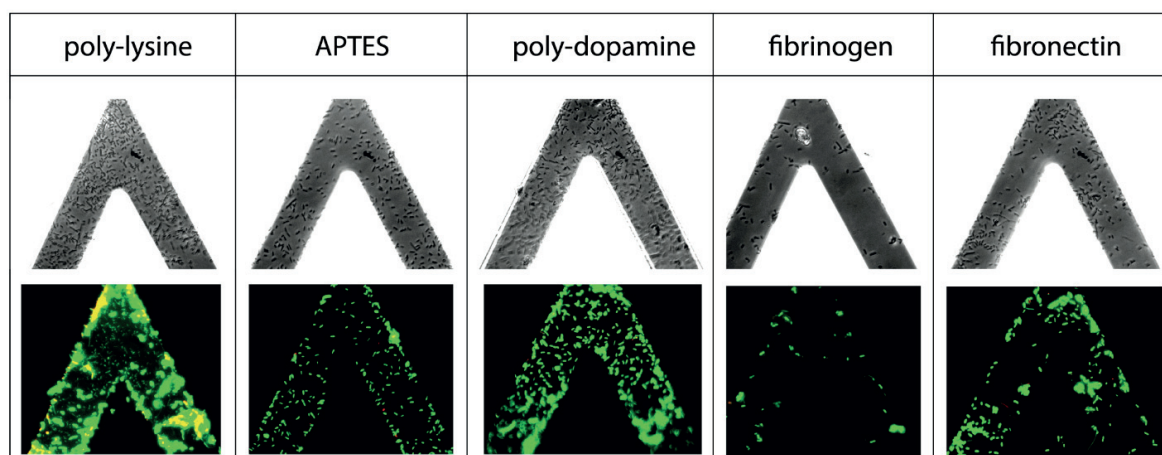


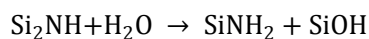
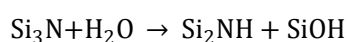
**Figure 3.6** Bacterial attachment yield and viability assessment after different cantilever functionalization procedures: poly-L-lysine, APTES, poly-dopamine, fibrinogen and fibronectin, respectively. Green – viable bacterial, red (yellow) – dead cells.

**Figure 3.6** shows bacterial attachment yields and their viability after different cantilever functionalization procedures. Fibrinogen, a glycoprotein, used as a functionalizing agent gives very few bacterial cells attached, at least in the case of tested *E. coli* (DH5alpha strain). Better results were obtained using an extracellular matrix protein – fibronectin. However, clumping structures are present, as seen on the fluorescence image. A more uniform attachment distribution is obtained using a non-biological chemical (3-aminopropyl)triethoxysilane (APTES), in a so-called silanization procedure. Largest amount of the attached bacteria was obtained using the polymerized amino acid – poly-L-lysine. Unfortunately, apart from the clumping structures, a portion of non-viable cells is stained. Yet another polymer, of dopamine – poly-dopamine gave a uniform, viable and dense layer of bacterial cells on the cantilever surface. This procedure, however, requires rather long polymerization time (about an hour).

Considering all the above-mentioned results, we have decided to continue using non-specific attachment capabilities of glutaraldehyde. In this regard, we did experiments to optimize the other parameters which are affecting the attachment yield, namely the bacterial suspension density and the number of centrifugation steps. **Figure 3.7** represents this optimization step and shows the attachment yield on both cantilever sides (silicon nitride and gold), using two concentrations of glutaraldehyde (0.5 and 5 %), centrifuging them once or 4 times, and using different bacterial suspension concentrations ( $OD_{595} = 1$  and  $OD_{595} = 2$ ). Looking at the figure, it is evident that the procedure on the lowest right corner produced the best bacterial attachment within the frame of the experiment (higher concentration of bacterial suspension, centrifuged 4 times and attached with 0.5% glutaraldehyde). The fact that there is a correlation between centrifugation steps and the attachment yield can be explained with two possible scenarios. One of them is that complex molecules from the growth media compete with proteins on bacterial surface for active moieties on the functionalized surface, as one centrifugation step might not be sufficient to wash them out.

Another possibility lies in the chemistry of bacterial surface, which is composed predominantly of glycolipid known as lipopolysaccharide (LPS). Under certain stress conditions, some *E. coli* isolates, for example, produce an exopolysaccharide (EPS) called colanic acid. Although LPS is covalently linked to the cell surface, EPS molecules appear to be released onto the cell surface with no means of attachment (232). Furthermore, it has been shown that centrifugation of bacterial suspension affects their surface chemistry and zeta potential (233,234). Those changes might influence the affinity of cell surface binding to the functionalized cantilever.

The functionalization is obtained in water solution of glutaraldehyde. Knowing that in the Si<sub>3</sub>N<sub>4</sub> bulk, each nitrogen atom is bonded to three silicon atoms, the electron pair on nitrogen is the only one available for hydrolysis (235):



The secondary amine can be transformed into primary amine group, as a major moiety on the surface, apart from silanol groups. These groups can then readily react with available aldehyde sites.

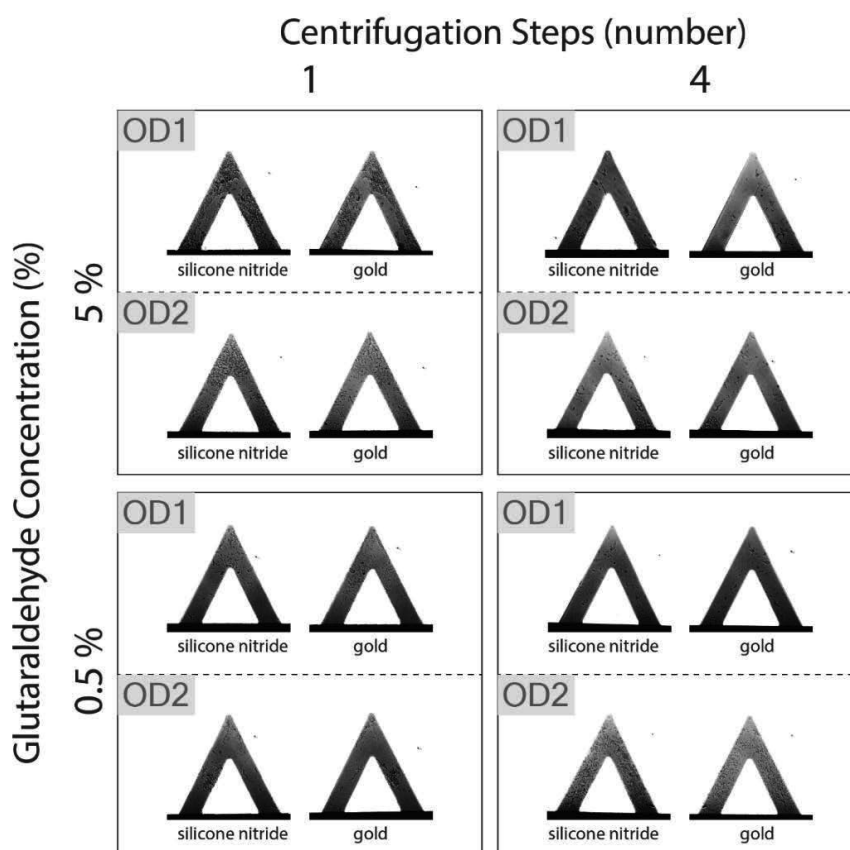


**Figure 3.7** Glutaraldehyde attachment test. Two concentrations of the chemical were used in combination with 1 or 4 centrifugation steps and two suspension concentrations, in order to assess the optimal preparatory procedure for the attachment with the best yield.

Seemingly simple chemical, glutaraldehyde reacts in a complex manner, and exists in 13 possible conformations and forms, depending on the solution pH, concentration, and temperature (236). However, at diluted concentrations (such as 0.5%) and within the pH range of 3 – 8 (such as ultra-pure water with pH of 5.5), glutaraldehyde is almost monomeric, being predominantly in cyclic hemiacetal form. Highly reactive around neutral pH, glutaraldehyde reacts with several functional groups of proteins, such as: amine, thiol, phenol, and imidazole. Reactions with amine groups are mostly irreversible at pH between 7-9, such as the one of the phosphate buffer saline (PBS) buffer. Most proteins contain many lysine residues, usually located on the protein surface, and unprotected amino groups are very reactive as nucleophilic agents. That could explain why the best attachment yield was obtained using water-diluted glutaraldehyde for functionalization, and PBS-suspended bacteria for the attachment step.

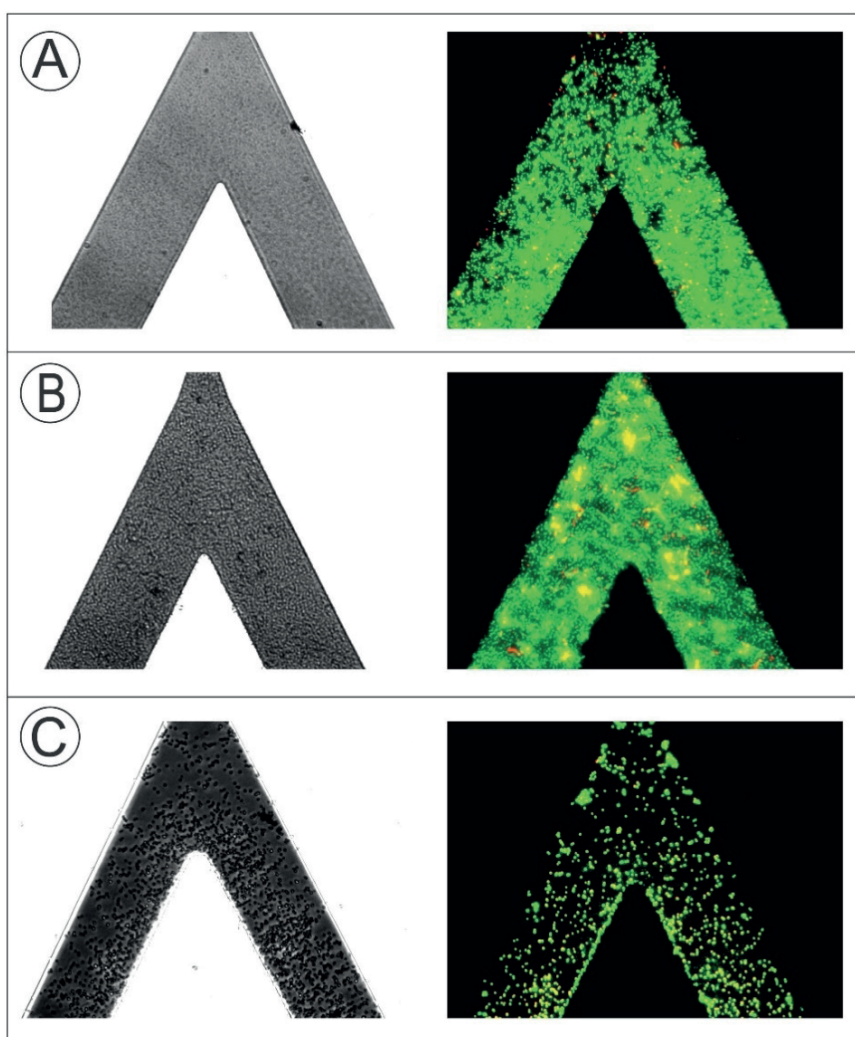


**Figure 3.8** Bacterial cell viability test after the described attachment procedure. Optical image (**left**) of the cantilever with different bacteria attached using glutaraldehyde-functionalized surface, and (**right**) LIVE/DEAD BacLight staining of the same bacteria shows most of them survived the procedure. **Panel A:** *Bordetella pertussis*. **Panel B:** *Streptococcus agalactiae*. **Panel C:** *Staphylococcus aureus*.

Once we chose the functionalization agent and optimized the attachment procedure, the next step was to test it on different bacterial species. **Figure 3.8** represents the cantilever with excellent attachment of *Bordetella pertussis*, *Streptococcus agalactiae*, and *Staphylococcus aureus* bacteria. The attachment is obtained only on the cantilever surface - no protruding or detaching parts, layers in between the cantilever sides, clumping structures, antennas, etc. Furthermore, viability staining showed that the majority of the attached cells retained their membrane integrity after the attachment procedure.

#### *Nanomotion as a susceptibility testing tool*

After the optimization of the functionalization and the attachment procedures, nanomotion experiments were done using different bacterial strains. In a typical experiment, we functionalized a sensor with glutaraldehyde (0.5%), washed it, dried it and prepared it for a non-specific bacterial attachment. After the attachment, the cantilever is placed into the analysis chamber of the chosen instrument, subjected to required growth medium and prepared for the recording of its deflection. **Figure 3.9** shows three deflection signals, plotted one after the other. The first deflection signal is of a bare cantilever, functionalized with glutaraldehyde, but containing no bacteria. Deflection of such a sensor is, as expected, uniform white-noise, and is correlated with the cantilever being in a thermal equilibrium with the surrounding environment. However, once the bacterial cells are attached, oscillatory signal shows additional noise and the oscillation amplitudes increase. Once the antibiotic is injected in the analysis chamber, oscillations of the cantilever continue to a certain extent to oscillate as in growth media. It takes time for the drug to have an effect on the attached bacterial cells. Experiments are showing that this time depends on the bacteria-antibiotic combination, the administration mode, and the nature of the liquid cell or the exchange process. As seen on the last deflection from the same figure, the oscillations steadily decrease and reverse to almost a basal level. The interpretation in this case would be that the drug has taken its effect, strongly affecting the metabolic activity of the attached cells, which subsequently reduces the oscillations of the cantilever.

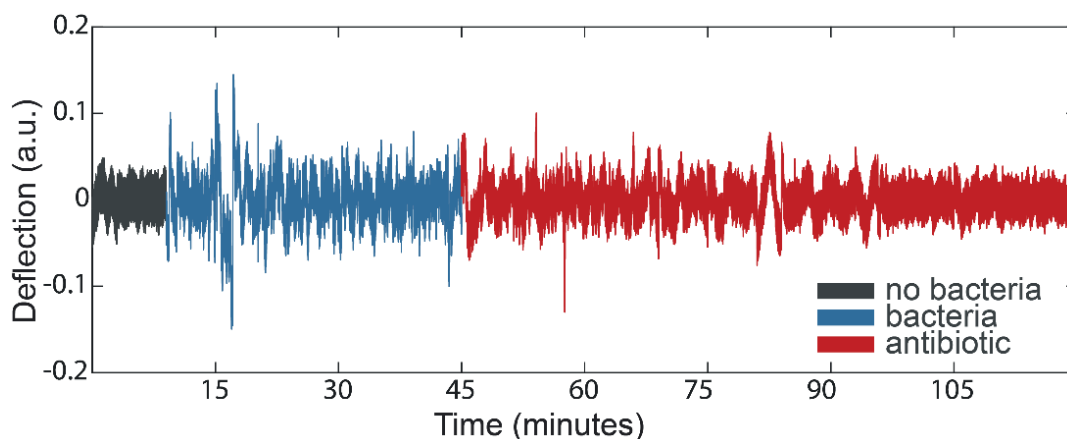


**Figure 3.9** An example data of the cantilever oscillations before attaching bacteria on it (**gray**), once bacteria are attached (**blue**) and during the antibiotic exposure (**red**). It is evident that the presence of bacteria on the cantilever induced additional oscillatory movement which goes away after certain time of the antibiotic exposure.

Deflection signal is the raw signal recorded in nanomotion experiments. It is, however, not always the best way to represent the signal and the biological event during the experiment. A more convenient and representative approach is to calculate the variance of oscillations and plot the values against time. This way, the evolution of variance shows how much oscillations deviate from the mean in a timely manner. **Figure 3.10** has been made to help to understand the signal representation. Once the variance is calculated in a windowed manner and plotted against time, an average of the signal may be a good quantitative measure of the cantilever oscillations in different conditions. As seen on the figure, the areas grayed out are the ones used for averaging and creating bar charts on the panel B. As explained, the drug effect takes certain amount of time, and averaging the area of the plot where the drug is still diffusing and not affecting bacterial cells, is not reasonable. Deflection signal in this area may be statistically explored using box plots, like on panel D. This procedure, however, is time and resource consuming, as sampling frequency of 20 kHz generates files of a large size.

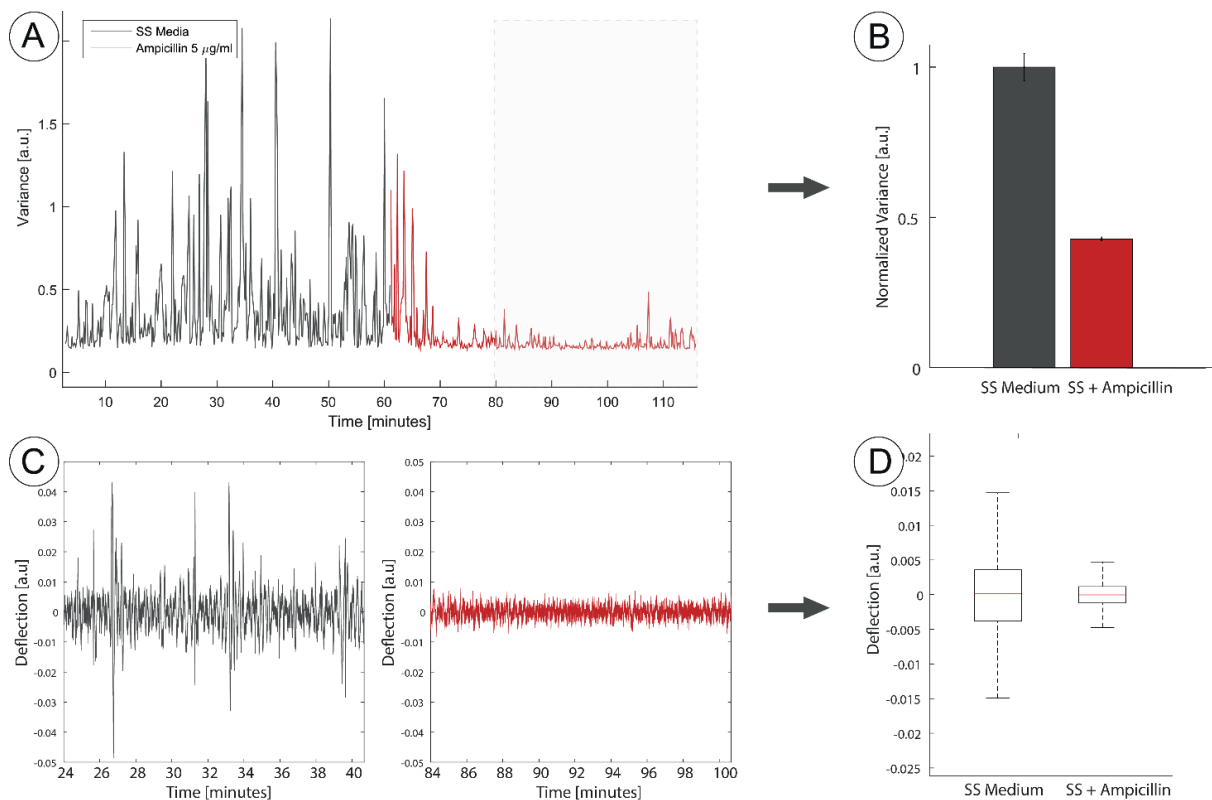


**Figure 3.10** An example of the nanomotion drug susceptibility assay using a in-house-made instrument. The response of *B. pertussis* to ampicillin at the MBC value ( $5.0 \mu\text{g}/\text{mL}$ ). **Panel A:** The evolution of oscillation variance across the entire experiment. 1h long measurements recorded in growth media and in growth media and antibiotic. A clear decrease in variance supports the premise of bacterial death due to the antibiotic action. Such signal is transformed into the normalized variance (**Panel B**), averaging the two conditions separately (after 20 min of each condition's start). **Panel C:** 15 min cuts that represent the cantilever deflection used to calculate the variance. Boxplots are obtained using the same data as those in panel C (**Panel D**).

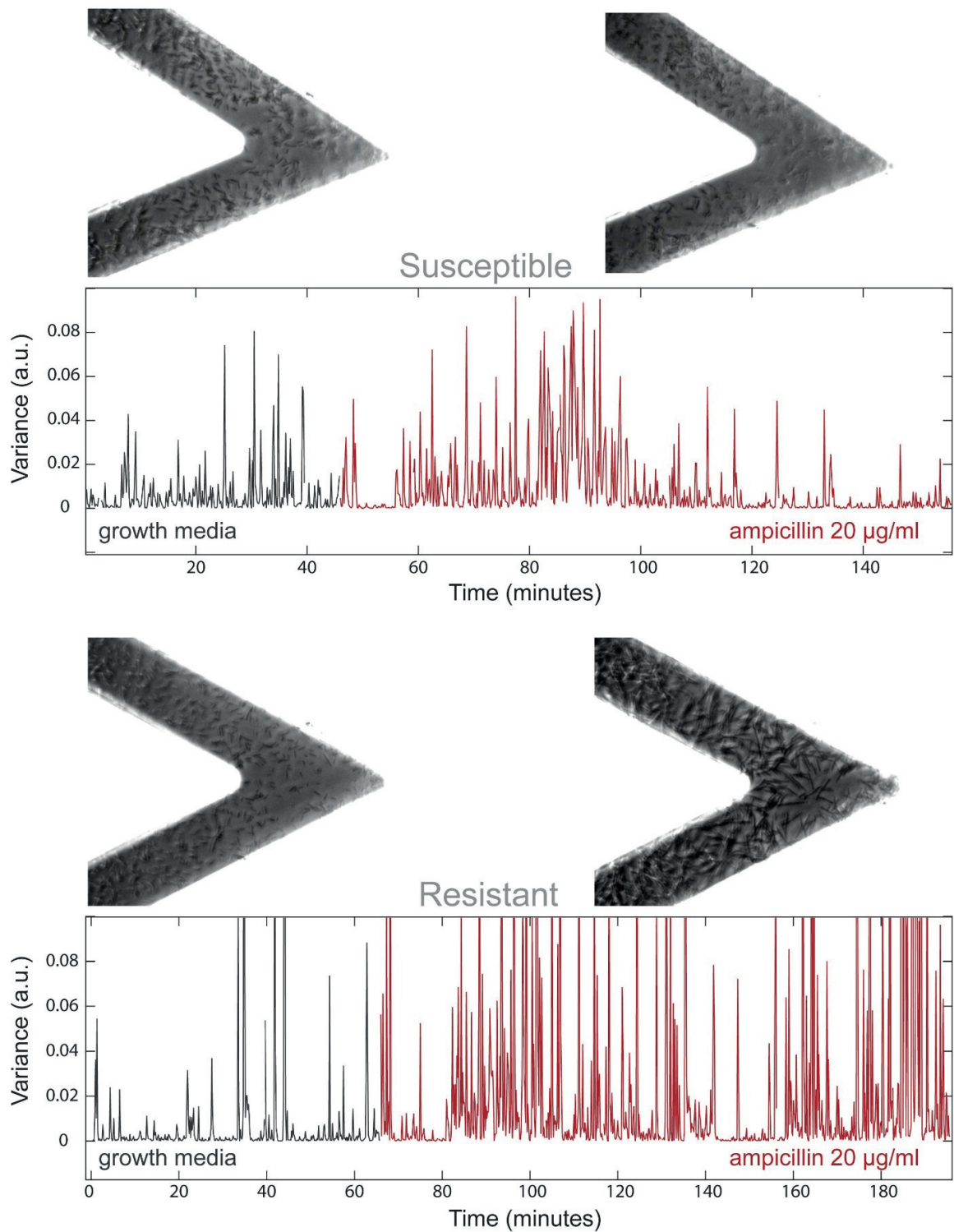


**Figure 3.11** An example of the nanomotion drug susceptibility assay using a commercial AFM (JPK). Graphs represent the response of the attached *E. coli* cells to ampicillin (susceptible strain – **top**, and resistant strain – **bottom**). Each case has two optical images showing the starting and the ending phases of the experiment.

In **Figure 3.11**, we showed a typical cantilever, coated with *E. coli* cells, either susceptible (**top**) or resistant (**bottom**) to a bactericidal antibiotic, namely ampicillin. The sensor's oscillations were measured, first in growth media and then upon the addition of 20  $\mu\text{g/ml}$  ampicillin. In about 1 hour, the addition of the antibiotic caused the reduction of the nanomotion oscillations, in the case of the susceptible cells. This suggests that the metabolic activity of the attached bacteria is compromised by the action of the applied antibiotic. On the other hand, in the same time-frame, the resistant *E. coli* increased their activity, indicating a strong response to the antibiotic pressure. Moreover, the optical images are showing differences in the cases of susceptible and resistant strains, after the experiment. Susceptible cells stop growing, have permeabilized membranes, turn into spheroplasts or lyse, after the ampicillin exposure. The resistant ones, however, continue to grow and be metabolically active, occupying a large portion of the cantilever surface.

A careful reader may observe an interesting phenomenon, looking at the variance signal of susceptible bacteria cells subjected to the antibiotic pressure. Namely, in the case of *E. coli* against ampicillin, depending on the fluid system used, the drug effect can take place sooner or later. Experiments show that on the commercial system, such as the JPK AFM, the use of a Petri dish and the manual injection without flow renders slower effect on the bacteria, compared to when a gravity-driven fluid flow is used in a customized setup. Ampicillin belongs to a class of  $\beta$ -lactams, known to exhibit time-dependent activity and slow bactericidal action, unless it is continuously infused or frequently dosed (237). Flow, in cases of customized setup, allows continuous flux of the drug and potentially large advantage in exposure to the attached bacteria within the fluid cell, whereas a simple and static deposition of the drug in a Petri dish allows action dependent on a diffusion only.

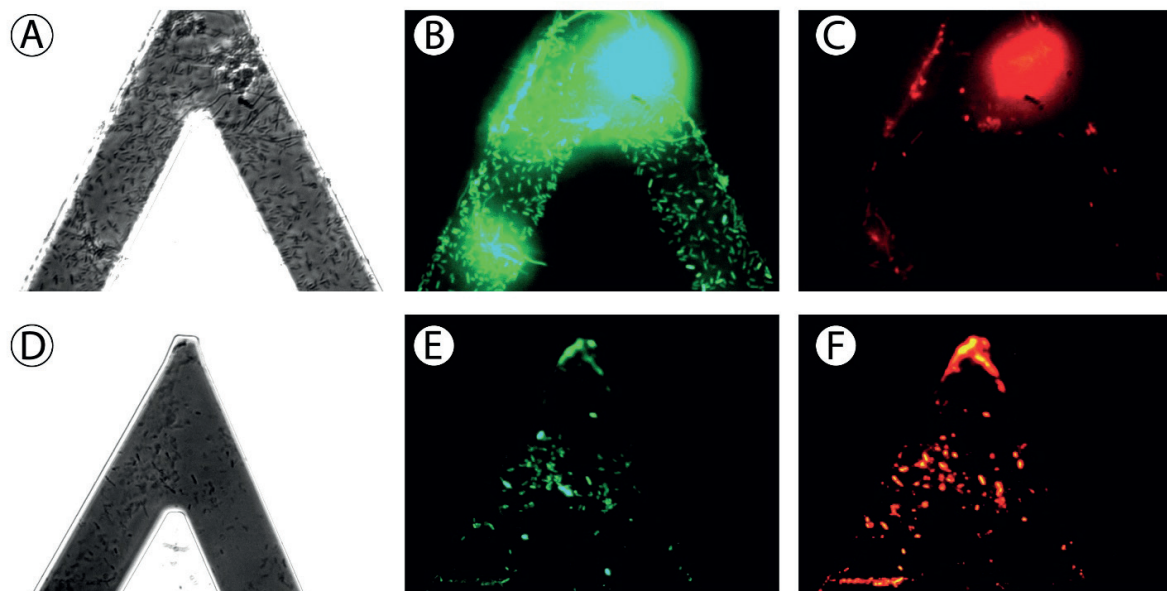


**Figure 3.12** Optical and fluorescent images of the cantilever with *E. coli* bacteria attached. Live/Dead staining shows the viability of the stained cells (**green** - viable, **red** - non viable). **Panels A-B-C** show the cantilever with freshly attached bacteria, while **panels D-E-F** show the cantilever after the nanomotion experiment using ampicillin as a drug.

One of the many controls we performed during these studies is the Live/Dead staining and viability assessments after the nanomotion experiment. **Figure 3.12** is a representation of such a control, where cantilever with the attached bacteria is subjected to fluorescence stains and observed under the microscope. The images A, B and C show viability of bacteria subjected to growth medium only. The other set of images (D, E, F) show another cantilever with the same bacterial type, but subjected to nanomotion experiment, and therefore the drug (ampicillin). As shown, the cells do remain viable after the attachment procedure, being only in growth media, while the ones used for the experiment do not.

**Table 3.1** Some examples of bacteria - antibiotic combinations tested using nanomotion technique. In the table, a sample type is named, stated which antibiotic and at what concentration, what is the percentage change from 100% in growth media, and time after which the average is calculated.

Bacterial type	Antibiotic	Concentration (µg/ml)	Change (%)	Time (min)
<i>Staphylococcus aureus</i>	Ciprofloxacin	6	16	50
<i>Bordetella pertussis</i>	Ampicillin	1	38	20
<i>Pseudomonas aeruginosa</i>	Ceftazidime	8	54	40
<i>Streptococcus agalactiae</i>	Ampicillin	20	18	10
<i>Mycobacterium smegmatis</i>	Ciprofloxacin	20	64	30
<i>Escherichia coli</i>	Kanamycin	1	42	60
<i>Escherichia coli</i>	Ciprofloxacin	6	40	60
<i>Candida albicans (yeast)</i>	Caspofungin	40	35	20

The experiments involving other types of bacteria and antibiotic combinations have been performed, and some of them are presented in the **Table 3.1**. Here, the type of bacteria, name of the antibiotic used and its concentration are reported. The change column represents the percentage of the change in variance if values in growth medium are considered 100%. As an example, *Staphylococcus aureus* subjected to ciprofloxacin at 6 µg/ml showed change of 16% after 50 minutes of drug exposure. This means that the variance average, calculated after 50 minutes of drug exposure, is only 16% of the value in growth media. Therefore, the value of 16% change corresponds to a variance drop of 84%.

#### *MIC and MBC determination*

The nanomotion experiments are not limited to testing one concentration of the drug in a single experiment. It is possible to subject the attached bacteria to an array of concentrations and observe the cantilever oscillatory movements during that time. An example study has been performed on *E. coli* cells against different concentration of ampicillin (0, 1, 2, 3, 4, 5 and 20 µg/ml). Doing the conventional, gold standard tests in parallel, allows verification and validation of nanomotion experiments. The same bacterial sample and the antibiotic solutions have been used for both sets of experiments, and the results were compared. Minimum inhibitory concentration starts at 2 µg/ml, while minimum bactericidal concentration turned out to be in between 5 and 20 µg/ml. Nanomotion experiments were done in the following manner: after placing a cantilever with attached *E. coli* c1895



bacteria into the fluid cell, growth medium was flushed and left for 25 minutes. That measurement is a control with no addition of ampicillin, and the other measurements were done with increasing the amount of ampicillin, one after the other, exposing the same bacteria on the same cantilever.

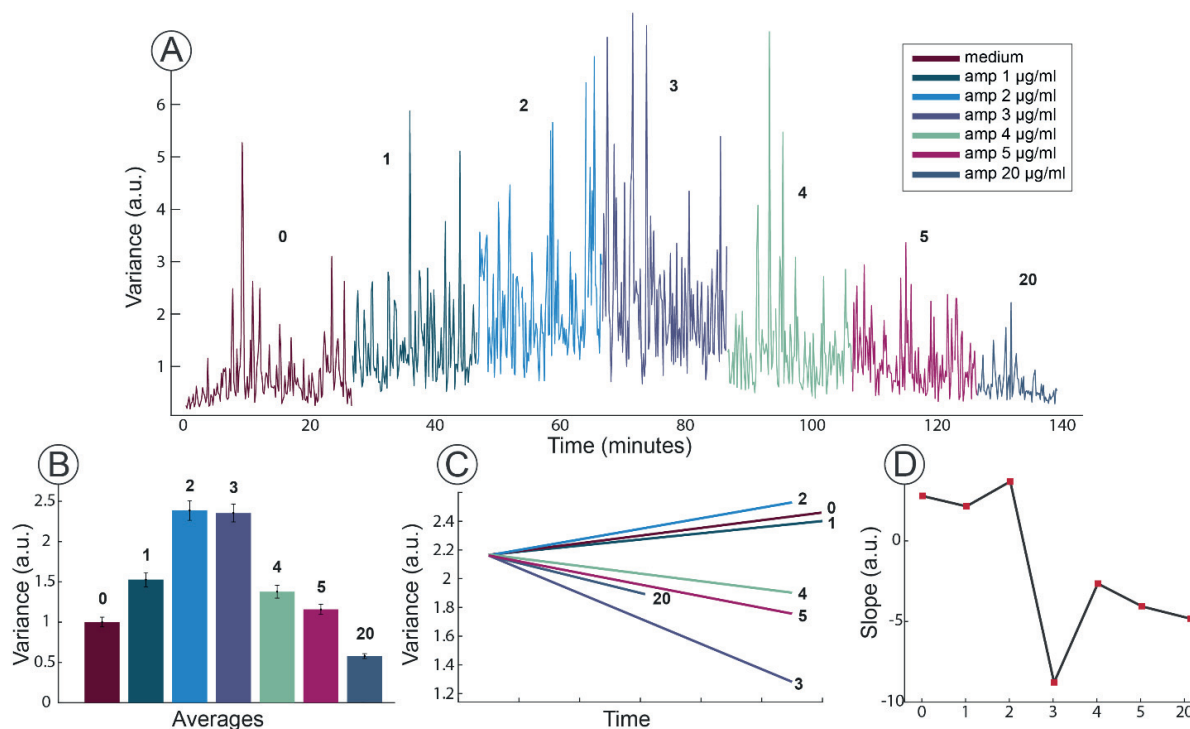


**Figure 3.12** MIC and MBC assessment using nanomotion. **Panel A:** The evolution of variance throughout the addition of increasing concentration of ampicillin to the attached *E. coli* c1895 bacteria. Each color represents a single ampicillin concentration. **Panel B:** averages of the variance presented in the panel A, for each concentration. **Panel C:** Time-kill curves as linear fits to the variance line plot from panel A. **Panel D:** Slopes of time-kill curves for each antibiotic concentration.

**Figure 3.12, Panel A** shows the evolution of variance throughout the entire experiment, with all the concentrations tested. It is evident that the signal – the cantilever oscillatory movement, is increasing with no antibiotic, and with sub-MIC concentrations. Once the conventionally-determined MIC is reached, the following concentrations of ampicillin create a sharp decrease in variance. The values drop only after the injection of the highest (20 µg/ml) concentration of the drug, reported as the MBC. To better visualize the phenomenon, **Panel B** shows the averages of the values from the previous panel. Variance increase up to the MIC value and subsequent decrease are evident from the bar chart. However, the presented bar plot does not show the trend that each individual drug concentration creates. Therefore, a set of linear fits of the variance evolution is proposed on the **Panel C**. These lines resemble time-kill curves, plots of cell number against time for different antibiotic concentrations. Here, instead of the number of colony forming units, we have variance against time. Linear fit is applied to a window of 10 variance points and the first coefficients (slopes) of the fit are shown on the **Panel D**. Considering that sub-MIC concentrations will not affect bacterial metabolic activity, time-kill curves at those conditions are expected to have a positive slope. Indeed, 0, 1, and 2 µg/ml

ampicillin show up as growing lines, while all the other curves descend. The above-MIC value (3 µg/ml) has the largest negative slope, while in higher concentrations, slope steadily decreases. Consulting all these types of data representations makes it much easier to pin-point the important parameters for determining the true MIC and MBC values. Visually clear and quantitative method needs to be optimized for any automatization and sophisticated algorithm.

Lastly, not just the antibiotic-killing of bacteria was the focus of this work. Another method of endangering bacterial viability and testing the kinetics of its action is the use of bacteriophages. These bacterial viruses are sophisticated machinery that infect the target cell, inject their DNA, which, if incorporated, creates other virus particle parts, assembles them and eventually, cell lysis happens with explosion of new virus particles. Calcium ions in the solution help phage adsorption to the bacterial surface, increasing the speed of new particle generation and producing more yield (238). In the experiment depicted in **Figure 3.13**, where bars represent 15-minute variance averages, it is evident that the addition of phage particles and calcium ions increases the variance at first. However, after a certain period of time, the signal sharply decreases and reduces to the noise level. The interpretation of such behavior could lie in the phage infection process, where first a dynamic change of bacterial metabolic and membrane activity happens, and then the release of new particles that follows the cell bursting and lysis.

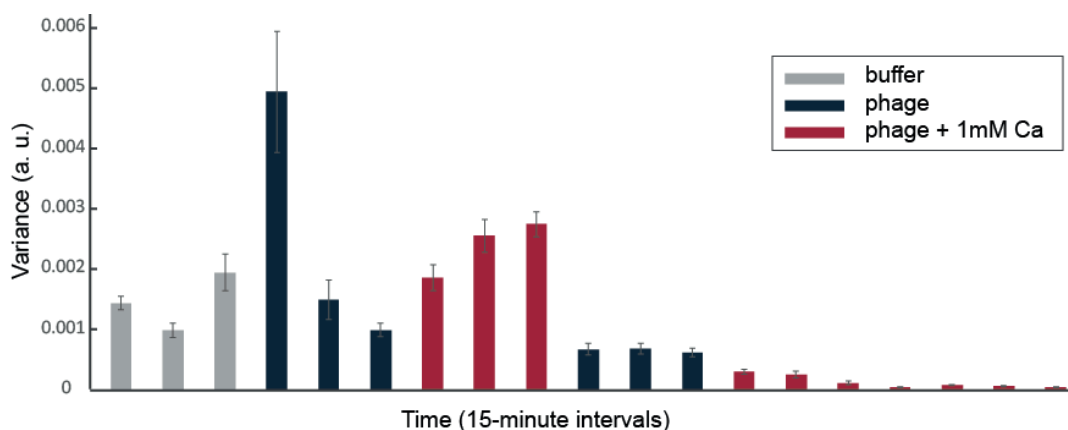


**Figure 3.13** Nanomotion investigation of bacteriophage infection process. The addition of phage particles with calcium ions at first increases the oscillation signal, then reduces it to basal levels.

### 3.2.4 Conclusion

The very first experiments we performed using nanomotion sensors involved the study of the response of bacteria to antibiotics. It is almost certain that in the near future antibiotics will lose the ability to kill pathogenic bacteria due to the insurgence of resistances, a natural process in which bacteria evolve to respond to the drug's selective pressure. The fast rise of new resistant strains is one of the great medical challenges of our time. Since new antibiotics require several years to be developed and tested there is an urgent need for new diagnostic tools to test new antibacterial substances and to rapidly track the development of resistance. With this in mind, we demonstrated

the ability of the nanomotion technique to test bacterial response to antibiotics within the time frame of 1 hour.

In this section, optimization of the cantilever functionalization and the sample attachment procedures have been presented. Images showing the attachment yield and the viability of the attached sample gave insight into the best practices and protocols to use. A sample of the signal is presented, where a clear distinction is made among a bare cantilever, the one with living bacteria attached and with bacteria exposed to an antibiotic. As mentioned, deflection signal is not always the preferred choice of representation, especially if the changes in the signal are not very evident. Therefore, other signal representation methods are also shown, such as: the variance evolution, variance averages, and boxplots. Another useful representation of the change in variance through time is a so-called time-kill curve. Being a linear fit of variance evolution chunks, a more reasonable name would be time-kill line. Regardless, the slope of those curves gives valuable information about the direction of the variance change.

It has been shown that nanomotion experiments can be performed using several concentrations of the drug in order to test MIC and MBC values for a particular bacterium. It may provide information on its response to subjected doses and reflect whether the conditions are favorable or not. In comparison with the conventional MIC and MBC testing, results suggest that the nanomotion technique could provide precise evaluations that are obtained much faster than conventional test itself. Furthermore, not only bacteria-antibiotic systems can be tested. Other biologically interesting and important phenomena may be explored using this technique. An example from this section was the infection process of *E. coli* by bacteriophage, but the applications span vastly, which shall be described in more detail in the following chapters.

### 3.3 Antibiotic susceptibility testing against agents of bloodstream infections

*This section contains published work:*

Stupar, P., Opota, O., Longo, G., Prod'hom, G., Dietler, G., Greub, G. and Kasas, S., 2017. **Nanomechanical sensor applied to blood culture pellets: a fast approach to determine the antibiotic susceptibility against agents of bloodstream infections.** *Clinical Microbiology and Infection*, 23(6), pp.400-405.

#### 3.3.1 Introduction

Rapid acquisition of a blood culture pellet, coupled with a subculture-independent technique allowing phenotypic determination of the antibiotic susceptibility, could significantly reduce the time to results, greatly benefitting patient care and reducing cost of treatment, especially empiric treatments with broad-range antibiotics. A reduction of this timeline to less than one working day would have a very high medical value, reducing morbidity and mortality and the overall costs for the healthcare systems (239). Furthermore, it would allow achieving faster treatments tailored to the patient, which would be more effective, better tolerated, with a reduced negative impact on beneficial bacteria. To achieve this, we have proposed a new technique to rapidly characterize bacterial resistance to antibiotics (213,240,241). This technique is based on the use of nanomechanical sensors (52,242,243) that oscillate if the attached bacteria are metabolically active. Oscillation detection is obtained using an optical lever method, where a laser beam is reflected off the cantilever and directed towards a detector (**Figure 3.14**). Even among other nanomechanical sensor systems, this technique stands out as one of the most sensitive and fast in the study of bacterial growth and antibiotic susceptibility (244–249). Nanomotion Antimicrobial Susceptibility Testing (Nanomotion-AST) has several advantages compared to conventional culture-based systems commonly used in microbiology. For instance, it does not rely on bacterial growth; hence it is not negatively impacted by the replication time of the bacteria, and this reduces the characterization of the microorganism's resistance to minutes, compared to hours or days needed by conventional AST systems (250,251). Furthermore, Nanomotion-AST requires a low number of bacteria (approximately  $10^2$  bacteria) to obtain a measurable signal (241). Overall, the speed and sensitivity of this technique allows an unprecedented insight on the bacterial response to environmental, chemical or physical stimuli.

Recently, an ammonium-chloride-based blood culture pellet preparation test has been developed, allowing to obtain a high bacterial amount of an isolated strain for rapid downstream characterization (252). This work demonstrates the feasibility of the combination of bacterial pellets prepared from positive blood cultures that was previously described (253) and nanomotion for rapid AST on *E. coli*, the most frequently recovered bacterial pathogen (254). The findings of this study suggest that these two innovative techniques might serve as a versatile system, delivering a vast impact in the microbiological field. Their combination would ensure a significant reduction of the time needed to characterize bacteria from positive blood cultures up to a complete analysis in less than 3 hours.

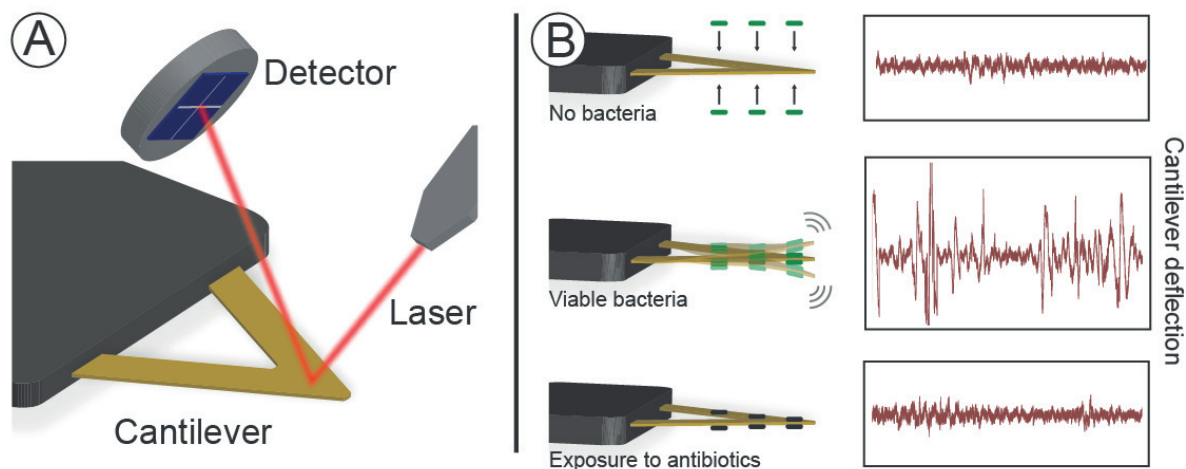


**Figure 3.14** Outline of the experimental setup and description of the experiments. **Panel A:** Schematics of a nanomotion detector setup with the cantilever sensor - a laser beam is focused on the surface of the sensor and the reflection is used to monitor the movements of the cantilever. **Panel B:** Representation of a typical nanomotion susceptibility test. When the bacteria are not attached to the sensor, the fluctuations are driven only by thermal motion and are low. After the attachment of live bacteria, the fluctuations are linked to their metabolic activity and are high. Finally, after exposure to a bactericidal drug, the bacteria are non-viable and the fluctuations return to low levels.

### 3.3.2 Materials and Methods

**Reagents and antibiotics.** All chemicals, phosphate buffered saline (PBS, pH 7.4), Luria broth (LB), glutaraldehyde, paraformaldehyde, and the antibiotics ampicillin, ciprofloxacin, ceftriaxone and ceftioxin, all with analytical grade, were supplied by Sigma-Aldrich (US).

**Bacterial preparation and isolation from blood cultures.** Bacterial strains, resistant and susceptible strains of *Escherichia coli* were either ATCC strains or clinical isolates of the bacterial repository of the Institute of Microbiology of the Lausanne University Hospital (Lausanne, CH). The susceptible *E. coli* strain used for this study was ATCC 25922 (MIC for ceftriaxone, ciprofloxacin and ampicillin are 0.06, 0.008 and 8 µg/ml, respectively). As resistant *E. coli* strain, we used a clinical isolate characterised using the Vitek device and E-test (BioMérieux SA, FR) methods, showing MIC for ceftriaxone, ciprofloxacin and ampicillin  $\geq 64$ ,  $\geq 4$  and  $\geq 256$  µg/ml, respectively. Working concentrations of the antibiotics were chosen according to the EUCAST interpretation guidelines, to allow discrimination between resistant and susceptible ([www.eucast.org](http://www.eucast.org)).

Bacteria were inoculated together with human blood in anaerobic culture bottles (BACTEC™ Lytic/10 Anaerobic/F Medium, Becton Dickinson, US), recovered from the transfusion centre of our hospital, in BD blood vials, and processed by a Bactec FX automated blood culture system (Becton Dickinson, US). This system automatically detects the growth of microorganisms by detecting pH change due to CO<sub>2</sub> production. When detected positive, blood vials were processed as previously described in order to rapidly obtain a bacterial pellet; the method is described in detail elsewhere (253). Briefly, 5 ml of the medium from a positive blood culture was mixed with 40 ml sterile water; after centrifugation (1000 g for 10 min) the supernatant was removed, and the remaining blood cells

were lysed by adding 1 ml ammonium chloride (0.15 M  $\text{NH}_4\text{Cl}$ , 1 mM  $\text{KHCO}_3$ , pH 7.31) to the bacterial pellet followed by a second centrifugation step (140 g for 10 min) to discard the lysed red blood cells.

Overall, this preparation protocol lasts less than one hour and ensures an enriched bacterial pellet to be characterised. This bacterial pellet was finally re-suspended in buffer and tagged with a code, in order to ensure a blind susceptibility test with the nanomotion sensor.

**Nanomotion-AST.** To perform the susceptibility tests, we have employed both, a homemade, small and portable prototype device, as well as a commercial JPK Nanowizard III microscope (JPK Instruments, DE) equipped with an Axiovert inverted optical microscope (Zeiss, DE). The sensors we used in these experiments were commercial atomic force microscope cantilevers (NP-O10, Bruker, US). Sensor deflections were measured using the conventional laser-based system common to most atomic force microscopes, which ensures a reliable determination of the movements of the sensor with a sensitivity of less than 0.1 nm. We equipped both instruments with a custom analysis chamber, which was made of polydimethylsiloxane (PDMS) and which allows performing experiments in liquid while changing the medium with very little disturbance (220,224).

The sensors were preliminarily functionalised with 0.5% glutaraldehyde for 7 minutes, in order to ensure a firm attachment of bacteria for the time frame of the characterization experiments and were subsequently washed and dried, as previously reported (241). Once prepared, the treated sensors were readily used to attach the bacteria. We incubated them with 10  $\mu\text{l}$  of the concentrated bacterial suspension for 30 minutes. Due to high turbidity, the working concentration for optimal attachment was determined by dilution test, namely, re-suspending 10  $\mu\text{l}$  of the suspension into 1 ml of PBS gave  $\text{OD}_{600}$  of 0.4 – 0.6, which indicated that the suspension was concentrated enough. Next, we gently washed the sensors in growth medium and introduced them in the analysis chamber for characterization. This procedure ensured that the sensor was covered with hundreds of viable and firmly attached bacteria. The chamber was then filled with LB to ensure the viability of the bacteria and to enhance the effectiveness of some antibiotics (255,256). After 5 minutes of stabilization of the entire system, we started the Nanomotion-AST measurements.

We recorded the dynamic fluctuations of the sensor in different conditions and we measured the fluctuations for at least 20 minutes, choosing an acquisition rate of 20 kHz. The first step was to obtain the signal while the attached bacteria were in LB medium. Then, we substituted the medium in the analysis chamber with the same one but containing the chosen antibiotic and continued the recording of the sensor's fluctuations. In this case, we measured for longer time (approximately 60 minutes) to ensure that the antibiotic effect was stable and that the bacteria had completed their response to the exposure of the drugs. In all cases, we collected time-dependent fluctuations of the sensor. The signal was flattened, and then filtered using a moving average filter. To evaluate the effective variation in the amplitude of the sensor's movements, the deflection curves were statistically analysed by calculating their variance. If applied in a windowed manner (of 10 seconds), this parameter allows following the evolution of the bacterial dynamics throughout each experiment. At this stage, obvious outliers are removed as few occurrences of non-biological signal are inevitable (accidental contact with the device). "Change" numbers have been calculated by averaging variance

values. For signal acquisition, we developed a software based on LabVIEW (version 2013, National Instruments), and for all signal processing purposes, the software was developed in a commercial MATLAB package (version 8.6, MathWorks).

We previously demonstrated that the reduction of the signal is synonymous with susceptibility to the antibiotic tested (240). We used this readout to categorize susceptible and resistant strains. In order to test the combination of our two methods: the rapid concentration and purification of bacteria from artificially inoculated positive blood cultures and the nanomotion-AST, we performed analyses on *E. coli* as the main blood infection pathogen, including both susceptible and resistant strains for the selected antibiotics. Susceptibility of *E. coli* was tested with ciprofloxacin, ampicillin, and ceftriaxone.

### 3.3.3 Results

The results presented in the **Figure 3.15 (A - C)** correspond to different blind experiments performed on *E. coli* exposed to ampicillin (16 µg/ml), ceftriaxone (2 µg/ml) and ciprofloxacin (2 µg/ml), respectively. **Figure 3.15** shows typical results from these experiments, presenting cantilever oscillations as the evolution of variance. In all cases, the attached bacteria induced measurable fluctuations of the sensor, that remained stable and indicated the sustained viability of the microbes throughout the experiments. Upon injection of the antibiotic-enriched medium, the fluctuations changed quite rapidly. Different drug-bacteria combination yielded a change of the signal at different time points. Exposure of susceptible strains to ampicillin produced sharp reduction in the fluctuations 20 minutes after the drug injection, while ceftriaxone and ciprofloxacin required 50 and 40 minutes to produce a stable response.

These experiments were all performed in a double blind type protocol, in order to ensure that results would not be influenced by the experimenter's knowledge of the bacterial characterization. The criteria used for classification were based on variance of the sensor's movement (**Figures 3.15 A1, 2B1, 2C1**), looking if a reduction occurred or not. When the blind labels were revealed, the positive identification rate was higher than 94% (16 out of 17 correct assessments). Results are summarised in **table 1**. Once the labels were known, we quantified the results by calculating the change value (%). The value represents the change of variance of the signal occurring when the nourishing medium is replaced by the one containing the antibiotic. Calculation points were taken 40, 50 and 20 minutes after the exposure to ciprofloxacin, ceftriaxone and ampicillin, respectively.

Overall, when testing resistant strains, we observed that the variance can surge to very high values (i.e. 190% of the initial signal before the antibiotic), or drop subtly (i.e. 80%), indicating the variability of bacterial response within the same bacterium-antibiotic conditions. In cases of susceptible strains, the reduction of the fluctuations after the antibiotic exposure was larger (to 10%, 24% or 27%).

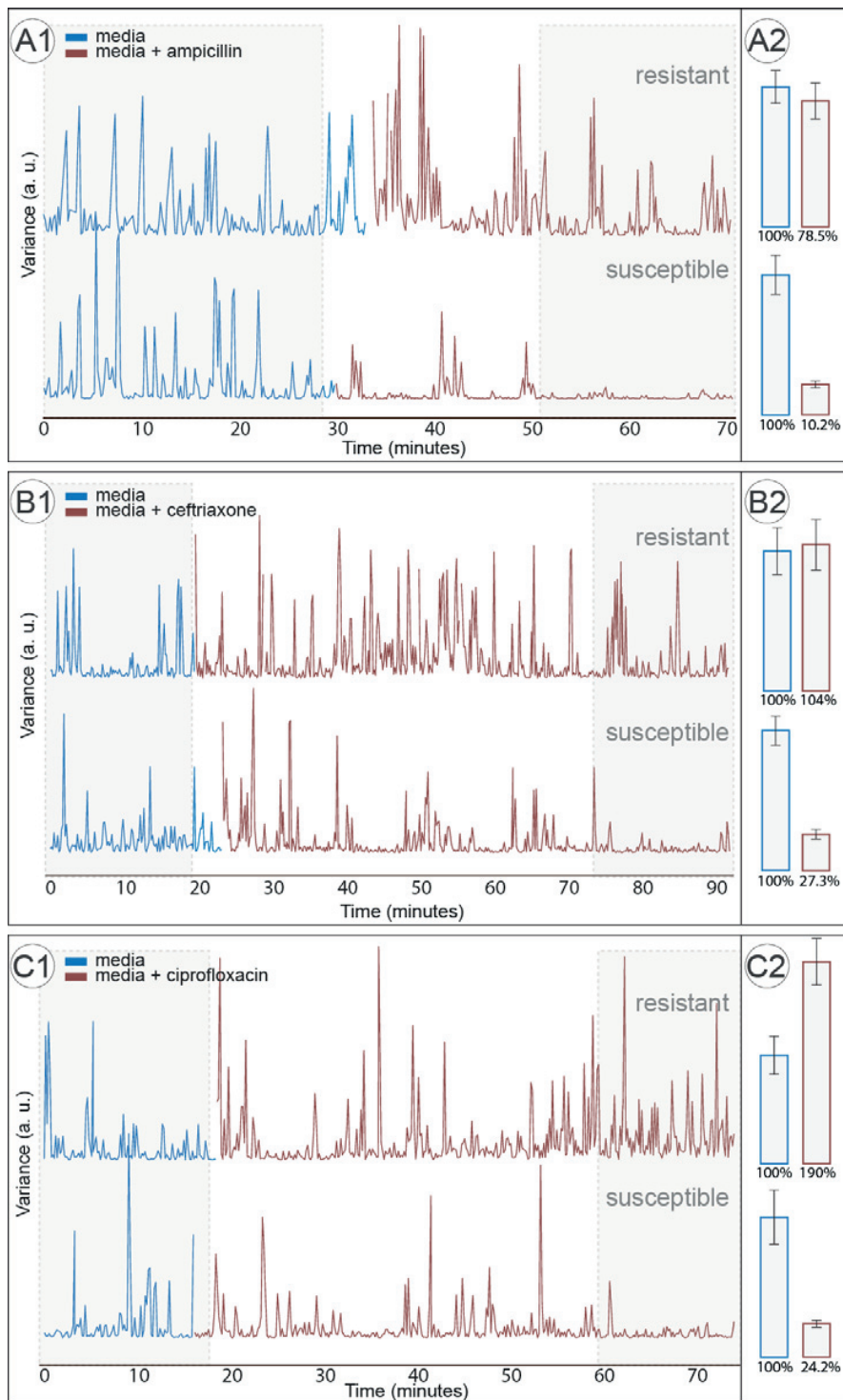


**Figure 3.15** Variance evolution throughout the experiments – effect of ampicillin (A), ceftriaxone (B) and ciprofloxacin (C) on *E. coli*. Typical examples of the resistant *E. coli* strain (top) and the susceptible strain (bottom) are presented. Blue colour shows the variance of sensor’s movement while only nourishing media is present in the system. The presence of antibiotic and the corresponding variance trend is shown in dark red. The area shaded in grey is used for averaging and presenting as change (in %) on the second panels of the figure.



**Table 3.1** Summary of the nanomotion-AST measurements and their evaluation against a conventional technique. 16 tests matched the correct response. \* Change in percentage represents how much of a signal is present after the drug injection, compared to the measurement in LB. The calculations were done after 40, 50 and 20 minutes of exposure to ciprofloxacin, ceftriaxone and ampicillin, respectively. \*\* N/A – not applicable, as the measurement failed due to a technical issue.

Species	Sample ID	Antibiotic	Concentration (µg/ml)	Nanomotion-AST result (before defining the threshold)	Correct (YES or NO)	Change* (%)
<i>Escherichia coli</i>	101	Ciprofloxacin	2	Resistant	YES	184
	102	Ciprofloxacin	2	Susceptible	YES	49
	103	Ciprofloxacin	2	Resistant	YES	190
	104	Ciprofloxacin	2	Susceptible	YES	28
	105	Ciprofloxacin	2	Resistant	YES	88
	106	Ciprofloxacin	2	Susceptible	YES	24
	100	Ceftriaxone	2	Susceptible	YES	27
	200	Ceftriaxone	2	Susceptible	YES	32
	107	Ceftriaxone	2	Resistant	YES	104
	207	Ceftriaxone	2	Susceptible	NO	80
	108	Ceftriaxone	2	Resistant	YES	86
	208	Ceftriaxone	2	Resistant	YES	97
	110	Ampicillin	16	Susceptible	YES	18
	210	Ampicillin	16	Resistant	YES	99
	111	Ampicillin	16	N/A**	N/A**	N/A**
	211	Ampicillin	16	Susceptible	YES	22
	112	Ampicillin	16	Resistant	YES	78
212	Ampicillin	16	Susceptible	YES	10	

In **Figure 3.16** we plotted the overall variance change values presented in **Table 3.2**, for each tested sample. The upper limit in variance changes considering susceptible cells is in the sample labelled 102, being 49%. Within the resistant bacteria dataset, the lower limit shows up in sample 112, and it is 78%. Based on these experiments, we defined a threshold in change of variance, allowing the classification between susceptible and resistant strains (**Figure 3.16**). A value of 60%, which is the upper boundary determined by the standard error of the uppermost value of susceptible samples, would correctly discriminate the susceptible and resistant strains, including the resistant sample 207. The latter was initially misclassified as susceptible based on the qualitative analysis of the variance graph.

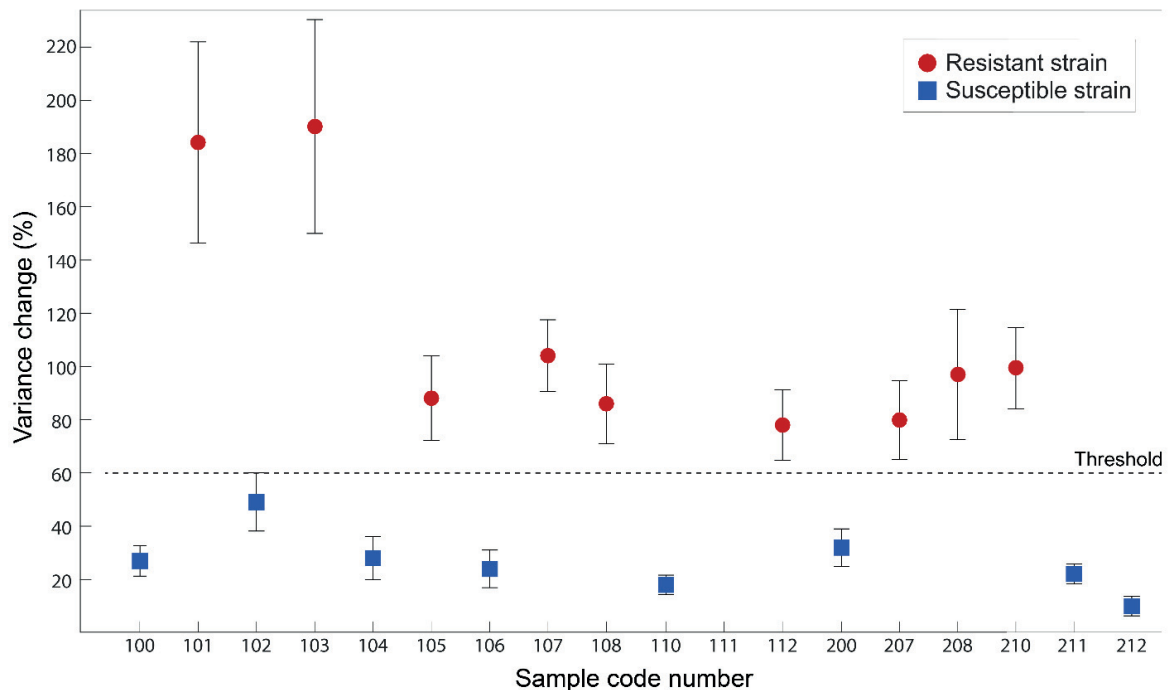


**Figure 3.16** Plot of change values from table 1, representing the percentage change of oscillatory movements before and after the addition of drugs. Susceptible strains fall below 60%, meaning that the addition of drug is reducing the oscillations for more than 40%. However, the resistant strains produced either unchanged movement (100%), increased movement, or movement with subtle change (lower limit around 80%). Therefore, a threshold value of 60% could be defined as a marker for distinguishing susceptible from resistant strains.

### 3.3.4 Conclusion

In this work, we have shown an innovative protocol as a combination of the ammonium chloride centrifugation technique to concentrate bacteria from positive blood cultures rapidly, and the fast and sensitive Nanomotion-AST. To determine the overall time needed to perform a complete characterization, we need to consider the purification of bacteria from the positive blood culture (time to obtain a bacterial pellet) and the time needed to perform the Nanomotion-AST. In all our experiments, the elapsed time, from determination of the positive blood culture to the end of the susceptibility test, was less than 3 hours. These results highlight the importance of combining the two innovative and rapid techniques and the potential of their application to the clinical setting.

Nanomotion-AST is one of the many important applications of the nanomechanical sensor. Such a sensitive system can be important in microbiology in a variety of additional applications. For instance, for slow growing bacteria such as mycobacteria, it may prove to be pivotal. Furthermore, the nanomotion-AST analysis can characterize bacterial species, as well as many other biological systems, with versatility and speed that are unachievable using the currently available methods (216,257). This might allow extracting more information on the interaction between bacteria and antibiotics: not only if an antibiotic has had an effect, but what kind of effect and the dynamics of the bacterial response.

The presented work currently stands as a proof of principle, and needs to be extended with **(i)** a higher biodiversity of bacterial species, including all 20 species most commonly recovered from blood, **(ii)** a larger range of antibiotics, and **(iii)** a variety of strains directly recovered from patient blood, including strains with intermediate antibiotic resistance. Specifically, our data suggest that susceptible and resistant strains could be correctly categorized using a specific threshold for change in variance before and after the exposure to a defined antibiotic. In the future, developing a highly parallelised and automated nanomechanical detection system could allow simultaneous rapid AST for various antibiotics generally used to treat a given isolated species. By multiplying the number of antibiotic concentrations tested it would be possible to determine precise MIC on bacterial pellets obtained from blood culture, as previously shown from agar-grown bacteria (240). Indeed, MIC is important for managing specific infections (e.g., *Streptococcus pneumoniae* and beta-lactams).

Altogether, the highly encouraging results presented in this work demonstrate the feasibility of the nanomotion-AST system coupled to blood culture pellet and efforts are under way to develop and accommodate this technique for clinical routine diagnostic laboratories. Future developments and studies might address the application of nanomotion-AST on bacteria recovered directly from samples if the bacterial load is sufficient or in combination with methods for the recovery of low numbers of bacteria in paucibacillary clinical samples. Such a procedure would have a large impact on the medical practice, changing the methodological approaches currently in use to face the health threats posed by bacterial infections, and particularly those arising from the increasing multi-drug resistances.

### 3.4 Antibiotic susceptibility testing against slow-growing bacteria

*This section contains published work:*

María Ines Villalba‡, Petar Stupar‡, Wojciech Chomicki, Massimiliano Bertacchi, Giovanni Dietler, Laura Arnal, María Elena Vela, Osvaldo Yantorno\*, Sandor Kasas\*, 2017. **Nanomotion Detection Method for Testing Antibiotic Resistance and Susceptibility of Slow-growing Bacteria**. Small.

‡ Authors contributed equally

#### 3.4.1 Introduction

Infectious diseases are one of the most important causes of human mortality worldwide. Therefore, rapid detection and identification of microbial pathogens are mandatory in order to treat patients appropriately. It is important to realize that antimicrobial susceptibility testing (AST) should be carried out for all pathogens recovered from an infectious process, since therapeutic measures cannot be consistently predicted based exclusively on the knowledge of the identity of the infecting microorganisms. Consequently, it is evident that physicians require rapid and reliable AST that allows them to make a fast decision and, as a result, improve patient outcomes and reduce healthcare-associated costs. A number of laboratory methods are currently available to characterize the in vitro susceptibility of microorganisms against antibiotics. Current culture-based methods include disk diffusion methods, antimicrobial gradient diffusion tests and broth dilution techniques as those recommended by the Clinical and Laboratory Standards Institute (CLSI) or by the European Committee on Antimicrobial Susceptibility Testing (EUCAST) (258,259). However, results obtained by these techniques are time consuming, needing at least 20 hours, or up to a month in case of tuberculosis. During the last decades, automated and semi-automated devices, such as: Becton Dickinson Phoenix, Siemens MicroScan Walk Away or Vitek 2, have been extensively used at hospital level (260–262). Nevertheless, they are currently used for the AST determination of fast growing organisms, have a high cost and, in addition, are not available for the full spectrum of bacteria.

Although it has been reported that antibiotics exert specific effects on growing microorganisms, few studies have attempted to quantify the dynamic changes induced by antibiotics in microbial growth patterns (263). We previously reported that atomic force microscope (AFM) based nanomotion sensors can be used to characterize metabolic activity of living bacteria within minutes, needing only  $10^2$  bacteria to have a measurable signal (**Figure 3.14**) (240,241,257).

Furthermore, we have described the use of such a device to determine the Minimal Inhibitory Concentration (MIC) and Minimal Bactericidal Concentration (MBC) of ampicillin, and the effects of kanamycin, ciprofloxacin and caspofungin, for different kinds of fast growing organisms, such as *Escherichia coli*, *Staphylococcus aureus* and *Candida albicans* (240,257). Nevertheless, it has not yet been determined whether this device is sensitive enough to detect cantilever fluctuations produced by slow growing bacteria, when incubated in culture media and in the presence of antibiotics. In this work, we explored the nanomotion sensor's ability to determine the MIC and MBC of macrolides antibiotics in slow growing bacteria (SGB).

We have previously assessed the growth kinetic of *Bordetella pertussis*, the etiological agent of whooping cough or pertussis, in both Stainer Scholte (SS) liquid medium as planktonic cells, and adhered to surfaces as sessile populations forming biofilm (264,265). *B. pertussis* can adhere and live attached to different surfaces (polypropylene, glass) where it shows a specific growth rate ( $\mu$ ) of 0.03 h<sup>-1</sup> (265). This growth rate is very slow compared to the one of *E. coli* (MG1655), which displayed a  $\mu$  value of 1.09 h<sup>-1</sup>, growing on polyethylene terephthalate (PET) surfaces (266). Accordingly, we decided to use *B. pertussis* as a representative organism of SGB in order to assess the impact of different antibiotic concentrations on its metabolic activity and to evaluate the time nanomotion detection requires to sense susceptibility to different antibiotics. Macrolides such as erythromycin or clarithromycin are regarded as antibiotics of choice in the treatment of pertussis. Co-trimoxazole (1:19 Trimethoprim /sulfamethoxazole) is often cited as an alternative where macrolides cannot be tolerated (267). In this work, we have focused on bacteriostatic antibiotics, for which bacteriostatic activity has been defined as a MBC/MIC ratio > 4 (268). Finally, the results obtained with the nanomotion sensor for AST analysis were compared with the ones coming from traditional techniques as broth dilution method (258).

#### 3.4.2 Materials and Methods

*B. pertussis* Tohama I strain (Collection of Institute Pasteur, Paris, France -CIP 8132-); BPSM, a streptomycin resistant (Smr) strain derivative from *B. pertussis* Tohama I(269); and *B. pertussis* clinical strain (Bp2723) collected at La Plata Children's Hospital (Hospital Sor Maria Ludovica, La Plata, Argentina), were employed throughout this study. The antibiotics used in the experiments were: erythromycin (Sigma- E6376); clarithromycin (Sigma A3487), trimethoprim-sulfamethoxazole, also known as co-trimoxazole, 1:19 (Sigma T7883 and Sigma S7507, respectively) [TMP-SMX] and ampicillin (Sigma- A0166). In the case of BPSM strain, streptomycin (Sigma S6501) was employed. SS liquid medium was used to culture *B. pertussis* strains (265,266). Bacteria were deposited onto triangular silicon nitride (Si<sub>3</sub>Ni<sub>4</sub>) cantilevers with spring constants typically 0.06 or 0.12 N/m. Before deposition, in order to promote bacterial attachment, the cantilevers were incubated with 10  $\mu$ L of 0.5% glutaraldehyde for 10 min, rinsed with ultrapure water, dried, and then incubated with 10  $\mu$ L of a high-density bacterial suspension (OD<sub>595</sub>: 0.5 with 100  $\mu$ l of suspension diluted in 1mL of phosphate buffer saline). The cantilevers with adhered bacteria were inserted into the analysis chamber of a home-made nanomotion device to analyze their vibrational response in growth medium and upon exposure to antibiotics (217). For each tested condition, 40 minutes measurements of the cantilever oscillations were done at room temperature. Variance of the deflection signal was calculated to define the variation in the amplitude of the sensor's movements. The evident outliers were removed in cases of inevitable non-biological signal. The information was recorded using custom software optimized for this application to register the cantilevers movement, and the Matlab R2013b™ software was employed to analyze the data.

#### 3.4.3 Results

The standard method of broth dilution was used to evaluate the MIC and MBC values for *B. pertussis* Tohama I reference strain and the clinical strain Bp2723 grown as planktonic cells. We found that the MIC values of planktonic cells for erythromycin and clarithromycin were between 0.06-0.12

$\mu\text{g/mL}$  and the MBC between 2.5-5.0  $\mu\text{g/mL}$ . The respective MBC/MIC ratios were greater than 4 for erythromycin, clarithromycin and co-trimoxazole. Thus, these antimicrobials could be considered as bacteriostatic.<sup>[14]</sup> We found that the MIC value for each antibiotic tested was the same for both the clinical strain and the reference strain, grown under planktonic condition. Similar results were found for the MBC values of the two strains. Tohama I strain showed MIC and MBC values of 3 and 10  $\mu\text{g/mL}$  of streptomycin, respectively, while BPSM strain survived the exposure to 200  $\mu\text{g/mL}$  of the same drug. In the first set of experiments, nanomotion measurements were done on Bp Tohama I reference strain in SS liquid media. The aim of the measurement was to assess the survivability of bacteria on a cantilever. Therefore, the cantilever oscillations were monitored during 13h of incubation under non-stressing conditions. After six hours from the start of the experiment, the oscillations continuously increased with time. This phenomenon could be associated with the beginning of replication of the adhered cells, since they are entering the exponential phase of growth, as we have previously reported for *B. pertussis* biofilm growth (264,265). **Figure 3.17** shows the variance of the cantilever oscillations during the time course of the experiment. In further experiments, we explored cantilever oscillations after the antibiotic exposure.

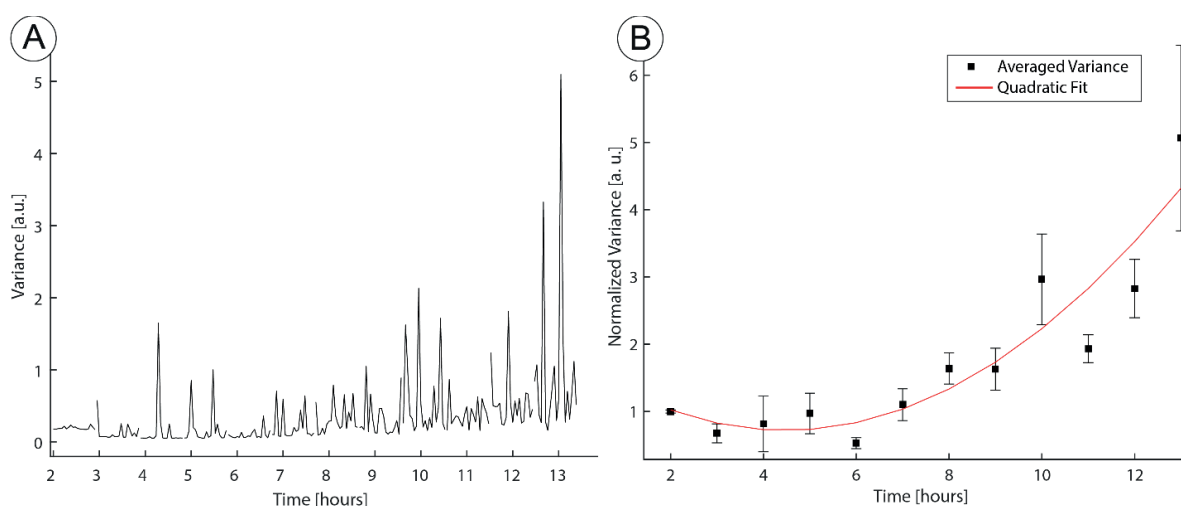


**Figure 3.17** Variance of the cantilever oscillation signal in time. *B. pertussis* cells were attached to the cantilever and tracked during 13h of incubation in SS media. **Panel A:** Line plot of the variance against time. **Panel B:** Variance averages of 1h window better reflect the increase in oscillations throughout time.

We chose clarithromycin's and erythromycin's MBC values previously determined by the broth dilution method to test the outcome on metabolic activity of *B. pertussis* Tohama I strain during three hours of incubation. Reduction of the sensor's oscillation amplitudes and of the corresponding variance took place after the antibiotic exposure (**Figure 3.18**).

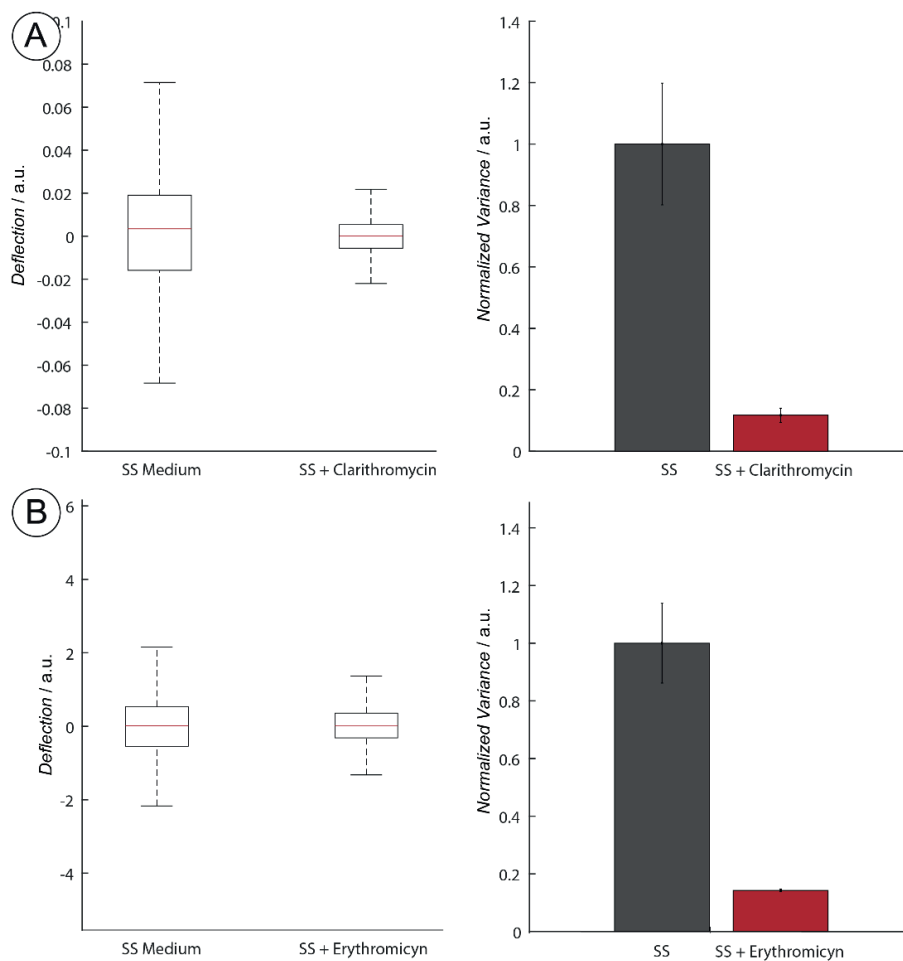


**Figure 3.18 Panel A:** Boxplots of the cantilever oscillation movement with *B. pertussis* cells adhered and incubated in SS medium with and without the addition of clarithromycin (5 $\mu$ g/mL). **Panel B:** Normalized variance averages across 15 minutes of incubation time (15 minute averages were taken after 40 minutes of incubation in the medium or antibiotic).

We have observed that 40 min incubation time is sufficient to register the effect of the clarithromycin and erythromycin, and less than 20 min for ampicillin. This result is in agreement with those previously reported with this device but using fast growing bacteria (217). In addition, we monitored the cantilever oscillations when *B. pertussis* BPSM, a Smr strain resistant to streptomycin, was incubated in presence and absence of specific antibiotics. The variance was higher for BPSM in SS medium with the addition of streptomycin at 50  $\mu$ g/mL, indicating that the metabolic activity was not reduced. The variance of the signal decreased significantly when the bacteria were exposed to SS medium with co-trimoxazole, which suggests a drop in metabolic activity in such environment (Figure 3.19).

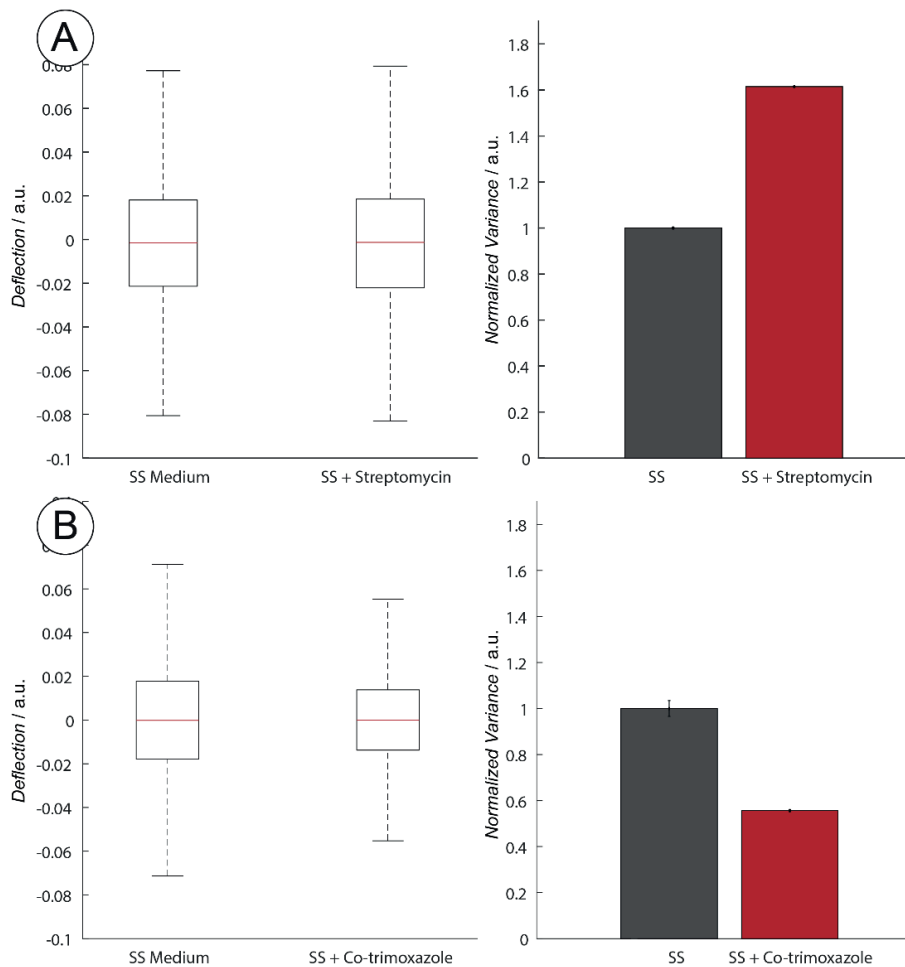


**Figure 3.19** Boxplots of cantilever movement with BPSM (streptomycin resistant) strain adhered and their corresponding variance averages. **Panel A:** After the introduction of streptomycin, boxplots suggest higher oscillation amplitudes, and variance bars confirm an increase in the movement. **Panel B:** Signal comparison between the exposure to medium and co-trimoxazole. Boxplots show a decrease in oscillation amplitudes, and variance bars support the same conclusion. The responses are connected with resistance (A) and susceptibility (B) of bacteria to the applied antibiotics. Variance bars are 15 min averages, taken after 40 min of incubation in the medium or the antibiotic).

To monitor the effect of different antibiotic concentrations on the reference strains and the clinical isolate, we incubated each strain in SS medium alone and in the presence of increased antibiotic concentrations from 0.002  $\mu\text{g}/\text{mL}$  to 10.0  $\mu\text{g}/\text{mL}$ . Macrolide clarithromycin and  $\beta$ -lactam ampicillin were employed for this set of experiments. The used concentration range includes MIC and MBC values. Surprisingly, we registered that the larger variance values correspond to the MIC in cases of clarithromycin. The metabolic activity of *B. pertussis* cells adhered to the cantilever increased when it was exposed to antibiotic concentrations lower than MIC in all cases. Culture experiments suggest high viability of the attached cells at MIC values. After reaching MIC, the variance values drastically decreased as the concentration of antibiotic in the culture medium was increased. This behavior was observed until the antibiotic concentration reached MBC value. Above MBC point, the variance of the



oscillation signal (which reflects the cellular metabolic activity) dropped to the lowest values measured in the experiment (**Figure 3.20**). Finally, we compared the MIC and MBC concentrations obtained with the device with the ones obtained by the conventional method and we found similarities between these two methodologies using the clinical strain and *B. pertussis* reference strain.

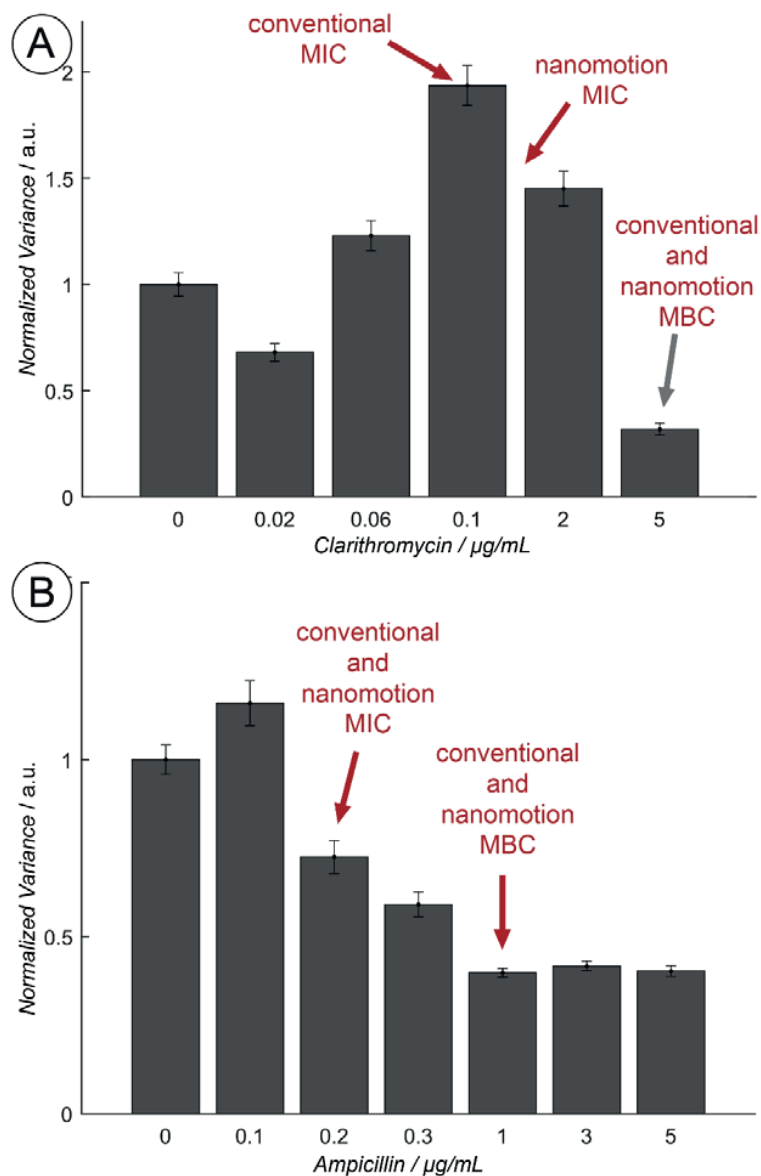


**Figure 3.20** Normalized variance of the cantilever movement obtained when *B. pertussis* was exposed to different concentrations of clarithromycin (**Panel A**) and ampicillin (**Panel B**). MIC and MBC values obtained by the conventional methods in parallel are marked in red. Results suggest a potential application of such a method for obtaining MIC and MBC values in a much shorter time frame. Each bar corresponds to 30-minute average. Considering that clarithromycin and erythromycin need at least 40 minutes of exposure for an effect to take place, the variance average is shown to be higher, whereas in case of ampicillin, the MIC action takes place within the variance average and the resulting value at MIC is lower than on the condition without the antibiotic.

#### 3.4.4 Conclusion

A first set of experiments measuring living *B. pertussis* cells on a cantilever during a prolonged period of time confirm the sensitivity of the device to register small signal changes originating from the increase in metabolic activity (from lag to log phase) and multiplication. In further experiments, we showed that a decrease in variance of the signal, compared to the one in growth media, suggests the action of clarithromycin and erythromycin on *B. pertussis* cells on the sensor. In case of resistance to streptomycin, the signal's variance does not decrease with the addition of the drug, however, on incubation with co-trimoxazole, the signal's variance reduction is apparent.

As in the case of resistance (BPSM strain's response to streptomycin), the high variance before and close to MIC values is possibly a consequence of the stress condition imposed by the presence of the antibiotic in the cellular environment. This observation is consistent with previously reported studies. Compensatory response to antibiotics has been observed in *Pasteurella multocida* under sub-MIC conditions (270).

The above results confirm that the nanomotion sensor not only detects the metabolic activity of a SGB like *B. pertussis*, but permits also to determine the MIC and MBC values in a shorter time than the traditional methods. It constitutes a great advantage for the SGB infectious diseases treatment. Such a rapid antibiotic susceptibility test could reduce treatment costs, and more importantly, diminish health risks. The new strategy for detecting antimicrobial resistance would be particularly useful in cases of infectious disease where the treatment lasts several weeks or months, thus helping to avoid the illness recurrence.

### 3.5 Mitochondrial activity detection through nanomotion

*This section contains published work:*

Stupar, P., Chomiccki, W., Maillard, C., Mikeladze, D., Kalauzi, A., Radotic, K., Dietler, G. and Kasas, S., 2017. **Mitochondrial activity detected by cantilever based sensor**. *Mechanical Sciences*, 8(1), p.23.

#### 3.5.1 Introduction

Mitochondria are 0.7-3 micrometer sized sub-cellular organelles that contain their own DNA, and it is nowadays believed that they were independent prokaryotic cells that long time ago colonized eukaryotes (271). Mitochondria live with eukaryotes in an endosymbiotic manner and are involved in numerous key physiological processes, such as energy production and regulation, signaling and programmed cellular death. Altered mitochondrial function is a key underlying mechanism of many pathological states, such as cardiac diseases, diabetes and numerous other neurological conditions (272). Precise assessment of mitochondrial function is necessary to understand those underlying mechanisms and the aging process. Furthermore, growing literature indicates that mitochondria are also targeted by environmental pollutants, making them an important subject in environmental toxicology and health research (273). However, the diagnosis of mitochondrial diseases is a complicated, expensive, and time-consuming process that involves mitochondrial isolation, DNA extraction and sequencing. Among the tools for probing mitochondrial properties, measurements of oxygen consumption and ATP production have been used to assess the function of freshly isolated mitochondria (274).

Few years ago, our team noticed that atomic force microscopy (AFM) cantilevers can be used as nanomotion sensors to detect subtle oscillations that characterize living organisms. Despite the fact that the origin of these oscillations is still not fully understood, we could observe that the amplitude (variance) of these oscillations reflect the metabolic state of the organism of interest. We also noticed that these nanoscale oscillations exist in every living biological sample we tested so far (bacteria, yeast, vegetal and mammalian cells) (212,214,216,219). In an attempt to simplify mitochondrial disease diagnostic, we carried out preliminary experiments to explore the putative nanoscale oscillation pattern of native mitochondria. The experiments consisted in attaching isolated mitochondria onto an AFM cantilever and recording its oscillations as a function of exposure to different chemicals.

Enzymes within the mitochondrial matrix (**Figure 3.21a**) are designed to oxidize the added substrates, in a cyclic manner (**Figure 3.21b**), so that every product of a reaction is a potential substrate for another reaction. In our experiments, human embryonic kidney cell mitochondria were submitted to malate, pyruvate, ADP, sodium azide and rotenone. Malate and pyruvate are the substrates involved in the citric acid cycle (Krebs' cycle), and their oxidation provides energy conserved in the structure of molecules like NADH and FADH<sub>2</sub>. These energy carriers lose energy by interacting with complexes embedded in the mitochondrial inner membrane. Complexes (I-IV) transfer energy by passing along the electrons in a process called the electron transport system. Starting with re-oxidation of a NADH molecule, a pair of electrons is passed through a series of

carriers to coenzyme Q, forcing protons from the matrix into the intermembrane space. The electrons are then passed through Complex III, forcing more protons out, and finally to Complex IV, where oxygen is reduced to water by using the electrons. In this process, some energy is released as heat, while the majority is conserved within the created proton gradient. The last link in the chain of complexes is the ATP synthase (F<sub>0</sub> and F<sub>1</sub> subunits). It holds a proton channel, where protons are pumped through, allowing energy for the synthesis of ATP by rotating F<sub>1</sub> subunit and changing the conformation of binding sites where ADP molecules react with available phosphate.

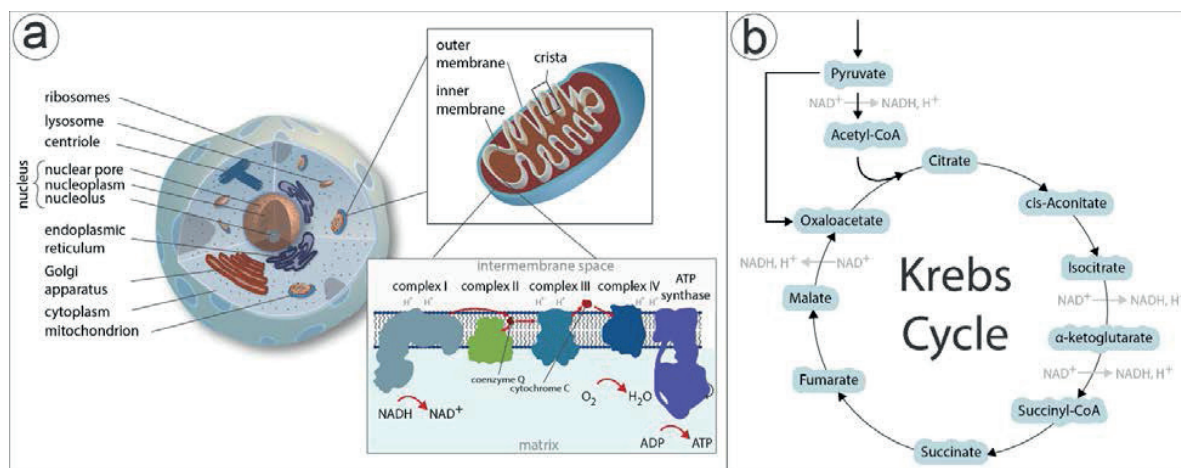


**Figure 3.21 Panel (a):** Schematic of a mammalian cell with labelled organelles, zoom on the mitochondrion showing its structure and most important components of the inner membrane (Complexes I-IV and ATP synthase). **Panel (b):** Krebs cycle (citric acid cycle) showing the sequence of metabolic reactions that generate energy within mitochondria.

Apart from the substrates, our experiments consisted in adding inhibitors, sodium azide and rotenone. Sodium azide inhibits the ATPase activity of F<sub>1</sub> subunit, but has no inhibitory effect on ATP synthesis (275). Rotenone is another inhibitor and it acts by inhibiting NADH dehydrogenase or Complex I of the electron transport chain (276).

The oscillation patterns that we observed with mitochondria on the cantilever were highly dependent on the chemicals to which they were exposed. These preliminary experiments indicate that mitochondria, similarly to bacteria, yeast, vegetal and mammalian cells also promote oscillations of the cantilever to which they are attached.

### 3.5.2 Materials and Methods

**Solutions and buffers.** Buffer 1 (HB): 210 mM mannitol, 70 mM sucrose, 5 mM HEPES (pH 7.12). Buffer 2 (HBS): HB + 1 mM EGTA + 1x Roche's Complete Mini EDTA-free protease inhibitor cocktail (1 tablet dissolved in 10 ml of buffer). 50 % Percoll: Percoll (Sigma P1644) diluted 1 to 1 with HB. Percoll solutions (22 % and 15 %): The 50 % Percoll stock is used to prepare all other Percoll solutions; to that effect dilutions of the 50 % Percoll solutions are done in HBS.

Substrate solutions were prepared in advance and stored at -20 °C. All substrates were dissolved in the working buffer (125 mM KCl, 10 mM TRIS, 0.1 mM EGTA, 1 mM KH<sub>2</sub>PO<sub>4</sub>, pH 7.4), while rotenone

was initially dissolved in 50 % ethanol and then diluted with the buffer. Malate and pyruvate were used in 5 mM final concentration, while ADP was added in 1 mM final concentration. Sodium azide was used in 10 mM, while rotenone in 1  $\mu$ M.

**Mitochondria isolation.** Mitochondria were isolated according to a modified protocol (277). Human embryonic kidney cells (293T) were grown to approximately 85 % in DMEM. Plates were placed on ice and washed twice with 8 ml of ice cold HB. Cells were collected by scraping directly in the Dounce Tissue Grinder and homogenized well. The obtained homogenate was spun at 1500g for 3 minutes. The supernatant was spun at 13000g for 17 minutes and the pellet was re-suspended in 1.4 ml of HBS. 5ml centrifuge tubes with a discontinued Percoll gradient were used (1 ml of 50 % Percoll solution followed by layering 3 ml of 22 % Percoll solution). To the re-suspended pellet, 0.6 ml of 50 % Percoll (final concentration of Percoll 15 %) was added and layered 1 ml of the 15 % Percoll sample on top of the described 50-22 % gradient. This was spun at 30700g for 6 minutes and mitochondria were recovered from 50-22 % Percoll interface. Mitochondria were finally washed by making 1 to 10 dilution with HBS and centrifuging at 15600g for 30 minutes.

**AFM imaging.** Atomic Force Microscopy measurements were made using Nanowizard III AFM from JPK Instruments (Berlin, Germany), coupled with a Zeiss Axiovert inverted optical microscope. A fluid cell was incorporated and all the images were obtained in buffered conditions. Images were collected using DNP-10 (Bruker) cantilevers, with a nominal spring constant of 0.06 N/m. Quantitative imaging mode has been used for the image acquisition, Gwyddion (v. 2.36) software for flattening and no further image processing has been carried out.

**Mitochondria attachment procedure.** Mitochondria were attached to cantilevers using glutaraldehyde functionalization and the following procedure. Conventional NP-010 cantilevers (Bruker) were functionalized using 0.5 % glutaraldehyde for 10 minutes. All cantilevers were washed afterwards, and placed to dry for the following 4 minutes. A droplet of solution containing concentrated mitochondria was placed onto the functionalized cantilevers and left for 30 minutes. After the attachment, the cantilevers were mounted and positioned inside a fluid cell, together with the working buffer.

**Data acquisition and processing.** Real time deflection of the cantilever was collected at the sampling frequency of 20 kHz. The signal was first flattened using a running window of 200 seconds. A linear fit was applied to each window and the raw signal was subtracted, so the outcome is a de-trended signal, centered around zero. Such signal was further processed by applying the moving average of 4 seconds. Finally, variance was calculated in the similar manner, using a running window of 10 seconds. Variance signal was used for line and bar plots in the presented figures. Error bars in **Figure 3.25** represent the standard error of the mean.

### 3.5.3 Results

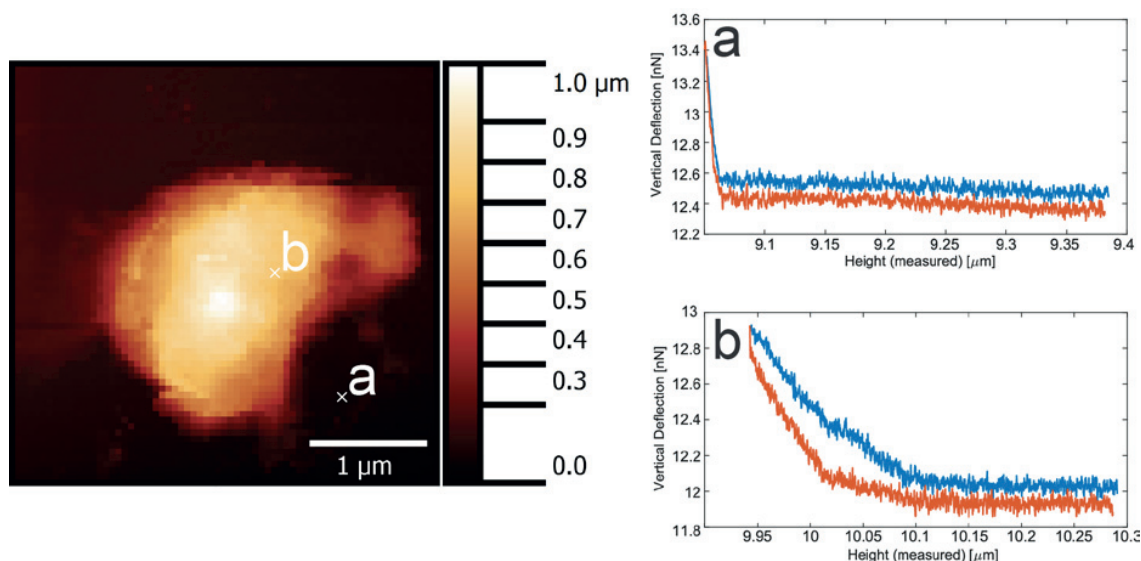


**Figure 3.22** The AFM image of isolated mitochondrion attached to glass, in buffered conditions. Structure shows 2.5 μm length, 2 μm width and 1.1 μm height. Force-distance curves from positions marked on the AFM image are shown on the right. The top figure (a) shows the stiffness of the substrate, while the other one (b) shows the softness of the biological structure.

Before exploring the mitochondrial sample with our technique, we imaged the attached mitochondria on a glass substrate in liquid media. **Figure 3.22** shows the obtained image with examples of force-distance curves at two different positions, one on the mitochondrion and the other one on the support. Curves show a typical response of the cantilever in contact with a soft and a hard sample, respectively.

Next, freshly isolated mitochondria were attached to the cantilever sensor and introduced into the analysis chamber. Real-time cantilever deflection recordings were made while mitochondria were submitted to different conditions by using the fluid cell that allowed us the fluid exchange. The first media to make a measurement was a plain buffer, after which we introduced substrates: malate and pyruvate. With introduction of the substrates, the oscillations increased, as presented on the variance plot in **Figure 3.23**. Oxygen consumption in this condition reflects state 2 respiration of mitochondria, specific to Complex I. Then, we introduced ADP to the medium to stimulate further the respiration in the presence of malate and pyruvate. In this condition, state 3 respiration, specific to Complexes I and II, appears to keep oscillations of the sensor increased. The example of oscillations, plotted as a real-time deflection, is presented on **Figure 3.24**. We continued the experiment by adding sodium azide and measuring the response. The oscillations showed a slow decrease, and were completely reduced only after the injection of media containing rotenone.

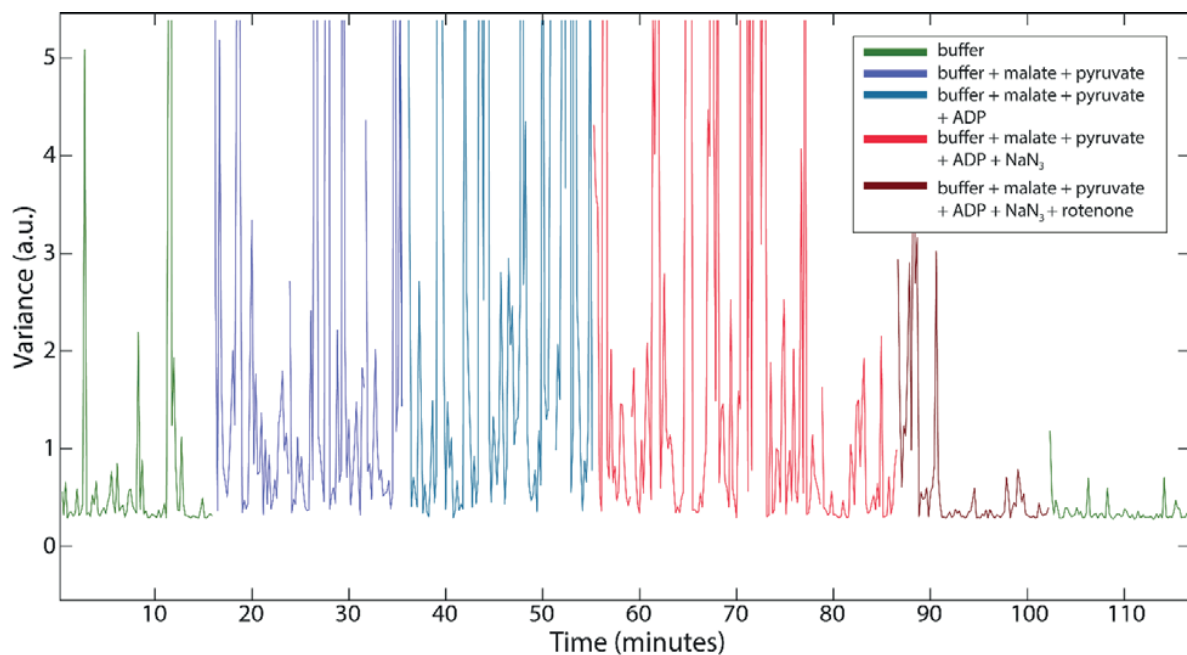


**Figure 3.23** The evolution of variance throughout the experiment. Variance was calculated from the deflection data for each measurement. Different colors represent different conditions to which mitochondria were subjected. In each condition, a new substance was added (substrates: malate, pyruvate, ADP; inhibitors:  $\text{NaN}_3$ , rotenone). Variance increases with the addition of substrates and decreases in presence of the inhibitors.

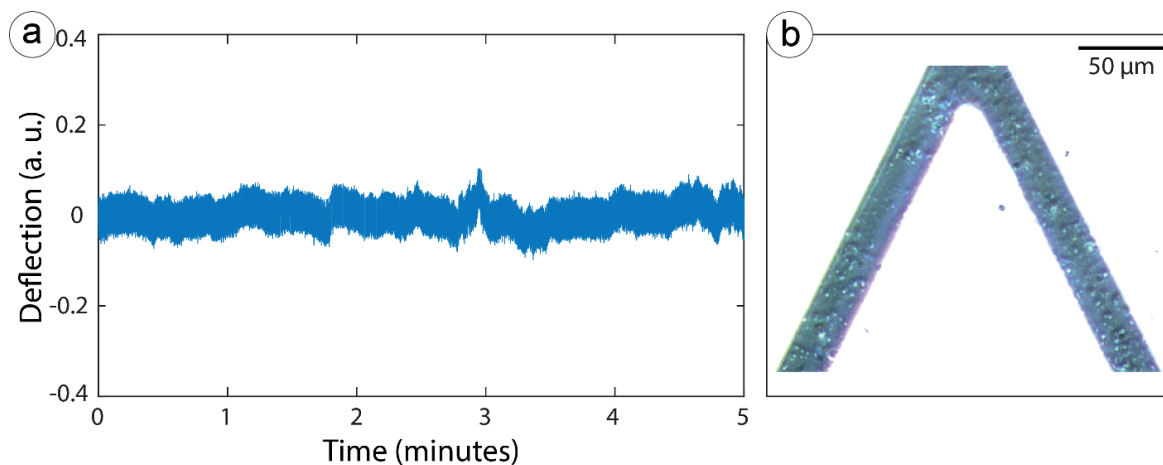


**Figure 3.24 Panel a:** Deflection of the cantilever with mitochondria attached. The recordings were made while the buffer with substrates (malate, pyruvate, ADP) was present in the analysis chamber. Figure shows a section of 5-minute oscillations. **Panel b:** A typical image of mitochondria attached to the cantilever.

Lastly, **Figure 3.25** shows the variance averaged over 15-minute intervals within different conditions. Two sets of bars are presented, one with the control cantilever (functionalized, but with no mitochondria attached), and the other one with mitochondria attached. Each set is normalized to the first measurement (buffer) separately, and represents the percentage change of variance once the substrates (and the inhibitor) are added. While the control cantilever oscillations remained

within the error interval, the one with mitochondria attached showed more than two times increase in oscillations in the presence of metabolic substrates compared to the buffer only. Values suggest that mitochondria do couple with the cantilever and induce oscillations greatly above the baseline thermal motion, when activated by substrates. These oscillations dropped with the introduction of the inhibitor, suggesting the complete inhibition of mitochondrial activity.

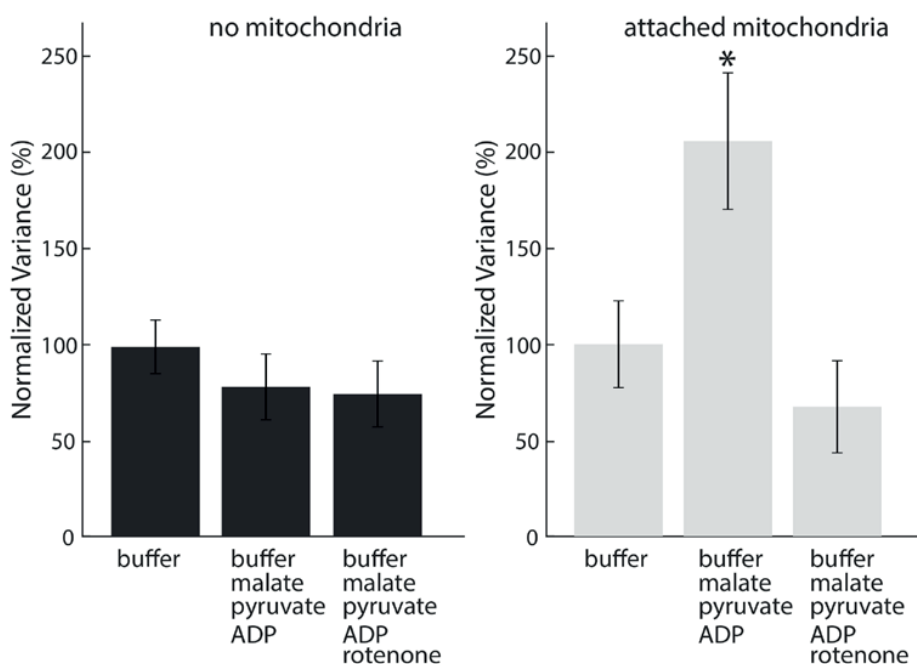


**Figure 3.25** Normalized and averaged variance over the 15-minute intervals in conditions of a plain buffer, buffer with substrates and lastly, with the inhibitor. Dark grey represents values without any mitochondria on the cantilever as a control, while light grey values show variance changes with the attached mitochondria. The two-sample t-test rejected the null hypothesis at the 5% significance level ( $p \leq 0.05$ ) only in the case of attached mitochondria with the addition of substrates.

In this work, we showed how nanometer scale oscillations arising from mitochondrial processes coupled with the cantilever and produced motion. Conventional FFT analysis, unfortunately, could not produce any distinct frequency components specific to the oscillations in different metabolic conditions. Therefore, we believe variance evolution is the best parameter to describe dynamic changes in oscillations. As showed on **Figure 3.23**, switching from plain buffer into a buffer with metabolic substrates caused oscillations to increase. Those oscillations were amplified with the addition of a diphosphate necessary for the series of conformational changes that precedes the ATP synthesis. Sodium azide is an inhibitor that acts by confining the activity of ATPase, without stopping the ATP synthesis coupled mechanically to the proton motive force across the inner membrane by the rotation of the subdomain ensemble (278). Furthermore, some reports show that the presence of inorganic phosphate could tamper the ability of azide as an inhibitor (279). Therefore, the observed slow and incomplete decrease of variance could be attributed to azide not being as potent inhibitor in our experimental setup. Rotenone, a specific NADH dehydrogenase inhibitor, stops the



electron transfer to coenzyme Q. This creates reactive oxygen species which can damage DNA and other components of mitochondria. This could suggest why in the presence of rotenone in our experiments, oscillations of the cantilever dropped to the lowest values.

Considering our previous work, it is not surprising that a cantilever with the attached mitochondria oscillates more than a control in the presence of metabolic substrates. The observed increase could be attributed to the complex dynamics of the mitochondrial metabolic system.

#### 3.5.4 Conclusion

Mitochondrial diseases are a public health issue nowadays and their diagnostic is unfortunately still a complicated, long, and expensive process. In these experiments, we demonstrated that the activity of native mitochondria can be detected, like in the case of other prokaryotes. We have also shown that their oscillation pattern is affected by the chemicals to which they were exposed. Having in mind these two facts, it can be speculated that the oscillation pattern of “healthy” and “diseased” mitochondria could also differ. Likewise, it could be expected that they react differently upon appropriate chemical exposure. Such a possibility would open novel avenues in mitochondrial disease diagnosis and research. Even if for the moment we did not explore these interesting hypotheses, the present work suggests that continuing the investigation might lead to a great benefit in terms of diagnostic speed and cost. The next step is to extend our studies to mitochondria isolated from patients suffering from mitochondrial diseases.

### 3.6 Cancer cell viability testing through nanomotion

*This section contains manuscript in preparation:*

Petar Stupar‡, Giovanni Longo‡, Carine Benadiba, Josiane Smith-Clerc<sup>1</sup>, Jasna Bankovic, Ana Podolski-Renic, Milica Pesic, and S. Kasas\*. **Cell viability testing through nanoscale motion.** In preparation.

‡ Authors contributed equally

#### 3.6.1 Introduction

Cancer is a multifunctional disease recognized as a major worldwide health problem, affecting men and women in economically developed countries as well as in developing regions (280). Unfortunately, cancer still remains an unsolved health issue despite the significant advances in our understanding of various aspects of its initiation, progression, metastasis, interactions with the immune system, and the tumor microenvironment. The obstacles for efficient cancer treatment such as diversity, heterogeneity and drug-resistance have gained significant importance for the development of personalized cancer therapy (281).

Resistance can occur prior to drug treatment (primary or innate resistance) or may develop over time after exposure to the drug (acquired resistance) (282–284). Treatment with a single chemotherapeutic agent may lead to the development of resistance to multiple structurally and functionally unrelated compounds, known as cross-resistance or multidrug resistance (MDR). MDR frequently correlates with overexpression of the ATP-Binding Cassette (ABC) transporters in cell membranes that actively pump anticancer drugs out of cells (285). Overexpression of membrane transporter P-glycoprotein (P-gp) is the most common alteration in cancer cells with MDR phenotype (281,286).

Since cancer is characterized by its pleomorphism and variations from patient to patient, personalized therapy emerged nowadays as the most efficient way to fight this incurable disease (287). In order to collect genetically accurate data and find appropriate personal therapy regimen, researchers need to propagate patient-derived primary tumor cells. This would allow the detection of possibly present intrinsic MDR as well as the identification of a specific medication that tumor is sensitive to. Additionally, this kind of treatment would minimize adverse effects and would be more effective (288). Unfortunately, the methods currently used for generating and culturing primary tumor cells are time-consuming, expensive and require specialized laboratories and personnel. Therefore, personalized cancer treatment requires major investments in infrastructure and in the development of assays to make it accessible to a wide range of patients (289). In addition, the studies of drug effects on artificially cultured tumor cells that change during propagation may not reflect the situation *in vivo*. Ideally, a drug profiling tool should be able to perform analyses as a function of drug concentration, and yet be simple, inexpensive and quick enough to allow extensive dose-response profiles for many drugs (290). Such an innovative and versatile technique would have the potential to greatly facilitate the development of new therapeutics and their combinations, but also contribute to the emerging field of personalized medicine.

Our technique that measures the fluctuations of a nanomechanical sensor to monitor the metabolic activity of living specimens in physiological medium has been introduced in the beginning of this section. We have exploited the technique at first to assess the sensitivity of bacteria to antibiotics (240,241). Later, we extended its application to proteins and different other biological systems, including mammalian and plant cells (216,257). Aforementioned works, in particular those involving the study of bacteria and mammalian cells, indicated that this technique can be extended to the field of oncology. As a rapid and single-cell diagnostic tool, nanomotion sensors could facilitate the search for the best chemotherapy regiment of different cancer types, most importantly the resistant ones. The final objective is testing of patient tumor tissue samples and obtaining the guidelines for personalized treatment.

To demonstrate the contribution that the nanomotion sensor can produce in the field of oncology, we studied six different human cancer cell lines, three sensitive and their three MDR counterparts. MDR cancer cell lines were established by continuous exposure to stepwise increasing concentrations of a classical chemotherapeutic - doxorubicin (DOX). They all overexpress P-gp. Specifically, the cell lines we used originate from non-small cell lung carcinoma (NCI-H460 and NCI-H460/R) (291); colorectal carcinoma (DLD1 and DLD1-TxR) (292) and glioblastoma multiforme (U87 and U87-TxR) (292). The aim of our study was to investigate whether this technique is suitable to quickly and efficiently classify sensitive from resistant cancer cells.

### 3.6.2 Materials Methods

**Drugs and Chemicals.** DOX solution was obtained from EBEWE Arzneimittel GmbH, Vienna, Austria and kept at  $-20^{\circ}\text{C}$ . RPMI 1640 medium, minimum essential medium (MEM), fetal bovine serum (FBS), antibiotic-antimycotic solution, penicillin-streptomycin solution, L-glutamine, and trypsin/EDTA were purchased from Bioind, Beit Haemek, Israel and Life Technologies, Switzerland.

**Cells and Cell Culture.** NCI-H460, DLD1, and U87 cell lines were purchased from the American Type Culture Collection, Rockville, MD. NCI-H460/R cells were selected originally from NCI-H460 cells in a medium containing 100 nM DOX (291). DLD1-TxR and U87-TxR cells were selected by continuous exposure to stepwise increasing concentrations of PTX (100–300 nM) for a period of ten and nine months from DLD1 and U87 cells, respectively (292). MDR cancer cell lines (NCI-H460/R and DLD1-TxR) and their sensitive counterparts (NCI-H460 and DLD1) were maintained in RPMI 1640 medium supplemented with 10 % FBS, 2mM L-glutamine and 10,000 U/ml penicillin, 10 mg/ml streptomycin, and 25  $\mu\text{g}/\text{ml}$  amphotericin B solution, while U87 and U87-TxR were grown in MEM with 10 % FBS, 2 mM L-glutamine and 5,000 U/ml penicillin, and 5 mg/ml streptomycin solution. All cell lines were subcultured at 72h intervals using 0.25 % trypsin/EDTA and seeded into a fresh medium at the following densities: 8,000 cells/cm<sup>2</sup> for NCI-H460, DLD1, and DLD1-TxR, 16,000 cells/cm<sup>2</sup> for U87 and NCI-H460/R, and 32,000 for U87-TxR.

**Assessment of cell proliferation in real-time.** Continuous cell proliferation of NCI-H460 and NCI-H460/R cancer cells untreated or treated with 0.5  $\mu\text{M}$  DOX was analyzed using the xCELLigence Real Time Cell Analyzer (ACEA Biosciences Inc., USA) which facilitates label free real-time cell analysis by measuring impedance-based signals across a series of gold electrodes. Using E-plates, 50  $\mu\text{l}$  of

complete medium RPMI 1640 was added to each well and the electrodes were allowed to stabilize for 30 min. The plates were then moved into the xCELLigence Real Time Cell Analyzer to set a base line without cells. The cells were then seeded on E-plate at a following density - 4,000 cells per well. Cells on the electrodes were monitored by reading and recording the cell impedance every 30 min through 165 h.

**Nanomotion sensor preparation.** For all our experiments, we used commercial tipless AFM cantilevers (NP-O10 Bruker, USA) with a nominal spring constant of 0.12 N/m. To ensure the adhesion and spread of the cells on the cantilevers, we chemically functionalized the sensors. Prior to introduction into the analysis chamber, we exposed them to 50  $\mu\text{g/ml}$  fibronectin for 15 minutes. After this period, we washed them with ultrapure water and used them for the nanomotion experiments.

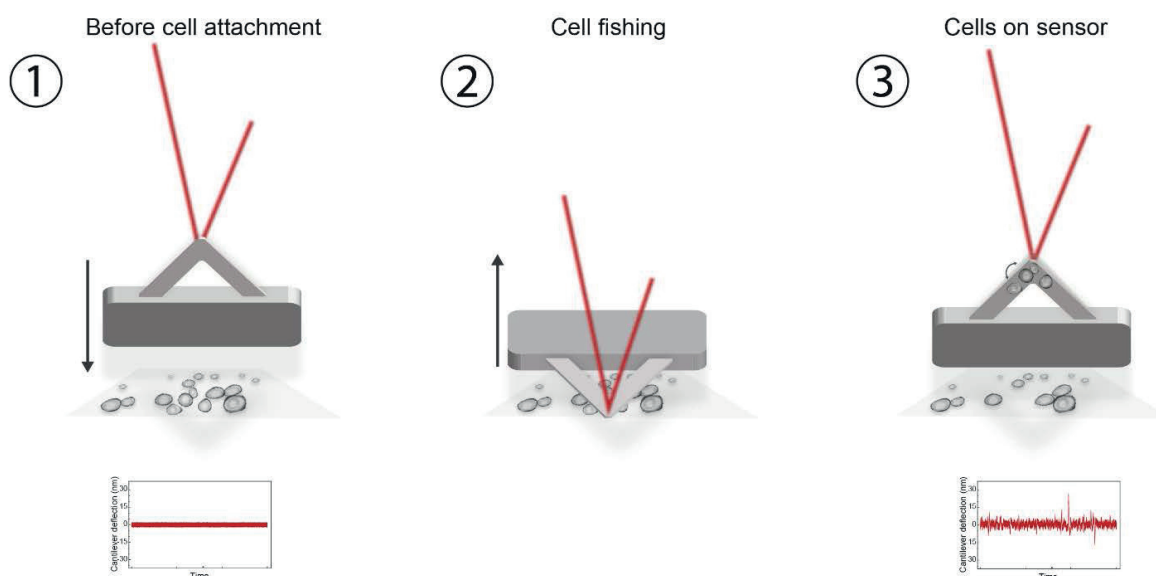


**Figure 3.26** Schematic representation of the set-up on cantilever. **1:** Representation of the cantilever before the attachment of cells; graph shows no fluctuations, **2:** Sensor attaching the cells, **3:** Cells attached to sensor, graph represents the fluctuations produced by cells adsorbed on sensor surface.

**Experimental procedure.** For all our experiments, we used a Nanowizard III AFM from JPK Instruments (Berlin, Germany), coupled with a Zeiss Axiovert inverted optical microscope. We produced a PDMS custom analysis chamber (220) which was then placed in the optical line of the microscope. At this point we introduced 3 ml of complete medium (appropriate for each cell line) in the chamber and added a small quantity (30-50  $\mu\text{l}$ ) of cells suspended in the medium. Before each experiment we performed a 5-minute measurement of the fluctuations of the sensor in medium without any cells attached. After this stabilization period, we immobilized some cells on the surface of the cantilever, using a cell “fishing” method we described in detail elsewhere (257). Specifically, we used the AFM coarse and fine movement capabilities to approach a single cell, attaching it near the apical region of the cantilever. Typically, we chose to attach 2-6 single cells to the sensor, ensuring

that all cells stayed on the apical region of the cantilever (**Figure 3.26**). After the attachment phase, we gradually retracted the sensor to avoid interference from the substrate and the cells were left one hour on the cantilever to spread. During this period, we continuously measured, at 10 kHz acquisition frequency, the fluctuations of the cantilever to determine the healthy state of the cells before the exposure to the drugs. After the stabilization period, we flushed the analysis chamber with the chosen concentration of doxorubicin and we followed the resulting response of the cells both by nanomotion analyses and using conventional optical microscopy. We used a FireWire 400 Color camera (The Imaging Source, Germany) connected to the inverted microscope to collect images of the cells on the sensor every 20 seconds.

### 3.6.3 Results

Our work investigates the possibility to use nanomotion sensor to differentiate susceptible and resistant cancer cells to chemotherapy. To address this question, we employed in vitro MDR model system that comprises three different sensitive human cancer cell lines and their MDR counterparts. P-gp that is overexpressed in tested MDR cancer cell lines is a member of ABC transporter family which reduces intracellular accumulation of anticancer drugs by increasing drug efflux, thus suppressing the interaction between drug and its intracellular target molecule (293). P-gp can bind a wide variety of hydrophobic drugs including DOX (294).

Cells were allowed to spread on a cantilever sensor coated with fibronectin, where integrin-mediated adhesion-dependent signaling supports cell cycle progression and survival. Fluctuations of the sensor produced by the presence of cells attached to its surface were well pronounced, in a frequency range of up to 1000 Hz and with amplitude which depends on the position and number of cells (**Figures 3.27, 3.28 and 3.29**). Our previous studies with bacteria and cells suggest that these movements represent the viability of cells and convey information about their metabolism, cytoskeleton rearrangements, etc. (216,240,257).

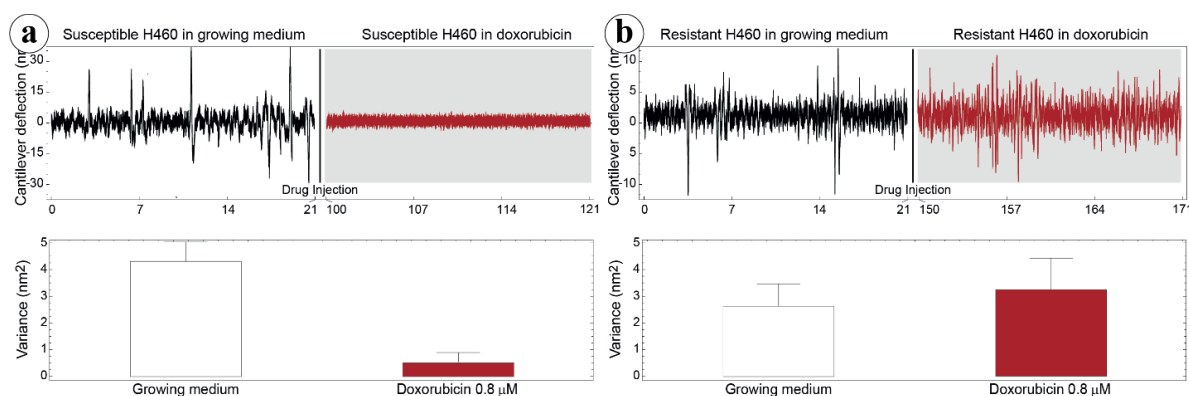


**Figure 3.27** Non-small cell lung carcinoma cell lines on nanomotion sensor. Deflection of the sensor (**top**) and corresponding variance(**bottom**) for NCI-H460 (**a**) and NCI-H460/R (**b**) cells. The traces represent 21min of recording for growing medium. DOX was injected at 21st minute. The error bars represent the variation of the variance values in measurements performed in similar conditions.

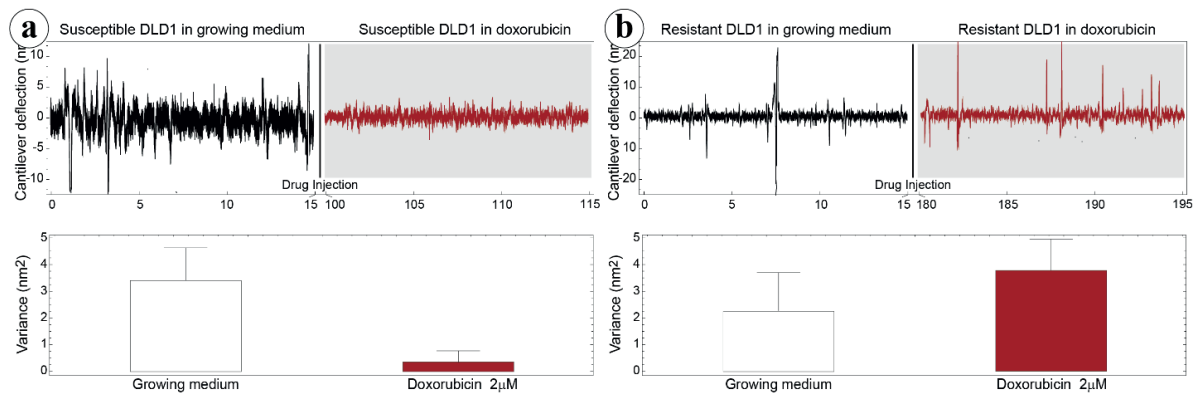


**Figure 3.28** Colorectal carcinoma cell lines on nanomotion sensor. Deflection of the sensor (**top**) and corresponding variance (**bottom**) for DLD1 (**a**) and DLD1-TxR (**b**) cells. The traces represent 15min of recording for growing medium. DOX was injected at 15th minute. The error bars represent the variation of the variance values in measurements performed in similar conditions.

The cells were exposed to different concentrations of DOX depending on their level of resistance to this drug. Glioblastoma cells were treated with the highest DOX concentration - 15  $\mu$ M (**Figure 3.29**). The resistance of U87 cells considered as sensitive in our model is probably due to the deregulation of the cell cycle and the absence of apoptosis (295). The death of tested sensitive cells (NCI-H460, DLD1 and U87) occurred after 80, 85 and 15 min (respectively) of drug injection, and the corresponding drops in variance are: 88%, 89% and 96% (**Figures 3.27, 3.28 and 3.29**). The movement of MDR cells (NCI-H460/R, DLD1-TxR and U87-TxR) continued during 150, 180 and 80 min (respectively) after drug injection, and the calculated increases in variance are: 24%, 66% and 15% (**Figure 3.20**).

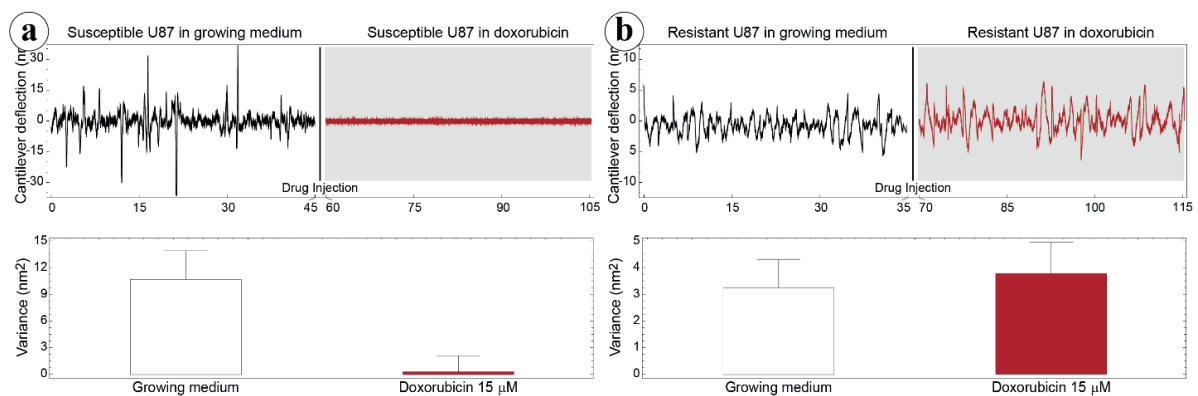


**Figure 3.29** Glioblastoma cell lines on nanomotion sensor. Deflection of the sensor (**top**) and corresponding variance (**bottom**) for U87 (**a**) and U87-TxR (**b**) cells. The traces represent 45min of recording for growing medium. DOX was injected at 45th minute. The error bars represent the variation of the variance values in measurements performed in similar conditions.

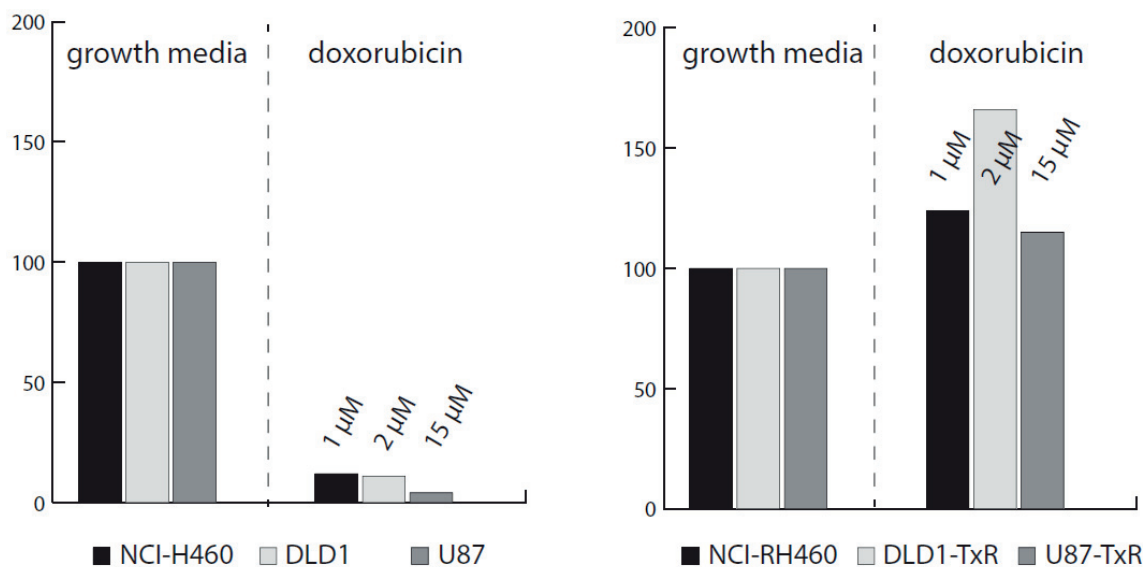


**Figure 3.30** Summary of the results normalized to the measurements in growth media. Bars represent variance values from figures 49, 50 and 51, for growth media (set to 100%) and corresponding values for doxorubicin exposure.

Comparing the variance of the nanomotion response before and after the exposure to the drug, we could see that in less than 2 h the susceptible cells decrease the fluctuation variance. The overall movement for these cells after this time period reverts to the basal level measured before the attachment of the cells. On the other hand, the resistant cells maintained their overall movement even several hours after the exposure to the DOX. In fact, the response of MDR cells to drug attack resulted in a slight increase in movement. The best interpretation of these results is that, in the case of susceptible cells, the loss of cell viability caused by the exposure to the drug halts all biological-related movement of the sensor. The resistant counterparts, on the other hand, retained their metabolic activity and viability, and the movement increase could indicate a metabolic response of the cells to the drug pressure. Hence, the methodology presented could be employed for the distinction of resistant from sensitive tumor cells. This is of great importance in the efforts to personalize cancer therapy. A patient-derived primary tumor cells could be tested accordingly, and every patient would obtain specific therapy. This would allow not only a treatment with less adverse effects but would also influence the lowering of the treatment cost.

The final outcome of the nanomotion experiments was confirmed by conventional optical microscopy. By combining the optical images collected throughout each experiment, we were able to produce a movie depicting the movements of the cells on the cantilever surface, allowing a direct comparison between these microscopic vibrations with the nanometric movements detected by the nanomotion sensor (**Figure 3.31, panels 1-2**).

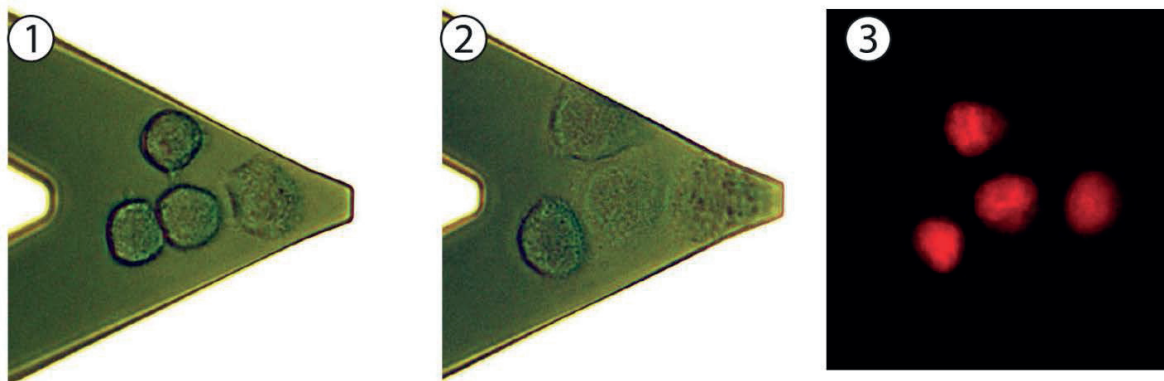


**Figure 3.31** Images of cells attached to the sensor: **1)** Optical image of 4 cells attached at the beginning of the experiment. **2)** Optical image of cells at the end of the experiment. **3)** Fluorescent image of cells at the end of the experiment. The drug used (doxorubicin) is self-fluorescent, accumulating in the nucleus.

Doxorubicin enters the cell via passive diffusion, generally accumulating to intracellular concentrations that exceed the extracellular compartments by 10 to 500 – fold, predominantly accumulating in the nuclear compartments (296). It has been reported that doxorubicin acts by free radical formation and DNA damage via inhibition of topoisomerase II, inducing different cell death pathways depending on the dose (low dose induces mitotic catastrophe, characterized by the formation of multiple micronuclei and loss of membrane integrity, and high dose induces apoptosis, characterized by reduction of cell volume, apoptotic blebbing) (297). To examine the localization of the drug, during each experiment we exploited the drug’s auto-fluorescence. We used the very same optical microscope to acquire several fluorescent images, which showed in all cases the accumulation of fluorescent doxorubicin predominantly in the cell nucleus (**Figure 3.31, panel 3**).

It is very important to use an inverted microscope and fluorescence aids in order to understand the signal coming from such a complex biological system as cells. Results are showing that the higher the concentration of doxorubicin used, the quicker the cells die. However, when dying, cells reverse their spreading and slowly detach from the cantilever. This process introduces noise and may mask the signal from their reduced metabolic activity. Care should be taken in the interpretation of such cases and looking at the recorded set of images helps deciphering it. An example experiment is presented in **Figure 3.32**. The evolution of variance throughout the entire experiment is combined with optical images for better signal interpretation. Separating signal into four different phases helps understanding it. First, at the beginning of the experiments, cells are attached to the cantilever and the signal is low. Next, the attached cells spread onto the cantilever surface, increasing the area they occupy and exposing it more to their inner dynamics. Therefore, the signal increases and the image shows cells spread (barely visible). After drug injection, the signal drops to very low values, showing the cellular activity ceased. However, dead cells are starting to detach from the cantilever surface and bleb, as a normal apoptotic process. With detachment and blebbing, the signal increases as the process is inducing cantilever oscillations to a certain degree.



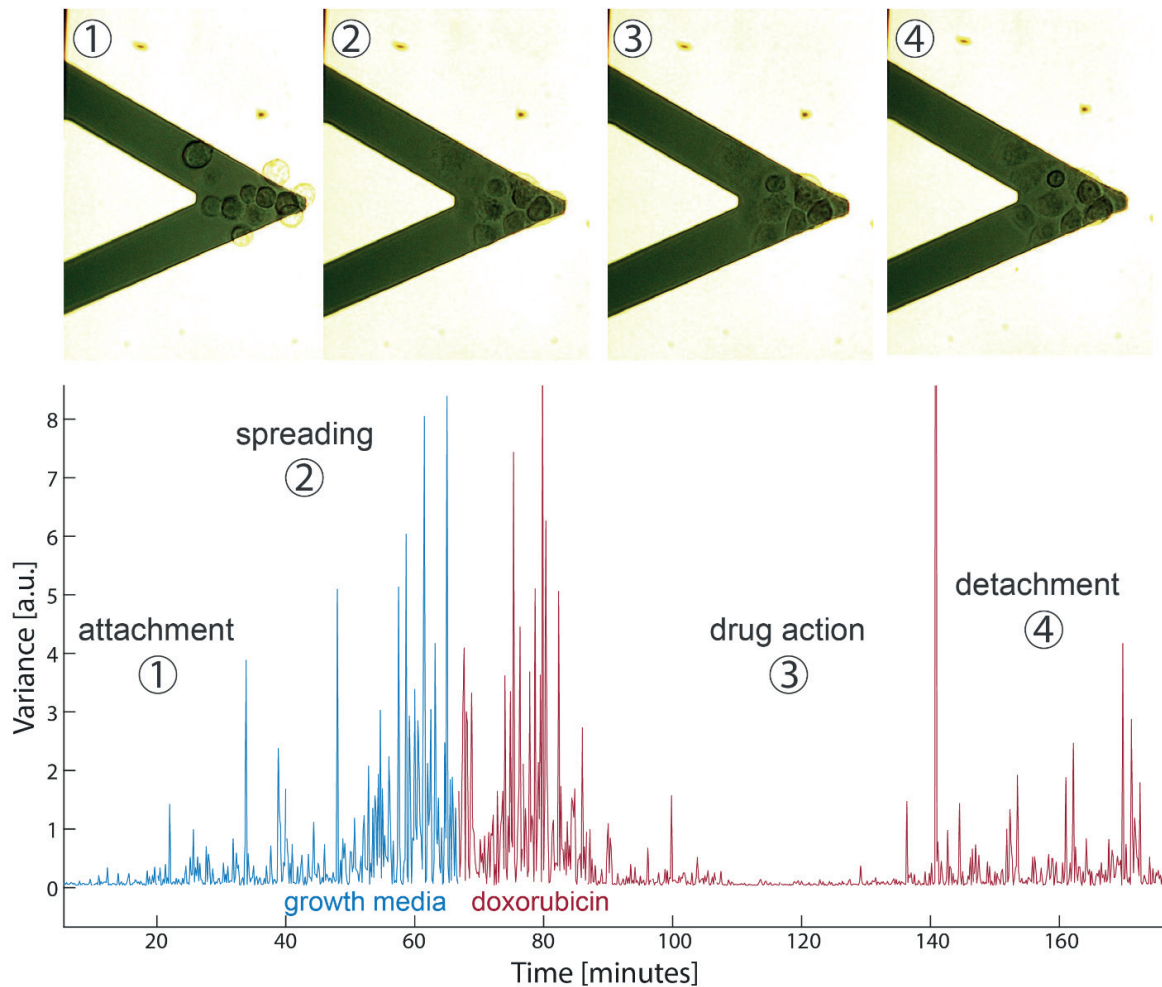


**Figure 3.32** Correlation between the optical images and the nanomotion signal. Graph represents the evolution of variance throughout the experiment while cells were in growth media (**blue**) and exposed to the drug – doxorubicin (**red**). There are several phases denoted with numbers: attachment, spreading, drug action and detachment. Corresponding optical images are presented on the top.

### 3.6.4 Conclusion

Living systems, such as cells, are highly dynamic and provide integrated functions that include metabolism, control, sensing, reorganizations, adherence, communication, growth etc. Knowing that, it is not surprising how their viability could be monitored measuring the deflection signal of a cantilever on which they reside. The presented experiments show that in all susceptible cell lines, the addition of a certain concentration of doxorubicin, deflection of the cantilever decreases, and subsequently the variance of the signal declined. The observed drop in variance is most likely attributed to a decline in cell viability, as doxorubicin affected cells and triggered their death. However, in case of doxorubicin-resistant lines, deflection of the cantilever and corresponding variance values did not decrease. Moreover, it increased as a response of resistant cells to the drug. Furthermore, depending on the drug dose, different processes may occur within cells – sudden

rupture of the membrane, slow mitotic catastrophe or apoptotic blebbing. Care should be taken when interpreting signal and correlation with optical images is highly advisable.

The findings of this study suggest that with the proposed nanomechanical sensing method, researchers and physicians might be able to obtain very fast (only in few hours) response profile of a tumor cell to different stimuli or a drug, with high temporal resolution and impressive sensitivity. Further investigation on patient tumor tissue sample is desirable, and it might provide more specific and accurate data on dosing and method applicability.

Having discussed the obtained results, we strongly believe our technique can contribute to the development of a drug profiling tool that is simple, inexpensive and quick enough to allow extensive dose-response profiles for a number of chemotherapeutics enabling the application of personalized treatment.

## 3.7 The origins of nanomotion

### 3.7.1 Introduction

In the previous sections, the nanomotion detection technique has been described. A number of potential applications were suggested by presenting the current results obtained using the technique. When detecting the resistance of either bacterial or cancer cells, the signal of the cantilever oscillation after the drug addition is always compared to the one in growth media. This “relative” approach is important, since we do not have a valid and proven method for calibration and absolute comparison of signals from two separate experiments. Furthermore, we have shown that the signal is in a strong correlation with metabolic activity of the attached sample. With various inhibiting and promoting chemical agents, we have concluded that the attached sample, if viable, causes the oscillations of the cantilever, and once it is inhibited, the oscillations stop. The cease of oscillatory movement is an important part of the signal, that tells us how and how long it took for the agent of interest to affect the tested sample. Apparently, the most important information can be extracted using the technique even without knowing what drives the oscillatory movement precisely. Seemingly simple, the quest of investigating the cause of cantilever vibrations in the presence of viable specimens is not an easy task. The findings in the following section are focused on providing clues in this regard, exploring possible scenarios and testing various oscillation contributions.

### 3.7.2 Materials and Methods

The experiments presented below mostly comprise of already mentioned techniques, procedures, chemicals, and instruments.

### 3.7.3 Results

Given the results obtained from various sets of control experiments and other tests, several potential contributions to the oscillatory signal of the cantilever may be considered. Once the viable and metabolically active sample is attached to the cantilever, it is forced to oscillate. These cantilever oscillations might be due to a mechanical, thermal, optical and/or local pH effects.

#### *Mechanical effect*

The mechanical effect comprises of the momentum transfer and impulses that bacteria exert onto the thin and soft cantilever. It should be pointed out that the thickness of cantilevers used in the presented experiments is around 0.6  $\mu\text{m}$  only. *E. coli* cells have dimensions of 1 – 3  $\mu\text{m}$  in length and around 0.5  $\mu\text{m}$  in diameter (298). To better visualize the comparability in their size, **Figure 3.33** depicts a hypothetical zoom onto a cantilever edge, with sizes in scale. *E. coli*, for instance, are peritrichous bacteria, having multiple flagella in all directions. Being a primary structure responsible in locomotion, the bacterial flagellum has a rotary motor in its base. It helps bacteria move towards the chemical attractants and away from the chemorepellents, in a process known as the chemotaxis. The motors can rotate with a frequency in a range of 15 – 300 Hz during swimming, and the *E. coli* cell swimming speed is in the range of 10 – 35  $\mu\text{m/s}$  (299). The power for that is provided by a protonmotive force, defined as the work per unit charge that a proton can do on crossing the cytoplasmic membrane (300).

In one of our initial experiments of such kind, we obtained that the oscillatory movement drops to approximately half, after the inhibition of bacterial flagella. We have made a conventional swarming assay in parallel, to validate the ability of bacteria to use their flagella. **Figure 3.34** shows that the metabolic activity increase, caused by the addition of glucose, is followed by a decrease, due to their biological response of abandoning flagella in highly nourishing environment. High salt concentration is also found to inhibit bacterial flagella, as an adverse effect which has been investigated using nanomotion (301) (**Figure 3.34, right**). The swarming assay below the variance bars confirm the inability of bacteria to use flagella for swarming after exposure to the mentioned conditions.

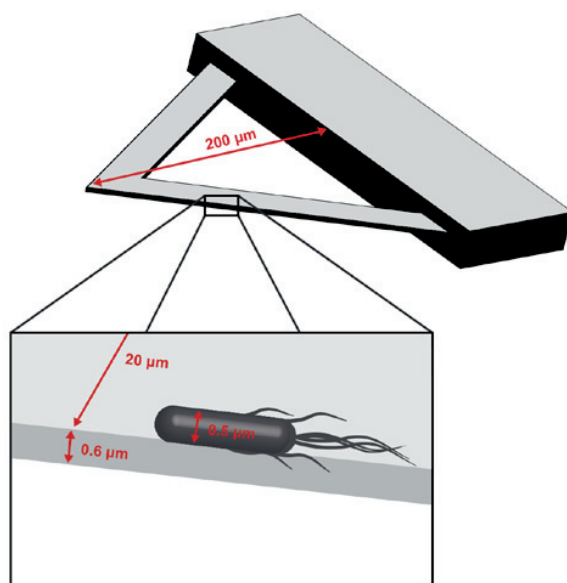


**Figure 3.33** Schematic of the cantilever and the attached bacterium, for purposes of highlighting comparability in dimensions of the cantilever (thickness) and the bacterium (radius).

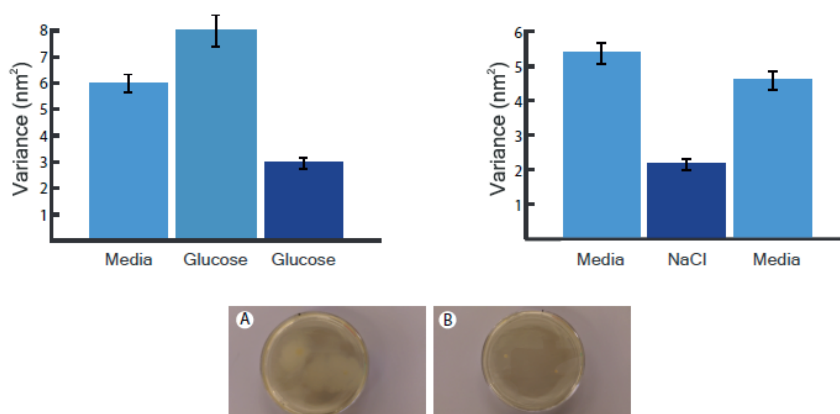


**Figure 3.34 Top** - Variance of the signal arising from cantilever oscillation while bacterial cells were subjected to growth media alone and with the addition of glucose at starting point and 1h later (**left**) or NaCl (**right**). **Bottom** - Results from the conventional plate swarming assay. Bacteria with flagella are swarming and that makes a blurry circle (**A**), while non-flagellated cells remain as a confined single colony (**B**).

Switching the focus to mammalian cells spreading on the cantilever, while recording oscillations, it is much easier to observe the dynamics of such large systems and correlate it with the signal. When mammalian cells are attached to the cantilever, at first, the signal is not largely increased due to their presence and activity. The attached surface area is not sufficiently large enough to allow cells to contribute to the motion of the cantilever. However, the cells spread, as the cantilever is functionalized with fibronectin – a molecule that promotes cell spreading. As spreading progresses, the signal subsequently increases. One particular experiment depicts this in a rather interesting manner.

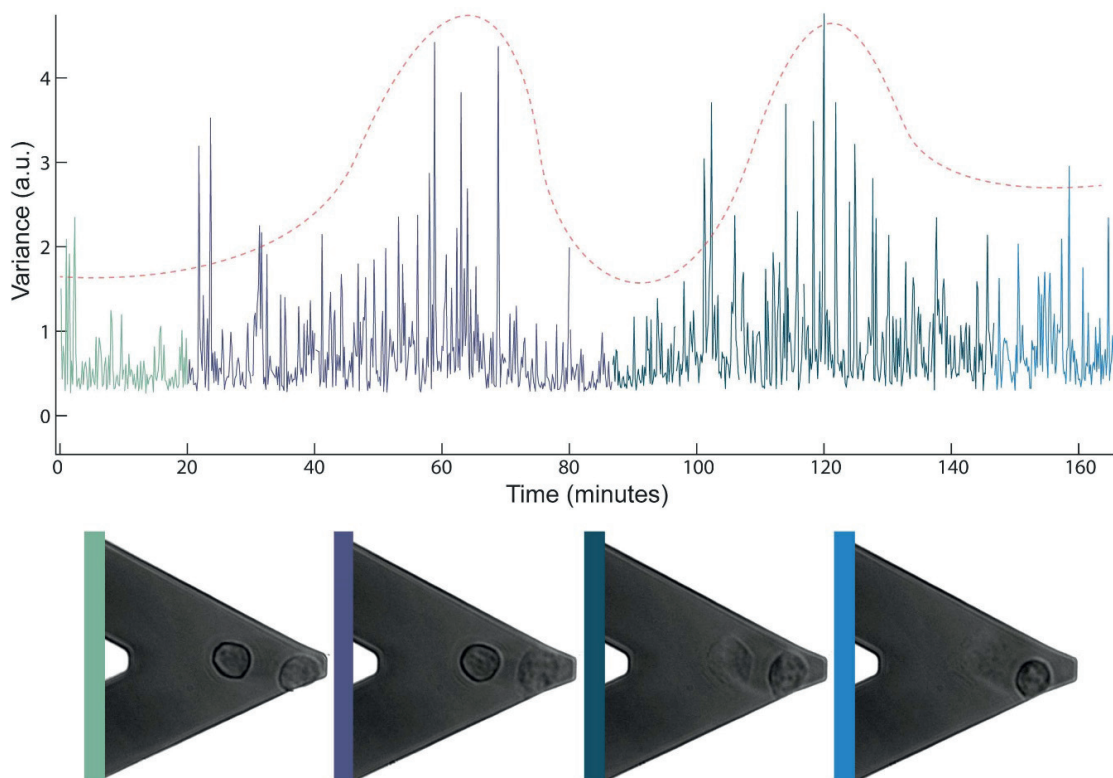


**Figure 3.35** Two attached cells spread consecutively and the nanomotion signal detects each individual contribution to the overall variance. **Top:** variance evolution with a visual guide – red dashed line. **Bottom:** Snapshots of cells in the process of a consecutive spreading on the cantilever surface.

**Figure 3.35** represents a consecutive spreading of two cells, one after the other, without any time points where both of them are spread at the same time. As one cell starts to spread, the variance of the oscillatory signal increases. After some time, the cell retracts back, while at the same time, the other cell starts to spread. This phenomenon is followed by another maximum in the variance evolution signal. In the end of the experiment, as one of the cells remained spread, the variance is larger than in the beginning.

**Figures 3.3, 3.32 and 3.35** bring the oscillatory signal in a very close relation with the structural rearrangement within the attached cells. Cells are not static systems. The intracellular transport of organelles and proteins is constantly active in ATP-driven processes or diffusion within the

cytoplasm. Molecular motors are responsible for highly directed motion that can scale up to complete rearrangement of the cell's architecture, in biologically crucial processes like division, migration and contraction. It has been shown that force fluctuations within the cell, driven by motor activity play a dominant role in the intracellular motion, even on the micron scale (302). This means that the random motion within cells is not a thermally-induced fluctuation, but a result of accumulated and random motor activity. Apart from that, large-scale motion of cells is also present, crawling, membrane extensions and protrusions, etc. The actin filaments are mostly responsible for the overall architectural stability of cells and play a dominant role in its rearrangements. We have shown previously that depolarization of the actin network leads to a significant decrease in cantilever oscillations, bringing them in a direct correlation (257). During mitosis (**Figure 3.3**), cells down-regulate focal adhesions and increase their cortical tension, intracellular pressure, and generate force to round up. A sustained counterforce to a pressing cantilever has been measured in a single cell, ranging 50 – 70 nN (303).

Reducing the biological complexity in the tested sample, yeast cells were investigated next. Using a commercial AFM system, we used a concanavalin-functionalized cantilever and approached onto a suspended *Saccharomyces cerevisiae* cell. This resulted in the attachment of a single cell at the cantilever apex. We then followed the motion of the cantilever, recording optical images in parallel. As presented on the **Figure 3.36**, a clear reduction in the noise level follows the detachment of the yeast cell from the cantilever. The result, and the correlation between the taken images and the signal, highlight a remarkable sensitivity in motion detection of a mechanical nature.

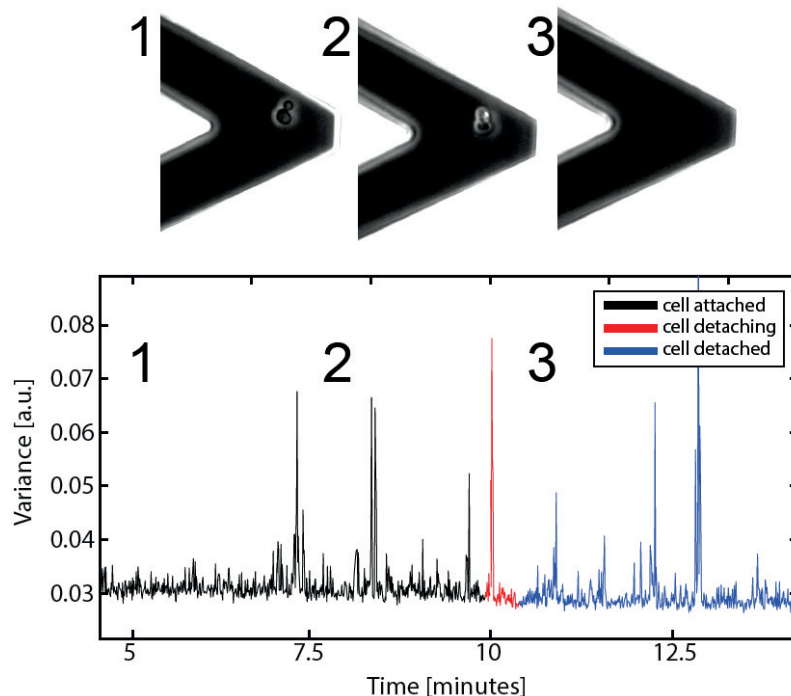


**Figure 3.36** *Saccharomyces cerevisiae* cell attached to the cantilever apex and investigated using nanomotion technique. Oscillatory signal's variance shows a slight reduction of the noise level after detachment of a single yeast cell.

There are many studies focusing on growth-related movements of bacteria and their connection with susceptibility to antibiotics. Only a handful of them exploited bacterial motion with nanometer resolution and correlated the nanomotion with bacterial metabolism and antibiotic action. For instance, a study using a plasmonic imaging technique correlated a sub-nanometer movement of a bacterium with its metabolic activity, exposing it to either glucose or the antibiotic, which acted within a timeframe of minutes (304). Another example is the approach where mechanical fluctuations of bacteria are sensed by a quartz crystal resonator in an electrical bridge, by measuring the resonant frequency change and the associated phase noise (305). The study claims to detect antibiotic action against a non-motile *E. coli* strain only after 15 minutes of the ampicillin exposure.

Yet another study used cantilevers as picobalance for measuring the mass of a single cell, and found that the cell's mass fluctuates intrinsically, by 1-4% over the timescale of seconds, during the whole cell cycle (306). Those fluctuations are found to have fast (around 2s) and slow (around 18s) components with amplitudes of around 15 pg. Moreover, the mass oscillations continued until the cell death. The authors concluded that mass fluctuations depend on cellular energy and fluid exchange, bringing them in close correlation with physiological processes and metabolism. These findings might be brought in connection with the cantilever fluctuation phenomena, as the oscillations are also in the low frequency range and present until the cell dies.

#### *Thermal effect*

The core of a thermal effect assumption is the fact that there is a heat production during the metabolic activity of cells. Studies using isothermal microcalorimetry have been conducted for determination of antimicrobial susceptibility (307,308). The principle of the method is to convert the heat flow rate or the total accumulation over time, produced by bacteria inside the measurement chamber into a voltage signal, in constant temperature conditions. During a logarithmic phase of growth, bacteria are expected to have a specific heat production rate of about 2 pW (309).

Cantilever coated with a gold layer (as in the case with all cantilevers used in presented experiments), acts as a bimetal. It bends with temperature changes, as surface stress is generated due to the difference in thermal expansion coefficients of the silicon substrate and the gold coating, even in femtojoule range (310). Small pulses of heat might be sufficient to induce short-termed vibrations of the cantilever that we are seeing in our signal.

In fact, a study that used microcalorimetry to follow heat release of bacteria during the bacteriophage infection process showed a very similar pattern in the signal as the one presented on the **Figure 3.13** (309). At first, the heat increased following an initial burst of cells, then dropped to a plateau before decreasing constantly.

Yet another study stresses out the significance of heat effects in biological systems by studying the diffusion of enzymes (311). They have found that the heat released during the catalysis creates an asymmetric pressure wave, displacing the center of mass of the enzyme via chemoacoustic effect.

Perhaps the most convenient way of investigating the heat release effect is to take a simpler biological system and test it specifically. In example, the metabolic processes of mitochondria are well-known,

as well as the effect of several disruptors and inhibitors. DNP (2, 4-dinitrophenol) is an uncoupling agent that acts as a proton ionophore, that is, transfers protons from one side of the membrane to the other. It disrupts the proton gradient, necessary for the active metabolic processes in mitochondria and inhibits the electron transport. Therefore, instead of the ATP production, the energy stored in the gradient is released as heat. **Figure 3.37** illustrates the effect of DNP on mitochondrial activity via nanomotion detection. As shown, switching from the buffer into the solution containing the necessary substrates for the respiration, the activity increases. However, once DNP is added and the electron transport is stopped, instead of a decrease, a slight increase has been observed. This may mean that the released heat influences the oscillations of cantilever as a bilayer.

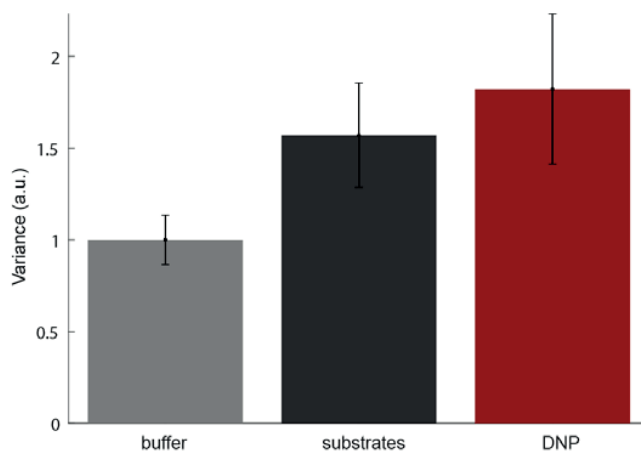


**Figure 3.37** Mitochondrial respiratory activity detected via nanomotion technique. The attached mitochondria were subjected to three conditions as follows: respiratory buffer, buffer with the addition of substrates, and with DNP.

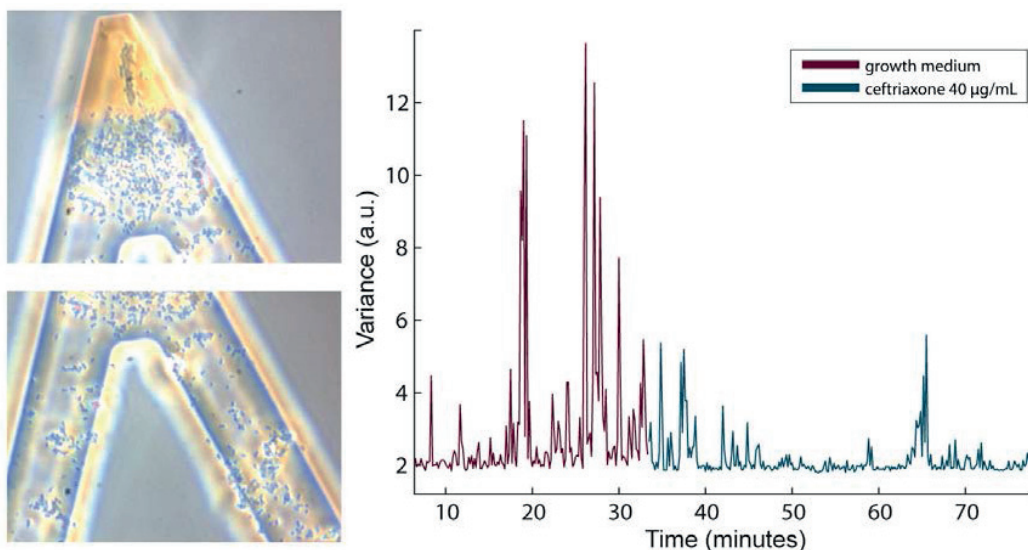


**Figure 3.38** Cantilever coated with gold only on its apex was used in a nanomotion experiment to investigate the response of *Staphylococcus aureus* against ceftriaxone.



As gold coating creates the bimetallic effect, we conducted an experiment using the cantilevers with coating only on the cantilever apex, and not over the whole cantilever surface. The image of the cantilever is shown on the **Figure 3.38**. Results are showing a decrease in oscillatory movement, even with such a cantilever setup, with a very small bimetallic effect. It would be hard to quantify the amount of decrease due to inability to attach bacterial cells at the same position and in the same amount across experiments. However, the results suggest that a thermal effect, if exists, would not have a dominant role in the overall signal, at least in more complex biological systems like bacteria or mammalian cells.

#### *Optical effect*

The surface plasmon resonance is a well-established optical detection technology for studying biomolecular interactions in real time. The principle is that the laser light is reflected off the backside of a sensor-chip surface into a detector. At a certain incidence angle (resonance), electrons on the surface are excited and in resonance (surface plasmons), which is a condition very sensitive to surface processes. The characteristics of surface plasmons depend on the refractive index of the dielectric material within 100 nm on the surface, and the change in refractive index alters the coupling efficiency and the optical phase of the reflected beam. One study used such a technique to test the effect of antibiotics on bacteria (312). Since the focus was to detect refractive index changes in the bacterial cells, authors used ampicillin – an antibiotic that inhibits the synthesis of the cell wall. They saw a change in refractive index of *E. coli* cells after 30 minutes of ampicillin exposure. Authors also used other antibiotics, showing a possibility of indirect changes in refractive index of bacteria after the exposure to antibiotics with different mode of action.

To obtain more information concerning the overall optical effect on nanomotion signal, a set of control experiments has been done. Cantilever resides on a large silicon nitride chip, that is similarly coated with gold on one side. The chip surface does not oscillate, as its thickness is rather large. Therefore, the chip was used as a stiff substrate with similar chemical composition. Experiments were done by collecting nanomotion data from the cantilever or the chip surface, in bacterial suspension or with the attached bacteria. The idea was to check the contribution of the optical effect, and the first experiment was to see whether diffraction from bacterial cells in solution would make an impact on the signal. Therefore, we were collecting data from the chip surface and introducing bacterial suspension into the analysis chamber. **Figure 3.39** shows the collected deflection from the chip while it was in growth media alone, with bacterial suspension at optical density of  $OD_{595} = 0.13$ , and in presence of the antibiotic. Both deflection signal and the resulting FFT spectrum do not show any visible difference among the three conditions. This means that the bacterial suspension at the tested optical density does not influence the signal.

The next step was to collect signal from the chip surface, but this time, with the bacteria attached to it. **Figure 3.40** represents data obtained from the chip surface in a clean medium, bacterial suspension and the suspension enriched with the antibiotic. An obvious change in the signal occurs once the bacteria were attached. The fact that bacterial cells are placed in one plane on a reflective surface does influence the signal. Noise is increased, predominantly in  $1/f$  region. However, the addition of the antibiotic does not seem to affect the signal or noise levels.

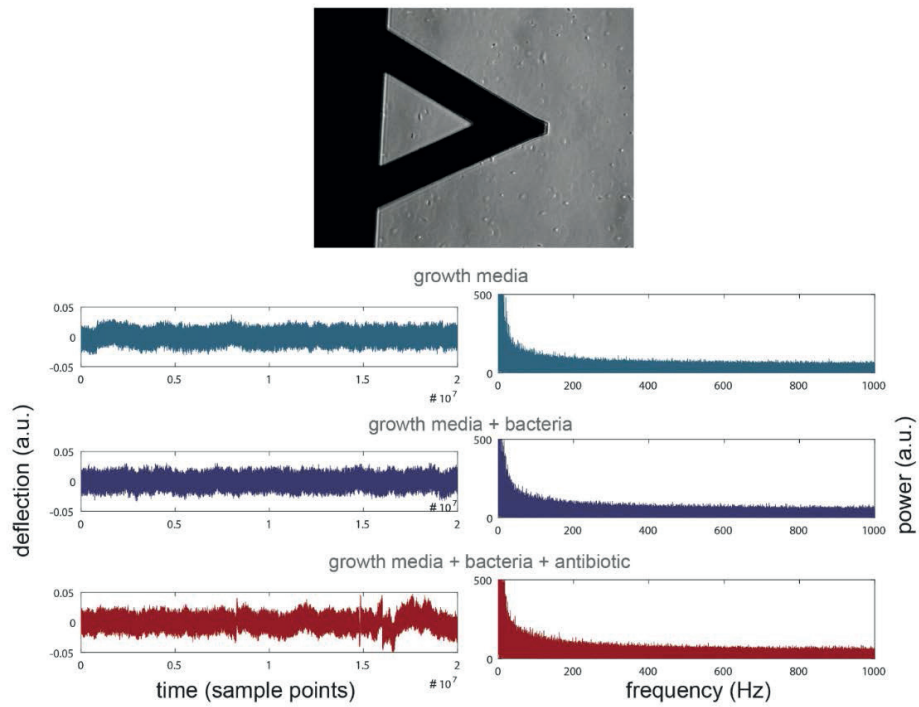


**Figure 3.39** Chip surface in bacterial suspension. Deflection data and corresponding FFT of the signal from the chip surface under: growth media, growth media with bacterial suspension, and antibiotic in addition to the latter.

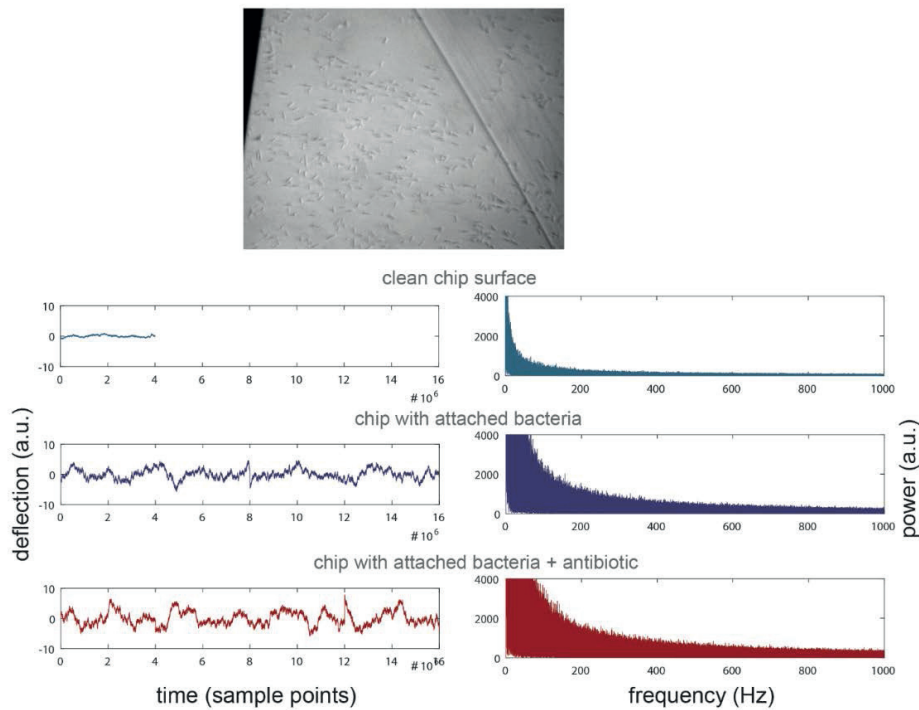


**Figure 3.40** Chip surface with the attached bacteria. Deflection data and corresponding FFT of the signal from the clean chip surface, the one with bacteria attached and with the introduction of antibiotic.

The last set of experiments included cantilever with attached bacterial cells under retracted configuration (as in regular nanomotion experiments), and in approached state (on a glass substrate) (**Figure 3.41**). During the measurements, the cantilever was kept close to the surface and switched from one to the other state under conditions of growth medium and the antibiotic. Retracted state gives the same results as all our previously presented nanomotion experiments, with reduction of the cantilever oscillations and a large decrease in  $1/f$  and white noise below 1000 Hz. However, the approached state of the cantilever produced no difference between the two conditions. In combination with the previous experiment, it can be concluded that the optical effect taking place with the attachment of bacteria, does not affect the signal reduction once they are killed.

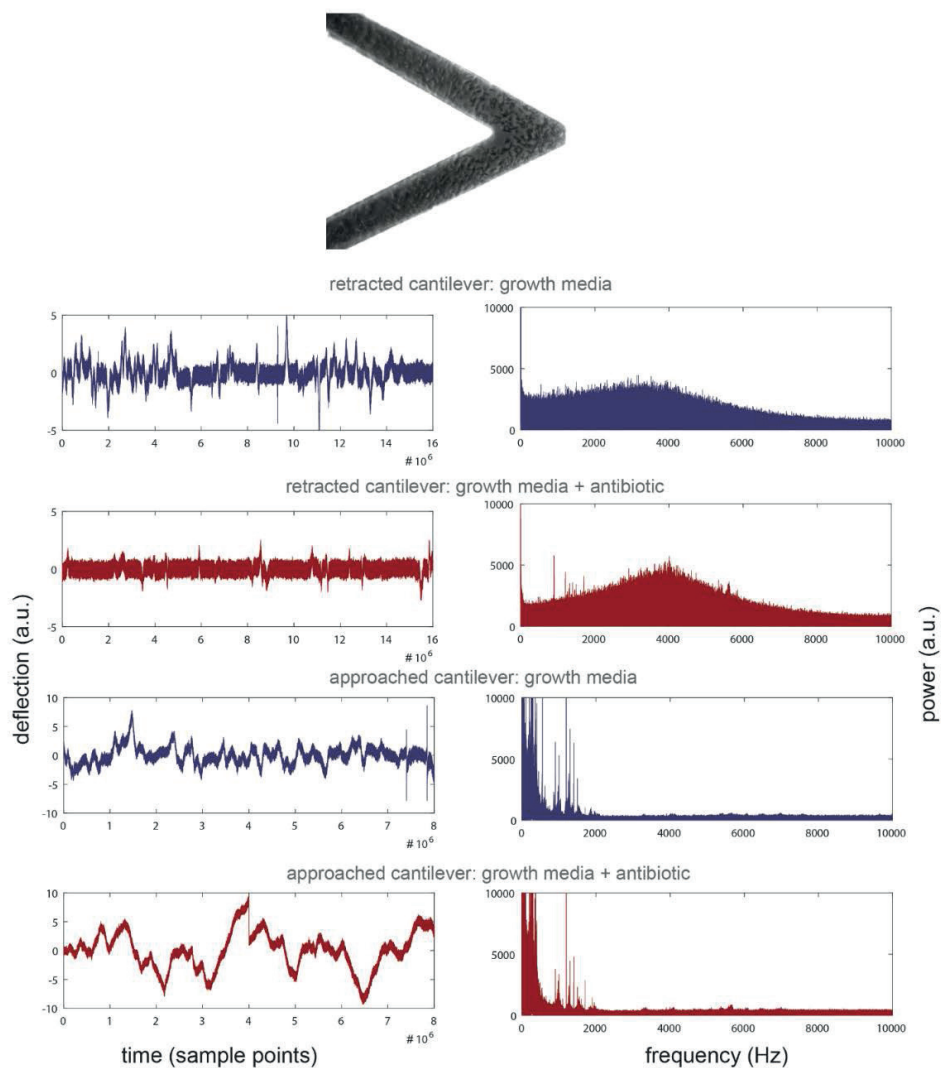


**Figure 3.41** Cantilever with attached bacteria under retracted and approached states. Both states are subjected to clean growth media and the one enriched with antibiotic.

### Local pH effect

It is well-known that the glucose metabolism in bacteria leads to release of organic acids (pyruvic, citric, and lactic acids). As a consequence, a rapid extracellular acidification occurs due to the catabolism of sugars (313).

A study on single-walled carbon nanotubes configured as field-effect transistors to detect *E. coli* cells below 100 cfu/mL has shown the expanded applicability for real-time detection of their metabolic activity and susceptibility to antibiotics (314). As cells are introduced into the measuring system, current drops over time, but not as an effect of their negatively charged surface. Authors hypothesize that the discharge of organic acids into the nano-gap between the nanotubes and the bacterial surface would significantly alter the local pH (the local electrochemical environment) at the vicinity of nanotubes, and therefore change the conductance. Their results support this hypothesis.

On the other end, cantilevers have been exploited for pH sensing purposes (315–318). The principle is the ionization of surface species on it as a function of solution pH. As one surface accumulates charge proportional to the pH of the surrounding media, the cantilever deflects as a result of differential surface stress (319).

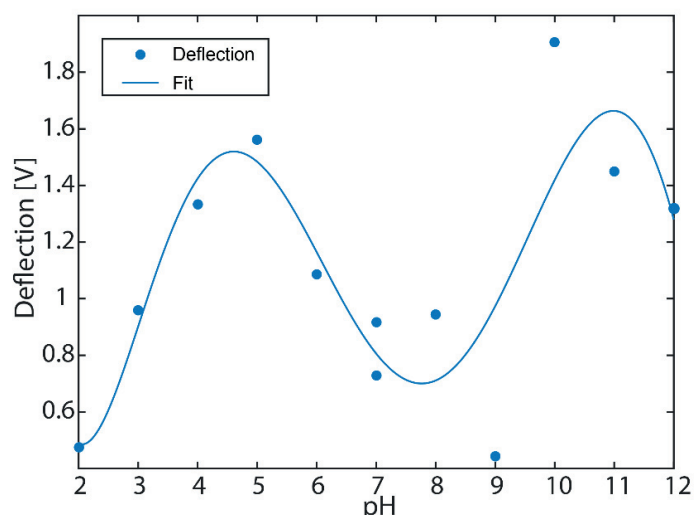


Figure 3.42 Deflection of a cantilever in response to different pH.

Boric acid, citric acid and tertiary sodium phosphate have been used to create solutions in a complete range of pH, according to the published protocol (320). To minimize ionic strength contribution to the cantilever bending effect, NaCl has been added to each solution according to calculations to keep it constant. **Figure 3.42** represents the deflection of the glutaraldehyde-functionalized cantilever subjected to different pH. One could imagine an effect of local pH changes due to the release of catabolized acids in the near vicinity of the cantilever surface, reflected as multiple short-termed deflections.

### 3.7.4 Conclusion

So far, it has been shown that despite the absence of flagellar motility, the oscillatory motion of the cantilever is well above the background noise levels due to the attached cells. It is not yet clear nor proved whether the effect that drives motion is the mechanical perturbation of the cell wall, the metabolic heat release, the change in optical properties or the local acidification. It is very likely that multiple effects are taking place at the same time. Depending on a setup, one effect might dominate the others. As an example, the attachment of highly dense layer of bacterial cells on a reflective surface, such as the cantilever golden back-coating, increases the noise of the signal on the photodiode. However, given that the antibiotic exposure does not reduce the very signal, mechanical motion of the cantilever has a dominant role in such a case, while the optical effect serves as an additional noise source. It should be pointed out that prokaryotic cells, as eukaryotes, contain internal cytoskeletal structures that exhibit a variety of dynamic behavior (321). These include the cellular reorganization of the cytoskeletal elements and oscillatory behavior of some helical elements. Different processes, acting on different time scales are taking place, make the signal an overall average of those events.



## Chapter 4: Conclusion

### AFM – a versatile tool for quantitative imaging

Nanomechanical properties of living cells have an important role in many cellular processes: mechano-transduction, motility and adhesion, morphogenesis, metastasis, etc. Proper functioning of certain biological processes in them strongly depends on a specific spatial compartmentalization of molecules in addition to chemical and molecular specificity. Therefore, knowing not just how elastic or adhesive the cell is, but also its spatial organization of such properties, is crucial to the understanding of processes that govern cell function. Time-varying interaction forces between the vibrating tip and the sample in a dynamic imaging mode contain detailed information regarding morphological, elastic, adhesive and dissipative response of the sample. In combination with a high spatial resolution, maps of the sample are obtained, either in terms of mechanical properties or the interactions between the tip and the sample surface molecules.

The introduction of this thesis, where details of the atomic force microscopy are presented, and the start of the second chapter, show the vast application area and the importance of AFM techniques in biological systems. The corresponding sections represent only a tip of an iceberg when it comes to the technique's utility. Study on relationship between changes in the osteoblast cytoskeleton architecture and different mechanical conditions that simulate space flight environment, is showing an increase in Young's modulus in the nuclear area, compared to the values when cells were kept in static condition. This is an important realization as it helps pinpointing what is the exact cause of the loss of bone mass during extended space flights, and would eventually help in preventing this critical biomedical obstacle. A similar technique was applied to investigate cell-surface localization and distribution of the *B. pertussis* adhesins using an antibody-functionalized AFM tip, which showed a non-homogeneous pattern. Moreover, these experiments showed a force-induced reorganization of the adhesin in the surface of the cells, which could explain a reinforced adhesive response under external forces. This single-molecule information contributes to the understanding of basic molecular mechanisms used by bacterial pathogens to cause an infectious disease and to gain insight into the structural features by which adhesins can act as force sensors under mechanical shear conditions. In a similar regard, an approach to plant cell investigation is also discussed.

All sections from the second chapter share that investigating surface properties of living cells at the molecular level is far from being an easy task, largely due to the complex and rather dynamic nature of the cell and the cell wall constituents. However, important information can still be obtained, connecting cell physiology and pathology to their nanomechanical properties, and the applicability of AFM techniques in this regard will continue to grow in the time to come.

### Nanomotion – a promising tool for viability assays

The insurgence of new, rapidly developing health threats is one of the most urgent issues of the modern world. The fast rising of new antibiotic-resistant bacterial strains and the need for rapid diagnostic tools for the most common diseases, call for the development of new and reliable tools for the analysis of the response of biological specimens to chemical or pharmaceutical stimuli. In this framework, there is a growing interest in tools capable of nanoscale characterization of biological systems and single-cell level analyses of their biological status. Chapter 3 contains experiments and suggestions that nanomechanical sensor-based devices can fulfil such a task. However, care should



be taken during the preparation, measurement and data analysis processes of this technique to achieve reliable results. Therefore, the chapter starts with details and best practices of the method, and continues with optimization of the cantilever functionalization and sample attachment procedures.

These novel devices, named nanomotion sensors, have a multitude of applications ranging from microbiology to cell biology. For instance, we have employed them to determine the drug-resistant profile of bloodstream bacterial infections in less than one working day, directly from positive blood culture bottles, without the need of bacterial subculture. The management of bloodstream infection, a life-threatening disease, largely relies on early detection of infecting microorganisms and an accurate determination of their antibiotic susceptibility, to reduce both mortality and morbidity. Based on the variance of the sensor movements, we were able to positively discriminate the resistant from the susceptible *E. coli* strains in 16 out of 17 blindly investigated cases. Furthermore, we defined a variance change threshold of 60% that discriminates susceptible from resistant strains.

One of the most important application areas of such sensors is towards rapid antimicrobial susceptibility of slow-growing bacteria. In such a case, time to fully characterize an infectious agent after sampling, as well as to find the right antibiotic and dose, is crucial factor in the overall success of patient's treatment. A low-cost nanomotion device is able to characterize *B. pertussis* sensitivity against specific antibiotics within several hours, instead of days or weeks, as it is still the case with conventional growth-based techniques. We could discriminate between resistant and susceptible *B. pertussis* strains, based on the changes of the sensor's signal before and after the antibiotic addition. Furthermore, minimum inhibitory and bactericidal concentrations of clinically applied antibiotics were compared using both techniques and the suggested similarity is discussed.

Expanding the applicability of the technique, we further demonstrated that the method can also be applied to sub-cellular organelles, such as mitochondria. Mitochondria are involved in cellular energy production and are present in most eukaryotic cells. Nowadays, it is believed that mitochondria were originally prokaryotes that colonized eukaryotic cells and that live in an endosymbiotic way ever since. We presented that mitochondria are also animated by nanometer scale oscillations that depend on their metabolic state and that stop once they are inhibited. This observation opens novel avenues to investigate the numerous mitochondria-related diseases in humans.

Understanding the toxicity characteristics of the potential drug is the major inspiration for the development of high-throughput screening platform for the early-phase drug discovery. Experiments concerning cancer cells, where we studied six different human cancer cell lines: three doxorubicin-sensitive and their three MDR counterparts, show that with the increase of doxorubicin concentration, deflection of the cantilever with attached susceptible cells decreases, whereas in case of drug resistant cell lines, the drop is not observed. Similarly to the signal interpretation from bacterial sources, the best interpretation of these results is that, in the case of susceptible cells, the loss of cell viability caused by the exposure to the drug halts all biological-related movement of the sensor. The resistant counterparts, on the other hand, retained their metabolic activity and viability, and the movement increase could indicate a metabolic response of the cells to the drug pressure.

Many fundamental biological processes manifest mechanics on a pico-newton scale forces, nanometer scale displacements, elasticity changes and mass variations. These changes easily fall in the range of the detection capabilities of nanomechanical systems such as the one described. As presented, the technique has been successfully used in studies regarding bacterial cells, mitochondria, and cancer cells. The attachment of viable living systems to the cantilever produces nanometer scale oscillatory movement of the cantilever. These fluctuations could be caused by very diverse metabolically related phenomena. Therefore, they allow determining the viability and reaction of cells to a specific stimulus. However, much work still needs to be done in order to precisely determine the source of such oscillatory motion. In a few attempts presented in the last section of the thesis, the aim was to investigate several hypotheses about the origins of nanomotion. It is very likely that not a single effect governs these oscillations, but a synergy of a few effects, where, depending on a particular scenario, one effect may dominate the others. Segregating a single effect and testing it individually turns out not to be an easy task, and future experiments are surely needed to decipher the exact cause of the cantilever oscillation and to discover whether mechanical nanomotion that stems from living systems is the only effect that takes place. Up to then, the application area of the technique is predicted to bloom further, taking place in many laboratories, clinical and even space research institutions.

## Appendices

---

# Signal Analysis Script - Nanomotion

## Table of Contents

.....	1
Loading files (just the vertical deflection) .....	1
Plot of the imported file(s) .....	2
Sampling frequency .....	3
Flattening .....	3
Plot of the flattened signal(s) .....	4
Variance Calculation .....	5

- **Author:** Petar Stupar - EPFL, Lausanne
- **Date:** August 10th 2016
- **Contact:** [petar.stupar@epfl.ch](mailto:petar.stupar@epfl.ch)

The script allows processing of Real-Time Measurement files obtained using JPK instruments. It is easily adaptable for any other files containing nanomotion signal. After running, it will open a file dialog to choose multiple files intended for the analysis, import them into a variable  $y$ , and use the sampling frequency stated. Imported signals are then flattened using a jumping window technique (of desired size), utilizing a linear (or a polynomial) fit in each window. After flattening, jumping window is also applied in order to calculate the variance in the desired time frame. The final step is plotted and represented as a line plot of variance evolution through time.

## Loading files (just the vertical deflection)

```
% Clears the workspace
clear all
clc

% Opens a file dialog and allows you to choose multiple files for the
analysis
[FileNames PathNames]=uigetfile('*.out', 'Chose files to
load:', 'MultiSelect', 'on');
FileNames=cellstr(FileNames);

h = waitbar (0, 'Loading...');
for i=1:length(FileNames)
    c= [];
    Path{i}=fullfile(PathNames, FileNames{i});
    fileID{i} = fopen(Path{i});
    while ~feof(fileID{i})
```

The following line is to be changed according to the file structure If files have only single column containing the data, use:

```
C = textscan(fileID{i}, '\t%f', 10000);

% Otherwise look for the "Vertical Deflection" column, and star others
% This part is for opening *JPK Real-Time Measurement* files
% Comments are ignored, in this case, character "#"
    %C = textscan(fileID{i}, '%*f %*f %f %*[\n]', 10000,
    'CommentStyle', '#');

    c=[c,C'];

end
fclose(fileID{i});
y{i}=cell2mat(c');

% Print file names without any extension
test=regexp(FileNames{1}, 'out', 'ONCE');
if isempty(test)
    Names{i}=FileNames{i};
else
    [~,Names{i}]=fileparts(FileNames{i});
end
waitbar (i/length(FileNames),h);
end

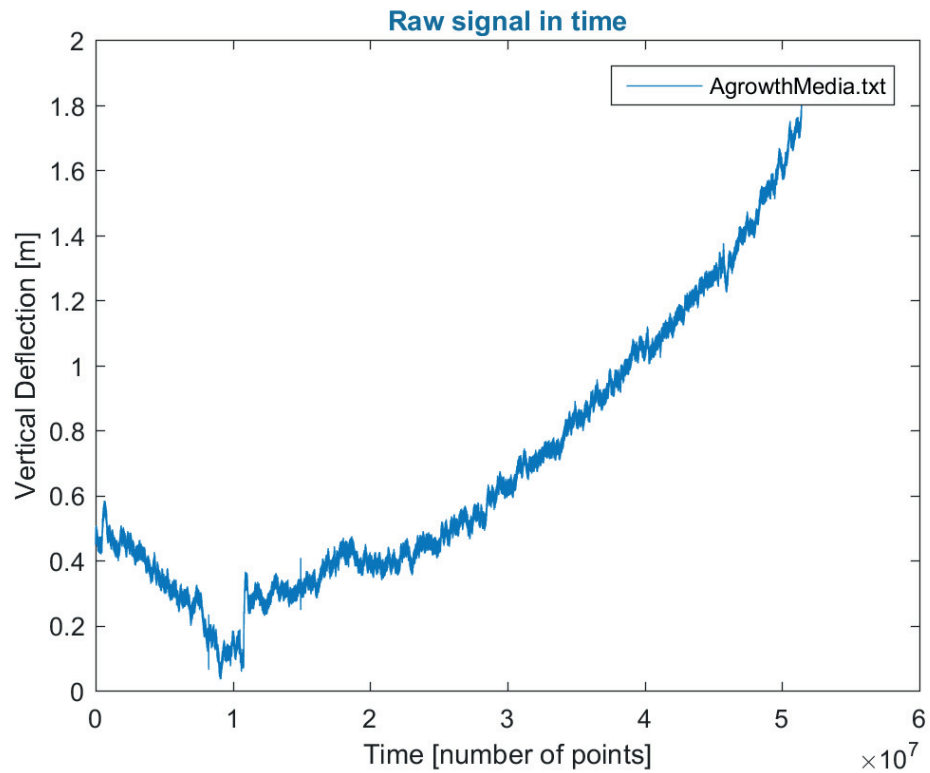
Names=cellstr(Names);
close(h);
disp('Files are loaded successfully!')
clear ans c C fileID FileNames h i mm Path PathNames test
```

*Files are loaded successfully!*

## Plot of the imported file(s)

This plot is to be avoided due to unnecessary memory consumption. It represents the necessity to use flattening for further analysis.

```
fileNumber = 1;
figure('Name', 'Raw Data Plot')
plot(y{fileNumber})
title('Raw signal in time', 'Color', [0 0.4 0.6])
xlabel('Time [number of points]')
ylabel('Vertical Deflection [m]')
legend(Names{fileNumber})
```



## Sampling frequency

This part automatically sets the sampling frequency of 20kHz Change according to the experimental setup.

```
ft = 20000;
```

## Flattening

The following code flattens the signal as described in the description.

First, an  $X$  axis is needed for fitting

```
for i=1:length(y)
    x{i}=(1:length(y{i}))';
end
```

The window size is configured here (incorporated in the script for easier flow). It should be stated in seconds.

```
n = 200; % Window size of 200 seconds
```

Now fitting takes place, saving coefficients into a variable *coeffs*, which is a cell array.

```
% Order of the polynomial fit, default = 1;
order = 1;
```

```
n = n * ft;
for ii=1:length(y)
    for k=1:length(y{ii})/n
        coeffs{ii}(k,:)=polyfit(x{ii}(n*(k-1)+1 : k*n),y{ii}
(n*(k-1)+1 : k*n),order);
        yfit{ii}(k,:) = polyval(coeffs{ii}(k,:), x{ii}(n*(k-1)+1 :
k*n));
    end
end

% Setting vectors within the cell array to be of the same size
for ii=1:length(y)
    dd{ii}= subsref(yfit{ii}., substruct('()', {':'})).';
    y{ii}=y{ii}(1:length(dd{ii}))-dd{ii}';
end

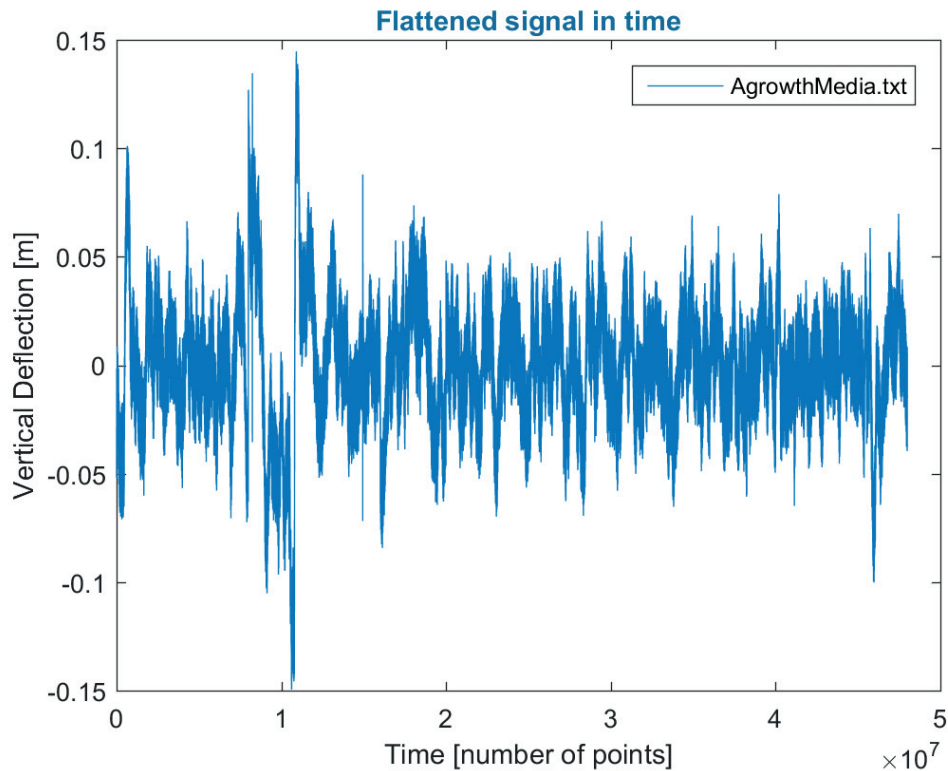
clear coeffs dd i ii ws yfit
```

**Please note that at this stage, the initial variable `y` has been overwritten!** If both raw and flat signals are desired, change the variable name in the last FOR loop.

## Plot of the flattened signal(s)

This plot is to be avoided due to unnecessary memory consumption. It shows the flat version of the chosen signal.

```
figure('Name', 'Flat Data Plot')
plot(y{fileNumber})
title('Flattened signal in time', 'Color',[0 0.4 0.6])
xlabel('Time [number of points]')
ylabel('Vertical Deflection [m]')
legend(Names{fileNumber})
```



## Variance Calculation

The final step of our processing aim is to calculate the variance in a windowed manner, and show how it evolves in time. The code below does that and plots variance lines of all imported and flattened signals.

Variance window is configured here. It is chosen to be 10 seconds, but can be changed if desired.

```
n = 10; % Window size of 10 seconds
```

Now, variance is calculated in a jumping window, or in chunks. Then, X-axis is also generated and presented in minutes.

```
n = n * ft;
for i=1:length(y)
    for k=1:length(y{i})/n
        a(k)=var(y{i}(n*(k-1)+1:k*n));
    end
    v{i}=a;
    a=[];
end

t{1}=1:length(v{1});
for i=2:length(y)
    t{i}=t{i-1}(end)+[1:length(v{i})];
```

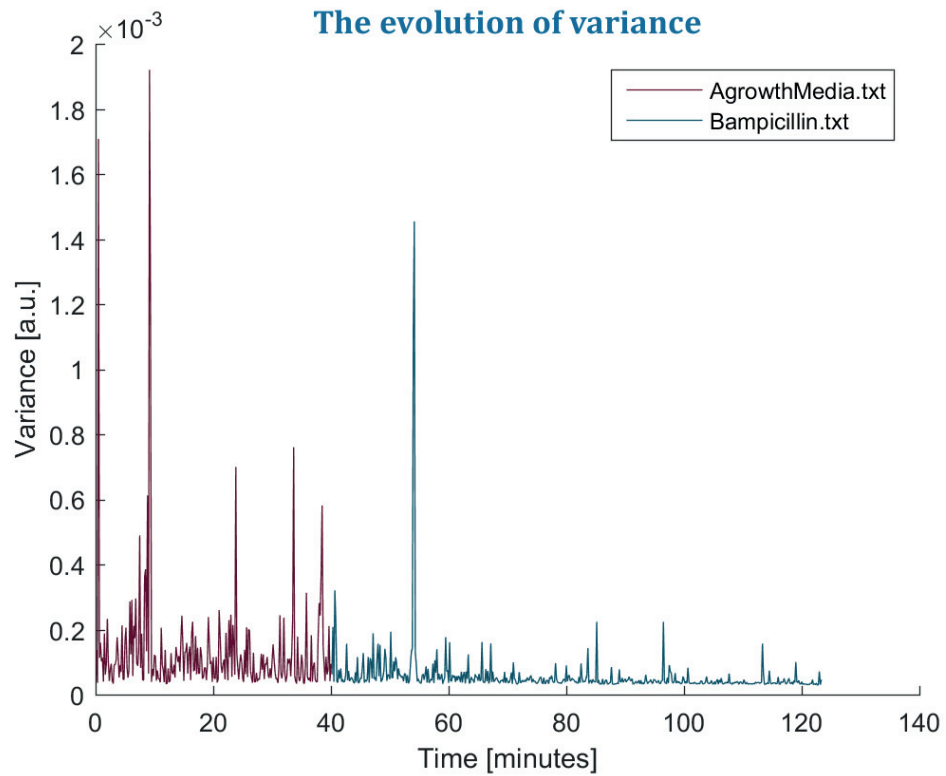


```
end

Color = repmat([0.4 0.1 0.2], [0 0.3 0.4], [0.1 0.5 0.8], [0.3 0.3
0.5], [0.5 0.7 0.6]),1,20);

figure('Name', 'Variance Evolution');
hold on
for i=1:length(v)
    plot(t{i}.*(n/ft)/60, v{i}, 'Color',Color{i})
end

xlabel('Time [minutes]');
ylabel('Variance [a.u.]');
title('The evolution of variance','Color',[0 0.4
0.6], 'FontName','Cambria','FontSize',13);
legend(Names)
%axis([0 inf 0 16e-4])
```



Published with MATLAB® R2015b

## NanoSignal: Signal analysis toolbox



Apart from scripts in MATLAB, to analyze the signals, record the analysis steps and prepare the results for presentation, a complete software solution in C++ has been developed. Qt library has been used for graphical user interface design and multithreading, while STL standard library for containers, data manipulation and algorithms. The signal analysis tool, named **NanoSignal**, has been published under GNU General Public License (GPL v3), and is available on the GitHub repository on the following page: [www.github.com/stup4r/NanoSignal](http://www.github.com/stup4r/NanoSignal).

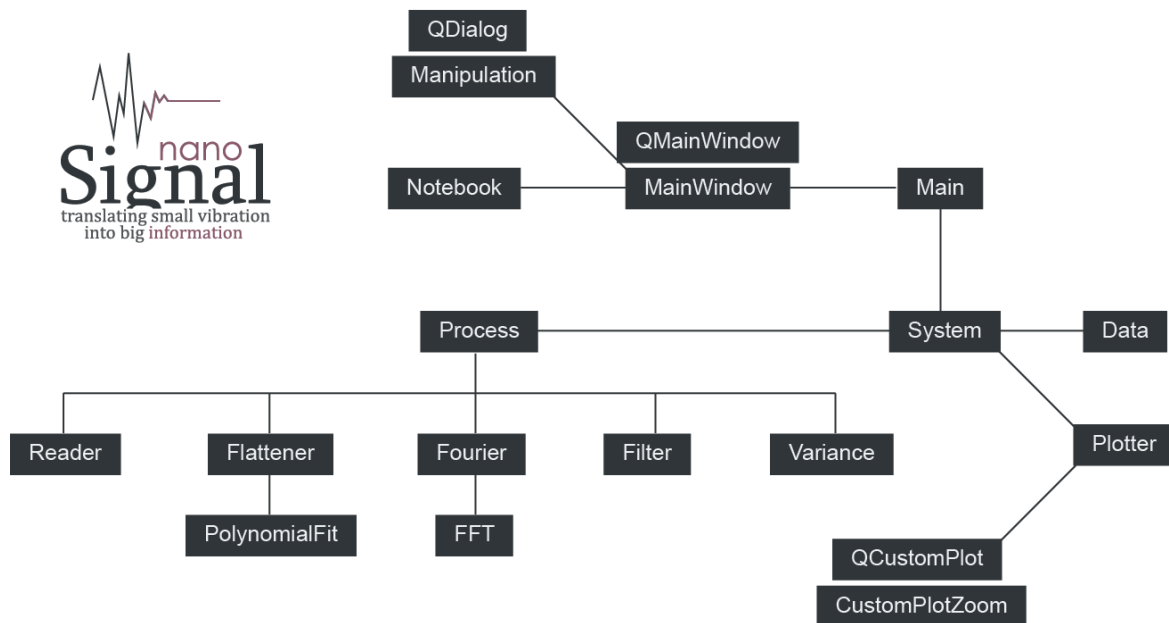


**Figure A1** NanoSignal: translating small vibration into big information. A simplified class diagram without showing methods and member variables.

NanoSignal class diagram is presented on the **Figure A1**, in a simplified version, without showing member variables or methods. Within the main function, three entities are initialized: the application programming interface (API), the main window and the object of the class *System*. The *Mainwindow* is responsible for getting the user input and transferring it to the appropriate class, *System* typically. It contains all the public slots for buttons and menu actions. *System* class is the core of all the operations and communicates with *Process*, an abstract class, used as a parent for all the other classes with calculation responsibilities (*Reader* – file import, *Flattener* – data fitting, *Fourier* – FFT analysis, *Filter* – data filtering, and *Variance* – variance calculations). *System* also talks to *Plotter*, which contains methods for different plotting approaches and that uses a sub-classed *CustomPlotZoom*. Through the main application window, a user can do *Manipulation* and *Notebook* class instantiation, which summons new windows with data manipulation and reporting capabilities, respectively. **Figure A2** and **A3** are a screenshots of the program’s main window while several files are imported simultaneously (using multithreading), plotted and processed in different ways. There are possibilities of signal fitting with a polynomial fit, either in a windowed manner or to the whole dataset. Implemented filtering allows a moving average, while FFT calculates the Fourier transform of the chosen signal. Variance tab allows to create a variance evolution plot, bar charts, boxplots and has the possibility of applying a cutoff. All the plots and analysis parameters can be extracted and saved into a notebook, that can be further exported as a report in PDF format. This is important when testing signal analysis approaches, as it allows saving each step of the analysis in a very convenient way.

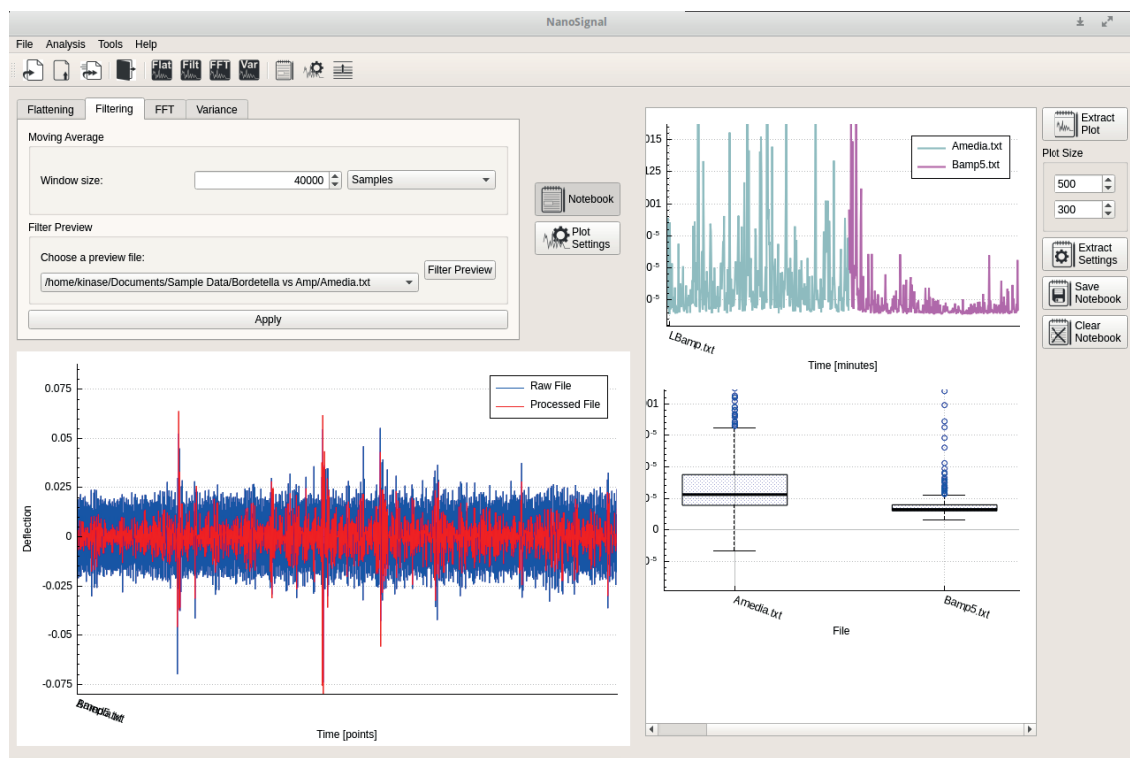


*Figure A2 NanoSignal screenshot. Main window of the application with open notebook and plotting widgets.*

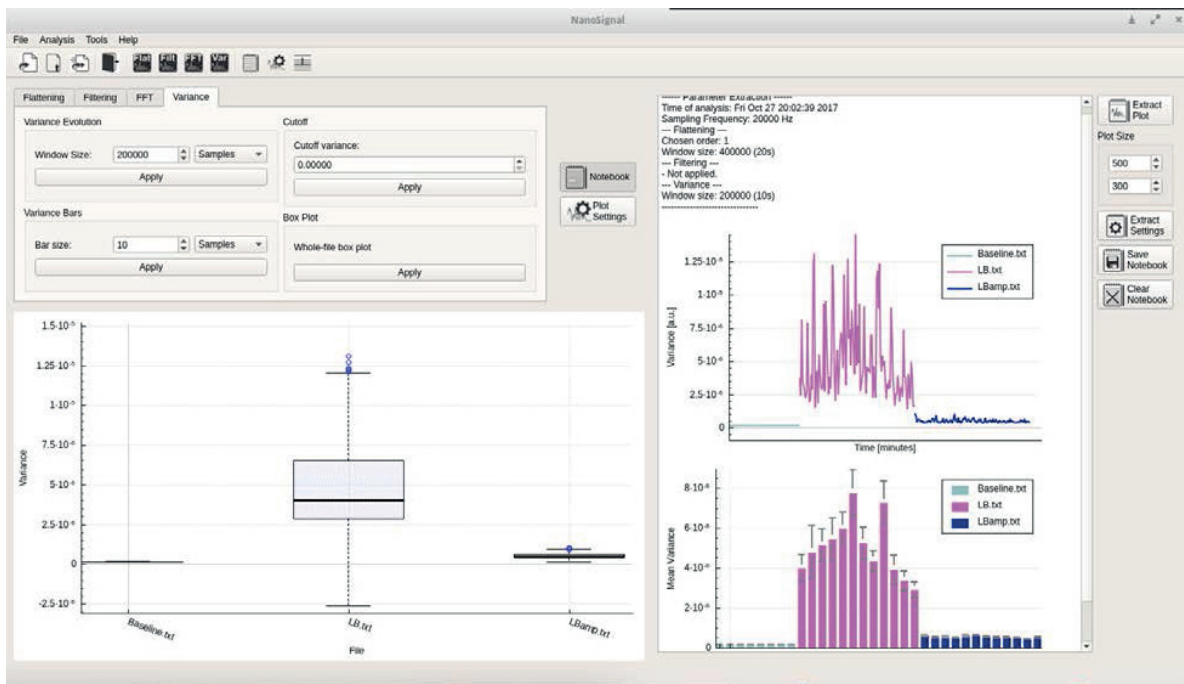


**Figure A3** NanoSignal screenshot. Main window of the application with variance calculation steps.

Listing of created classes, methods and member variables

A non-exhaustive list of classes, methods (*italic text*) and member variables (normal text) is presented. For more information, visit the stated GitHub link.

### Main

Main function.

```
QApplication a(argc, argv);
System system;
MainWindow w;
designSplash();
w.setSystem(&system);
w.show();
```

### MainWindow (QMainWindow)

Main Window class.

```
void setState();
void setSystem(System*);
void populateCombos(QStringList&);
void checkInputValues(bool, int);
private slots not listed
Ui::MainWindow *ui;
System *system;
Notebook notebook;
```

### *System*

Data manager class used for calling most of the processing objects, plotters etc.

```
void doImport(QStringList);
void doAppend(QStringList);
void doFlat();
void doFilt();
void doFFT();
void doVar();
void doVarCut(double);
void doVarBars();
void doVarBox();
void doSubsequentialPlot(int);
void doPlot(int, int);
void doPreview(int, int);
void doBarPlot();
void doBoxPlot();
void checkInputValue(vector<vector<dataType> >&, int&);
void doReorder(vector<size_t>&);
vector<string> getFileNames();
void setParam(std::string, int);
int getParam(std::string);
void setPlotWidget(CustomPlotZoom*);
std::map<std::string, int> getAllParams();
Data data;
CustomPlotZoom* plotWidget = NULL;
```

### *Data*

Data container. Contains the imported files, filenames, processed data, calculated values and parameters.

```
void reorderVec(vector<T> &v, vector<size_t> const &order)
void clearAll();
void reorderData(vector<size_t>&);
vector<string> fileNames;
vector< vector<dataType> > defData;
vector< vector<dataType> > varData;
vector< vector<dataType> > varMeans;
vector< vector<dataType> > statistic;
map<string, int> parameters;
```

### *Process*

An abstract class used as a parent for other processing classes (Flattener, Filter, Fourier, Variance, Reader).

The DataLink struct Helper struct that points to single filename, deflection and FFT file.

```
struct DataLink;
```

```
virtual void doProcessOne(DataLink&)=0;
```

```

void doProcessMulti(Data&);
QVector<DataLink> dataExtraction(Data&);
void setIsWindowed(bool);
void setOrder(int);
void setWindow(int);
bool isWindowed = false;
int order = 1;
int windowSize = 10;

```

#### *Reader (Process)*

Child class of Process that imports and appends files.

```

void doProcessOne(DataLink&);
void setIsDownsampled(bool);
void setDownSamplingStep(int);
bool isDownsampled = false;
int downSamplingStep = 200;

```

#### *Flattener (Process)*

Class that allows flattening of the signal. Class inherits from the Process class. doProcessOne is a member of the class Flattener and overrides the function from the mother class Process.

```

void doProcessOne(DataLink&);

```

#### *Filter (Process)*

Class that allows filtering of the signal. Class inherits from the Process class. doProcessOne is a member of the class Filter and overrides the function from the mother class Process.

```

void doProcessOne(DataLink&);

```

#### *Fourier (Process)*

Class that allows FFT calculation of the signal. Class inherits from the Process class. doProcessOne is a member of the class Fourier and overrides the function from the mother class Process.

```

void setSamplingFreq(int);
unsigned long getSizeN();
void doProcessOne(DataLink&);
int samplingFreq = 20000;
unsigned long sizeN = 1;

```

#### *Variance (Process)*

Child class of Process that calculates and manipulates variance.

```

dataType oneVariance(vector<dataType>&);
void doProcessOne(DataLink&);
void cutoffVariance(vector<vector<dataType>>&, double);
void averageBars(Data&);
dataType getMean(vector<dataType>&);

```

```
dataType getError(vector<dataType>&);
dataType getMedian(vector<dataType>);
void getBoxplotStat(Data&);
```

#### *Manipulation (QDialog)*

Manipulation window. Class contains necessary members and methods for function of a manipulation window. The window allows the change of sampling frequency, subsampling and file re-ordering.

```
void setVecList(std::vector<std::string>);
bool ifOrderChanged();
bool ifDownsampling();
void setSampleFreq(int);
int getSampleFreq();
int getNewSampleFreq();
void on_buttonBox_accepted();
Ui::Manipulation *ui;
std::vector<std::string> listNames;
bool orderChanged = false;
```

#### *CustomPlotZoom (QCustomPlot)*

Subclass of the QCustomPlot to allow zooming in. The class overrides mouse event methods to allow interactive zooming with right mouse key.

```
void mousePressEvent(QMouseEvent * event) override;
void mouseMoveEvent(QMouseEvent * event) override;
void mouseReleaseEvent(QMouseEvent * event) override;
bool mZoomMode;
QRubberBand * mRubberBand;
QPoint mOrigin;
```

#### *Notebook*

Notebook window class. The Notebook is used to write notes and extract graphs and settings. Class method names are self-explanatory.

```
void setTextEdit(QTextEdit*);
void extractPlot(QCustomPlot*, double, double);
void extractSettings(std::map<std::string, int>&);
void saveNotebook(QString&);
void clearNotes();
QTextEdit* notebookTextEdit;
```

#### *Plotter*

Plotting class that takes care of all the plot generation and parsing to the plotting widget.

```
string finePrintName(string&);
void setMinMaxRange(dataType, dataType);
void plotProcessPreview(vector<dataType>&, vector<dataType>&);
```

```
void plot(vector<dataType>&, vector<dataType>&, int);
void subsequentialPlot(Data&, int);
void varBarPlot(Data&);
void varBoxPlot(Data&);
void plot(Data&, int, int);
CustomPlotZoom* plotWidget;
dataType minRange = 0;
dataType maxRange = 1;
```

*PolynomialFit – additional header*

```
std::vector<T> polynomialFit(vector<T>& x, vector<T>& y, int n)
std::vector<T> linearfit(vector<T>& x, vector<T>& y)
```

*FFT – additional header*

```
void FFT(int dir, unsigned long m, vector<T>& x, vector<T>& y);
template<typename T> T power(T m);
```



## Bacterial attachment protocol

# Bacterial Attachment Protocol

*Petar Stupar*

## Chemicals and Items



- Ultra pure water
- ! Pay attention to have 0.055  $\mu\text{S}/\text{cm}$  conductivity (let the water run until you do)
- PBS
- ! Pay attention to mix the stock solution if on shelf for long time. Dissolved tablets.
- LB
- ! Pay attention to contamination! Dissolved ready-powder.
- Glutaraldehyde
- ! Pay attention to have it freshly open (not older than approx. 12 months), close rapidly!
- Hood work: gloves, tubes, eppendorfs, tips, pipettes, centrifuge, incubator, spectrophotometer
- Outside hood work: small Petri dish, parafilm, scissors, sharp tweezers, cantilevers, timer, microscope, patience!



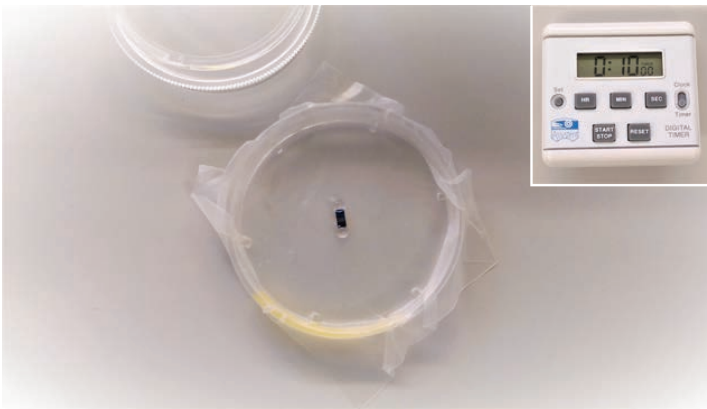
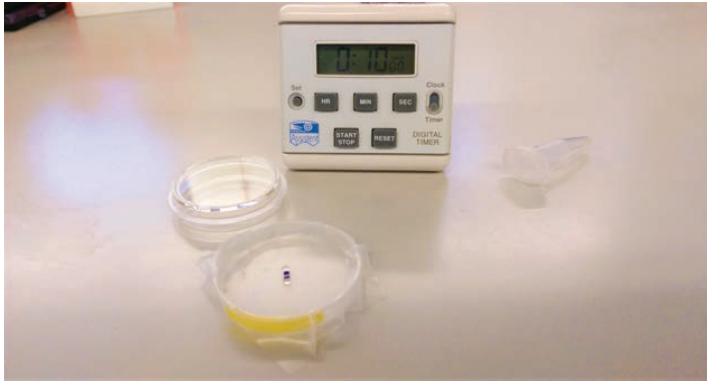
## Bacterial Growth

Bacteria should be grown in the appropriate media and conditions. As this varies with the type of bacteria, I will explain it for a standard strain *Escherichia coli* – DH5 $\alpha$ . I assume you know how to work with the hood under sterile environment and are careful with opening stock solutions (LB, PBS).

- Fill in the growth tube with approx. 6 ml of sterile LB
- From the -80°C freezer, quickly take a stock solution of *E. coli* (leave the freezer open)
- With a sterilized tip, scratch a frozen surface of the stock
- Disperse the scratched amount of bacteria in LB
- As quickly as possible, return the stock into the freezer (close the freezer)
- The freezer door must not be open for longer than several seconds (do the steps quickly)
- Place the tube with the appropriate holder into the incubator
- Conditions: 37°C, 160 rpm (shaking), overnight

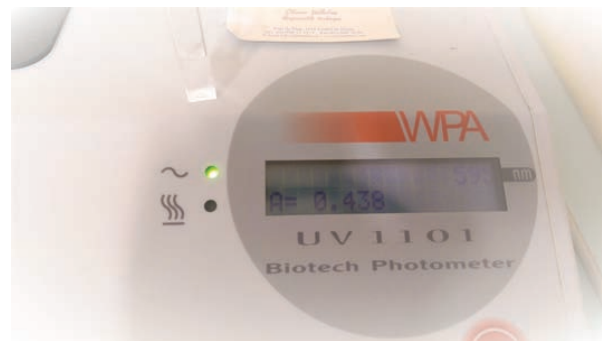
For optimum conditions in the experiments, you can use the exponentially growing bacteria by resuspending 1 ml of overnight culture into few milliliters of fresh LB early in the morning. After few hours, the stationary phase bacteria will resume and start (after lag phase) the log phase when greatest activity is observed.

## Cantilever Functionalization



- Cantilever will be functionalized with glutaraldehyde. Typically, stocks are aqueous solutions of 25%. It should be operated with care, in fume hood, quickly. Make a dilution to 0.5% in ultra pure water ( $20 \mu$  in  $980 \mu$  of ultra pure water). Make always fresh.
- Take a small Petri dish and parafilm the top part. Gently place a chip (straight from the box) and push it a bit with tweezers, so that it doesn't fall off.
- Place a droplet of previously diluted glutaraldehyde on both sides of the chip (coat all cantilevers).
- Wait for 10 minutes.
- Wash using 1 ml of ultra pure water – bend the Petri dish top towards the waste container and pour the water on its top end, so that the droplets fall and wash out the glutaraldehyde.
- Leave it dry few minutes (few minutes after drying, you should already have finished with the bacterial suspension preparation step described below – synchronize them).

## Bacterial Suspension Preparation



- After overnight growth (or log phase wait in the morning), place the suspension into the sufficient number of eppendorfs.
- Centrifuge them all (pay attention to the balance) at 5000 rpm for 5 minutes.
- The supernatant (LB) should be removed (by a pipette or vacuum machine).  
LB interferes with the bacterial attachment, so PBS should be used as a solvent for bacterial suspension in the attachment phase.

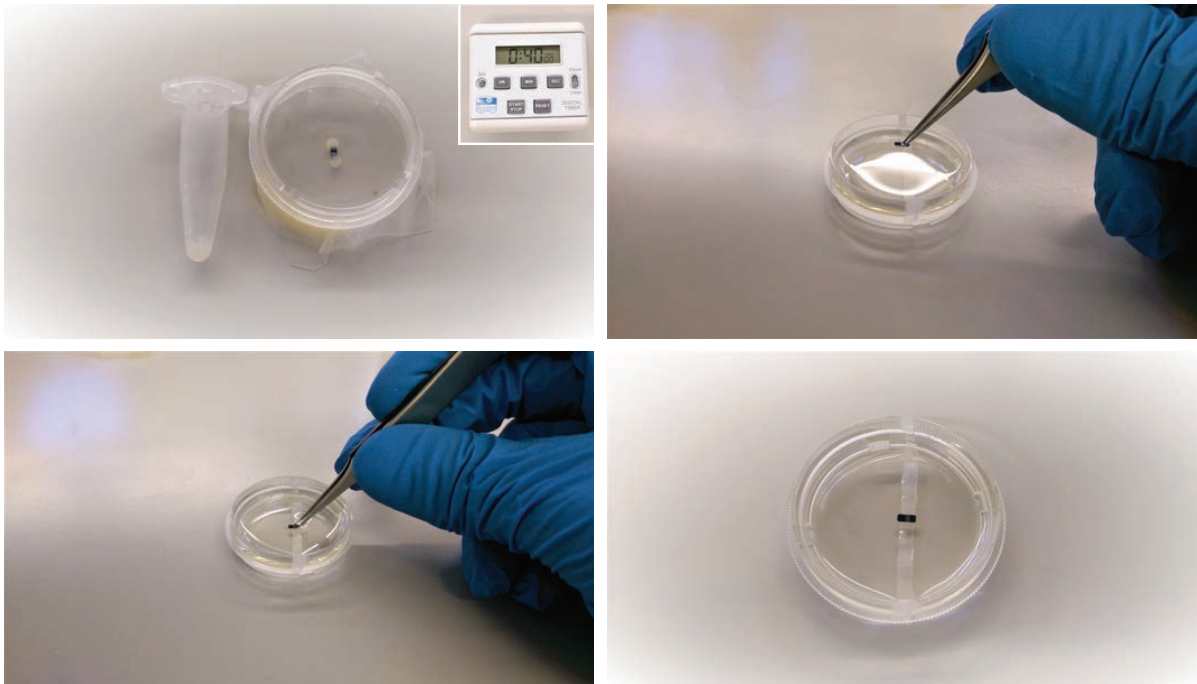
- ! • Resuspend (collect) all the bacterial pellets into 1 ml PBS (one eppendorf) and wash 3 times (each time spin and resuspend in a fresh 1 ml of PBS). This is very important.

Do not be lazy, you need to wash them 3 times.

- After the final wash, concentrate the pellet into a small quantity of PBS (depends on the amount of bacteria present, but typically around 150  $\mu$ l). The final suspension MUST be very concentrated, milky and viscous. If 10  $\mu$ l are placed into 1 ml of UPW or PBS, OD<sub>595</sub> gives around 0.4 – 0.6.

- The suspension must be mixed well (using a pipette), so that clumps do not form. Use it right away for the attachment.

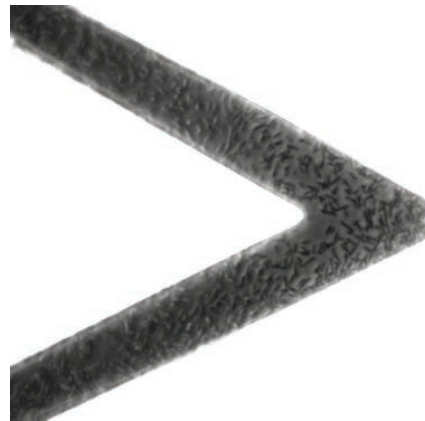
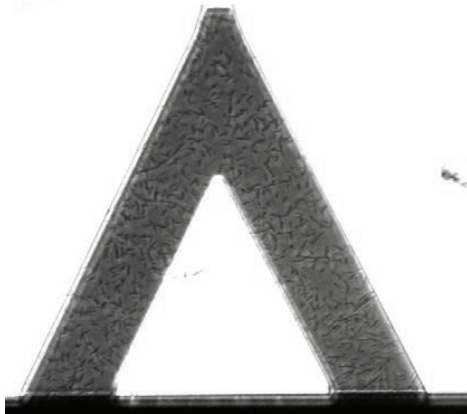
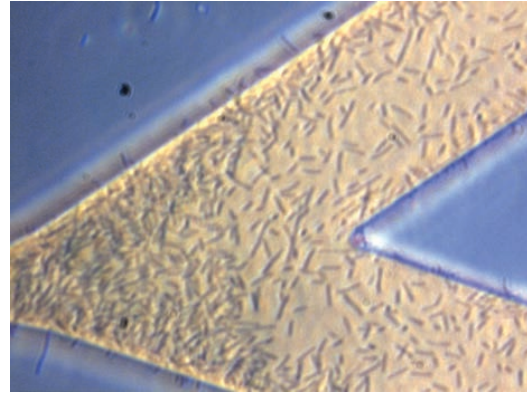
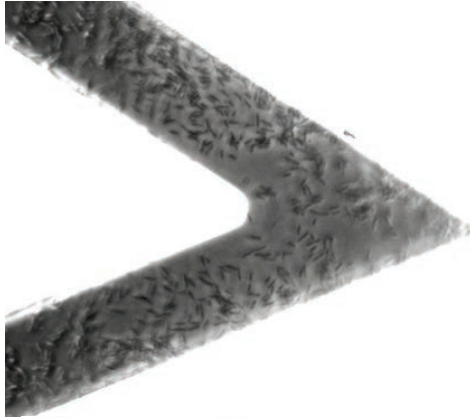
## Bacterial Attachment



- The suspension obtained previously should be used quickly, before the sedimentation of bacteria.
- Place approx. 10  $\mu$ l of suspension on both sides of the chip. Close with the bottom part of the Petri dish to avoid evaporation of the droplets.
- Wait 35 – 40 minutes.
- Nearing the end, place a thin line of parafilm on the bottom part of the Petri dish. Pour 3 ml of LB in it. Parafilm serves as a support to place the chip into LB without a risk of it floating around.
- ! • The following step introduces biggest variation in the attachment! Place the chip from the top of the Petri dish into the bottom part, immersing it into the LB and positioning it in the middle of the parafilm line. This will enable you to observe both sides of the chip under microscope.
- Cantilever should be uniformly covered with bacteria, and any floating or loosely attached bacterial clump should be avoided. Other washes are desirable in the latter case. Washing is obtained by taking a chip out of the LB and back in. Pay attention that certain number of bacteria are lost in each wash. It may be good to leave them around 10 minutes in LB before washes.

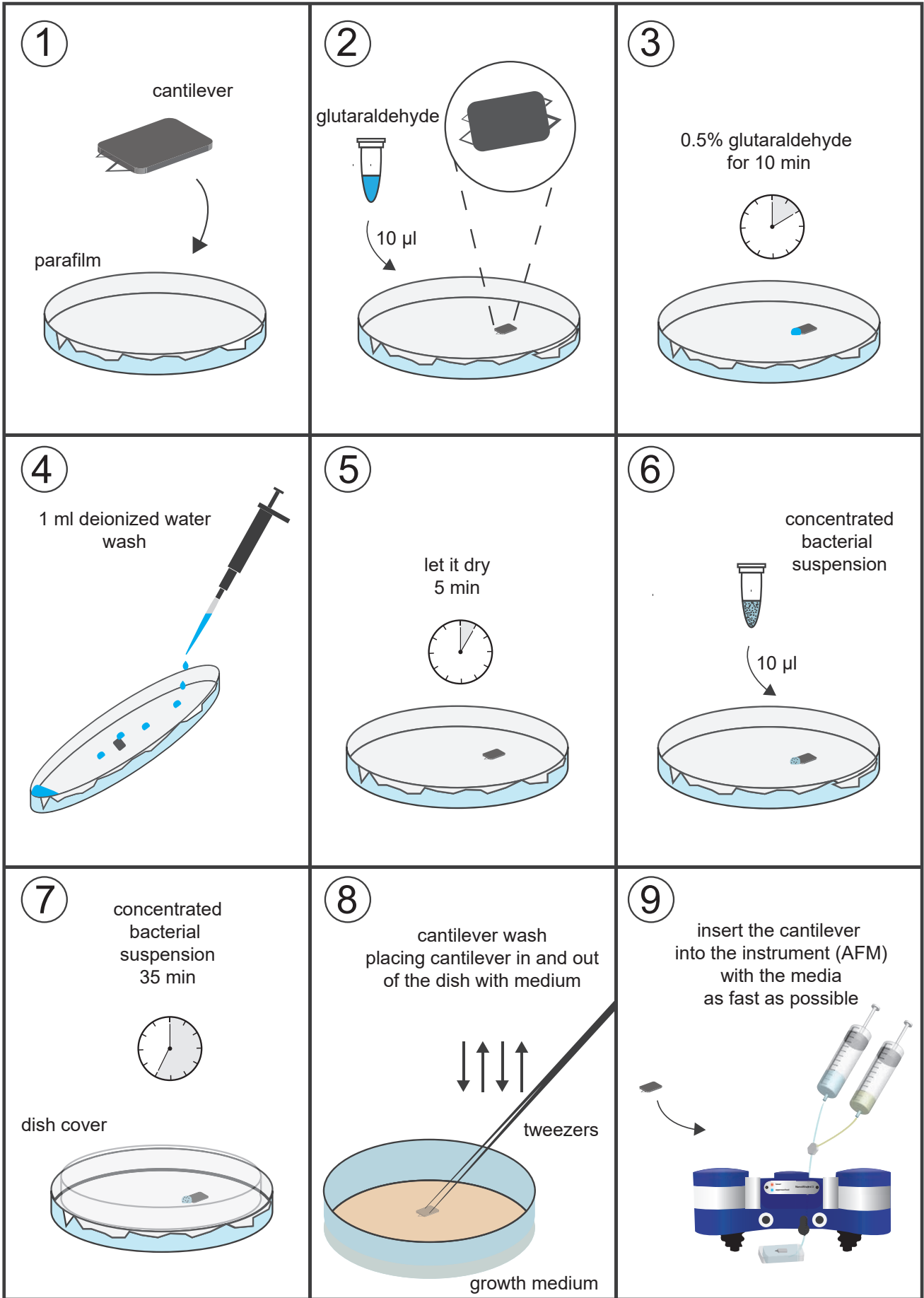
## Final Steps

After the attachment and placement of the chip in LB, observe it under microscope. What you need to pay attention to is the way bacteria are attached. I would suggest to have a uniform attachment like in the images below, without having loosely adhered bacteria in between the cantilever sides (triangles). Loose bacteria have an antenna effect and it will contaminate the signal with hard-to-interpret signal.



Petar Stupar  
LPMV EPFL  
[petar.stupar@epfl.ch](mailto:petar.stupar@epfl.ch)

- ! Refer to the summary on the next page ONLY after you have read carefully the detailed protocol!
- ! This protocol is a starting point for your experiments and further optimizations are necessary. Especially when dealing with new bacterial types, although it has proven to be fine for most of my tests.



## Bibliography

1. Binnig G, Quate C, Gerber C. Atomic Force Microscope. *Phys Rev Lett*. 1986 Mar 3;56(9):930–3.
2. Rugar D, Hansma P. Atomic force microscopy. *Phys Today*. 1990 Oct 1;43:23–30.
3. Sugawara Y, Ishizaka T, Morita S, Imai S, Mikoshiba N. Anomalous Corrugation Height of Atomically Resolved AFM Images of a Graphite Surface. *Jpn J Appl Phys*. 1990 Mar;29(3A):L502.
4. Ohnesorge F, Binnig G. True Atomic Resolution by Atomic Force Microscopy Through Repulsive and Attractive Forces. *Science*. 1993 Jun 4;260(5113):1451–6.
5. Hutter JL, Bechhoefer J. Calibration of atomic-force microscope tips. *Rev Sci Instrum*. 1993 Jul 1;64(7):1868–73.
6. Proksch R, Schäffer TE, Cleveland JP, Callahan RC, Viani MB. Finite optical spot size and position corrections in thermal spring constant calibration. *Nanotechnology*. 2004;15(9):1344.
7. Sader JE, Lu J, Mulvaney P. Effect of cantilever geometry on the optical lever sensitivities and thermal noise method of the atomic force microscope. *Rev Sci Instrum*. 2014 Nov 1;85(11):113702.
8. Sader JE, Borgani R, Gibson CT, Haviland DB, Higgins MJ, Kilpatrick JI, et al. A virtual instrument to standardise the calibration of atomic force microscope cantilevers. *Rev Sci Instrum*. 2016 Sep 1;87(9):093711.
9. Tamayo J, Humphris ADL, Owen RJ, Miles MJ. High-Q Dynamic Force Microscopy in Liquid and Its Application to Living Cells. *Biophys J*. 2001 Jul 1;81(1):526–37.
10. Sader JE. Frequency response of cantilever beams immersed in viscous fluids with applications to the atomic force microscope. *J Appl Phys*. 1998 Jun 19;84(1):64–76.
11. Korayem MH, Ebrahimi N, Sotoudegan MS. Frequency response of atomic force microscopy microcantilevers oscillating in a viscous liquid: A comparison of various methods. *Sci Iran*. 2011 Oct 1;18(5):1116–25.
12. Göddenhenrich T, Lemke H, Hartmann U, Heiden C. Force microscope with capacitive displacement detection. *J Vac Sci Technol Vac Surf Films*. 1990 Jan 1;8(1):383–7.
13. Giessibl FJ. High-speed force sensor for force microscopy and profilometry utilizing a quartz tuning fork. *Appl Phys Lett*. 1998 Dec 23;73(26):3956–8.
14. Rugar D, Mamin HJ, Guethner P. Improved fiber-optic interferometer for atomic force microscopy. *Appl Phys Lett*. 1989 Dec 18;55(25):2588–90.
15. Meyer G, Amer NM. Novel optical approach to atomic force microscopy. *Appl Phys Lett*. 1988 Sep 19;53(12):1045–7.

16. Alexander S, Hellemans L, Marti O, Schneir J, Elings V, Hansma PK, et al. An atomic-resolution atomic-force microscope implemented using an optical lever. *J Appl Phys* [Internet]. 1989;101 [cited 2017 Aug 8]; Available from: <http://aip.scitation.org/doi/10.1063/1.342563>
17. Bolton WC. *Mechanical Science*. John Wiley & Sons; 2013. 498 p.
18. Meyer G, Amer NM. Simultaneous measurement of lateral and normal forces with an optical-beam-deflection atomic force microscope. *Appl Phys Lett*. 1990 Nov 12;57(20):2089–91.
19. Zhong Q, Inniss D, Kjoller K, Elings VB. Fractured polymer/silica fiber surface studied by tapping mode atomic force microscopy. *Surf Sci Lett*. 1993 Jun 10;290(1):L688–92.
20. Albrecht TR, Grütter P, Horne D, Rugar D. Frequency modulation detection using high-Q cantilevers for enhanced force microscope sensitivity. *J Appl Phys*. 1991 Jan 15;69(2):668–73.
21. Meyer E, Heinzelmann H, Grütter P, Jung T, Weisskopf T, Hidber H-R, et al. Comparative study of lithium fluoride and graphite by atomic force microscopy (AFM). *Mon Microsc J*. 1870 Feb 1;3(2):269–80.
22. Ernst-Ludwig F, Vincent M, Hermann G. Adhesion forces between individual ligand-receptor pairs. *Sci Wash*. 1994 Apr 15;264(5157):415.
23. Cappella B, Dietler G. Force-distance curves by atomic force microscopy. *Surf Sci Rep*. 1999 Jan 1;34(1):1–104.
24. Vinckier A, Semenza G. Measuring elasticity of biological materials by atomic force microscopy. *FEBS Lett*. 1998 Jun 23;430(1):12–6.
25. Heinrich H. Ueber die Berührung fester elastischer Körper. *J Für Reine Angew Math Crelles J*. 2009;1882(92):156–171.
26. Sneddon IN. The relation between load and penetration in the axisymmetric boussinesq problem for a punch of arbitrary profile. *Int J Eng Sci*. 1965 May 1;3(1):47–57.
27. Tatara Y. Extensive Theory of Force-Approach Relations of Elastic Spheres in Compression and in Impact. *J Eng Mater Technol*. 1989 Apr 1;111(2):163–8.
28. Bonilla MR, Stokes JR, Gidley MJ, Yakubov GE. Interpreting atomic force microscopy nanoindentation of hierarchical biological materials using multi-regime analysis. *Soft Matter*. 2015 Feb 4;11(7):1281–92.
29. Digiuni S, Berne-Dedieu A, Martinez-Torres C, Szecsi J, Bendahmane M, Arneodo A, et al. Single Cell Wall Nonlinear Mechanics Revealed by a Multiscale Analysis of AFM Force-Indentation Curves. *Biophys J*. 2015 May 5;108(9):2235–48.
30. Fan X, White IM, Shopova SI, Zhu H, Suter JD, Sun Y. Sensitive optical biosensors for unlabeled targets: A review. *Anal Chim Acta*. 2008 Jul 14;620(1):8–26.



31. Ko S, Grant SA. A novel FRET-based optical fiber biosensor for rapid detection of *Salmonella typhimurium*. *Biosens Bioelectron*. 2006 Jan 15;21(7):1283–90.
32. L. C. C. Monitor and control of blood and tissue oxygen tensions. [Internet]. LWW. [cited 2017 Aug 30]. Available from: [http://journals.lww.com/asaiojournal/Fulltext/1956/04000/MONITOR\\_AND\\_CONTROL\\_OF\\_BLOOD\\_AND\\_TISSUE\\_OXYGEN.7.aspx](http://journals.lww.com/asaiojournal/Fulltext/1956/04000/MONITOR_AND_CONTROL_OF_BLOOD_AND_TISSUE_OXYGEN.7.aspx)
33. Wang J. Electrochemical biosensors: Towards point-of-care cancer diagnostics. *Biosens Bioelectron*. 2006 Apr 15;21(10):1887–92.
34. Tilmaciu C-M, Morris MC. Carbon nanotube biosensors. *Front Chem* [Internet]. 2015 Oct 27;3. Available from: <http://www.ncbi.nlm.nih.gov/pmc/articles/PMC4621484/>
35. Ramanathan K, Danielsson B. Principles and applications of thermal biosensors. *Biosens Bioelectron*. 2001 Aug 1;16(6):417–23.
36. Llandro J, Palfreyman JJ, Ionescu A, Barnes CHW. Magnetic biosensor technologies for medical applications: a review. *Med Biol Eng Comput*. 2010 Oct 1;48(10):977–98.
37. Marx KA. Quartz Crystal Microbalance: A Useful Tool for Studying Thin Polymer Films and Complex Biomolecular Systems at the Solution–Surface Interface. *Biomacromolecules*. 2003 Sep 1;4(5):1099–120.
38. Länge K, Rapp BE, Rapp M. Surface acoustic wave biosensors: a review. *Anal Bioanal Chem*. 2008 Jul 1;391(5):1509–19.
39. Fritz J, Baller MK, Lang HP, Rothuizen H, Vettiger P, Meyer E, et al. Translating Biomolecular Recognition into Nanomechanics. *Science*. 2000 Apr 14;288(5464):316–8.
40. Godin M, Tabard-Cossa V, Miyahara Y, Monga T, Williams PJ, Beaulieu LY, et al. Cantilever-based sensing: the origin of surface stress and optimization strategies. *Nanotechnology*. 2010 Feb 19;21(7):075501.
41. Berger R, Gerber C, Gimzewski JK, Meyer E, Güntherodt HJ. Thermal analysis using a micromechanical calorimeter. *Appl Phys Lett*. 1996 Jul 1;69(1):40–2.
42. Rodahl M, Höök F, Krozer A, Brzezinski P, Kasemo B. Quartz crystal microbalance setup for frequency and Q-factor measurements in gaseous and liquid environments. *Rev Sci Instrum*. 1995 Jul 1;66(7):3924–30.
43. Ramos D, Tamayo J, Mertens J, Calleja M, Zaballos A. Origin of the response of nanomechanical resonators to bacteria adsorption. *J Appl Phys*. 2006 Nov 15;100(10):106105.
44. Ramos D, Tamayo J, Mertens J, Calleja M, Villanueva LG, Zaballos A. Detection of bacteria based on the thermomechanical noise of a nanomechanical resonator: origin of the response and detection limits. *Nanotechnology*. 2008;19(3):035503.

45. Braun T, Barwich V, Ghatkesar MK, Bredekamp AH, Gerber C, Hegner M, et al. Micromechanical mass sensors for biomolecular detection in a physiological environment. *Phys Rev E*. 2005 Sep 14;72(3):031907.
46. Ghatkesar MK, Braun T, Barwich V, Ramseyer J-P, Gerber C, Hegner M, et al. Resonating modes of vibrating microcantilevers in liquid. *Appl Phys Lett*. 2008 Jan 28;92(4):043106.
47. Sushko ML, Harding JH, Shluger AL, McKendry RA, Watari M. Physics of Nanomechanical Biosensing on Cantilever Arrays. *Adv Mater*. 2008 Oct 17;20(20):3848–53.
48. Ilic B, Craighead HG, Krylov S, Senaratne W, Ober C, Neuzil P. Attogram detection using nanoelectromechanical oscillators. *J Appl Phys*. 2004 Mar 18;95(7):3694–703.
49. Chaste J, Eichler A, Moser J, Ceballos G, Rurali R, Bachtold A. A nanomechanical mass sensor with yoctogram resolution. *Nat Nanotechnol*. 2012 May;7(5):301–4.
50. Cleland AN, Roukes ML. Noise processes in nanomechanical resonators. *J Appl Phys*. 2002 Aug 16;92(5):2758–69.
51. Álvarez M, Tamayo J, Plaza JA, Zinoviev K, Domínguez C, Lechuga LM. Dimension dependence of the thermomechanical noise of microcantilevers. *J Appl Phys*. 2006 Jan 15;99(2):024910.
52. Tamayo J, Kosaka PM, Ruz JJ, San Paulo Á, Calleja M. Biosensors based on nanomechanical systems. *Chem Soc Rev*. 2013 Feb 7;42(3):1287–311.
53. Alvarez M, Lechuga LM. Microcantilever-based platforms as biosensing tools. *The Analyst*. 2010;135(5):827.
54. Ilic B, Czaplowski D, Zalalutdinov M, Craighead HG, Neuzil P, Campagnolo C, et al. Single cell detection with micromechanical oscillators. *J Vac Sci Technol B Microelectron Nanometer Struct Process Meas Phenom*. 2001 Nov 1;19(6):2825–8.
55. Gupta A, Akin D, Bashir R. Single virus particle mass detection using microresonators with nanoscale thickness. *Appl Phys Lett*. 2004 Mar 10;84(11):1976–8.
56. Lee JH, Hwang KS, Park J, Yoon KH, Yoon DS, Kim TS. Immunoassay of prostate-specific antigen (PSA) using resonant frequency shift of piezoelectric nanomechanical microcantilever. *Biosens Bioelectron*. 2005 Apr 15;20(10):2157–62.
57. Wu G, Ji H, Hansen K, Thundat T, Datar R, Cote R, et al. Origin of nanomechanical cantilever motion generated from biomolecular interactions. *Proc Natl Acad Sci*. 2001 Feb 13;98(4):1560–4.
58. Kwon T, Park J, Yang J, Yoon DS, Na S, Kim C-W, et al. Nanomechanical In Situ Monitoring of Proteolysis of Peptide by Cathepsin B. *PLoS ONE*. 2009 Jul 16;4(7):e6248.
59. Means GE, Feeney RE. Reductive alkylation of amino groups in proteins. *Biochemistry (Mosc)*. 1968 Jun 1;7(6):2192–201.

60. Smolyakov G, Formosa-Dague C, Severac C, Duval RE, Dague E. High speed indentation measures by FV, QI and QNM introduce a new understanding of bionanomechanical experiments. *Micron*. 2016 Jun 1;85(Supplement C):8–14.
61. Chan YL, Ngan AHW. Invariant elastic modulus of viscoelastic materials measured by rate-jump tests. *Polym Test*. 2010 Aug 1;29(5):558–64.
62. Zhou ZL, Ngan AHW, Tang B, Wang AX. Reliable measurement of elastic modulus of cells by nanoindentation in an atomic force microscope. *J Mech Behav Biomed Mater*. 2012 Apr 1;8(Supplement C):134–42.
63. Raman A, Trigueros S, Cartagena A, Stevenson APZ, Susilo M, Nauman E, et al. Mapping nanomechanical properties of live cells using multi-harmonic atomic force microscopy. *Nat Nanotechnol*. 2011;6(12):809–14.
64. Cartagena A, Hernando-Pérez M, Carrascosa JL, Pablo PJ de, Raman A. Mapping in vitro local material properties of intact and disrupted virions at high resolution using multi-harmonic atomic force microscopy. *Nanoscale*. 2013 May 16;5(11):4729–36.
65. Roduit C, Sekatski S, Dietler G, Catsicas S, Lafont F, Kasas S. Stiffness Tomography by Atomic Force Microscopy. *Biophys J*. 2009 Jul 22;97(2):674–7.
66. Roduit C, Saha B, Alonso-Sarduy L, Volterra A, Dietler G, Kasas S. OpenFovea: open-source AFM data processing software. *Nat Methods*. 2012 Aug;9(8):774–5.
67. Longo G, Rio LM, Roduit C, Trampuz A, Bizzini A, Dietler G, et al. Force volume and stiffness tomography investigation on the dynamics of stiff material under bacterial membranes. *J Mol Recognit*. 2012 May 1;25(5):278–84.
68. Tetard L, Passian A, Venmar KT, Lynch RM, Voy BH, Shekhawat G, et al. Imaging nanoparticles in cells by nanomechanical holography. *Nat Nanotechnol*. 2008 Aug;3(8):501–5.
69. Dufrière YF, Pelling AE. Force nanoscopy of cell mechanics and cell adhesion. *Nanoscale*. 2013 May 3;5(10):4094–104.
70. Xu W, Mulhern PJ, Blackford BL, Jericho MH, Firtel M, Beveridge TJ. Modeling and measuring the elastic properties of an archaeal surface, the sheath of *Methanospirillum hungatei*, and the implication for methane production. *J Bacteriol*. 1996 Jun;178:3106–12.
71. Amoldi M, Kacher CM, Bauerlein E, Radmacher M, Fritz M. Elastic properties of the cell wall of *Magnetospirillum gryphiswaldense* investigated by atomic force microscopy. *Appl Phys -Mater Sci Process*. 1998 Mar;66:S613–7.
72. Arce FT, Carlson R, Monds J, Veeh R, Hu FZ, Stewart PS, et al. Nanoscale Structural and Mechanical Properties of Nontypeable *Haemophilus influenzae* Biofilms. *J Bacteriol*. 2009 Apr 15;191:2512–20.

73. Lau PCY, Dutcher JR, Beveridge TJ, Lam JS. Absolute Quantitation of Bacterial Biofilm Adhesion and Viscoelasticity by Microbead Force Spectroscopy. *Biophys J*. 2009 Apr 8;96:2935–48.
74. Wang HB, Wilksch JJ, Lithgow T, Strugnell RA, Gee ML. Nanomechanics measurements of live bacteria reveal a mechanism for bacterial cell protection: the polysaccharide capsule in *Klebsiella* is a responsive polymer hydrogel that adapts to osmotic stress. *Soft Matter*. 2013;9:7560–7.
75. Pinzon-Arango PA, Nagarajan R, Camesano TA. Effects of L-Alanine and Inosine Germinants on the Elasticity of *Bacillus anthracis* Spores. *Langmuir*. 2010 May 4;26:6535–41.
76. Li AG, Burggraf LW, Xing Y. Nanomechanical Characterization of *Bacillus anthracis* Spores by Atomic Force Microscopy. *Appl Environ Microbiol*. 2016 May;82:2988–99.
77. Arnal L, Serra DO, Cattelan N, Castez MF, Vazquez L, Salvarezza RC, et al. Adhesin Contribution to Nanomechanical Properties of the Virulent *Bordetella pertussis* Envelope. *Langmuir*. 2012 May 15;28:7461–9.
78. Longo G, Rio LM, Trampuz A, Dietler G, Bizzini A, Kasas S. Antibiotic-induced modifications of the stiffness of bacterial membranes. *J Microbiol Methods*. 2013 May;93(2):80–4.
79. Bailey RG, Turner RD, Mullin N, Clarke N, Foster SJ, Hobbs JK. The Interplay between Cell Wall Mechanical Properties and the Cell Cycle in *Staphylococcus aureus*. *Biophys J*. 2014 Dec;107:2538–45.
80. Loskill P, Pereira PM, Jung P, Bischoff M, Herrmann M, Pinho MG, et al. Reduction of the Peptidoglycan Crosslinking Causes a Decrease in Stiffness of the *Staphylococcus aureus* Cell Envelope. *Biophys J*. 2014 Sep;107:1082–9.
81. Tokarska-Rodak M, Koziol-Montewka M, Skrzypiec K, Chmielewski T, Mendyk E, Tylewska-Wierzbanowska S. Analysis of nanomechanical properties of *Borrelia burgdorferi* spirochetes under the influence of lytic factors in an in vitro model using atomic force microscopy. *Postepy Hig Med Dosw*. 2015 Nov;69:1222–7.
82. Ramalingam B, Parandhaman T, Das SK. Antibacterial Effects of Biosynthesized Silver Nanoparticles on Surface Ultrastructure and Nanomechanical Properties of Gram-Negative Bacteria viz. *Escherichia coli* and *Pseudomonas aeruginosa*. *Acs Appl Mater Interfaces*. 2016 Feb;8:4963–76.
83. Longo G, Kasas S. Effects of antibacterial agents and drugs monitored by atomic force microscopy. *Wiley Interdiscip Rev Nanomed Nanobiotechnol*. 2014 May 1;6(3):230–44.
84. Dufrene YF, Pelling AE. Force nanoscopy of cell mechanics and cell adhesion. *Nanoscale*. 2013;5:4094–104.
85. Pillet F, Chopinet L, Formosa C, Dague E. Atomic Force Microscopy and pharmacology: From microbiology to cancerology. *Biochim Biophys Acta-Gen Subj*. 2014 Mar;1840:1028–50.
86. Touhami A, Nysten B, Dufrene YF. Nanoscale mapping of the elasticity of microbial cells by atomic force microscopy. *Langmuir*. 2003 May 27;19:4539–43.

87. Suchodolskis A, Feiza V, Stirke A, Timonina A, Ramanaviciene A, Ramanavicius A. Elastic properties of chemically modified baker's yeast cells studied by AFM. *Surf Interface Anal.* 2011 Dec;43:1636–40.
88. El-Kirat-Chatel S, Beaussart A, Alsteens D, Jackson DN, Lipke PN, Dufrene YF. Nanoscale analysis of caspofungin-induced cell surface remodelling in *Candida albicans*. *Nanoscale.* 2013;5:1105–15.
89. Formosa C, Schiavone M, Martin-Yken H, Francois JM, Duval RE, Dague E. Nanoscale Effects of Caspofungin against Two Yeast Species, *Saccharomyces cerevisiae* and *Candida albicans*. *Antimicrob Agents Chemother.* 2013 Aug;57:3498–506.
90. Dague E, Alsteens D, Latgé J-P, Verbelen C, Raze D, Baulard AR, et al. Chemical Force Microscopy of Single Live Cells. *Nano Lett.* 2007 Oct 1;7:3026–30.
91. Mercade-Prieto R, Thomas CR, Zhang ZB. Mechanical double layer model for *Saccharomyces Cerevisiae* cell wall. *Eur Biophys J Biophys Lett.* 2013 Aug;42:613–20.
92. Goldenbogen B, Giese W, Hemmen M, Uhlendorf J, Herrmann A, Klipp E. Dynamics of cell wall elasticity pattern shapes the cell during yeast mating morphogenesis. *Open Biol.* 2016 Sep;6.
93. Francois JM, Formosa C, Schiavone M, Pillet F, Martin-Yken H, Dague E. Use of atomic force microscopy (AFM) to explore cell wall properties and response to stress in the yeast *Saccharomyces cerevisiae*. *Curr Genet.* 2013 Nov;59:187–96.
94. Geitmann A, Ortega JKE. Mechanics and modeling of plant cell growth. *Trends Plant Sci.* 2009 Sep;14:467–78.
95. Wei CF, Lintilhac PM. Loss of stability: A new look at the physics of cell wall behavior during plant cell growth. *Plant Physiol.* 2007 Nov;145:763–72.
96. Lesniewska E, Adrian M, Klinguer A, Pugin A. Cell wall modification in grapevine cells in response to UV stress investigated by atomic force microscopy. *Ultramicroscopy.* 2004 Aug;100:171–8.
97. Isaacson T, Kosma DK, Matas AJ, Buda GJ, He YH, Yu BW, et al. Cutin deficiency in the tomato fruit cuticle consistently affects resistance to microbial infection and biomechanical properties, but not transpirational water loss. *Plant J.* 2009 Oct;60:363–77.
98. Peaucelle A, Braybrook SA, Le Guillou L, Bron E, Kuhlemeier C, Hofte H. Pectin-Induced Changes in Cell Wall Mechanics Underlie Organ Initiation in *Arabidopsis*. *Curr Biol.* 2011 Oct;21:1720–6.
99. Fernandes AN, Chen XY, Scotchford CA, Walker J, Wells DM, Roberts CJ, et al. Mechanical properties of epidermal cells of whole living roots of *Arabidopsis thaliana*: An atomic force microscopy study. *Phys Rev E.* 2012 Feb;85.

100. Radotic K, Roduit C, Simonovic J, Hornitschek P, Fankhauser C, Mutavdzic D, et al. Atomic Force Microscopy Stiffness Tomography on Living *Arabidopsis thaliana* Cells Reveals the Mechanical Properties of Surface and Deep Cell-Wall Layers during Growth. *Biophys J*. 2012 Aug 8;103:386–94.
101. Zdunek A, Kurenda A. Determination of the Elastic Properties of Tomato Fruit Cells with an Atomic Force Microscope. *Sensors*. 2013 Sep;13:12175–91.
102. Xi XN, Kim SH, Tittmann B. Atomic force microscopy based nanoindentation study of onion abaxial epidermis walls in aqueous environment. *J Appl Phys*. 2015 Jan;117.
103. Vogler H, Felekis D, Nelson BJ, Grossniklaus U. Measuring the Mechanical Properties of Plant Cell Walls. *Plants Basel Switz*. 2015 Mar;4:167–82.
104. Dokukin M, Ablaeva Y, Kalaparathi V, Seluanov A, Gorbunova V, Sokolov I. Pericellular Brush and Mechanics of Guinea Pig Fibroblast Cells Studied with AFM. *Biophys J*. 2016 Jul;111:236–46.
105. Simon M, Dokukin M, Kalaparathi V, Spedden E, Sokolov I, Staii C. Load Rate and Temperature Dependent Mechanical Properties of the Cortical Neuron and Its Pericellular Layer Measured by Atomic Force Microscopy. *Langmuir*. 2016 Feb;32:1111–9.
106. Liang XB, Shi XT, Ostrovidov S, Wu HK, Nakajima K. Probing stem cell differentiation using atomic force microscopy. *Appl Surf Sci*. 2016 Mar;366:254–9.
107. Roduit C, van der Goot FG, De Los Rios P, Yersin A, Steiner P, Dietler G, et al. Elastic membrane heterogeneity of living cells revealed by stiff nanoscale membrane domains. *Biophys J*. 2008 Feb 15;94:1521–32.
108. Rotsch C, Radmacher M. Drug-induced changes of cytoskeletal structure and mechanics in fibroblasts: An atomic force microscopy study. *Biophys J*. 2000 Jan;78:520–35.
109. Kasas S, Wang X, Hirling H, Marsault R, Huni B, Yersin A, et al. Superficial and deep changes of cellular mechanical properties following cytoskeleton disassembly. *Cell Motil Cytoskeleton*. 2005 Oct;62:124–32.
110. Fallqvist B, Fielden ML, Pettersson T, Nordgren N, Kroon M, Gad AKB. Experimental and computational assessment of F-actin influence in regulating cellular stiffness and relaxation behaviour of fibroblasts. *J Mech Behav Biomed Mater*. 2016 Jun;59:168–84.
111. Grady ME, Composto RJ, Eckmann DM. Cell elasticity with altered cytoskeletal architectures across multiple cell types. *J Mech Behav Biomed Mater*. 2016 Aug;61:197–207.
112. Kuznetsova TG, Starodubtseva MN, Yegorenkov NI, Chizhik SA, Zhdanov RI. Atomic force microscopy probing of cell elasticity. *Micron*. 2007;38:824–33.
113. Argyropoulos AJ, Robichaud P, Balimunkwe RM, Fisher GJ, Hammerberg C, Yan Y, et al. Alterations of Dermal Connective Tissue Collagen in Diabetes: Molecular Basis of Aged-Appearing Skin. *Plos One*. 2016 Apr;11.

114. Dulinska I, Targosz M, Strojny W, Lekka M, Czuba P, Balwierz W, et al. Stiffness of normal and pathological erythrocytes studied by means of atomic force microscopy. *J Biochem Biophys Methods*. 2006 Mar;66:1–11.
115. Pretorius E, Swanepoel AC, Buys AV, Vermeulen N, Duim W, Kell DB. Eryptosis as a marker of Parkinson's disease. *Aging-U.S.* 2014 Oct;6:788–819.
116. Bester J, Buys AV, Lipinski B, Kell DB, Pretorius E. High ferritin levels have major effects on the morphology of erythrocytes in Alzheimer's disease. *Front Aging Neurosci*. 2013 Dec;5.
117. Mukherjee R, Saha M, Routray A, Chakraborty C. Nanoscale Surface Characterization of Human Erythrocytes by Atomic Force Microscopy: A Critical Review. *Ieee Trans Nanobioscience*. 2015 Sep;14:625–33.
118. Hayashi K, Higaki M. Stiffness of Intact Endothelial Cells From Fresh Aortic Bifurcations of Atherosclerotic Rabbits-Atomic Force Microscopic Study. *J Cell Physiol*. 2017 Jan;232:7–13.
119. Yan B, Ren J, Liu Y, Huang HR, Zheng X, Zou QZ. Study of Cholesterol Repletion Effect on Nanomechanical Properties of Human Umbilical Vein Endothelial Cell Via Rapid Broadband Atomic Force Microscopy. *J Biomech Eng-Trans Asme*. 2017 Mar;139.
120. Szymonski M, Targosz-Korecka M, Malek-Zietek KE. Nano-mechanical model of endothelial dysfunction for AFM-based diagnostics at the cellular level. *Pharmacol Rep*. 2015;67:728–35.
121. Wu X, Muthuchamy M, Reddy DS. Atomic Force Microscopy Protocol for Measurement of Membrane Plasticity and Extracellular Interactions in Single Neurons in Epilepsy. *Front Aging Neurosci*. 2016 May;8.
122. Spedden E, Staii C. Neuron Biomechanics Probed by Atomic Force Microscopy. *Int J Mol Sci*. 2013 Aug;14:16124–40.
123. Morton KC, Baker LA. Atomic force microscopy-based bioanalysis for the study of disease. *Anal Methods*. 2014;6:4932–55.
124. Gautier HOB, Thompson AJ, Achouri S, Koser DE, Holtzmann K, Moeendarbary E, et al. Atomic force microscopy-based force measurements on animal cells and tissues. In: Paluch EK, editor. *Biophysical Methods in Cell Biology*. 2015. p. 211–35. (Methods in Cell Biology; vol. 125).
125. Dong CB, Hu X, Dinu CZ. Current status and perspectives in atomic force microscopy-based identification of cellular transformation. *Int J Nanomedicine*. 2016;11:2107–18.
126. Rianna C, Radmacher M. Cell Mechanics as a Marker for Diseases: Biomedical Applications of AFM. In: Gutmanas EY, Naimark OB, Sharkeev YP, editors. *Physics of Cancer: Interdisciplinary Problems and Clinical Applications*. 2016. (AIP Conference Proceedings; vol. 1760).
127. Lekka M, Pogoda K, Gostek J, Klymenko O, Prauzner-Bechcicki S, Wiltowska-Zuber J, et al. Cancer cell recognition - Mechanical phenotype. *Micron*. 2012 Dec;43:1259–66.

128. Lekka M. Discrimination Between Normal and Cancerous Cells Using AFM. *Bionanoscience*. 2016 Mar;6:65–80.
129. Plodinec M, Loparic M, Monnier CA, Obermann EC, Zanetti-Dallenbach R, Oertle P, et al. The nanomechanical signature of breast cancer. *Nat Nanotechnol*. 2012 Nov;7:757–65.
130. Coceano G, Yousafzai MS, Ma W, Ndoye F, Venturelli L, Hussain I, et al. Investigation into local cell mechanics by atomic force microscopy mapping and optical tweezer vertical indentation. *Nanotechnology*. 2016 Feb;27.
131. Ansardamavandi A, Tafazzoli-Shadpour M, Omidvar R, Jahanzad I. Quantification of effects of cancer on elastic properties of breast tissue by Atomic Force Microscopy. *J Mech Behav Biomed Mater*. 2016 Jul;60:234–42.
132. Smolyakov G, Thiebot B, Campillo C, Labdi S, Severac C, Pelta J, et al. Elasticity, Adhesion, and Tether Extrusion on Breast Cancer Cells Provide a Signature of Their Invasive Potential. *ACS Appl Mater Interfaces*. 2016 Oct;8:27426–31.
133. Calzado-Martin A, Encinar M, Tamayo J, Calleja M, Paulo AS. Effect of Actin Organization on the Stiffness of Living Breast Cancer Cells Revealed by Peak-Force Modulation Atomic Force Microscopy. *ACS Nano*. 2016 Mar;10:3365–74.
134. Abidine Y, Laurent VM, Michel R, Duperray A, Verdier C. Local mechanical properties of bladder cancer cells measured by AFM as a signature of metastatic potential. *Eur Phys J Plus*. 2015 Oct;130.
135. Zhao XQ, Zhong YX, Ye T, Wang DJ, Mao BW. Discrimination Between Cervical Cancer Cells and Normal Cervical Cells Based on Longitudinal Elasticity Using Atomic Force Microscopy. *Nanoscale Res Lett*. 2015 Dec;10:1–8.
136. Park S, Jang WJ, Jeong CH. Nano-biomechanical Validation of Epithelial-Mesenchymal Transition in Oral Squamous Cell Carcinomas. *Biol Pharm Bull*. 2016 Sep;39:1488–95.
137. Wang XL, Yang YJ, Hu XH, Kawazoe N, Yang YN, Chen GP. Morphological and Mechanical Properties of Osteosarcoma Microenvironment Cells Explored by Atomic Force Microscopy. *Anal Sci*. 2016 Nov;32:1177–82.
138. Zhang GC, Fan N, Lv XY, Liu YY, Guo J, Yang LX, et al. Investigation of the Mechanical Properties of the Human Osteosarcoma Cell at Different Cell Cycle Stages. *Micromachines*. 2017 Mar;8.
139. Efremov YM, Dokrunova AA, Efremenko AV, Kirpichnikov MP, Shaitan KV, Sokolova OS. Distinct impact of targeted actin cytoskeleton reorganization on mechanical properties of normal and malignant cells. *Biochim Biophys Acta-Mol Cell Res*. 2015 Nov;1853:3117–25.
140. Han YM, Wang JH, Wang K, Dong S. Fabrication of atomic force microscope spherical tips and its application in determining the mechanical property of cancer cells. *Micro Nano Lett*. 2016 Dec;11:881–4.



141. Ciasca G, Sassun TE, Minelli E, Antonelli M, Papi M, Santoro A, et al. Nano-mechanical signature of brain tumours. *Nanoscale*. 2012;8:1–16.
142. Kung ML, Hsieh CW, Tai MH, Weng CH, Wu DC, Wu WJ, et al. Nanoscale characterization illustrates the cisplatin-mediated biomechanical changes of B16-F10 melanoma cells. *Phys Chem Chem Phys*. 2016 Mar;18:7124–31.
143. Lian SZ, Shi RY, Huang X, Hu XL, Song B, Bai YS, et al. Artesunate attenuates glioma proliferation, migration and invasion by affecting cellular mechanical properties. *Oncol Rep*. 2016 Aug;36:984–90.
144. Li M, Liu LQ, Xiao XB, Xi N, Wang YC. Effects of methotrexate on the viscoelastic properties of single cells probed by atomic force microscopy. *J Biol Phys*. 2016 Oct;42:551–69.
145. Nguyen N, Shao Y, Wineman A, Fu JP, Waas A. Atomic force microscopy indentation and inverse analysis for non-linear viscoelastic identification of breast cancer cells. *Math Biosci*. 2016 Jul;277:77–88.
146. Stylianou A, Stylianopoulos T. Atomic Force Microscopy Probing of Cancer Cells and Tumor Microenvironment Components. *Bionanoscience*. 2016 Mar;6:33–46.
147. Maheraly Z, Smith JR, Ghoneim MK, Dickson L, An Q, Fillmore HL, et al. Silencing of CD44 in Glioma Leads to Changes in Cytoskeletal Protein Expression and Cellular Biomechanical Deformation Properties as Measured by AFM Nanoindentation. *Bionanoscience*. 2016 Mar;6:54–64.
148. Morey ER, Baylink DJ. Inhibition of bone formation during space flight. *Science*. 1978 Sep 22;201(4361):1138–41.
149. Hughes-Fulford M. Review of the biological effects of weightlessness on the human endocrine system. *Receptor*. 1993;3(3):145–54.
150. Hughes-Fulford M, Lewis ML. Effects of Microgravity on Osteoblast Growth Activation. *Exp Cell Res*. 1996 Apr 10;224(1):103–9.
151. Al FRM et. Adaptation of *Bordetella pertussis* to Vaccination: A Cause for Its Reemergence? - Volume 7, Number 7—June 2001 - *Emerging Infectious Disease journal* - CDC. [cited 2017 Oct 17]; Available from: [https://wwwnc.cdc.gov/eid/article/7/7/01-7708\\_article](https://wwwnc.cdc.gov/eid/article/7/7/01-7708_article)
152. Hellenbrand W, Beier D, Jensen E, Littmann M, Meyer C, Oppermann H, et al. The epidemiology of pertussis in Germany: past and present. *BMC Infect Dis*. 2009 Feb 25;9:22.
153. Conover MS, Sloan GP, Love CF, Sukumar N, Deora R. The Bps polysaccharide of *Bordetella pertussis* promotes colonization and biofilm formation in the nose by functioning as an adhesin. *Mol Microbiol*. 2010 Sep 1;77(6):1439–55.
154. Sloan GP, Love CF, Sukumar N, Mishra M, Deora R. The *Bordetella* Bps Polysaccharide Is Critical for Biofilm Development in the Mouse Respiratory Tract. *J Bacteriol*. 2007 Nov 15;189(22):8270–6.

155. Serra DO, Conover MS, Arnal L, Sloan GP, Rodriguez ME, Yantorno OM, et al. FHA-Mediated Cell-Substrate and Cell-Cell Adhesions Are Critical for *Bordetella pertussis* Biofilm Formation on Abiotic Surfaces and in the Mouse Nose and the Trachea. *PLOS ONE*. 2011 Dec 22;6(12):e28811.
156. Donlan RM, Costerton JW. Biofilms: Survival Mechanisms of Clinically Relevant Microorganisms. *Clin Microbiol Rev*. 2002 Apr 1;15(2):167–93.
157. Conover MS, Sloan GP, Love CF, Sukumar N, Deora R. The Bps polysaccharide of *Bordetella pertussis* promotes colonization and biofilm formation in the nose by functioning as an adhesin. *Mol Microbiol*. 2010 Sep 1;77(6):1439–55.
158. Melvin JA, Scheller EV, Miller JF, Cotter PA. *Bordetella pertussis* pathogenesis: current and future challenges. *Nat Rev Microbiol*. 2014 Apr;12(4):274–88.
159. Prasad SM, Yin Y, Rodzinski E, Tuomanen EI, Masure HR. Identification of a carbohydrate recognition domain in filamentous hemagglutinin from *Bordetella pertussis*. *Infect Immun*. 1993 Jul 1;61(7):2780–5.
160. Menozzi FD, Gantiez C, Loch C. Interaction of the *Bordetella pertussis* filamentous hemagglutinin with heparin. *FEMS Microbiol Lett*. 1991 Feb 1;78(1):59–64.
161. Loch C, Berlin P, Menozzi FD, Renaud† G. The filamentous haemagglutinin, a multifaceted adhesin produced by virulent *Bordetella* spp. *Mol Microbiol*. 1993 Aug 1;9(4):653–60.
162. Serra D, Bosch A, Russo DM, Rodríguez ME, Zorreguieta Á, Schmitt J, et al. Continuous nondestructive monitoring of *Bordetella pertussis* biofilms by Fourier transform infrared spectroscopy and other corroborative techniques. *Anal Bioanal Chem*. 2007 Mar 1;387(5):1759–67.
163. Heinisch JJ, Dupres V, Wilk S, Jendretzki A, Dufrêne YF. Single-Molecule Atomic Force Microscopy Reveals Clustering of the Yeast Plasma-Membrane Sensor Wsc1. *PLOS ONE*. 2010 Jun 14;5(6):e11104.
164. Müller DJ, Dufrêne YF. Force nanoscopy of living cells. *Curr Biol*. 2011 Mar 22;21(6):R212–6.
165. Verbelen C, Raze D, Dewitte F, Loch C, Dufrêne YF. Single-Molecule Force Spectroscopy of Mycobacterial Adhesin-Adhesin Interactions. *J Bacteriol*. 2007 Dec 15;189(24):8801–6.
166. Dufrene YF, Martinez-Martin D, Medalsy I, Alsteens D, Muller DJ. Multiparametric imaging of biological systems by force-distance curve-based AFM. *Nat Methods*. 2013 Sep;10:847–54.
167. Tripathi P, Beaussart A, Andre G, Rolain T, Lebeer S, Vanderleyden J, et al. Towards a nanoscale view of lactic acid bacteria. *Micron*. 2012 Dec 1;43(12):1323–30.
168. Alsteens D, Garcia MC, Lipke PN, Dufrêne YF. Force-induced formation and propagation of adhesion nanodomains in living fungal cells. *Proc Natl Acad Sci*. 2010 Nov 30;107(48):20744–9.

169. Lipke PN, Garcia MC, Alsteens D, Ramsook CB, Klotz SA, Dufrêne YF. Strengthening relationships: amyloids create adhesion nanodomains in yeasts. *Trends Microbiol.* 2012 Feb 1;20(2):59–65.
170. El-Kirat-Chatel S, Beaussart A, Boyd CD, O'Toole GA, Dufrêne YF. Single-Cell and Single-Molecule Analysis Deciphers the Localization, Adhesion, and Mechanics of the Biofilm Adhesin LapA. *ACS Chem Biol.* 2014 Feb 21;9(2):485–94.
171. Locht C, Geoffroy MC, Renauld G. Common accessory genes for the *Bordetella pertussis* filamentous hemagglutinin and fimbriae share sequence similarities with the papC and papD gene families. *EMBO J.* 1992 Sep;11(9):3175–83.
172. Burks GA, Velegol SB, Paramonova E, Lindenmuth BE, Feick JD, Logan BE. Macroscopic and Nanoscale Measurements of the Adhesion of Bacteria with Varying Outer Layer Surface Composition. *Langmuir.* 2003 Mar 1;19(6):2366–71.
173. Vadillo-Rodríguez V, Busscher HJ, Norde W, Vries J de, Dijkstra RJB, Stokroos I, et al. Comparison of Atomic Force Microscopy Interaction Forces between Bacteria and Silicon Nitride Substrata for Three Commonly Used Immobilization Methods. *Appl Environ Microbiol.* 2004 Sep 1;70(9):5441–6.
174. Yersin A, Hirling H, Steiner P, Magnin S, Regazzi R, Hüni B, et al. Interactions between synaptic vesicle fusion proteins explored by atomic force microscopy. *Proc Natl Acad Sci.* 2003 Jul 22;100(15):8736–41.
175. Steiner P, Alberi S, Kulangara K, Yersin A, Sarria J-CF, Regulier E, et al. Interactions between NEEP21, GRIP1 and GluR2 regulate sorting and recycling of the glutamate receptor subunit GluR2. *EMBO J.* 2005 Aug 17;24(16):2873–84.
176. Strunz T, Oroszlan K, Schumakovitch I, Güntherodt H-J, Hegner M. Model Energy Landscapes and the Force-Induced Dissociation of Ligand-Receptor Bonds. *Biophys J.* 2000 Sep 1;79(3):1206–12.
177. Dupres V, Menozzi FD, Locht C, Clare BH, Abbott NL, Cuenot S, et al. Nanoscale mapping and functional analysis of individual adhesins on living bacteria. *Nat Methods.* 2005 Jul;2(7):515–20.
178. Bonanni B, Kamruzzahan ASM, Bizzarri AR, Rankl C, Gruber HJ, Hinterdorfer P, et al. Single Molecule Recognition between Cytochrome C 551 and Gold-Immobilized Azurin by Force Spectroscopy. *Biophys J.* 2005 Oct 1;89(4):2783–91.
179. Müller DJ, Helenius J, Alsteens D, Dufrêne YF. Force probing surfaces of living cells to molecular resolution. *Nat Chem Biol.* 2009 Jun;5(6):383–90.
180. Radmacher M, Cleveland JP, Fritz M, Hansma HG, Hansma PK. Mapping interaction forces with the atomic force microscope. *Biophys J.* 1994 Jun 1;66(6):2159–65.
181. Touhami A, Nysten B, Dufrêne YF. Nanoscale Mapping of the Elasticity of Microbial Cells by Atomic Force Microscopy. *Langmuir.* 2003 May 1;19(11):4539–43.

182. Polyakov P, Soussen C, Duan J, Duval JFL, Brie D, Francius G. Automated Force Volume Image Processing for Biological Samples. PLOS ONE. 2011 Apr 29;6(4):e18887.
183. Gaboriaud F, Dufrêne YF. Atomic force microscopy of microbial cells: Application to nanomechanical properties, surface forces and molecular recognition forces. Colloids Surf B Biointerfaces. 2007 Jan 15;54(1):10–9.
184. Arnoldi M, Fritz M, Bäuerlein E, Radmacher M, Sackmann E, Boulbitch A. Bacterial turgor pressure can be measured by atomic force microscopy. Phys Rev E. 2000 Jul 1;62(1):1034–44.
185. Gaboriaud F, Bailet S, Dague E, Jorand F. Surface structure and nanomechanical properties of *Shewanella putrefaciens* bacteria at two pH values (4 and 10) determined by atomic force microscopy. J Bacteriol. 2005 Jun;187:3864–8.
186. Velegol SB, Logan BE. Contributions of Bacterial Surface Polymers, Electrostatics, and Cell Elasticity to the Shape of AFM Force Curves. Langmuir. 2002 Jun 1;18(13):5256–62.
187. A-Hassan E, Heinz WF, Antonik MD, D'Costa NP, Nageswaran S, Schoenenberger CA, et al. Relative microelastic mapping of living cells by atomic force microscopy. Biophys J. 1998 Mar;74:1564–78.
188. Willemsen OH, Snel MME, van der Werf KO, de Groot BG, Greve J, Hinterdorfer P, et al. Simultaneous Height and Adhesion Imaging of Antibody-Antigen Interactions by Atomic Force Microscopy. Biophys J. 1998 Nov;75(5):2220–8.
189. Hinterdorfer P, Baumgartner W, Gruber HJ, Schilcher K, Schindler H. Detection and localization of individual antibody-antigen recognition events by atomic force microscopy. Proc Natl Acad Sci. 1996 Apr 16;93(8):3477–81.
190. Wiley: Atomic Force Microscopy in Liquid: Biological Applications - Arturo M. Baro, Ronald G. Reifenberger [Internet]. [cited 2017 Oct 17]. Available from: <http://www.wiley.com/WileyCDA/WileyTitle/productCd-3527327584.html>
191. 9789380026442: Textbook of Microbiology - AbeBooks - Naveen Kango: 9380026447 [Internet]. [cited 2017 Oct 17]. Available from: <https://www.abebooks.com/9789380026442/Textbook-Microbiology-Naveen-Kango-9380026447/plp>
192. Kienberger F, Kada G, Mueller H, Hinterdorfer P. Single Molecule Studies of Antibody–Antigen Interaction Strength Versus Intra-molecular Antigen Stability. J Mol Biol. 2005 Apr 1;347(3):597–606.
193. Gao H, Zhang X-X, Chang W-B. Study on the interaction in single antigen-antibody molecules by AFM. Front Biosci J Virtual Libr. 2005 Feb 1;10:1539–45.

194. Kajava AV, Cheng N, Cleaver R, Kessel M, Simon MN, Willery E, et al. Beta-helix model for the filamentous haemagglutinin adhesin of *Bordetella pertussis* and related bacterial secretory proteins. *Mol Microbiol.* 2001 Oct 1;42(2):279–92.
195. Ido S, Kimiya H, Kobayashi K, Kominami H, Matsushige K, Yamada H. Immunoactive two-dimensional self-assembly of monoclonal antibodies in aqueous solution revealed by atomic force microscopy. *Nat Mater.* 2014 Mar;13(3):264–70.
196. Alsteens D, Martinez N, Jamin M, Jacob-Dubuisson F. Sequential Unfolding of Beta Helical Protein by Single-Molecule Atomic Force Microscopy. *PLOS ONE.* 2013 Aug 29;8(8):e73572.
197. Kuo K, Hoch HC. Germination of *Phyllosticta ampellicida* Pycnidiospores: Prerequisite of Adhesion to the Substratum and the Relationship of Substratum Wettability. *Fungal Genet Biol.* 1996 Mar 1;20(1):18–29.
198. DeZwaan TM, Carroll AM, Valent B, Sweigard JA. Magnaporthe grisea pth11p is a novel plasma membrane protein that mediates appressorium differentiation in response to inductive substrate cues. *Plant Cell.* 1999 Oct;11(10):2013–30.
199. Yakubov GE, Bonilla MR, Chen H, Doblin MS, Bacic A, Gidley MJ, et al. Mapping nano-scale mechanical heterogeneity of primary plant cell walls. *J Exp Bot.* 2016 Apr;67(9):2799–816.
200. Milani P, Gholamirad M, Traas J, Arneodo A, Boudaoud A, Argoul F, et al. In vivo analysis of local wall stiffness at the shoot apical meristem in *Arabidopsis* using atomic force microscopy. *Plant J.* 2011 Sep;67:1116–23.
201. Ruggeri FS, Longo G, Faggiano S, Lipiec E, Pastore A, Dietler G. Infrared nanospectroscopy characterization of oligomeric and fibrillar aggregates during amyloid formation. *Nat Commun.* 2015 Jul 28;6:ncomms8831.
202. Japaridze A, Muskhelishvili G, Benedetti F, Gavriilidou AFM, Zenobi R, De Los Rios P, et al. Hyperplectonemes: A Higher Order Compact and Dynamic DNA Self-Organization. *Nano Lett.* 2017 Mar 8;17(3):1938–48.
203. Roduit C, Longo G, Benmessaoud I, Volterra A, Saha B, Dietler G, et al. Stiffness tomography exploration of living and fixed macrophages. *J Mol Recognit JMR.* 2012 May;25(5):241–6.
204. Kasas S, Longo G, Dietler G. Mechanical properties of biological specimens explored by atomic force microscopy. *J Phys Appl Phys.* 2013;46(13):133001.
205. Arnal L, Longo G, Stupar P, F. Castez M, Cattelan N, C. Salvarezza R, et al. Localization of adhesins on the surface of a pathogenic bacterial envelope through atomic force microscopy. *Nanoscale.* 2015;7(41):17563–72.
206. Tamayo J, Kosaka PM, Ruz JJ, Paulo ÁS, Calleja M. Biosensors based on nanomechanical systems. *Chem Soc Rev.* 2013 Jan 16;42(3):1287–311.

207. Kosaka PM, Pini V, Ruz JJ, Silva RA da, González MU, Ramos D, et al. Detection of cancer biomarkers in serum using a hybrid mechanical and optoplasmonic nanosensor. *Nat Nanotechnol.* 2014 Dec;9(12):1047–53.
208. M. Kosaka P, Tamayo J, J. Ruz J, Puertas S, Polo E, Grazu V, et al. Tackling reproducibility in microcantilever biosensors: a statistical approach for sensitive and specific end-point detection of immunoreactions. *Analyst.* 2013;138(3):863–72.
209. Ndieyira JW, Kappeler N, Logan S, Cooper MA, Abell C, McKendry RA, et al. Surface-stress sensors for rapid and ultrasensitive detection of active free drugs in human serum. *Nat Nanotechnol.* 2014 Mar;9(3):225–32.
210. Longo G. Cancer biomarkers: Detected twice for good measure. *Nat Nanotechnol.* 2014 Dec;9(12):959–60.
211. Kasas S, Longo G, Alonso-Sarduy L, Dietler G. Nanoscale motion detector.
212. Longo G, Alonso-Sarduy L, Rio LM, Bizzini A, Trampuz A, Notz J, et al. Rapid detection of bacterial resistance to antibiotics using AFM cantilevers as nanomechanical sensors. *Nat Nanotechnol.* 2013 Jul;8(7):522–6.
213. Longo G, Alonso-Sarduy L, Pekkanen J, Dietler G, Kasas S. Rapid Evaluation of Bacterial Antibiotic Resistance. In: *Bio Sensors, Instruments, Medical, Environment and Energy* [Internet]. p. 111–4. (Nanotechnology 2013; vol. 3). Available from: <http://www.nsti.org/procs/Nanotech2013v3/1/T5.918>
214. Aghayee S, Benadiba C, Notz J, Kasas S, Dietler G, Longo G. Combination of fluorescence microscopy and nanomotion detection to characterize bacteria. *J Mol Recognit.* 2013 Nov 1;26(11):590–5.
215. Ruggeri FS, Mahul-Mellier A-L, Kasas S, Lashuel HA, Longo G, Dietler G. Amyloid single-cell cytotoxicity assays by nanomotion detection. *Cell Death Discov.* 2017 Aug 21;3:cddiscovery201753.
216. Alonso-Sarduy L, De Los Rios P, Benedetti F, Vobornik D, Dietler G, Kasas S, et al. Real-time monitoring of protein conformational changes using a nano-mechanical sensor. *PloS One.* 2014;9(7):e103674.
217. Stupar P, Opota O, Longo G, Prod'hom G, Dietler G, Greub G, et al. Nanomechanical sensor applied to blood culture pellets: a fast approach to determine the antibiotic susceptibility against agents of bloodstream infections. *Clin Microbiol Infect.* 2017;
218. Kasas S, Stupar P, Longo G, Dietler G. Detecting life thanks to the atomic force microscope. *médecine/sciences.* 2015 Apr 1;31(4):369–71.
219. Kasas S, Ruggeri FS, Benadiba C, Maillard C, Stupar P, Tourneu H, et al. Detecting nanoscale vibrations as signature of life. *Proc Natl Acad Sci.* 2015 Jan 13;112(2):378–81.

220. Kasas S, Radotic K, Longo G, Saha B, Alonso-Sarduy L, Dietler G, et al. A universal fluid cell for the imaging of biological specimens in the atomic force microscope. *Microsc Res Tech*. 2013 Apr;76(4):357–63.
221. Lissandrello C, Inci F, Francom M, Paul MR, Demirci U, Ekinici KL. Nanomechanical motion of Escherichia coli adhered to a surface. *Appl Phys Lett* [Internet]. 2014 Sep 15;105(11). Available from: <http://www.ncbi.nlm.nih.gov/pmc/articles/PMC4187256/>
222. Wu S, Liu X, Zhou X, Liang XM, Gao D, Liu H, et al. Quantification of cell viability and rapid screening anti-cancer drug utilizing nanomechanical fluctuation. *Biosens Bioelectron*. 2016 Mar 15;77:164–73.
223. Nelson SL, Proctor DT, Ghasemloonia A, Lama S, Zareinia K, Ahn Y, et al. Vibrational Profiling of Brain Tumors and Cells. *Theranostics*. 2017;7(9):2417–30.
224. Kasas S, Alonso L, Jacquet P, Adamcik J, Haeberli C, Dietler G. Microcontroller-driven fluid-injection system for atomic force microscopy. *Rev Sci Instrum*. 2010 Jan;81(1):013704.
225. Kasas S, Ikai A. A method for anchoring round shaped cells for atomic force microscope imaging. *Biophys J*. 1995 May;68(5):1678–80.
226. Kalauzi A, Nikolić L, Savić D, Radotić K. Cell death parameters as revealed by whole-cell patch-clamp and interval weighted spectra averaging: changes in membrane properties and current frequency of cultured mouse microglial cells induced by glutaraldehyde. *J Membr Biol*. 2015 Feb;248(1):117–23.
227. Scholkmann F, Cifra M, Moraes TA, Gallep C de M. Using multifractal analysis of ultra-weak photon emission from germinating wheat seedlings to differentiate between two grades of intoxication with potassium dichromate. *J Phys Conf Ser*. 2011;329(1):012020.
228. Burnos S, Hilfiker P, Sürücü O, Scholkmann F, Kraysenbühl N, Grunwald T, et al. Human Intracranial High Frequency Oscillations (HFOs) Detected by Automatic Time-Frequency Analysis. *PLOS ONE*. 2014 Apr 10;9(4):e94381.
229. Holper L, Scholkmann F, Wolf M. The relationship between sympathetic nervous activity and cerebral hemodynamics and oxygenation: a study using skin conductance measurement and functional near-infrared spectroscopy. *Behav Brain Res*. 2014 Aug 15;270:95–107.
230. Gao J, Hu J, Liu F, Cao Y. Multiscale entropy analysis of biological signals: a fundamental bi-scaling law. *Front Comput Neurosci* [Internet]. 2015 Jun 2;9. Available from: <http://www.ncbi.nlm.nih.gov/pmc/articles/PMC4451367/>
231. Blair JMA, Webber MA, Baylay AJ, Ogbolu DO, Piddock LJV. Molecular mechanisms of antibiotic resistance. *Nat Rev Microbiol*. 2015 Jan;13(1):42–51.
232. Roberts IS. The Biochemistry and Genetics of Capsular Polysaccharide Production in Bacteria. *Annu Rev Microbiol*. 1996;50(1):285–315.

233. Peterson BW, Sharma PK, Mei HC van der, Busscher HJ. Bacterial Cell Surface Damage Due to Centrifugal Compaction. *Appl Environ Microbiol.* 2012 Jan 1;78(1):120–5.
234. Pembrey RS, Marshall KC, Schneider RP. Cell Surface Analysis Techniques: What Do Cell Preparation Protocols Do to Cell Surface Properties? *Appl Environ Microbiol.* 1999 Jul 1;65(7):2877–94.
235. Haramé DL, Bousse LJ, Shott JD, Meindl JD. Ion-sensing devices with silicon nitride and borosilicate glass insulators. *IEEE Trans Electron Devices.* 1987 Aug;34(8):1700–7.
236. Migneault I, Dartiguenave C, Bertrand MJ, Waldron KC. Glutaraldehyde: behavior in aqueous solution, reaction with proteins, and application to enzyme crosslinking. *Biotechniques.* 2004;37(5):790–806.
237. Leekha S, Terrell CL, Edson RS. General Principles of Antimicrobial Therapy. *Mayo Clin Proc.* 2011 Feb 1;86(2):156–67.
238. Kay D, Fildes P. The calcium requirement of a typhoid bacteriophage. *Br J Exp Pathol.* 1950 Jun;31(3):338–48.
239. Goff DA, Jankowski C, Tenover FC. Using rapid diagnostic tests to optimize antimicrobial selection in antimicrobial stewardship programs. *Pharmacotherapy.* 2012 Aug;32(8):677–87.
240. Longo G, Alonso-Sarduy L, Rio LM, Bizzini A, Trampuz A, Notz J, et al. Rapid detection of bacterial resistance to antibiotics using AFM cantilevers as nanomechanical sensors. *Nat Nanotechnol.* 2013 Jul;8(7):522–6.
241. Aghayee S, Benadiba C, Notz J, Kasas S, Dietler G, Longo G. Combination of fluorescence microscopy and nanomotion detection to characterize bacteria. *J Mol Recognit JMR.* 2013 Nov;26(11):590–5.
242. Boisen A, Dohn S, Keller SS, Schmid S, Tenje M. Cantilever-like micromechanical sensors. *Rep Prog Phys.* 2011 Mar 1;74(3):036101.
243. Waggoner PS, Craighead HG. Micro- and nanomechanical sensors for environmental, chemical, and biological detection. *Lab Chip.* 2007 Oct;7(10):1238–55.
244. Tamayo J, Pini V, Kosaka P, Martinez NF, Ahumada O, Calleja M. Imaging the surface stress and vibration modes of a microcantilever by laser beam deflection microscopy. *Nanotechnology.* 2012 Aug 10;23(31):315501.
245. Gfeller KY, Nugaeva N, Hegner M. Rapid biosensor for detection of antibiotic-selective growth of *Escherichia coli*. *Appl Environ Microbiol.* 2005 May;71(5):2626–31.
246. Detzel AJ, Campbell GA, Mutharasan R. Rapid assessment of *Escherichia coli* by growth rate on piezoelectric-excited millimeter-sized cantilever (PEMC) sensors. *Sens Actuators B Chem.* 2006 Sep 12;117(1):58–64.



247. Paul Wali R, Wilkinson PR, Eaimkhong SP, Hernando-Garcia J, Sánchez-Rojas JL, Ababneh A, et al. Fourier transform mechanical spectroscopy of micro-fabricated electromechanical resonators: A novel, information-rich pulse method for sensor applications. *Sens Actuators B Chem.* 2010 Jun 3;147(2):508–16.
248. Reed J, Wilkinson P, Schmit J, Klug W, Gimzewski JK. Observation of nanoscale dynamics in cantilever sensor arrays. *Nanotechnology.* 2006 Aug 14;17(15):3873.
249. Park K, Millet LJ, Kim N, Li H, Jin X, Popescu G, et al. Measurement of adherent cell mass and growth. *Proc Natl Acad Sci U S A.* 2010 Nov 30;107(48):20691–6.
250. Horvat RT. Review of Antibiogram Preparation and Susceptibility Testing Systems. *Hosp Pharm.* 2010 Oct 22;45(Supplement 1):S6–9.
251. Pfyffer GE, Welscher HM, Kissling P, Cieslak C, Casal MJ, Gutierrez J, et al. Comparison of the Mycobacteria Growth Indicator Tube (MGIT) with radiometric and solid culture for recovery of acid-fast bacilli. *J Clin Microbiol.* 1997 Feb;35(2):364–8.
252. Croxatto A, Prod'hom G, Durussel C, Greub G. Preparation of a blood culture pellet for rapid bacterial identification and antibiotic susceptibility testing. *J Vis Exp JoVE.* 2014;(92):e51985.
253. Prod'hom G, Durussel C, Greub G. A simple blood-culture bacterial pellet preparation for faster accurate direct bacterial identification and antibiotic susceptibility testing with the VITEK 2 system. *J Med Microbiol.* 2013 May;62(Pt 5):773–7.
254. Opota O, Croxatto A, Prod'hom G, Greub G. Blood culture-based diagnosis of bacteraemia: state of the art. *Clin Microbiol Infect Off Publ Eur Soc Clin Microbiol Infect Dis.* 2015 Apr;21(4):313–22.
255. Berg CM, Anderson SV. Penicillin-Induced Lysis of *Escherichia coli* in Medium That Does Not Support Sustained Growth. *Antimicrob Agents Chemother.* 1976 Apr;9(4):713–5.
256. Boman HG, Eriksson KG. Penicillin Induced Lysis in *Escherichia coli*. *J Gen Microbiol.* 1963 Jun 1;31(3):339–52.
257. Kasas S, Ruggeri FS, Benadiba C, Maillard C, Stupar P, Tournu H, et al. Detecting nanoscale vibrations as signature of life. *Proc Natl Acad Sci.* 2015 Jan 13;112(2):378–81.
258. Wayne P. USA: CLSI; 2012. *Clin Lab Stand Inst Perform Stand Antimicrob Susceptibility Test Twenty-Second Informational Suppl CLSI Doc M100-S22.*
259. Testing EC on AS, others. Antimicrobial susceptibility testing EUCAST disk diffusion method. Available Accessed [Internet]. 2017;27. Available from: [http://www.eucast.org/fileadmin/src/media/PDFs/EUCAST\\_files/Disk\\_test\\_documents/Version\\_5/Manual\\_v\\_6.0\\_EUCAST\\_Disk\\_Test\\_final.pdf](http://www.eucast.org/fileadmin/src/media/PDFs/EUCAST_files/Disk_test_documents/Version_5/Manual_v_6.0_EUCAST_Disk_Test_final.pdf)

260. Mittman SA, Huard RC, Della-Latta P, Whittier S. Comparison of BD phoenix to vitek 2, microscan MICroSTREP, and Etest for antimicrobial susceptibility testing of *Streptococcus pneumoniae*. *J Clin Microbiol*. 2009 Nov;47(11):3557–61.
261. Chatzigeorgiou K-S, Sergentanis TN, Tsiodras S, Hamodrakas SJ, Bagos PG. Phoenix 100 versus Vitek 2 in the Identification of Gram-Positive and Gram-Negative Bacteria: a Comprehensive Meta-Analysis. *J Clin Microbiol*. 2011 Sep 1;49(9):3284–91.
262. Snyder JW, Munier GK, Johnson CL. Direct comparison of the BD phoenix system with the MicroScan WalkAway system for identification and antimicrobial susceptibility testing of Enterobacteriaceae and nonfermentative gram-negative organisms. *J Clin Microbiol*. 2008 Jul;46(7):2327–33.
263. Theophel K, Schacht VJ, Schlüter M, Schnell S, Stingu C-S, Schaumann R, et al. The importance of growth kinetic analysis in determining bacterial susceptibility against antibiotics and silver nanoparticles. *Front Microbiol*. 2014;5:544.
264. Arnal L, Grunert T, Cattelan N, de Gouw D, Villalba MI, Serra DO, et al. Bordetella pertussis Isolates from Argentinean Whooping Cough Patients Display Enhanced Biofilm Formation Capacity Compared to Tohama I Reference Strain. *Front Microbiol* [Internet]. 2015 Dec 8 [cited 2017 Oct 18];6. Available from: <https://www.ncbi.nlm.nih.gov/pmc/articles/PMC4672677/>
265. Serra DO, Lücking G, Weiland F, Schulz S, Görg A, Yantorno OM, et al. Proteome approaches combined with Fourier transform infrared spectroscopy revealed a distinctive biofilm physiology in *Bordetella pertussis*. *Proteomics*. 2008 Dec;8(23–24):4995–5010.
266. Wang L, Fan D, Chen W, Terentjev EM. Bacterial growth, detachment and cell size control on polyethylene terephthalate surfaces. *Sci Rep*. 2015 Oct 14;5:15159.
267. Altunaiji SM, Kukuruzovic RH, Curtis NC, Massie J. Antibiotics for whooping cough (pertussis). *Cochrane Database Syst Rev* [Internet]. 2007;(3). Available from: <http://dx.doi.org/10.1002/14651858.CD004404.pub3>
268. Pankey GA, Sabath LD. Clinical relevance of bacteriostatic versus bactericidal mechanisms of action in the treatment of Gram-positive bacterial infections. *Clin Infect Dis Off Publ Infect Dis Soc Am*. 2004 Mar 15;38(6):864–70.
269. Menozzi FD, Gantiez C, Loch C. Identification and purification of transferrin- and lactoferrin-binding proteins of *Bordetella pertussis* and *Bordetella bronchiseptica*. *Infect Immun*. 1991 Nov;59(11):3982–8.
270. Nanduri B, Lawrence ML, Peddinti DS, Burgess SC. Effects of subminimum inhibitory concentrations of antibiotics on the *Pasteurella multocida* proteome: a systems approach. *Comp Funct Genomics*. 2008;254836.
271. Yang D, Oyaizu Y, Oyaizu H, Olsen GJ, Woese CR. Mitochondrial origins. *Proc Natl Acad Sci*. 1985 Jul 1;82(13):4443–7.

272. Schapira AH. Mitochondrial diseases. *The Lancet*. 2012 May 18;379(9828):1825–34.
273. Meyer JN, Leung MCK, Rooney JP, Sandoel A, Hengartner MO, Kisby GE, et al. Mitochondria as a Target of Environmental Toxicants. *Toxicol Sci*. 2013 Jul;134(1):1–17.
274. Lanza IR, Nair KS. Functional Assessment of Isolated Mitochondria In Vitro. *Methods Enzymol*. 2009;457:349–72.
275. Hong S, Pedersen PL. ATP Synthase and the Actions of Inhibitors Utilized To Study Its Roles in Human Health, Disease, and Other Scientific Areas. *Microbiol Mol Biol Rev*. 2008 Dec 1;72(4):590–641.
276. Li N, Ragheb K, Lawler G, Sturgis J, Rajwa B, Melendez JA, et al. Mitochondrial Complex I Inhibitor Rotenone Induces Apoptosis through Enhancing Mitochondrial Reactive Oxygen Species Production. *J Biol Chem*. 2003 Mar 7;278(10):8516–25.
277. Kristián T, Hopkins IB, McKenna MC, Fiskum G. Isolation of mitochondria with high respiratory control from primary cultures of neurons and astrocytes using nitrogen cavitation. *J Neurosci Methods*. 2006 Apr 15;152(1–2):136–43.
278. Bowler MW, Montgomery MG, Leslie AGW, Walker JE. How azide inhibits ATP hydrolysis by the F-ATPases. *Proc Natl Acad Sci*. 2006 Jun 6;103(23):8646–9.
279. Minkov IB, Strotmann H. The effect of azide on regulation of the chloroplast H<sup>+</sup>-ATPase by ADP and phosphate. *Biochim Biophys Acta BBA - Bioenerg*. 1989 Jan 1;973(1):7–12.
280. Balmain A, Gray J, Ponder B. The genetics and genomics of cancer. *Nat Genet*. 2003 Mar 1;33:238–44.
281. Palmeira A, Sousa E, Helena Vasconcelos M, Pinto M, X. Fernandes M. Structure and Ligand-based Design of P-glycoprotein Inhibitors: A Historical Perspective. *Curr Pharm Des*. 2012 Sep 1;18(27):4197–214.
282. Podolski-Renić A, Jadranin M, Stanković T, Banković J, Stojković S, Chiourea M, et al. Molecular and cytogenetic changes in multi-drug resistant cancer cells and their influence on new compounds testing. *Cancer Chemother Pharmacol*. 2013 Aug 10;72(3):683–97.
283. Holohan C, Van Schaeybroeck S, Longley DB, Johnston PG. Cancer drug resistance: an evolving paradigm. *Nat Rev Cancer*. 2013 Oct;13(10):714–26.
284. Bredel M. Anticancer drug resistance in primary human brain tumors. *Brain Res Brain Res Rev*. 2001 Apr;35(2):161–204.
285. Stavrovskaya AA. Cellular mechanisms of multidrug resistance of tumor cells. *Biochem Biokhimiia*. 2000 Jan;65(1):95–106.
286. Leslie EM, Deeley RG, Cole SPC. Multidrug resistance proteins: role of P-glycoprotein, MRP1, MRP2, and BCRP (ABCG2) in tissue defense. *Toxicol Appl Pharmacol*. 2005 May 1;204(3):216–37.

287. Rosa M. Advances in the Molecular Analysis of Breast Cancer: Pathway Toward Personalized Medicine. *Cancer Control J Moffitt Cancer Cent.* 2015 Apr;22(2):211–9.
288. Zhang SY, Zhang SQ, Nagaraju GP, El-Rayes BF. Biomarkers for personalized medicine in GI cancers. *Mol Aspects Med* [Internet]. [cited 2015 Aug 5]; Available from: <http://www.sciencedirect.com/science/article/pii/S0098299715000370>
289. Ali MY, Anand SV, Tangella K, Ramkumar D, Saif TA. Isolation of Primary Human Colon Tumor Cells from Surgical Tissues and Culturing Them Directly on Soft Elastic Substrates for Traction Cytometry. *J Vis Exp* [Internet]. 2015 Jun 4 [cited 2015 Aug 5];(100). Available from: <http://www.jove.com/video/52532/isolation-primary-human-colon-tumor-cells-from-surgical-tissues>
290. Perlman ZE, Slack MD, Feng Y, Mitchison TJ, Wu LF, Altschuler SJ. Multidimensional Drug Profiling By Automated Microscopy. *Science.* 2004 Nov 12;306(5699):1194–8.
291. Pesic M, Markovic J z., Jankovic D, Kanazir S, Markovic I d., Rakic L, et al. Induced Resistance in the Human Non Small Cell Lung Carcinoma (NCI-H460) Cell Line In Vitro by Anticancer Drugs. *J Chemother.* 2006 Feb 1;18(1):66–73.
292. Podolski-Renić A, Anđelković T, Banković J, Tanić N, Ruždijić S, Pešić M. The role of paclitaxel in the development and treatment of multidrug resistant cancer cell lines. *Bioméd Pharmacother Bioméd Pharmacothérapie.* 2011 Aug;65(5):345–53.
293. Gottesman MM, Fojo T, Bates SE. Multidrug resistance in cancer: role of ATP-dependent transporters. *Nat Rev Cancer.* 2002 Jan;2(1):48–58.
294. Scotto KW. Transcriptional regulation of ABC drug transporters. *Oncogene.* 2003;22(47):7496–511.
295. Longley DB, Johnston PG. Molecular mechanisms of drug resistance. *J Pathol.* 2005 Jan;205(2):275–92.
296. Tacar O, Sriamornsak P, Dass CR. Doxorubicin: an update on anticancer molecular action, toxicity and novel drug delivery systems. *J Pharm Pharmacol.* 2013 Feb 1;65(2):157–70.
297. Eom Y-W, Kim MA, Park SS, Goo MJ, Kwon HJ, Sohn S, et al. Two distinct modes of cell death induced by doxorubicin: apoptosis and cell death through mitotic catastrophe accompanied by senescence-like phenotype. *Oncogene.* 2005 May 2;24(30):4765–77.
298. Trueba FJ, Woldringh CL. Changes in cell diameter during the division cycle of *Escherichia coli*. *J Bacteriol.* 1980 Jun 1;142(3):869–78.
299. Kumar MS, Philominathan P. The physics of flagellar motion of *E. coli* during chemotaxis. *Biophys Rev.* 2009 Dec 18;2(1):13–20.
300. Berg HC. Torque generation by the flagellar rotary motor. *Biophys J.* 1995 Apr;68(4 Suppl):163S–167S.

301. Li C, Louise CJ, Shi W, Adler J. Adverse conditions which cause lack of flagella in *Escherichia coli*. *J Bacteriol.* 1993 Apr;175(8):2229–35.
302. Guo M, Ehrlicher AJ, Jensen MH, Renz M, Moore JR, Goldman RD, et al. Probing the Stochastic, Motor-Driven Properties of the Cytoplasm Using Force Spectrum Microscopy. *Cell.* 2014 Aug 14;158(4):822–32.
303. Cattin CJ, Düggelin M, Martinez-Martin D, Gerber C, Müller DJ, Stewart MP. Mechanical control of mitotic progression in single animal cells. *Proc Natl Acad Sci.* 2015 Sep 8;112(36):11258–63.
304. Syal K, Iriya R, Yang Y, Yu H, Wang S, Haydel SE, et al. Antimicrobial Susceptibility Test with Plasmonic Imaging and Tracking of Single Bacterial Motions on Nanometer Scale. *ACS Nano.* 2016 Jan 26;10(1):845–52.
305. Johnson WL, France DC, Rentz NS, Cordell WT, Walls FL. Sensing bacterial vibrations and early response to antibiotics with phase noise of a resonant crystal. *Sci Rep [Internet].* 2017 Sep 22 [cited 2017 Oct 29];7. Available from: <https://www.ncbi.nlm.nih.gov/pmc/articles/PMC5610186/>
306. Martínez-Martín D, Fläschner G, Gaub B, Martin S, Newton R, Beerli C, et al. Inertial picobalance reveals fast mass fluctuations in mammalian cells. *Nature.* 2017 Oct 26;550(7677):500–5.
307. Mårdh P-A, Ripa T, Andersson K-E, Wadsö I. Kinetics of the Actions of Tetracyclines on *Escherichia coli* as Studied by Microcalorimetry. *Antimicrob Agents Chemother.* 1976 Oct 1;10(4):604–9.
308. von Ah U, Wirz D, Daniels A. Isothermal micro calorimetry – a new method for MIC determinations: results for 12 antibiotics and reference strains of *E. coli* and *S. aureus*. *BMC Microbiol.* 2009 May 26;9:106.
309. Lerchner J, Mueller-Hagen D, Roehr H, Wolf A, Mertens F, Mueller R, et al. Chip-calorimetric evaluation of the efficacy of antibiotics and bacteriophages against bacteria on a minute-timescale. *J Therm Anal Calorim.* 2011 Jan 8;104(1):31–6.
310. Ramos D, Mertens J, Calleja M, Tamayo J. Study of the Origin of Bending Induced by Bimetallic Effect on Microcantilever. *Sensors.* 2007 Sep 5;7(9):1757–65.
311. Riedel C, Gabizon R, Wilson CAM, Hamadani K, Tsekouras K, Marqusee S, et al. The heat released during catalytic turnover enhances the diffusion of an enzyme. *Nature [Internet].* 2014 Dec 10 [cited 2014 Dec 13];advance online publication. Available from: <http://www.nature.com/nature/journal/vaop/ncurrent/full/nature14043.html>
312. Chiang Y-L, Lin C-H, Yen M-Y, Su Y-D, Chen S-J, Chen H. Innovative antimicrobial susceptibility testing method using surface plasmon resonance. *Biosens Bioelectron.* 2009 Mar 15;24(7):1905–10.
313. Solé M, Rius N, Lorén JG. Rapid extracellular acidification induced by glucose metabolism in non-proliferating cells of *Serratia marcescens*. *Int Microbiol.* 2000;3(1):39–43.

314. Huang Y, Sudibya HG, Chen P. Detecting metabolic activities of bacteria using a simple carbon nanotube device for high-throughput screening of anti-bacterial drugs. *Biosens Bioelectron.* 2011 Jun 15;26(10):4257–61.
315. Bashir R, Hilt JZ, Elibol O, Gupta A, Peppas NA. Micromechanical cantilever as an ultrasensitive pH microsensor. *Appl Phys Lett.* 2002;81(16):3091–3.
316. Zhang J, Lang HP, Yoshikawa G, Gerber C. Optimization of DNA Hybridization Efficiency by pH-Driven Nanomechanical Bending. *Langmuir.* 2012 Apr 17;28(15):6494–501.
317. Thakur G, Jiang K, Lee D, Prashanthi K, Kim S, Thundat T. Investigation of pH-Induced Protein Conformation Changes by Nanomechanical Deflection. *Langmuir.* 2014 Mar 4;30(8):2109–16.
318. Li J, Albri F, Maier RRJ, Shu W, Sun J, Hand DP, et al. A Micro-Machined Optical Fiber Cantilever as a Miniaturized pH Sensor. *IEEE Sens J.* 2015 Dec;15(12):7221–8.
319. Ji H, Hansen KM, Hu Z, Thundat T. Detection of pH variation using modified microcantilever sensors. *Sens Actuators B Chem.* 2001 Feb 10;72(3):233–8.
320. Carmody WR. Easily prepared wide range buffer series. *J Chem Educ.* 1961 Nov 1;38(11):559.
321. Vats P, Yu J, Rothfield L. The dynamic nature of the bacterial cytoskeleton. *Cell Mol Life Sci.* 2009 Jul 30;66(20):3353–62.

CV

## Key Skills

atomic force microscopy  
imaging & biosensing  
IT solutions  
responsible team-player  
creative communicator



p.stupar@outlook.com



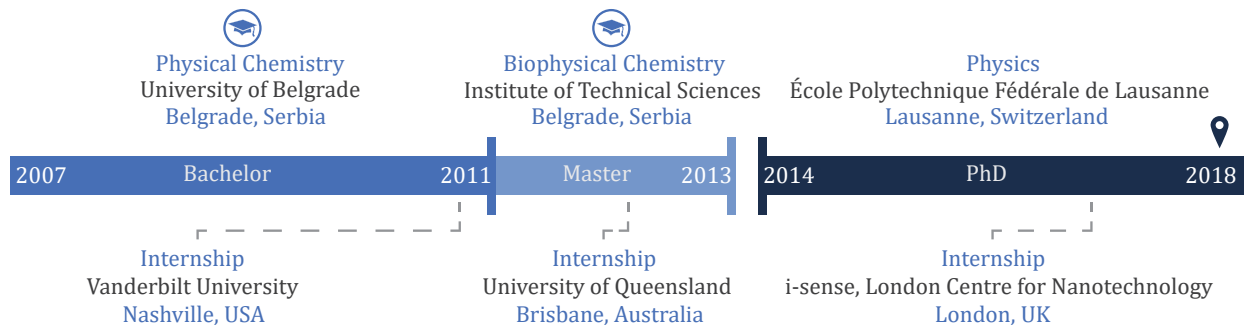
+41 78 / 769-52-13



**LinkedIn**  
www.linkedin.com/in/petar-stupar

# Petar Stupar

## Education Timeline



## Core Experience

### 2014 - present Institute of Physics - Lausanne, Switzerland Research Scientist

- Atomic force microscopy (AFM) high-resolution imaging and force mapping
  - Characterization of nano-mechanical properties: height, adhesion and stiffness mapping of mammalian, plant and bacterial cells under different physiological conditions
- Development of a new AFM-based nano-mechanical (nanomotion) biosensor
  - Cantilever-based sensing as a fast drug-screening tool against bacteria or cancer cells
- Engagement in 10+ research projects with analytical and problem solving tasks
  - Promoting team-work and international collaborations with 10+ research groups from Argentina, Switzerland (CHUV), Serbia, USA (NASA), Georgia, Belgium, UK
- Signal and image analysis, MATLAB and C++ software development for signal processing
- Teaching and supervision of undergraduate and master students, AFM coaching
- Co-organizing ColdTech meetings, student visits and designing promotional material
- Results published in 7+ international journals (PNAS, small, CMI, etc.), invited as a reviewer
- Speaker and presenter at 5 international conferences (awarded at 2/5)
- Appearing in "Living Universe" Documentary by ZED, Essential Media, ARTE and ABC

### 2012-2013 Institute of Technical Sciences - Belgrade, Serbia Master Student

- MSc in Biophysical Chemistry, 10/10 GPA
- Special Recognition Award from Serbian Chemical Society
- Characterization and cytocompatibility of polymeric nanoparticles for biomedical applications
- Main techniques used: polymer synthesis, infrared spectroscopy, TEM, MTT assay

### 2012 (10 weeks) Institute for Molecular Bioscience - Brisbane, Australia Research Intern

- Awarded with fully funded international research scholarship
- Synthesis of grafted cyclized peptides for pharmaceutical applications
- Structural characterization of synthesized peptides (HPLC, MS-TOF, 2D NMR)

### 2011 (8 weeks) Chemistry Department - Nashville, USA Research Intern

- Awarded with fully funded international research scholarship and obtained prize for the work
- Drug delivery system for targeted cancer chemotherapy (HPLC, MS, Fmoc synthesis, NMR)



## Additional Experience

- 2016 (2 weeks)** **i-sense, London Centre for Nanotechnology - London, UK**  
 Research Collaborator
- Early Warning Sensing Systems for Infectious Diseases
  - Awarded £5000 worth Mobility Fellowship
  - Strengthening collaboration and transferring nanomechanical sensing technology
  - Presenting signal analysis and experimental methods
- 2013-2014** **Freelance Graphic Design - Work Online**  
 Designer
- Logo and promotional material design, website design, design for publications
- 2007 - 2011** **Faculty of Physical Chemistry - Belgrade, Serbia**  
 Student
- BSc in physical chemistry: 9.3/10 GPA, top 1% of the class
  - Scholarship for exceptional students by Ministry of Education, Serbia
  - Student association activities, faculty info-section website admin
  - Raman Spectroscopy of tumorous and healthy tissues, matlab data analysis

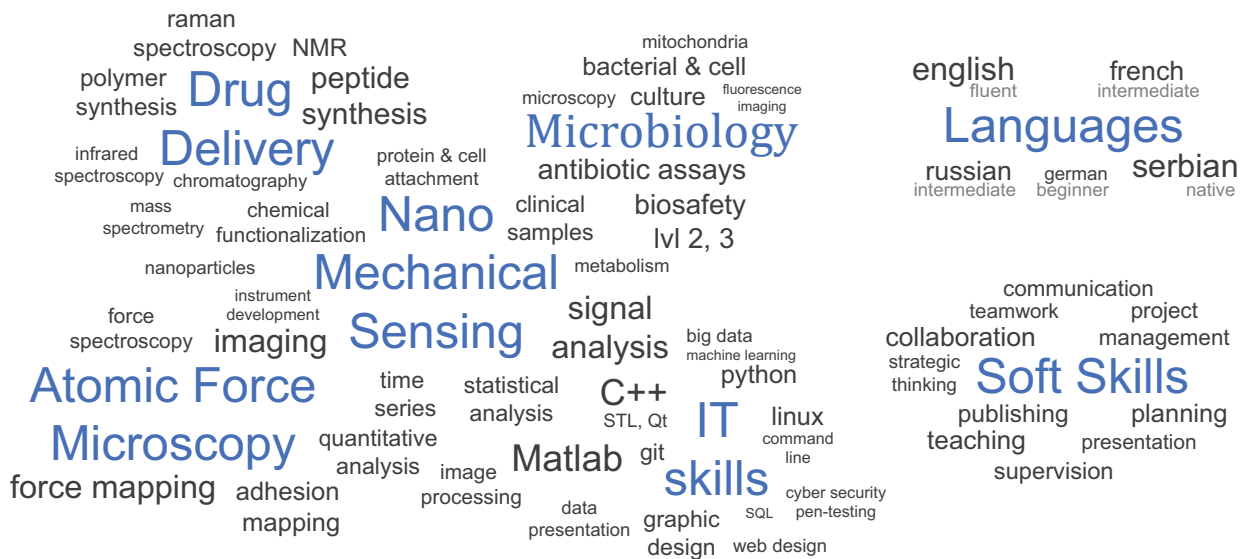
## Recent Publications

- **P. Stupar**, M. I. Villalba, et al. 2017  
 Nanomotion detection method for testing antibiotic resistance and susceptibility of slow-growing bacteria *Small*
- S. Kasas, **P. Stupar**, G. Dietler 2017  
 AFM contribution to unveil pro- and eukaryotic cell mechanical properties *Seminars in cell & developmental biology*
- **P. Stupar**, O. Opota, G. Longo, et al. 2017  
 Nanomechanical sensor applied to blood culture pellets: a fast approach to determine the antibiotic susceptibility against agents of bloodstream infections *Clinical microbiology and infection*
- **P. Stupar**, W. Chomiccki, et al. 2017  
 Mitochondrial activity detected by cantilever based sensor *Mechanical Sciences*





List of all publications:

**PubMed** **ORCID**  
[orcid.org/0000-0001-7309-0586](https://orcid.org/0000-0001-7309-0586)


## Skills



## Personal Information

-  Chemin de la Prairie 60  
Lausanne, Switzerland
-  1988, Serbian
-  Single
-  No military obligations

## Hobbies

-  drawing  
acrylic painting
-  violin
-  programming  
cyber security
-  graphic design  
video editing
-  sports
-  learning